Identification of Deep Levels in SiC and Their Elimination for Carrier Lifetime Enhancement

2013

Koutarou KAWAHARA

Electronic Science and Engineering
Kyoto University

Abstract

In this thesis, deep levels in silicon carbide (SiC) are studied to realize low-loss SiC bipolar power devices. SiC is a fascinating wide-bandgap semiconductor for realizing power devices with high performance: high blocking voltages with low energy loss. To realize high-performance SiC power devices, deep levels in SiC devices have to be controlled as in Si devices. Deep levels in semiconductors have impacts on the device performance such as reduction of the conductivity, reduction of the carrier lifetime, and enhancement of the leakage current. In SiC, the impact on a carrier lifetime is especially severe and important, which determines the ON-state loss of high-power SiC bipolar devices. However, most of the features and origins of deep levels in SiC are still an open question.

Deep levels are generated during device fabrication processes as well as growth of SiC epitaxial layers (epilayers). In this thesis, deep levels in whole range of the bandgap of SiC after device processes are investigated. These deep levels are sought to be eliminated by thermal oxidation, which was recently found to be effective for a trap reduction in as-grown materials. To control the trap reduction by thermal oxidation, the reduction mechanisms are analyzed. In addition, the origin of the $Z_{1/2}$ center, which is a deep level suppressing carrier lifetimes in n-type SiC epilayers, is attempted to be identified using both deep level transient spectroscopy (DLTS) and electron paramagnetic resonance (EPR). Taking account of the all results obtained in this study, the author discusses the control of carrier lifetimes in SiC epilayers.

In Chapter 2, the principle of DLTS and the sample preparation process for evaluation of deep levels in SiC by DLTS are explained. The typical deep levels detected in as-grown n-type and p-type SiC by DLTS are introduced.

In Chapter 3, the author investigates deep levels generated by ion implantation and reactive ion etching (RIE), which are essential processes for SiC device fabrication. As implanted ion species, N^+, P^+, and Al^+ are chosen, which are commonly used for the control of SiC conduction types (n-type and p-type). After ion implantation, the $Z_{1/2}$ ($E_C - 0.67$ eV) and $EH_{6/7}$ ($E_C - 1.5$ eV) centers are dominant in the upper half of bandgap, whereas the HS1 ($E_V + 0.39$ eV) and HK4 ($E_V + 1.4$ eV) centers are in the lower half of bandgap. The origins of these deep levels should be intrinsic defects because they are generated independently of the implanted species. In RIE-etched p-type samples, a thick semi-insulating (SI) region is formed due to compensation or deactivation of the acceptors.

Although the SI region disappears after Ar annealing at 1000°C, various deep levels remain with a high concentration in the samples.

In Chapter 4, using thermal oxidation, the author seeks to reduce the deep levels generated by the device processes (observed in Chapter 3). In ion-implanted epilayers, most deep levels is reduced by oxidation at 1150°C, whereas new deep levels such as the HK0 center ($E_V + 0.79$ eV) appear. The new levels are reduced by subsequent annealing at 1400°C in Ar ambient. In RIE-etched samples, almost all deep levels are reduced by thermal oxidation followed by Ar annealing at 1400°C.

In Chapter 5, the mechanism of the trap reduction by thermal oxidation is discussed. As deep-level-reduction processes, C^+ implantation followed by Ar annealing has been known as well as thermal oxidation. To reveal the reduction mechanism, thus, the author compares the defect behaviors (reduction, generation, and change of the depth profiles) for the two processes. Based on the results, the author proposes a model to calculate $Z_{1/2}$ distribution after thermal oxidation. In SiC epilayers with different initial $Z_{1/2}$ concentrations, this model can reproduce the depth profiles of the $Z_{1/2}$ center after oxidation at any temperatures and for any oxidation periods. The $Z_{1/2}$ center with an initial concentration of 1.3×10^{13} cm^{-3} is eliminated to a depth of > 90 μm after oxidation at 1400°C for 16.5 h.

In Chapter 6, the origin of the $Z_{1/2}$ center is identified using DLTS and EPR. Electrical properties of point defects (deep levels) are obtained from DLTS and the configuration is from EPR. The $Z_{1/2}$ concentration in SiC epilayers is changed by irradiation with various electron fluences. In each sample, concentrations of deep levels (measured by DLTS) are compared with those of point defects (measured by EPR). The $Z_{1/2}$ center and carbon vacancy (V_C) defect are found to be the dominant defects responsible for the carrier compensation observed in the irradiated samples. Furthermore, the $Z_{1/2}$ concentration corresponds to the V_C concentration irrespective of the doping concentration and the electron fluence, indicating that the $Z_{1/2}$ center originates from single V_C.

In Chapter 7, the origins of deep levels generated by thermal oxidation, ON1 ($E_C - 0.84$ eV), ON2 ($E_C - 1.1$ eV), HK0 ($E_V + 0.79$ eV), and HK2 ($E_V + 0.98$ eV), are investigated. These levels are also detected in samples after C^+ or Si^+ implantation and electron irradiation. From the behaviors (generation condition, thermal stability, and change of depth profiles) in these samples, the ON1 and ON2 centers may originate from the same defect at different charge states, related to both of a carbon interstitial (C_I) and an N atom. In contrast, the HK0 and HK2 centers may originate from a complex including carbon interstitial(s) such as $(C_I)_2$, $(C_3)_{Si}$, and $((C_2)_{Si})_2$. PL signals corresponding to these C_I-related complexes have been reported in electron-irradiated SiC, thermal stability of which is similar to that of the HK0 center.

In Chapter 8, carrier lifetimes in SiC epilayers are controlled by controlling the concentration of a lifetime killer: $Z_{1/2}$ center. A carrier lifetime is reduced with a high density of the $Z_{1/2}$ center generated by electron irradiation, whereas it is improved by the reduction of the $Z_{1/2}$ center by thermal oxidation. The $Z_{1/2}$ concentration generated by electron irradia-

tion can be controlled by adjusting the electron energy and fluence. By thermal oxidation, in contrast, a $Z_{1/2}$-free region is formed near the surface, thickness of which can be controlled using the calculation model for $Z_{1/2}$ profiles after oxidation described in Chapter 5. Comparing carrier lifetimes measured by microwave photoconductance decay (μ-PCD) with those calculated from a diffusion equation, the bulk carrier lifetime in the $Z_{1/2}$-free-region is found to be substantially long ($\sim$ 50 μs), which is sufficiently long for high conductivity modulation in SiC bipolar devices. Therefore, combination of electron irradiation and thermal oxidation should lead to the control of carrier lifetimes in SiC epilayers.

In Chapter 9, a summary of the present work is given, together with the remaining issues to be solved and suggestions for future work.

Acknowledgements

I wrote this thesis based on the study at Kyoto University Japan with support from numerous people. I would like to thank all of them. Here, I would again like to give acknowledgments to a part of them.

First of all, I would like to express my most sincere gratitude to Professor Tsunenobu Kimoto for his continuous and attentive supervision, invaluable advice and suggestions, and ceaseless encouragement during whole my study life at this university. I am also deeply grateful to Professor Gikan Takaoka and Associate Professor Mitsuru Funato for their invaluable comments and suggestions through regular discussions and refereeing my Ph.D. thesis. I am much indebted to Associate Professor Jun Suda for a great deal of his insightful comments and advice. I have also greatly benefited from Assistant Professor Yusuke Nishi for his constructive comments and support in my daily work.

My heartfelt appreciation goes to Professor Erik Janzén and Professor Nguyen Tien Son at Linköping University, Sweden, for their very kind hospitality extended to me during my stay in Sweden and their insightful comments and suggestions through fruitful discussions. I would also like to express my gratitude to Professor Gerhard Pensl and Dr. Michael Krieger at University of Erlangen-Nürnberg, Germany, for their illuminating comments through the collaborative study and at the international conferences.

My acknowledgments also go to Dr. Giovanni Alfieri, who considerately taught how to prepare samples and investigate deep levels by deep level transient spectroscopy (DLTS) to me. I am also obliged to Dr. Gan Feng for his kind instructing me on how to use hot-wall chemical vapor deposition (CVD) system and how to grow SiC epilayers. I owe a very important debt to Dr. Masato Noborio for his kind instruction on several experimental apparatuses and support of my experiments. My deep appreciation also goes to Dr. Masahiro Horita, Dr. Hiroki Miyake, and Dr. Hironori Okumura for their meaningful comments and various support in my daily work. I am also very grateful to Mr. Xuan Thang Trinh and Mr. Thien Duc Tran for their great help in my daily life in Sweden. I am also indebted to Dr. Katsunori Danno and Mr. Toru Hiyoshi. Without their illuminating studies, I could not achieve the study results in this thesis. I would like to thank very much Mr. Naoki Watanabe and Mr. Yuichiro Nanen. In my daily work, I could have fruitful discussions and enjoyable time with them. I am also grateful to Mr. Naoya Morioka and Mr. Takafumi Okuda for their stimulating comments through various discussions.

My special thanks also go to Dr. Atsushi Koizumi, Mr. Kei Senga, Mr. Ryota Suzuki, Mr. Kazuki Yamaji, Dr. Bernd Zippelius, Dr. Hironori Yoshioka, Mr. Toshihiko Hayashi, Mr. Satoru Nakagawa, Mr. Takeshi Fujimoto, Mr. Shunsaku Ueta, Mr. Tatsuya Iwata, Mr. Yibo Zhang, Mr. Yuichiro Hayashi, Mr. Xiaowei Song, Mr. Hirofumi Yamamoto, Mr. Muneharu Kato, Mr. Ryosuke Kikuchi, Mr. Ryohei Kanno, Mr. Sho Sasaki, Mr. Daisuke Harata, Mr. Daisuke Horie, Mr. Hiroki Niwa, Mr. Seigo Mori, Mr. Kouhei Adachi, Mr. Mitsuaki Kaneko, Mr. Naoki Kaji, Mr. Naoki Okimoto, Mr. Seiya Nakazawa, Mr. Shuhei Ichikawa, Mr. Chihiro Kawahara, Mr. Hajime Tanaka, Mr. Kousei Sato, Mr. Takahiro Higashi, Mr. Zeho Youn. Through discussions, chats, and sometimes trips with them, I could spend meaningful and enjoyable time in this laboratory. For very kind support in my daily work, I also wish to thank Ms. Yoriko Ohnaka and Ms. Mizuki Yamada.

This work was supported by the Funding Program for World-Leading Innovative R&D on Science and Technology (FIRST Program) and a Grant-in-Aid for Scientific Research (21226008 and 80225078) from the Japan Society for the Promotion of Science.

Finally, I sincerely wish to thank my parents, my sister and brother, and all of my friends for their understanding, support, and heartfelt encouragement.

February, 2013
Koutarou KAWAHARA

Contents

Chapter 1

Introduction

1.1 Background

Everyone knows now that the energy problems threaten the future of humanity. Fossil fuel, which human beings have depended on for a long time as an energy source, could be used up within one or two centuries; total oil reserves in the world meet about 54 years of global production, while about 64 years for natural gas and about 112 years for coal (data in 2011) [1]. Although study for developing alternative energy sources such as solar, wind, and geothermal energy has been promoted to cover the increasing of energy consumption year by year (Fig. 1.1) [2], the energy generated by the alternative sources is only 0.8% of the total energy supply today [2]. Therefore, reduction of energy consumption itself is also essential to solve the energy problems.

Reduction of energy loss in electronic power devices is one of the most effective ways for achieving the reduction of energy consumption. In these days, electricity has become more important and been widely used as shown in Fig. 1.1. In 2009, the ratio of electric energy consumption to total energy consumption is about 17% as world average, which will be higher in the future because developing countries will be industrialized and use more electricity. Electricity is partly lost at many electronic power devices during power transmission from power plants to terminal devices, which yields enormous waste of energy. Taking into account that the market of power devices has rapidly enlarged as shown in Fig. 1.2 [3], realizing low-loss electronic power devices is key issue for the reduction of energy consumption.

Silicon (Si) is the most commonly used semiconductor for electronic power devices, which has been extensively investigated and optimized for low-loss and low-cost devices. Although the continuous progress has been made until today, these devices are approaching the theoretical limit determined from the material properties of Si, indicating that a next-generation semiconductor material has to be applied for further improvements of power devices. Silicon carbide (SiC) is a fascinating candidate as a new semiconductor with superior properties.

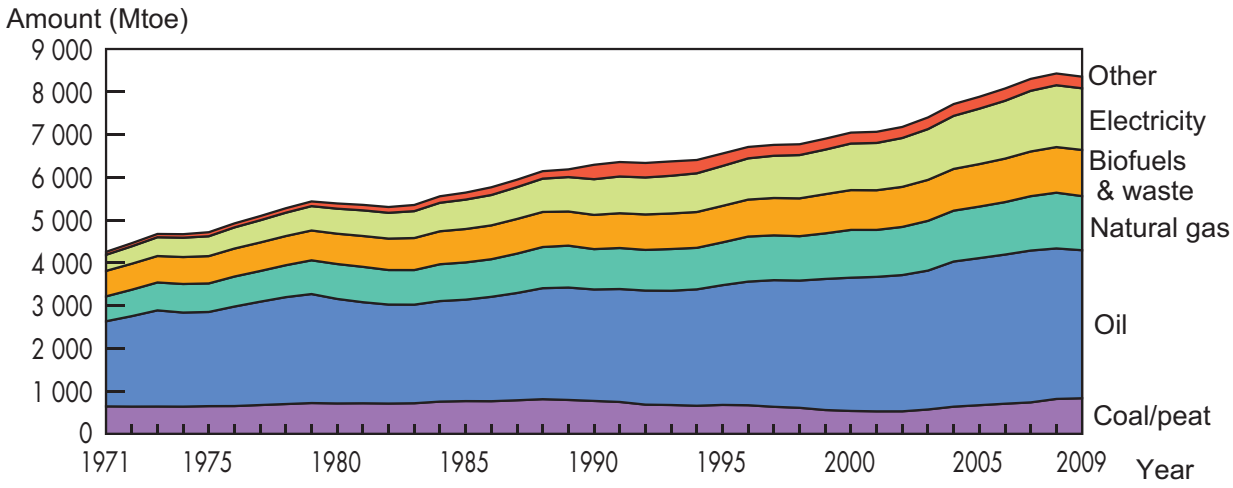

Figure 1.1: World total energy consumption from 1971 to 2009 [2]. The unit "Mtoe" means million tonnes of oil equivalent.

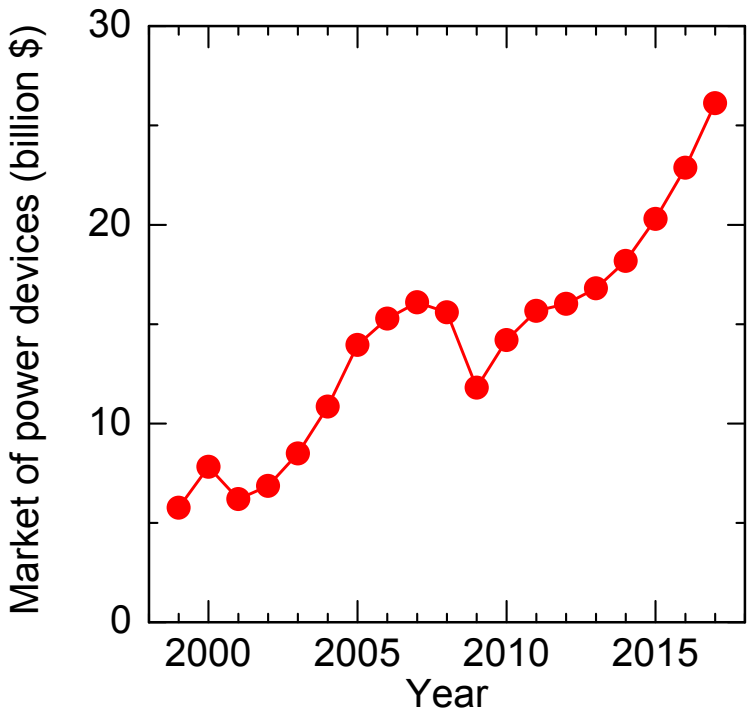

Figure 1.2: Transition and prediction of power device market [3]. The data earlier than 2011 are defined values while the others are predicted values.

1.2 SiC Power Devices for High Energy Efficiency

1.2.1 Properties of SiC

As a promising wide-bandgap semiconductor realizing high-power, high-temperature, and high-frequency devices, SiC has attracted increasing attention and extensively investigated [4–10]. Table 1.1 shows physical properties and technological status of various polytypes of SiC along with other common semiconductor materials. SiC has numerous crystal structures called polytypes, among of which, 3C-, 4H-, and 6H-SiC are the most popular and important for electronic device applications. Schematic crystal structure of the major polytypes is shown in Fig. 1.3. Note that SiC, especially 4H-SiC, possesses a wide bandgap (4H-SiC: 3.26 eV) and high breakdown field (4H-SiC: 3 MV/cm) as shown in Table 1.1. The wide bandgap suppresses thermal excitation of electrons from the valence band to the conduction band in SiC, which allows high operating temperature of SiC devices above 500°C. In addition, the high breakdown field leads to high breakdown voltage and low ON-resistance of SiC devices [11]. Fig. 1.4 shows relationship between ON-resistance and breakdown voltage for Si (dashed line) and SiC (solid line) unipolar devices. The breakdown voltage (V_{B}) is represented as the area of triangle shown in Fig. 1.5, and is described as:

$$V_{\mathrm{B}} = \frac{E_{\mathrm{B}} W_{\mathrm{M}}}{2}, \tag{1.1}$$

where E_{B} is the breakdown electric field and W_{M} the maximum width of depletion region. At the breakdown, the maximum depletion width is given by:

$$W_{\mathrm{M}} = \frac{\varepsilon E_{\mathrm{B}}}{e N_{\mathrm{b}}}, \tag{1.2}$$

where ε is the permittivity of the semiconductor, e the elementary charge, and N_{b} the doping concentration of the semiconductor. From Eqs. (1.1) and (1.2), the breakdown voltage of semiconductor devices is expressed as:

$$V_{\mathrm{B}} = \frac{\varepsilon {E_{\mathrm{B}}}^2}{2 e N_{\mathrm{b}}}. \tag{1.3}$$

Note that E_{B} is inherent to the semiconductor material, so that only the N_{b} (and the device thickness) is a parameter to adjust V_{B} of semiconductor devices. Because E_{B} of SiC is about ten times larger than that of Si as shown in Table 1.1, SiC devices show a hundred times higher V_{B} than Si devices at a given N_{b}, whereas SiC devices can have a hundred times higher N_{b} to obtain the same V_{B}. N_{b} also directly influences ON-resistance R_{ON}, which is another important performance determining ON-state loss in power semiconductor devices. When drift resistance is the dominant component of the ON-resistance and other components such as contact resistance can be negligible, R_{ON} of unipolar devices with a non-punch-through structure can be calculated simply by the following equation, taking into account that the drift region behaves as a resistor under forward bias condition:

$$R_{\mathrm{ON}} = \frac{4 {V_{\mathrm{B}}}^2}{\varepsilon \mu {E_{\mathrm{B}}}^3}, \tag{1.4}$$

Table 1.1: Physical properties and technological status of various polytypes of SiC along with other common semiconductor materials (data given at room temperature).

Property	SiC			Si	GaAs	GaN
	3C	4H	6H			
Crystal Structure	ZB	4H	6H	Dia.	ZB	W
Lattice Constant (Å)	4.36	$a = 3.09$ $c = 10.08$	$a = 3.09$ $c = 15.12$	5.43	5.65	$a = 3.19$ $c = 5.19$
Band Structure	I.D.	I.D.	I.D.	I.D.	D.	D.
Bandgap (eV)	2.3	3.26	3.02	1.12	1.42	3.42
Electron Mobility (cm^2/Vs)	1000	1000 ($\perp$ c) 1200 (// c)	450 ($\perp$ c) 100 (// c)	1350	8500	1500
Hole Mobility (cm^2/Vs)	50	120	100	450	400	50
Electron Saturation Velocity (10^7 cm/s)	2.7	2.2	1.9	1	1	2.7
Breakdown Field (MV/cm)	2	3	3	0.3	0.4	3
Thermal Conductivity (W/cmK)	4.9	4.9	4.9	1.5	0.46	1.3
Relative Permittivity	10	9.7 ($\perp$ c) 10.2 (// c)	9.7 ($\perp$ c) 10.2 (// c)	11.9	12.8	10.4
Conductivity Control	△	◯	◯	◯	◯	△
Thermal Oxide	◯	◯	◯	◯	×	×
Conductive Wafer	△ (Si)	◯	◯	◯	◯	△ (SiC)
Insulating Wafer	×	◯	◯	△ (SOI)	◯	△ (Sapphire)

ZB: Zincblende Dia.: Diamond W: Wurtzite
I.D.: Indirect D.: Direct
◯: Good △: Fair ×: Difficult

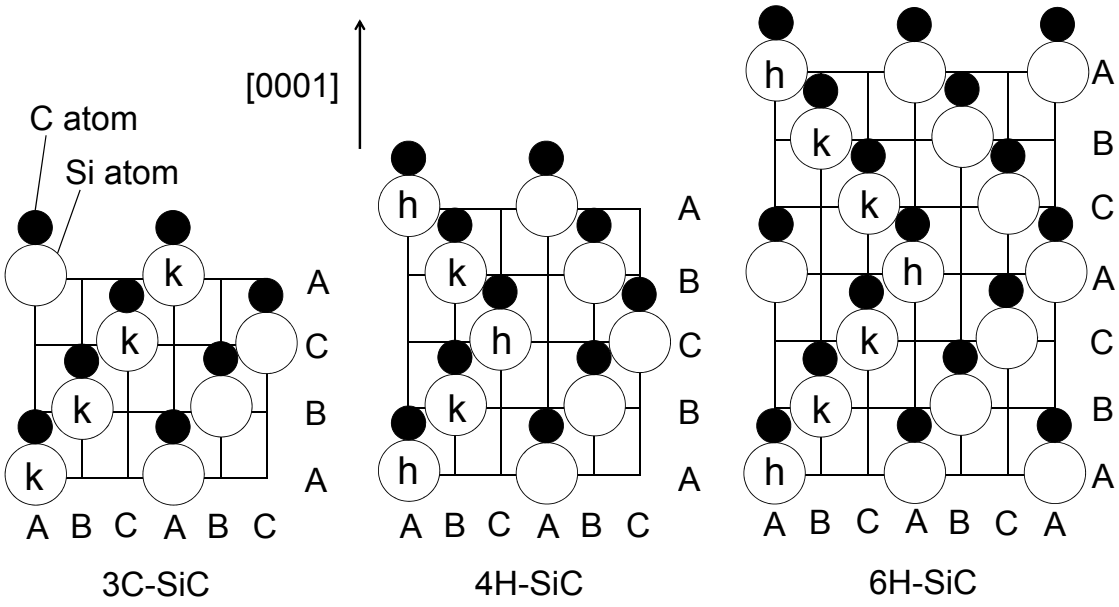

Figure 1.3: Schematic crystal structures of major SiC polytypes. SiC has three possible occupation sites denoted by A, B, and C, which are also categorized as cubic site (k) or hexagonal site (h).

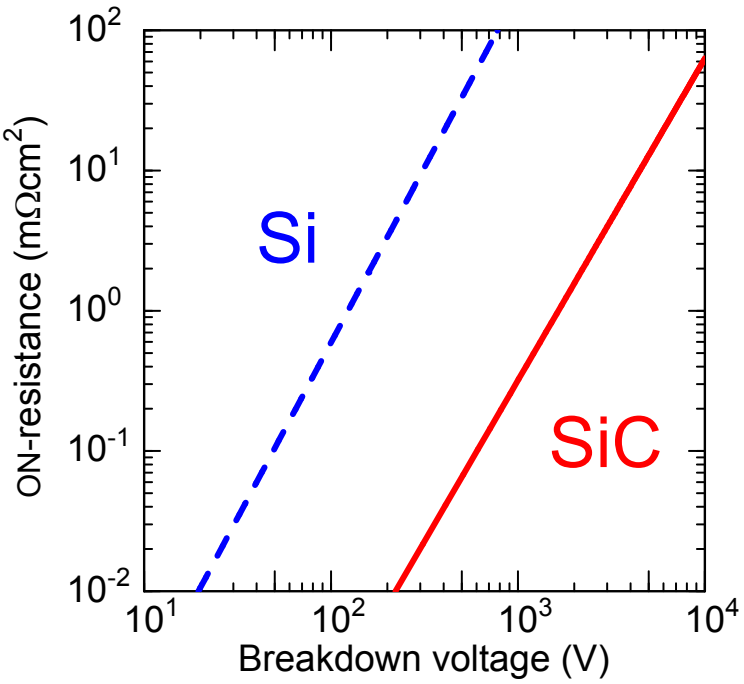

Figure 1.4: Relationship between ON-resistance and breakdown voltage for Si (dashed line) and SiC (solid line) unipolar devices.

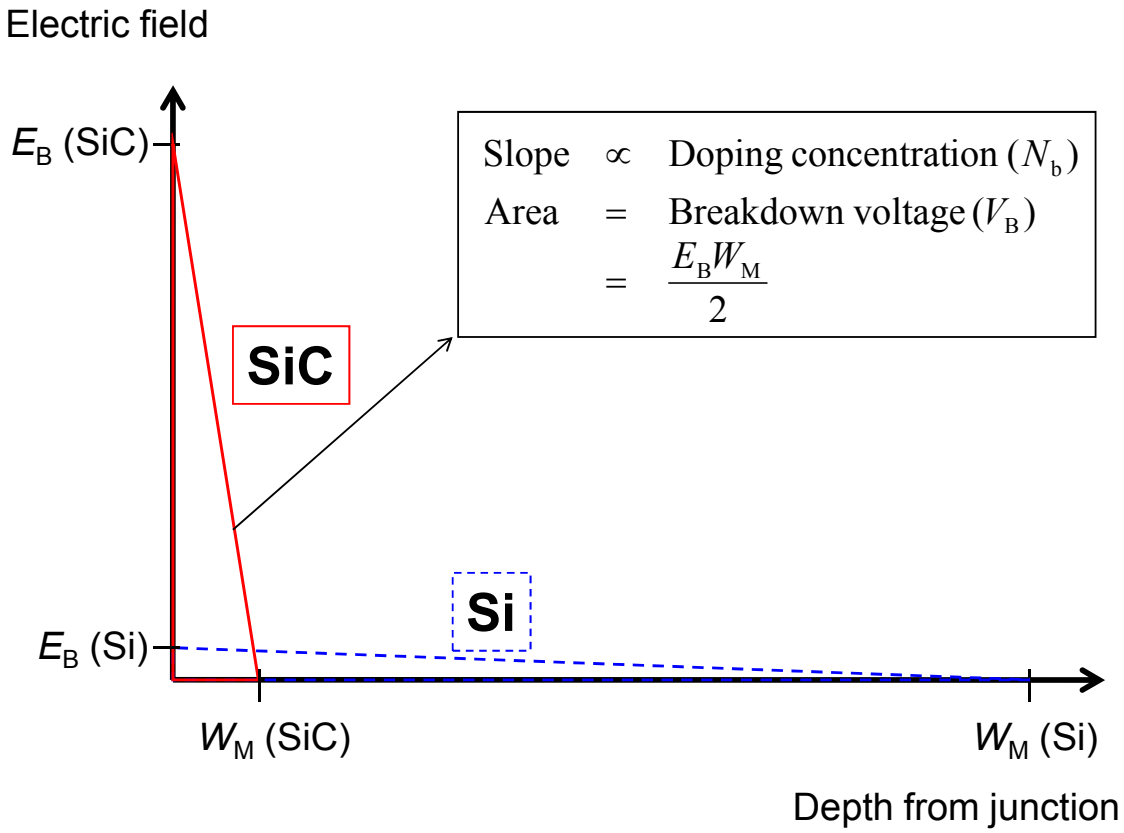

Figure 1.5: Distribution of electric field for Si (dashed line) and SiC (solid line) Schottky or one-sided abrupt *pn* junction.

where μ is the carrier mobility in the semiconductor. As shown in Fig. 1.4, with given V_B lower R_{ON} can be achieved in SiC unipolar devices compared with Si due to the higher E_B of SiC.

1.2.2 SiC Bipolar Devices

As mentioned in the last section, unipolar devices with higher blocking voltage have higher R_{ON} due to lower N_b and a thicker epilayer. In contrast, R_{ON} of bipolar devices can be kept low even in epilayers with low N_b thanks to the "conductivity modulation". Fig. 1.6 shows the carrier distribution profile in a PiN diode under forward bias condition. The carrier (both electron and hole) concentration in the n^- layer increases by injection of electrons (from the n^+ layer) and holes (from the p^+ layer), leading to lower R_{ON} compared to that in unipolar devices with the same blocking voltage. Therefore, SiC bipolar devices should be applied for a blocking voltage higher than several kV. To realize high-performance SiC bipolar devices, it is key issue to control a carrier lifetime in SiC epilayers, which determines the on-state resistance as well as the switching speed.

1.3 Deep Levels

1.3.1 Effects of Deep Levels on SiC Devices

A semiconductor crystal contains various kinds of defects, planar defects (stacking faults (SFs)), line defects (dislocations), and point defects. In particular, point defects have very wide variety such as impurity atoms, intrinsic defects (e.g. vacancies, interstitials), and complexes of these. A part of point defects forms trap levels in the bandgap of the semiconductor, which are roughly categorized to shallow levels and deep levels based on the energy position. In addition, a trap level being in the negative charge state with an electron (e.g. $(-/0)$, $(2-/-)$) is called acceptor-like trap, while a trap in the positive with a hole (e.g. $(0/+)$, $(+/2+)$) is donor-like trap. A donor-like shallow level near the conduction band edge works as a donor, while an acceptor-like shallow level near the valence band edge works as a acceptor, which are important levels to determine the conductivity of the semiconductor. The other shallow levels, an acceptor-like trap near the conduction band edge or a donor-like trap near the valence band edge, trap carriers in each band but rapidly emit the carriers. Repeated transitions of electrons (or holes) between shallow traps and each band will lead to degradation of the effective carrier mobility in the semiconductor. In contrast, carriers trapped at deep levels cannot be easily emitted because the energy barriers (from the deep levels to each band edge) are much higher than the thermal energy of carriers. Thus, deep levels have a great effect on the electrical properties of the semiconductor; deep levels (i) reduce the conductivity by compensating donors in n-type materials (in the case of acceptor-like levels) or acceptors in p-type materials (in the case of donor-like levels),

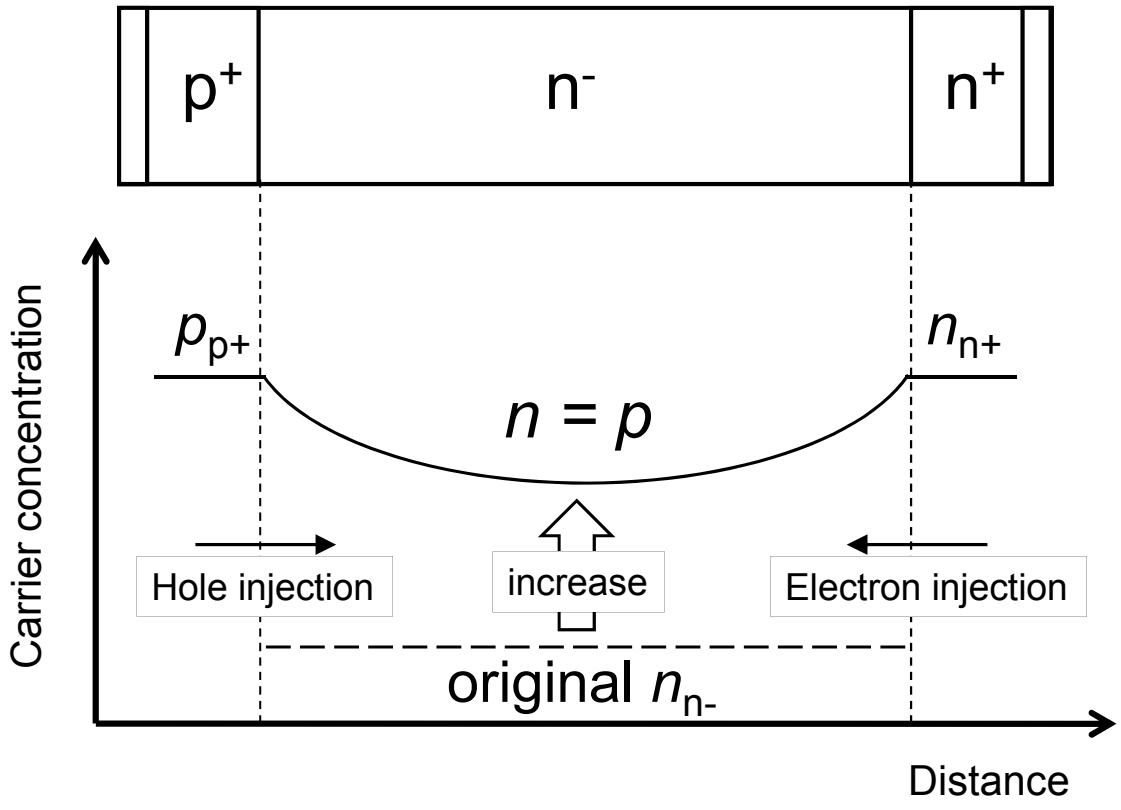

Figure 1.6: Carrier distribution profile in PiN diode under forward bias condition.

(ii) reduce carrier lifetimes when these work as recombination centers [12], (iii) increase the leakage current when these work as generation centers under reverse bias condition. The types and the effects of deep levels are summarized in Table 1.2 and Fig. 1.7.

For SiC devices fabricated on the state-of-art epitaxial layers, the effect of isolated deep levels on the leakage current can be ignored because intrinsic carrier concentration (to which carrier generation ratio is approximately in proportion) of SiC is about nineteen orders of magnitude lower than that of Si at room temperature (about ten orders of magnitude lower at 300°C). In contrast, the effect on a carrier lifetime is, as mentioned in the last section, a big issue for SiC bipolar devices with high blocking voltage, indicating that control of deep levels is one of the most important subjects for realization of high-performance SiC devices.

1.3.2 Present Knowledge of Deep Levels in SiC and Key Issues

Point defects in Si have very well been characterized by deep level transient spectroscopy (DLTS) [13–27], photoluminescence (PL) [17, 24, 28, 29], electron paramagnetic resonance (EPR) [17, 30–33], infrared absorption spectrometry (IR) [34, 35], and so on, leading to the control of carrier lifetimes in Si crystals [14, 36–38]. To identify origins of deep levels in Si crystals has been tough due to the great variety of the configurations: intrinsic defects (e.g. vacancy, di-vacancy, interstitial), impurities (e.g. hydrogen, oxygen, carbon, transition metals), and the complexes. Furthermore, a point defect in different charge state forms a different deep level.

Investigation of deep levels in SiC is much harder than in Si because SiC is a compound semiconductor consisting of silicon and carbon atoms, which means that there are six kinds of defects even as a single intrinsic defect: silicon vacancy (V_{Si}), carbon vacancy (V_C), silicon interstitial (Si_I), carbon interstitial (C_I), silicon antisite (Si_C), and carbon antisite (C_{Si}). As shown in Fig. 1.3, in addition, SiC has two kinds of sites, cubic and hexagonal sites, for each constituent atom (Si and C), resulting in a huge variety of deep levels.

Deep levels are generated during epitaxial growth [8, 39–52] and device fabrication steps. So far, many papers have been published on deep levels in as-grown and irradiated 4H-SiC [8, 39–63]. Through fundamental studies on SiC growth and characterization in the last decade, deep levels in as-grown 4H-SiC, both n- and p-type materials, have been mostly elucidated, although the microscopic structures of almost all the deep levels are still an open question. In contrast, insights on deep levels introduced by device fabrication processes are limited [39, 64–72]. Thus, the clarification and reduction of deep levels generated by device processes are a part of key issues in this study.

A deep level named $Z_{1/2}$ ($E_C - 0.67$ eV) center has been identified as a lifetime killer in n-type 4H-SiC [73–75]. A typical carrier lifetime for commercially available SiC epilayers is only 0.6–1 μs due to a high $Z_{1/2}$ concentration of about 10^{13} cm^{-3}, while over 5-μs lifetime is required for 10-kV PiN-diodes. Therefore, the control of the $Z_{1/2}$ center and improving a carrier lifetime in SiC are other key issues in this study.

Table 1.2: Categorization of deep levels and the effects on semiconductor materials.

Type	Working as	Sign	occupied 	empty
Acceptor like	Electron trap, Recombination center, Generation center	(2−/−)	double negative	single negative
		(−/0)	single negative	neutral
Donor like	Hole trap, Recombination center, Generation center	(0/+)	neutral	single positive
		(+/2+)	single positive	double positive

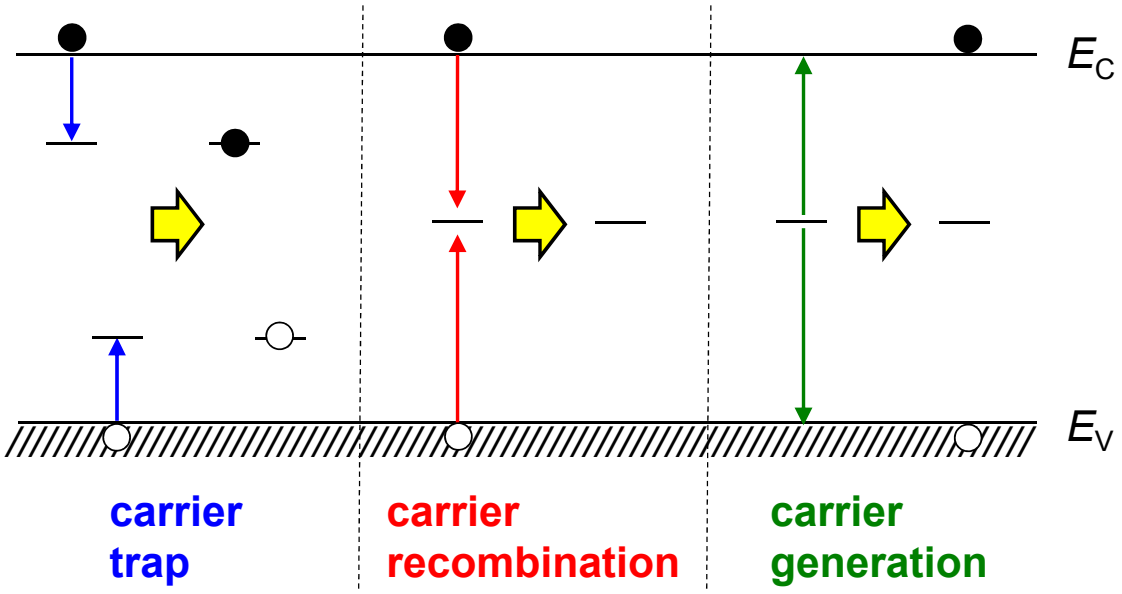

Figure 1.7: Schematic diagram of carrier trapping by deep levels, and carrier recombination or generation via a deep level.

1.4 Aim of This Study and Outline of This Thesis

The end goal of this study is to control carrier lifetimes in SiC epitaxial layers (epilayers) for low-loss SiC bipolar power devices. To attain the goal, the author seeks to (i) clarify deep levels generated by device fabrication processes, (ii) establish methods to reduce deep levels, and (iii) reveal origins of deep levels in SiC epilayers. From insights obtained these investigations, the author will control carrier lifetimes in SiC via the control of deep levels.

In Chapter 2, the principle of DLTS, and the sample preparation process for evaluation of deep levels in SiC by DLTS are explained. The typical deep levels detected in as-grown n-type and p-type SiC epilayers are introduced.

In Chapter 3, the author investigates deep levels generated by the essential processes for SiC device fabrication: ion implantation and reactive ion etching (RIE). As implanted ion species, N^+, P^+, and Al^+ are chosen, which are commonly used for the control of SiC conduction types. Comparing deep levels generated by each ion implantation and RIE, the author discusses the origins of these deep levels.

In Chapter 4, the author attempts to reduce the deep levels generated by the device processes observed in Chapter 3. Thermal oxidation, a process recently found to reduce deep levels in as-grown SiC epilayers, is performed to ion-implanted samples and RIE-etched samples. From the results of the DLTS measurements, the optimal condition of post-implantation or post-etching treatments for the reduction of deep levels generated by the device processes is discussed.

In Chapter 5, to use thermal oxidation for the control of carrier lifetimes in SiC epilayers, the mechanism of deep-level reduction by oxidation is discussed. To reveal the mechanism, the author compares defect behaviors (reduction, generation, and change of the depth profiles) for the two deep-level-reduction processes: thermal oxidation and C^+ implantation followed by Ar annealing. In addition, depth profiles of deep levels after oxidation are calculated based on a "interstitial diffusion model".

In Chapter 6, the origin of the $Z_{1/2}$ center is investigated by DLTS and EPR. A $Z_{1/2}$ concentration in SiC epilayers is changed by electron irradiation with various fluences. Comparing $Z_{1/2}$ concentrations measured by DLTS to V_C concentrations by EPR, the author seeks to reveal that the $Z_{1/2}$ center originates from a single V_C defect.

In Chapter 7, the origins of deep levels generated by thermal oxidation in SiC epilayers are discussed. To reveal the origins, the author generates the deep levels by several methods, thermal oxidation, electron irradiation, and C^+/Si^+ implantation, and compares their depth profiles and thermal stability.

In Chapter 8, carrier lifetimes in SiC epilayers are controlled by controlling a concentration of a lifetime killer: $Z_{1/2}$ center. Taking account of all the insights obtained in this study, methods to control $Z_{1/2}$ concentration using electron irradiation and thermal oxidation are discussed. Moreover, using numerical calculation, the author evaluates carrier lifetimes measured by microwave photoconductance decay (μ-PCD) in oxidized samples

with different $Z_{1/2}$ profiles, and determines bulk carrier lifetimes, which govern R_{ON} and switching speed of SiC bipolar power devices.

In Chapter 9, conclusions of this study and suggestions for future work are presented.

References

[1] *BP Statistical Review of World Energy June 2012*, British Petroleum (BP), http://www.bp.com/statisticalreview.

[2] *Key World Energy STATISTICS*, International Energy Agency (IEA), http://www.iea.org.

[3] *Power Semiconductor Market 2011 to 2012*, Yano Research Institute Ltd., http://www.yanoresearch.com/market_reports.

[4] H. Morkoç, S. Strite, G. Gao, M. Lin, B. Sverdlov, and M. Burns, *Journal of Applied Physics* **76**, 1363 (1994).

[5] L. Porter and R. Davis, *Materials Science and Engineering B* **34**, 83 (1995).

[6] J. Casady and R. Johnson, *Solid-State Electronics* **39**, 1409 (1996).

[7] H. Matsunami and T. Kimoto, *Materials Science and Engineering* **R20**, 125 (1997).

[8] A. Lebedev, *Semiconductors* **33**, 107 (1999).

[9] W. J. Choyke, H. Matsunami, and G. Pensl, *Silicon Carbide*, Springer-Verlag Berlin Heidelberg New York, 2004.

[10] H. Matsunami, N. Ohtani, T. Kimoto, and T. Nakamura, *Technology of Semiconductor SiC and Its Application*, The Nikkan Kogyo Shimbun, Ltd., Japan, 2011.

[11] B. J. Baliga, *Fundamentals of Power Semiconductor Devices*, Springer Science+Business Media, LLC, NY, USA, 2008.

[12] D. V. Lang and C. H. Henry, *Physical Review Letters* **35**, 1525 (1975).

[13] A. O. Evwaraye and E. Sun, *Journal of Applied Physics* **47**, 3776 (1976).

[14] S. D. Brotherton and P. Bradley, *Journal of Applied Physics* **53**, 5720 (1982).

[15] B. G. Svensson, K.-H. Rydén, and B. M. S. Lewerentz, *Journal of Applied Physics* **66**, 1699 (1989).

[16] B. G. Svensson, B. Mohadjeri, A. Hallén, J. H. Svensson, and J. W. Corbett, *Physical Review B* **43**, 2292 (1991).

[17] F. Priolo, G. Franz, S. Coffa, A. Polman, S. Libertino, R. Barklie, and D. Carey, *Journal of Applied Physics* **78**, 3874 (1995).

[18] J. Benton, P. Stolk, D. Eaglesham, D. Jacobson, J.-Y. Cheng, J. Poate, N. Ha, T. Haynes, and S. Myers, *Journal of Applied Physics* **80**, 3275 (1996).

[19] S. Coffa, V. Privitera, F. Priolo, S. Libertino, and G. Mannino, *Journal of Applied Physics* **81**, 1639 (1997).

[20] J.-U. Sachse, E. Sveinbjörnsson, W. Jost, J. Weber, and H. Lemke, *Physical Review B* **55**, 16176 (1997).

[21] B. G. Svensson, C. Jagadish, A. Hallén, and J. Lalita, *Physical Review B* **55**, 10498 (1997).

[22] A. Istratov, H. Hedemann, M. Seibt, O. Vyvenko, W. Schröter, T. Heiser, C. Flink, H. Hieslmair, and E. Weber, *Journal of the Electrochemical Society* **145**, 3889 (1998).

[23] K. Bonde Nielsen, B. Bech Nielsen, J. Hansen, E. Andersen, and J. Andersen, *Physical Review B* **60**, 1716 (1999).

[24] S. Libertino, S. Coffa, and J. Benton, *Physical Review B* **63**, 1952061 (2001).

[25] P. Pellegrino, P. Lévêque, J. Lalita, A. Hallén, C. Jagadish, and B. G. Svensson, *Physical Review B* **64**, 195211 (2001).

[26] E. Monakhov, B. Avset, A. Hallén, and B. Svensson, *Physical Review B* **65**, 2332071 (2002).

[27] V. Markevich, A. Peaker, S. Lastovskii, L. Murin, and J. Lindström, *Journal of Physics Condensed Matter* **15**, S2779 (2003).

[28] G. Davies, *Physics Reports* **176**, 83 (1989).

[29] J. Coutinho, R. Jones, P. Briddon, S. Öberg, L. Murin, V. Markevich, and J. Lindström, *Physical Review B* **65**, 141091 (2002).

[30] G. D. Watkins and J. W. Corbett, *Physical Review* **121**, 1001 (1961).

[31] G. D. Watkins and J. W. Corbett, *Physical Review* **138**, A543 (1965).

[32] E. Weber, *Applied Physics A Solids and Surfaces* **30**, 1 (1983).

[33] L. Song and G. Watkins, *Physical Review B* **42**, 5759 (1990).

[34] J. W. Corbett, G. D. Watkins, R. M. Chrenko, and R. S. McDonald, *Physical Review* **121**, 1015 (1961).

[35] L. J. Cheng, J. C. Corelli, J. W. Corbett, and G. D. Watkins, *Physical Review* **152**, 761 (1966).

[36] K. P. Lisiak and A. G. Milnes, *Journal of Applied Physics* **46**, 5229 (1975).

[37] B. Baliga and E. Sun, *IEEE Transactions on Electron Devices* **ED-24**, 685 (1977).

[38] R. O. Carlson, Y. Sun, and H. B. Assalit, *IEEE Transactions on Electron Devices* **ED-24**, 1103 (1977).

[39] T. Dalibor, G. Pensl, H. Matsunami, T. Kimoto, W. J. Choyke, A. Schöner, and N. Nordell, *Physica Status Solidi (A)* **162**, 199 (1997).

[40] S. G. Sridhara, L. L. Clemen, R. P. Devaty, W. J. Choyke, D. J. Larkin, H. S. Kong, T. Troffer, and G. Pensl, *Journal of Applied Physics* **83**, 7909 (1998).

[41] T. Kimoto, T. Yamamoto, Z. Y. Chen, H. Yano, and H. Matsunami, *Journal of Applied Physics* **89**, 6105 (2001).

[42] T. Kimoto, S. Nakazawa, K. Hashimoto, and H. Matsunami, *Applied Physics Letters* **79**, 2761 (2001).

[43] I. Pintilie, L. Pintilie, K. Irmscher, and B. Thomas, *Applied Physics Letters* **81**, 4841 (2002).

[44] J. Zhang, L. Storasta, J. P. Bergman, N. T. Son, and E. Janzén, *Journal of Applied Physics* **93**, 4708 (2003).

[45] T. Kimoto, K. Hashimoto, and H. Matsunami, *Japanese Journal of Applied Physics* **42**, 7294 (2003).

[46] Y. Negoro, T. Kimoto, and H. Matsunami, *Applied Physics Letters* **85**, 1716 (2004).

[47] H. Fujiwara, K. Danno, T. Kimoto, T. Tojo, and H. Matsunami, *Journal of Crystal Growth* **281**, 370 (2005).

[48] C. W. Litton, D. Johnstone, S. Akarca-Biyikli, K. S. Ramaiah, I. Bhat, T. P. Chow, J. K. Kim, and E. F. Schubert, *Applied Physics Letters* **88**, 121914 (2006).

[49] K. Danno and T. Kimoto, *Journal of Applied Physics* **100**, 113728 (2006).

[50] I. Pintilie, U. Grossner, B. G. Svensson, K. Irmscher, and B. Thomas, *Applied Physics Letters* **90**, 062113 (2007).

[51] K. Danno and T. Kimoto, *Journal of Applied Physics* **101**, 103704 (2007).

[52] T. Hori, K. Danno, and T. Kimoto, *Journal of Crystal Growth* **306**, 297 (2007).

[53] C. Hemmingsson, N. T. Son, O. Kordina, J. P. Bergman, E. Janzén, J. L. Lindström, S. Savage, and N. Nordell, *Journal of Applied Physics* **81**, 6155 (1997).

[54] L. Storasta, F. H. C. Carlsson, S. G. Sridhara, J. P. Bergman, A. Henry, T. Egilsson, A. Hallén, and E. Janzén, *Applied Physics Letters* **78**, 46 (2001).

[55] M. Weidner, T. Frank, G. Pensl, A. Kawasuso, H. Itoh, and R. Krause-Rehberg, *Physica B* **308-310**, 633 (2001).

[56] A. Kawasuso, F. Redmann, R. Krause-Rehberg, M. Weidner, T. Frank, G. Pensl, P. Sperr, W. Triftshauser, and H. Itoh, *Applied Physics Letters* **79**, 3950 (2001).

[57] A. Hallén, M. S. Janson, A. Y. Kuznetsov, D. Åberg, M. K. Linnarsson, B. G. Svensson, P. O. Persson, F. H. C. Carlsson, L. Storasta, J. P. Bergman, S. G. Sridhara, and Y. Zhang, *Nuclear Instruments and Methods in Physics Research Section B* **186**, 186 (2002).

[58] L. Storasta, J. P. Bergman, E. Janzén, A. Henry, and J. Lu, *Journal of Applied Physics* **96**, 4909 (2004).

[59] M. L. David, G. Alfieri, E. M. Monakhov, A. Hallén, C. Blanchard, B. G. Svensson, and J. F. Barbot, *Journal of Applied Physics* **95**, 4728 (2004).

[60] H. K. Nielsen, A. Hallén, and B. G. Svensson, *Physical Review B* **72**, 085208 (2005).

[61] G. Alfieri, E. V. Monakhov, B. G. Svensson, and M. K. Linnarsson, *Journal of Applied Physics* **98**, 043518 (2005).

[62] G. Alfieri, E. V. Monakhov, B. G. Svensson, and A. Hallén, *Journal of Applied Physics* **98**, 113524 (2005).

[63] G. Alfieri and T. Kimoto, *Journal of Applied Physics* **101**, 103716 (2007).

[64] T. Troffer, M. Schadt, T. Frank, H. Itoh, G. Pensl, J. Heindl, H. P. Strunk, and M. Maier, *Physica Status Solidi (A)* **162**, 277 (1997).

[65] T. Dalibor, H. Trageser, G. Pensl, T. Kimoto, H. Matsunami, D. Nizhner, O. Shigiltchoff, and W. J. Choyke, *Materials Science and Engineering B* **61-62**, 454 (1999).

[66] D. Åberg, A. Hallén, and B. G. Svensson, *Physica B* **273-274**, 672 (1999).

[67] T. Kimoto, N. Miyamoto, A. Schöner, A. Saitoh, H. Matsunami, K. Asano, and Y. Sugawara, *Journal of Applied Physics* **91**, 4242 (2002).

[68] S. Mitra, M. V. Rao, N. Papanicolaou, K. A. Jones, M. Derenge, O. W. Holland, R. D. Vispute, and S. R. Wilson, *Journal of Applied Physics* **95**, 69 (2004).

[69] Y. Negoro, T. Kimoto, and H. Matsunami, *Journal of Applied Physics* **98**, 043709 (2005).

[70] F. Schmid, S. A. Reshanov, H. B. Weber, G. Pensl, M. Bockstedte, A. Mattausch, O. Pankratov, T. Ohshima, and H. Itoh, *Physical Review B* **74**, 245212 (2006).

[71] D. Menichelli, M. Scaringella, F. Moscatelli, M. Bruzzi, and R. Nipoti, *Diamond and Related Materials* **16**, 6 (2007).

[72] J. Wong-Leung and B. G. Svensson, *Applied Physics Letters* **92**, 142105 (2008).

[73] P. B. Klein, B. V. Shanabrook, S. W. Huh, A. Y. Polyakov, M. Skowronski, J. J. Sumakeris, and M. J. O'Loughlin, *Applied Physics Letters* **88**, 052110 (2006).

[74] K. Danno, D. Nakamura, and T. Kimoto, *Applied Physics Letters* **90**, 202109 (2007).

[75] P. B. Klein, *Journal of Applied Physics* **103**, 033702 (2008).

Chapter 2

Investigation of Deep Levels in SiC by Deep Level Transient Spectroscopy

2.1 Introduction

Deep level transient spectroscopy (DLTS) [1] is a very powerful method to measure deep levels in semiconductor materials, and has commonly been used for trap detection in Si and other semiconductors. By the DLTS measurements, the energy position, the concentration, and the capture cross section of deep levels can be obtained. Measurement temperature is the most different point of DLTS for SiC compared with for Si, since much higher temperature, about 700 K, is required to monitor the midgap region of 4H-SiC due to the wide bandgap. As mentioned in Chapter 1, the investigation of deep levels in as-grown SiC has produced important results.

In this chapter, the principle of DLTS, the sample preparation process for evaluation of deep levels in SiC, and the measurement condition of DLTS are explained. The typical deep levels detected in as-grown n-type and p-type 4H-SiC by DLTS are also introduced.

2.2 Principles of Deep Level Transient Spectroscopy

The principles of DLTS are explained in this section. DLTS is a way to detect deep levels by monitoring capacitance transients accompanied by electron/hole emissions from deep levels. Fig. 2.1 shows a schematic diagram for a DLTS measurement on a sample containing a deep level. There are three phases during the measurement: (A) steady phase under reverse voltage, (B) electron-filling phase under pulse voltage, and (C) transient phase under reverse voltage.

At the steady state under a reverse bias (phase A), the capacitance C_{st} of a Schottky barrier diode (SBD) formed on an n-type semiconductor is given as:

$$C_{\mathrm{st}} = \sqrt{\frac{e\varepsilon N_{\mathrm{d}}}{2(V_{\mathrm{d}} - V)}}, \tag{2.1}$$

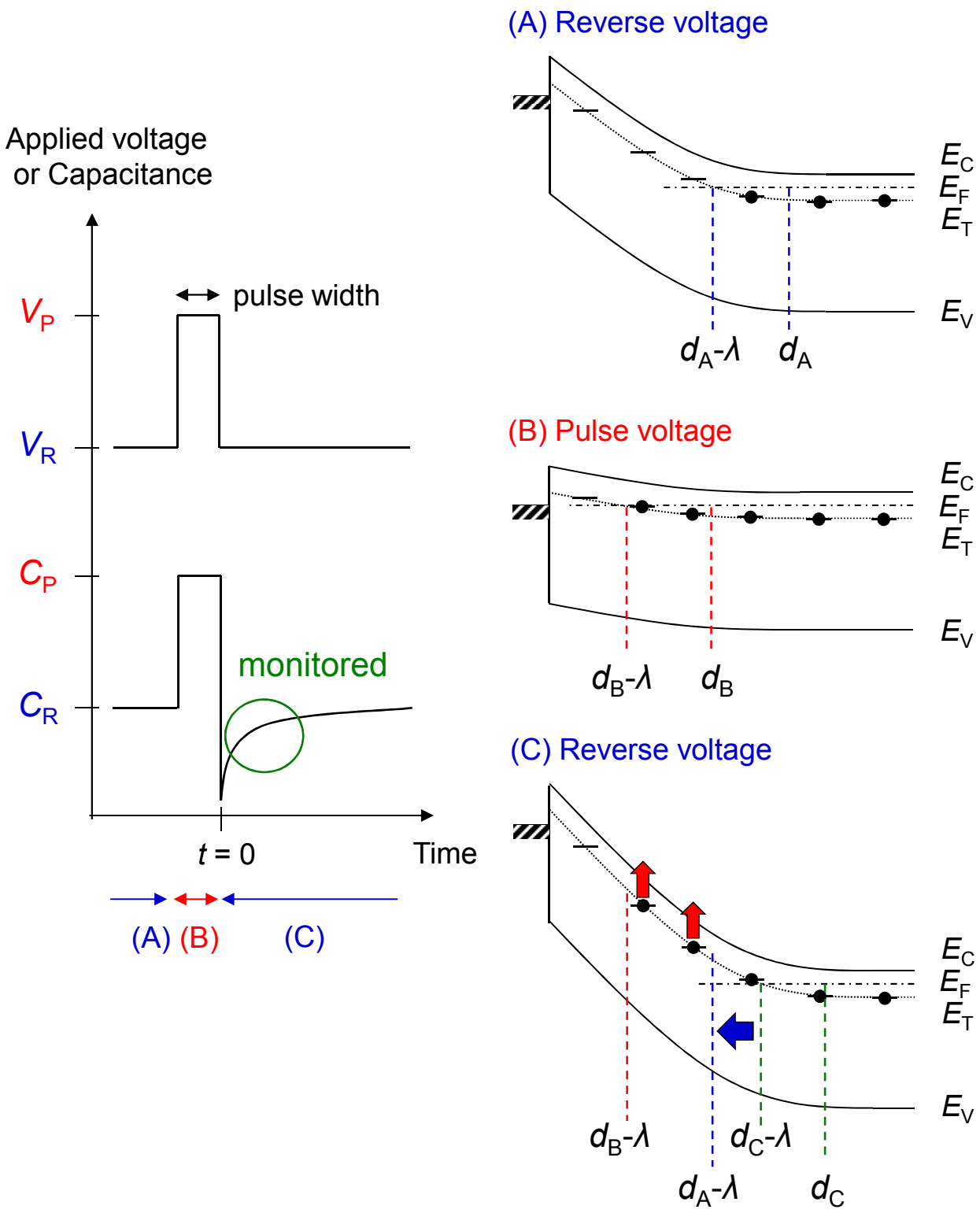

Figure 2.1: Schematic diagram explaining DLTS principles. The left-hand side figure indicates applied voltage and capacitance as a time, while the right is band diagram in each phase.

where e is the elementary charge, ε the permittivity of the semiconductor, N_d the doping concentration, V_d the built-in potential, and V the applied voltage. When the magnitude of reverse bias is decreased (phase B), the width of depletion region decreases from d_A to d_B, and carriers (electrons) are captured by the deep level in the region expressed as $(d_\mathrm{A}-\lambda)-(d_\mathrm{B}-\lambda)$. The λ region is defined as a gap between the depletion region edge and the point of $E_\mathrm{F}=E_\mathrm{T}$, where the deep level is occupied by electrons (lambda effect) [2]. The distance λ is determined by the Fermi level E_F, the trap position E_T, and the effective charge density in the λ region N'_d ($\simeq N_\mathrm{d}-N_\mathrm{T}$ for an acceptor-like trap (N_T: trap concentration) and $\simeq N_\mathrm{d}$ for a donor-like trap):

$$\lambda=\sqrt{\frac{2\varepsilon(E_\mathrm{F}-E_\mathrm{T})}{e^2N'_\mathrm{d}}}. \tag{2.2}$$

After the reverse bias is returned to the original value (phase C), the depletion region expands to d_C, which is larger than d_A due to electrons captured by the deep level in the depletion region. Therefore, the capacitance at the beginning of phase C ($t=0$) is smaller than C_st. The captured electrons are gradually emitted from the trap with the emission time constant τ, and the depletion region width and the capacitance return to the value at the steady state.

At $t\geq 0$, the concentration of electrons captured by the trap n_T is written as:

$$n_\mathrm{T}(t)=N_\mathrm{T}\exp\left(-\frac{t}{\tau}\right). \tag{2.3}$$

The emission time constant τ is generally expressed as:

$$\tau(T)=\frac{g}{\sigma_\mathrm{n}v_\mathrm{th}N_\mathrm{C}}\exp\left(\frac{E_\mathrm{C}-E_\mathrm{T}}{kT}\right), \tag{2.4}$$

where g and σ_n are the degeneracy factor and the electron capture-cross-section of the trap, respectively, and v_th, k and T are the thermal velocity of electrons, the Boltzmann constant, and the absolute temperature. N_C denotes the effective density of states in the conduction band of the semiconductor. E_C and E_T mean the energy level of the conduction band minima and the trap.

2.2.1 Approximated Evaluation

As mentioned above, electron emission from deep levels occurs in the region from $(d_\mathrm{B}-\lambda)$ to $(d_\mathrm{A}-\lambda)$. When this region is approximated to the whole depletion region (from 0 to d_A), using Eqs. (2.1) and (2.3), the capacitance transient $C(t)$ is given by:

$$C(t)=\sqrt{\frac{e\varepsilon(N_\mathrm{d}-n_\mathrm{T})}{2(V_\mathrm{d}-V)}}=C_\mathrm{st}\sqrt{1-\frac{N_\mathrm{T}\exp\left(-t/\tau\right)}{N_\mathrm{d}}}. \tag{2.5}$$

When $N_\mathrm{T}\ll N_\mathrm{d}$, Eq. 2.5 can be rewritten as:

$$C(t)\simeq C_\mathrm{st}\left\{1-\frac{N_\mathrm{T}}{2N_\mathrm{d}}\exp\left(-\frac{t}{\tau}\right)\right\}. \tag{2.6}$$

At various temperatures, differences of the capacitance at times of t_1 and t_2 (ΔC) are measured in DLTS. The pair of t_1/t_2 is called "rate window". ΔC is presented as:

$$\Delta C = C(t_2) - C(t_1) = \frac{C_{\mathrm{st}} N_{\mathrm{T}}}{2N_{\mathrm{d}}} \left\{ \exp\left(-\frac{t_2}{\tau}\right) - \exp\left(-\frac{t_1}{\tau}\right) \right\}. \tag{2.7}$$

The ΔC value becomes maximum at a certain temperature T_{M} when the emission time constant is given as:

$$\tau(T_{\mathrm{M}}) = t_{\mathrm{w}}(t_1, t_2) = \frac{t_1 - t_2}{\ln(t_1/t_2)}. \tag{2.8}$$

From the peak height of ΔC (at $\tau(T_{\mathrm{M}})$), the trap concentration can be estimated. A set of measurements with various rate windows gives a relation between $\tau(T_{\mathrm{M}})$ and T_{M}. Here, Eq. 2.4 can be converted to the equation:

$$\ln\left(\frac{\tau(T_{\mathrm{M}}) N_{\mathrm{C}} v_{\mathrm{th}}}{g}\right) = \frac{E_{\mathrm{C}} - E_{\mathrm{T}}}{k} \frac{1}{T_{\mathrm{M}}} - \ln \sigma_{\mathrm{n}}. \tag{2.9}$$

From the Arrhenius plot, the activation energy ($E_{\mathrm{C}} - E_{\mathrm{T}}$) and the capture cross section (σ_{n}) can be estimated from the slope and the ordinate intercept of the extrapolation of the plot, respectively.

2.2.2 Correction of Trap Concentrations

Because only a part of deep levels in the depletion region, deep levels located at $d_{\mathrm{B}} - \lambda < x < d_{\mathrm{A}} - \lambda$, contributes DLTS signals, the trap concentration obtained in the last section is underestimated. The real trap concentration ($N_{\mathrm{T,real}}$) is calculated as:

$$N_{\mathrm{T,real}} = \frac{d_{\mathrm{A}}^2}{(d_{\mathrm{A}} - \lambda)^2 - (d_{\mathrm{B}} - \lambda)^2} N_{\mathrm{T,appr}}, \tag{2.10}$$

where $N_{\mathrm{T,appr}}$ is the trap concentration obtained in the last section. All the trap concentrations shown in this thesis are corrected by this equation.

2.2.3 Deep Level Transient Fourier Spectroscopy

In deep level transient Fourier spectroscopy (DLTFS) [3], which is used in this study, the measurement can be performed in shorter time with smaller noise compared to conventional DLTS. In conventional DLTS, only two capacitances, $C(t_1)$ and $C(t_2)$, are measured for every transient. In DLTFS, the capacitance transient $C(t)$ is measured in periodically in a period width T_{W}, and then developed into Fourier series as:

$$C(t) = a_0 - \sum a_n \cos(\omega t) - \sum b_n \sin(\omega t), \tag{2.11}$$

$$a_0 = C_{\mathrm{st}} - \frac{C_{\mathrm{st}} N_{\mathrm{T}}}{T_{\mathrm{W}} N_{\mathrm{d}}} \left\{ 1 - \exp\left(-\frac{T_{\mathrm{W}}}{\tau}\right) \right\}, \tag{2.12}$$

$$a_n = \frac{C_{\mathrm{st}} N_{\mathrm{T}}}{T_{\mathrm{W}} N_{\mathrm{d}}} \left\{ 1 - \exp\left(-\frac{T_{\mathrm{W}}}{\tau}\right) \right\} \frac{1/\tau}{1/\tau^2 + n^2\omega^2}, \tag{2.13}$$

$$b_n = \frac{C_{\mathrm{st}} N_{\mathrm{T}}}{T_{\mathrm{W}} N_{\mathrm{d}}} \left\{ 1 - \exp\left(-\frac{T_{\mathrm{W}}}{\tau}\right) \right\} \frac{n\omega}{1/\tau^2 + n^2\omega^2}, \tag{2.14}$$

where ω equals to $2\pi/T_{\mathrm{W}}$. In the DLTFS system employed in this study, b_1 is used as a signal. The peak height is proportional to the trap concentration, and the peak temperature is governed by the emission time constant and the period width. By the Arrhenius plot of emission time constant obtained with various T_{W} and Fourier series (a_n and b_n), the activation energy and the capture cross section can be obtained.

2.3 Fabrication of Schottky Barrier Diodes and Measurement Condition of Deep Level Transient Spectroscopy

Here, the sample preparation process and the measurement condition of DLTS used in this study are described.

For current-voltage (I–V), capacitance-voltage (C–V), and DLTS measurements, Schottky barrier diodes (SBDs) are fabricated. Ni and Ti are employed as Schottky contacts (typical diameter: 1 mm) on n-type and p-type SiC, respectively, resulting in a high Schottky barrier and thereby low leakage current at a high temperature. For p-type materials, the backside ohmic contacts were made of a Ti/Al/Ni (20 nm/100 nm/80 nm) layer annealed at 1000°C for 2 min. For n-type samples, silver paste or Al metal was used as backside contacts.

In DLTS measurements, the filling pulse is applied for 10 ms/100 ms to n-type/p-type materials, and the period width for transient measurements is 0.205 s. Depth profiles of deep levels are measured by changing (filling and reverse) bias voltages (0–100 V) in DLTS measurements. Note that as shown in Fig. 2.2 a monitored depth depends on a bias voltage and also a doping concentration of samples.

2.4 Deep Levels Detected in As-Grown n-type 4H-SiC

Fig. 2.3 (a) shows the typical DLTS spectrum in an as-grown N-doped n-type 4H-SiC (a commercially available epilayer, N_{d}: 1.6×10^{15} cm^{-3}). In this sample, the $Z_{1/2}$ ($E_{\mathrm{C}} - 0.67$ eV) [4, 5] and $EH_{6/7}$ ($E_{\mathrm{C}} - 1.5$ eV) [6] centers were observed, which are often dominant in as-grown n-type 4H-SiC epilayers and have a key role in this study. The trap concentration of these deep levels was about 2×10^{13} cm^{-3}, which is a standard value for commercially available epilayers.

DLTS spectrum observed in a different as-grown n-type 4H-SiC (a self-made epilayer, N_{d}: 1.4×10^{14} cm^{-3}) is shown in Fig. 2.3 (b), where the GN1 ($E_{\mathrm{C}} - 0.39$ eV), GN2 ($E_{\mathrm{C}} - 0.50$ eV), $Z_{1/2}$ ($E_{\mathrm{C}} - 0.67$ eV), GN3 ($E_{\mathrm{C}} - 1.1$ eV), UT_1 ($E_{\mathrm{C}} - 1.4$ eV) [7], and $EH_{6/7}$ ($E_{\mathrm{C}} - 1.5$ eV) centers were detected. The GN1 and GN2 centers may be assigned to

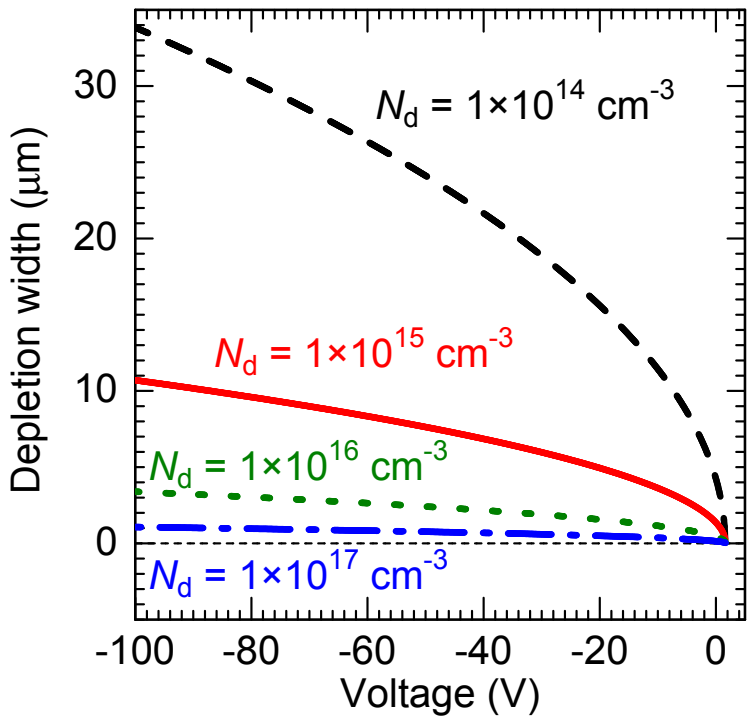

Figure 2.2: Depletion widths as a function of a bias voltage in n-type 4H-SiC SBD with different doping concentrations. The λ effect is not taken into account in this figure.

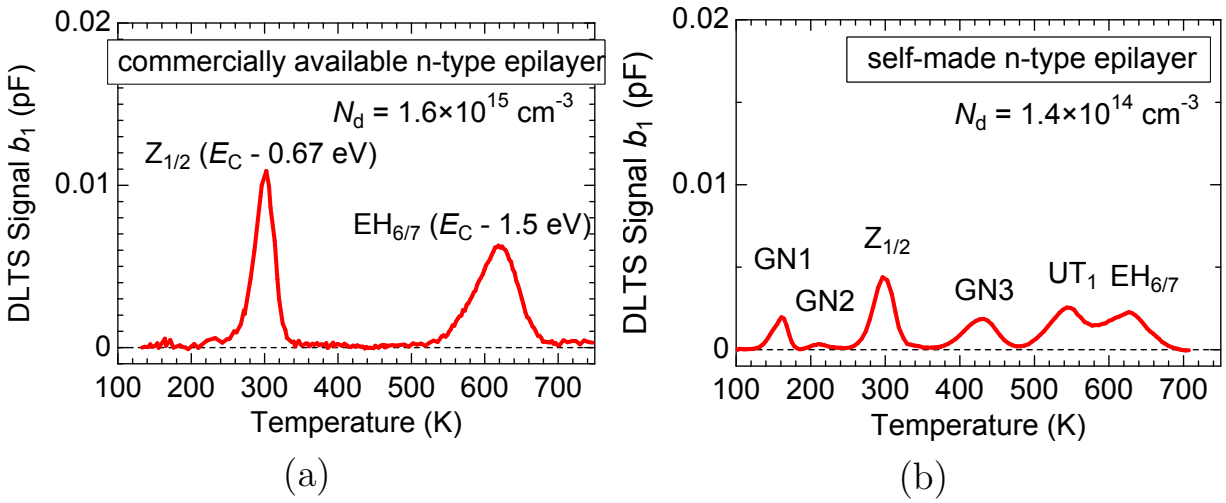

Figure 2.3: DLTS spectra observed in (a) commercially available and (b) self-made as-grown n-type 4H-SiC epilayers. The concentrations of the $Z_{1/2}$ center are (a) 2×10^{13} cm^{-3} and (b) 2×10^{12} cm^{-3}.

the ET1 [7] and EH_1 [6] centers, respectively, which are often observed after electron irradiation and annealed out at 950°C [6–8]. A higher density of the UT_1 center is observed in epilayers grown with higher C/Si ratio or at lower temperatures [7]. The trap concentration of the $Z_{1/2}$ center in the sample (b) is about 2×10^{12} cm^{-3}, which is one order of magnitude lower than that in the sample (a). Note that the intensity of a DLTS signal is affected by the doping concentration of the sample as well as the trap concentration. A different growth condition leads to different kinds of deep levels and different trap concentrations.

2.5 Deep Levels Detected in As-Grown *p*-type 4H-SiC

Fig. 2.4 (a) shows the typical DLTS spectrum in an as-grown Al-doped p-type 4H-SiC (a commercially available epilayer, N_a: 8.0×10^{15} cm^{-3}), where the GP1 center ($E_V + 0.46$ eV) and the D center ($E_V + 0.63$ eV) [9, 10] are observed. The D center has been reported to originate from a boron atom at a silicon site with an adjacent carbon vacancy (V_C) (B_{Si}-V_C) [10–12].

In Fig. 2.4 (b), a DLTS spectrum observed in a different as-grown p-type 4H-SiC (a self-made epilayer, N_a: 1.6×10^{15} cm^{-3}) is shown. The HK4 center ($E_V + 1.4$ eV) is often observed in as-grown samples and also samples after electron irradiation followed by Ar annealing at 950°C, which is annealed out at 1550°C [13]. The trap concentration of the D center in the sample (b) is about 8×10^{11} cm^{-3}, which is a half of that in the sample (a).

As shown in Fig. 2.3 and Fig. 2.4, deep levels and their concentrations in as-grown samples can be controlled to some extent by controlling the growth condition such as a C/Si ratio and a growth temperature. When the growth condition is optimized, the concentration of deep levels in as-grown n-type and p-type 4H-SiC epilayers can be suppressed to about 1×10^{12} cm^{-3}.

References

[1] D. V. Lang, *Journal of Applied Physics* **45**, 3023 (1974).

[2] S. D. Brotherton, *Solid-State Electronics* **26**, 987 (1983).

[3] S. Weiss and R. Kassing, *Solid-State Electronics* **31**, 1733 (1988).

[4] T. Dalibor, G. Pensl, H. Matsunami, T. Kimoto, W. J. Choyke, A. Schöner, and N. Nordell, *Physica Status Solidi (A)* **162**, 199 (1997).

[5] M. Weidner, T. Frank, G. Pensl, A. Kawasuso, H. Itoh, and R. Krause-Rehberg, *Physica B* **308-310**, 633 (2001).

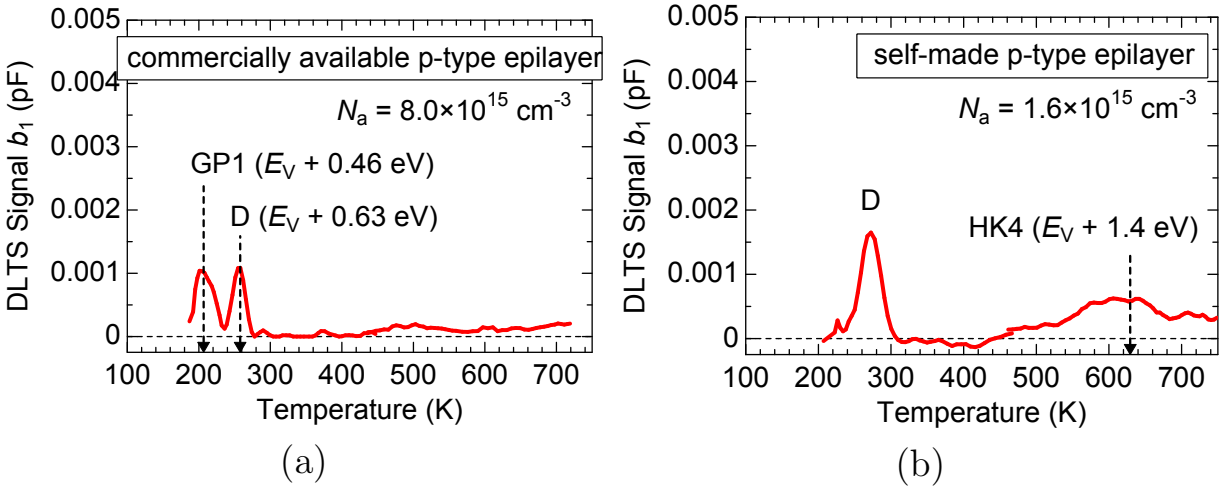

Figure 2.4: DLTS spectra observed in (a) commercially available and (b) self-made as-grown *p*-type 4H-SiC epilayers. The concentrations of the D center are (a) 1.6×10^{12} cm^{-3} and (b) 8×10^{11} cm^{-3}.

[6] C. Hemmingsson, N. T. Son, O. Kordina, J. P. Bergman, E. Janzén, J. L. Lindström, S. Savage, and N. Nordell, *Journal of Applied Physics* **81**, 6155 (1997).

[7] K. Danno and T. Kimoto, *Journal of Applied Physics* **100**, 113728 (2006).

[8] L. Storasta, J. P. Bergman, E. Janzén, A. Henry, and J. Lu, *Journal of Applied Physics* **96**, 4909 (2004).

[9] T. Troffer, M. Schadt, T. Frank, H. Itoh, G. Pensl, J. Heindl, H. P. Strunk, and M. Maier, *Physica Status Solidi (A)* **162**, 277 (1997).

[10] S. G. Sridhara, L. L. Clemen, R. P. Devaty, W. J. Choyke, D. J. Larkin, H. S. Kong, T. Troffer, and G. Pensl, *Journal of Applied Physics* **83**, 7909 (1998).

[11] A. Duijn-Arnold, T. Ikoma, O. G. Poluektov, P. G. Baranov, E. N. Mokhov, and J. Schmidt, *Physical Review B* **57**, 1607 (1998).

[12] P. Baranov, I. Il'in, and E. Mokhov, *Physics of the Solid State* **40**, 31 (1998).

[13] K. Danno and T. Kimoto, *Journal of Applied Physics* **101**, 103704 (2007).

Chapter 3

Generation of Deep Levels by Device Fabrication Processes

3.1 Introduction

In SiC epilayers, deep levels are generated during device fabrication as well as during growth. Ion implantation and reactive ion etching (RIE) are the most popular processes for SiC device fabrication. Ion implantation is essential for selective doping in SiC, whereas RIE is to etch SiC. Fig. 3.1 shows fabrication processes of an SiC trench metal-oxide-semiconductor field-effect transistor (MOSFET) and an SiC mesa PiN diode. For fabrication of an SiC trench MOSFET, ion implantation is used to form an n^+ region for source contact and p^+ regions for body contact, whereas RIE is used to form a trench structure. For an SiC mesa PiN diode, RIE is used to form a mesa structure, whereas ion implantation is used to form junction termination extension (JTE) regions, which reduce electric field crowding at the mesa edges and thereby realize a high blocking voltage.

Here, note that the both device-fabrication processes should have severe impacts on deep levels in SiC because the samples are bombarded by ions during these processes. Investigations on deep levels after RIE, however, have not been reported, and those after ion implantation have been very limited. Thus, the author investigates deep levels in n-type and p-type 4H-SiC after these device processes.

3.2 Deep Levels Generated by Ion Implantation

For fabrication of any kinds of SiC devices, ion implantation is essential because of the low diffusion coefficients of dopants in SiC [1]. Nevertheless, studies on deep levels in ion-implanted SiC have been very limited, leading to the lack of fundamental understanding of physical properties of implanted SiC and thereby SiC device performance. Although a few groups have reported DLTS measurements on H^+/He^+/Ti^+/V^+-implanted n-type SiC [2–4], H^+-implanted p-type SiC [5], N^+/P^+-implanted n-type SiC [6–8], Al^+/B^+-implanted n-

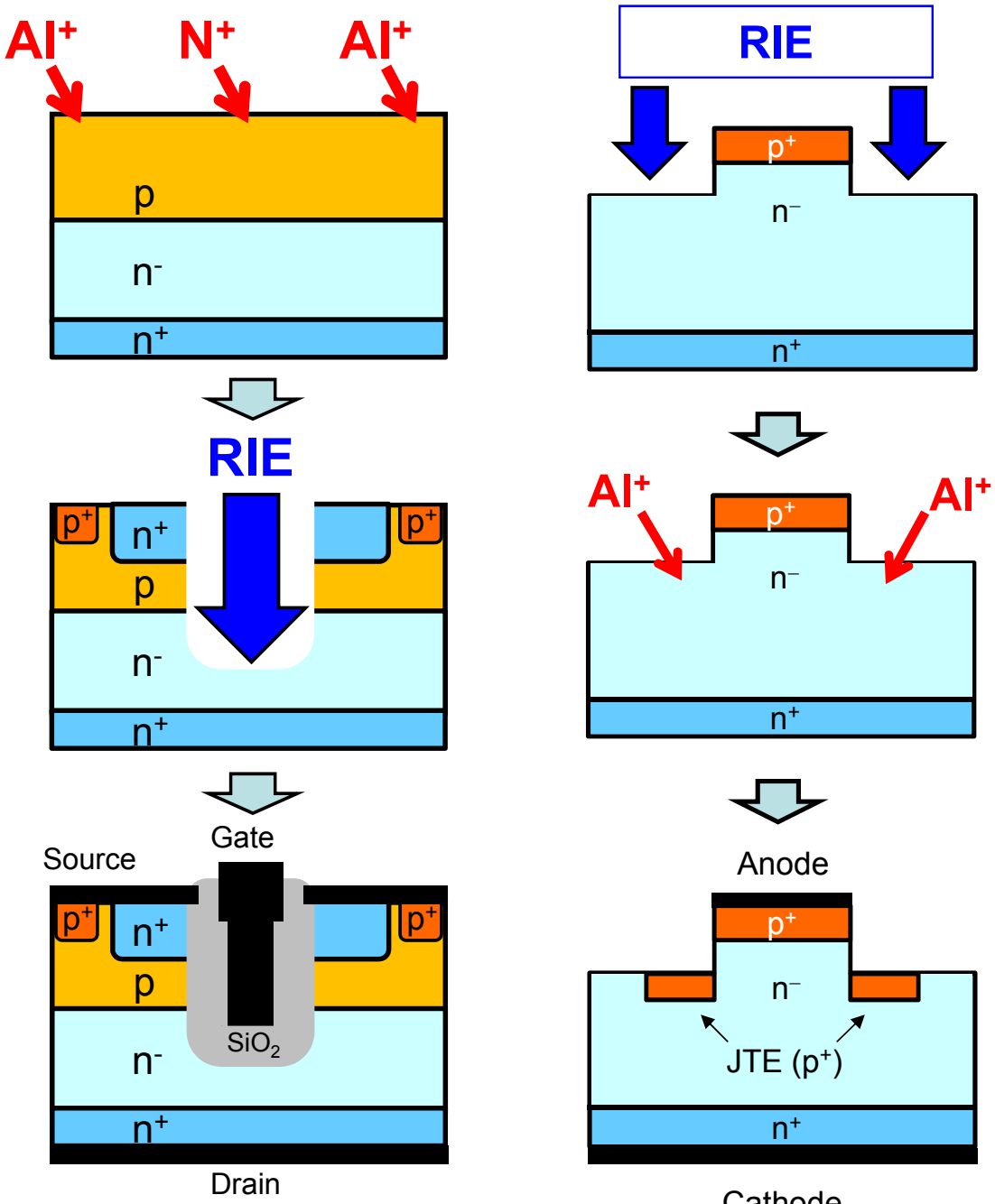

(a) Trench MOSFET (b) Mesa *PiN* diode

Figure 3.1: Fabrication processes of (a) an SiC trench MOSFET and (b) an SiC mesa *PiN* diode. Ion implantation is used for selective doping, whereas RIE is used to etch SiC.

type SiC [9, 10], and Al^+/B^+-implanted p-type SiC [6, 11], in these studies only deep levels energetically located in the upper half or lower half of the bandgap, respectively, were detected. In addition, many of the implantation condition in these studies differ from condition used for SiC device fabrications.

Nitrogen is commonly employed for n-type doping in SiC, which is also suitable for deep-range implantation. Phosphorus has higher solubility limit than nitrogen in SiC and is used for lower sheet resistance of n-type layers [12]. In contrast, aluminum is commonly used as a dopant for p-type doping [11, 13]. Ar annealing at a high temperature (e.g. 1700°C) is commonly performed after ion implantation for activation of dopants. In the whole energy range of the bandgap in 4H-SiC, the author presents deep levels generated by N^+, P^+, and Al^+ implantation and these behaviors for high temperature annealing.

3.2.1 Experiments

The starting materials were N-doped n-type or Al-doped p-type 4H-SiC epilayers grown on 8° off-axis 4H-SiC (0001). The thickness and doping concentration of epilayers were 10–15 μm and (7–8) $\times 10^{15}$ cm^{-3}, respectively. Multiple N^+, P^+, Al^+ implantation was performed into separate samples at room temperature to form a (0.7–0.8)-μm-deep box profile. The implantation energies and doses for each multiple implantation are summarised in Table 3.1. Fig. 3.2 shows the depth profile of implanted N atoms simulated by a TRIM code [14]. The total implant dose is 5.6×10^{10} cm^{-2} (low-dose condition, implanted atom concentration $N_\mathrm{I} \simeq 7 \times 10^{14}$ cm^{-3}) or 8.0×10^{13} cm^{-2} (high-dose condition, $N_\mathrm{I} \simeq 1 \times 10^{18}$ cm^{-3}). High-dose condition is generally used to form pn junctions. Under the low-dose condition, the concentration of implanted impurities (about 7×10^{14} cm^{-3}) is lower than the original doping level of the epilayers. Although this implant dose is unusually low for device fabrication, the implanted region can simulate the "implant-tail" region. Because the samples keep the original conduction type (n- or p-type) under this implantation condition, deep levels located in the upper half of the bandgap can be monitored by using n-type epilayers, irrespective of implanted species, and in the same way, deep levels in the lower half of the bandgap by using p-type materials. Ne^+-implanted samples with the same implant dose were also prepared to investigate the pure implantation damage. Post-implantation annealing was carried out at 1000°C for 2 min or 1700°C for 30 min in Ar ambient. In the high-temperature annealing at 1700°C, a carbon cap was employed to suppress the surface roughening [15].

For deep level transient spectroscopy (DLTS) measurements, Schottky barrier diodes (SBDs) were fabricated in the same manner as described in Chapter 2. The reverse and pulse voltages were adjusted so that deep levels in the box-profile region could be monitored (typical reverse voltage: -2 V for n-type samples or 2 V for p-type samples, typical pulse voltage: 0 V). The depth profiles of deep-level concentrations were also measured by changing the voltages in DLTS measurements. To measure the trap concentration

Table 3.1: Implantation energies and doses for forming box profiles with a mean implanted atom concentration of about 7×10^{14} cm^{-3} and a depth of about 0.8 μm (low dose condition, total dose: 5.6×10^{10} cm^{-2}). To obtain box profiles of 1×10^{18} cm^{-3}, about 1.43×10^{3} times higher doses are employed (high dose condition, total dose: 8.0×10^{13} cm^{-2}).

(a) N^+

energy (keV)	dose ($\times10^9$ cm^{-2})
700	11.7
500	9.74
330	9.74
220	7.79
140	6.42
80	5.35
40	3.30
18	1.94

(b) P^+

energy (keV)	dose ($\times10^9$ cm^{-2})
700	19.9
450	12.9
300	8.61
180	6.99
100	3.77
50	2.15
22	1.08
10	0.59

(c) Al^+

energy (keV)	dose ($\times10^9$ cm^{-2})
700	18.7
450	13.3
300	8.46
180	7.47
100	3.83
55	2.31
24	1.42
10	0.49

(d) Ne^+

energy (keV)	dose ($\times10^9$ cm^{-2})
700	15.6
450	12.5
280	10.2
180	7.30
100	5.43
50	2.84
24	1.42
10	0.69

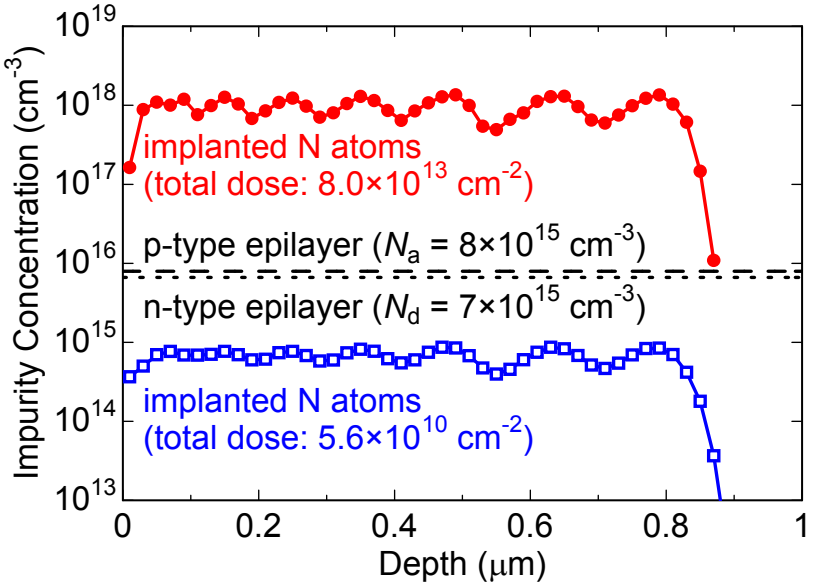

Figure 3.2: Depth profiles of implanted N atoms simulated by TRIM code (filled circles: high-dose-implanted N atoms, squares: low-dose-implanted N atoms, dotted/dashed lines: doping levels in n-/p-type starting materials).

far below from the surface, samples were etched down to a depth of about 0.7 μm by RIE.

3.2.2 Electron Traps Detected in *n*-type Epilayers

In the DLTS spectra of nonimplanted n-type 4H-SiC (both as-grown and annealed at 1700°C), the $Z_{1/2}$ ($E_C - 0.67$ eV) [2] and $EH_{6/7}$ ($E_C - 1.5$ eV) [16] centers were dominant with a concentration of about 2×10^{13} cm^{-3}.

In DLTS measurements on implanted samples, the region (depth) monitored by DLTS should be taken into account because generation of a high density traps can result in formation of highly-resistive compensated region. Fig. 3.3 shows the depth profiles of the net donor concentration obtained from C-V measurements on Al^+- and N^+-implanted samples (low-dose condition). In the Al^+/N^+-implanted samples annealed at 1000°C (Al-1000/N-1000), a high-resistance region was formed near the surface ranged to a depth of about 0.75 μm/0.50 μm, which was derived from the fitting of the C-V curve. Thus, the region monitored by DLTS measurements on Al^+-implanted samples annealed at 1000°C is deeper than a depth of 0.75 μm (0.50 μm for N^+-implanted samples). In the samples annealed at 1700°C, in contrast, the box-profile region could be monitored due to the absence of the compensated region.

Low-Dose Implantation

Fig. 3.4 represents the DLTS spectra obtained from low-dose (5.6×10^{10} cm^{-2}, $N_I \simeq 7 \times 10^{14}$ cm^{-3}) Al^+-, N^+-, and Ne^+-implanted samples annealed at 1000°C and 1700°C in Ar ambient. In the Al^+-implanted sample after Ar annealing at 1000°C, at least, seven peaks labeled IN1, IN3–IN6, IN8, IN9 were detected. After annealing at 1700°C, however, most DLTS peaks disappeared, whereas the IN3 and IN9 centers survived. The energy levels and the capture cross sections of observed traps are summarized in Table 3.2. In this table, the trap concentration in the Al^+-implanted samples annealed at 1000°C/1700°C is also shown. Note that the trap concentration obtained for the samples annealed at 1000°C may suffer from a large error because the trap concentration is close to the doping level, and that the monitored region in Al^+-implanted samples is different from that in N^+-implanted samples as mentioned above. The dominant levels after 1700°C annealing, IN3 and IN9, can be assigned to the $Z_{1/2}$ and $EH_{6/7}$ centers, respectively, based on their energy levels and thermal stability.

In the N^+-implanted sample, although the DLTS spectrum after implantation and annealing at 1000°C looks different from that for the Al^+-implanted sample, the author speculates that there are also seven (or eight) traps because the two peaks around 440 K and 630 K are too broad to be assigned to a single level. Fig. 3.5 shows the fitting results for DLTS spectra presented in Fig. 3.4. In the fitting, eight traps (IN1, IN3–IN6, IN8–IN10) with the fixed energy levels and capture cross sections were assumed, and the trap concentrations were varied, which means that the temperature position of each peak was fixed and

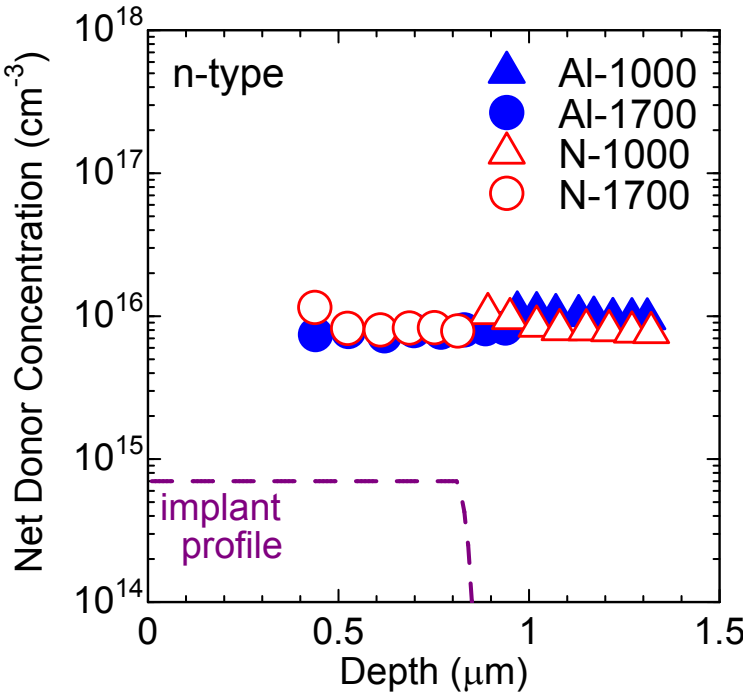

Figure 3.3: Depth profiles of net donor concentration (Al-1000: Al^+-implanted sample annealed at 1000°C, Al-1700: Al^+-implanted sample annealed at 1700°C, N-1000: N^+-implanted sample annealed at 1000°C, N-1700: N^+-implanted sample annealed at 1700°C). The high-resistance region does not exist in the samples annealed at 1700°C.

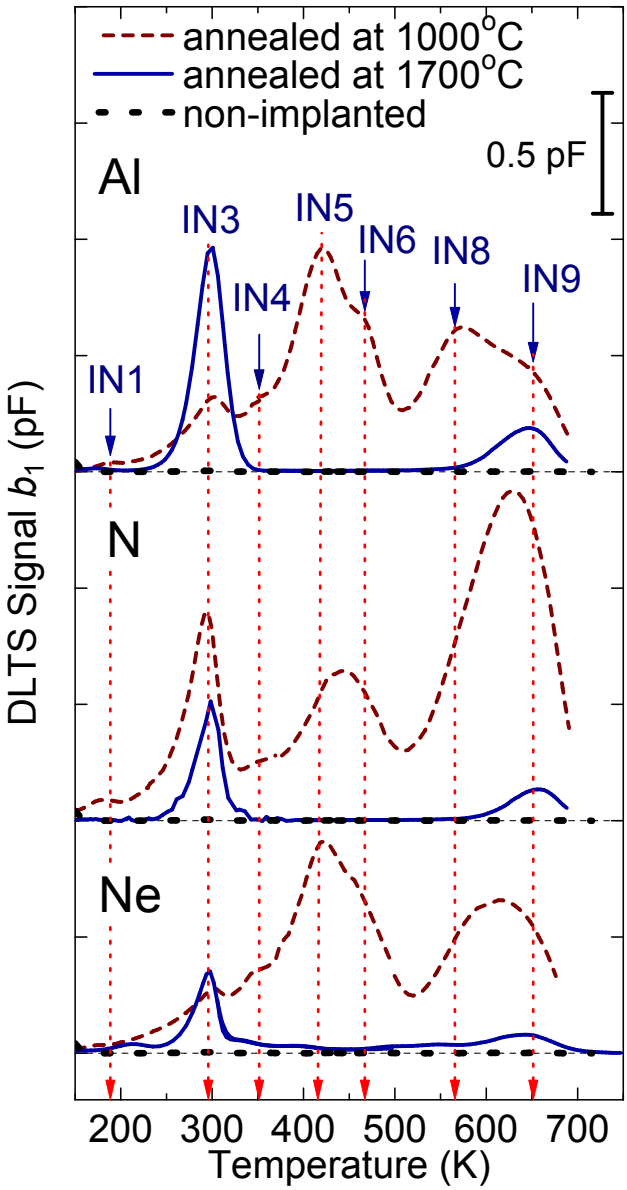

Figure 3.4: DLTS spectra of n-type 4H-SiC implanted with Al^+, N^+, and Ne^+ (implant dose: 5.6×10^{10} cm^{-2}) annealed at 1000°C (dashed line) and 1700°C (solid line). The spectrum of nonimplanted sample is indicated with a dotted line. The signal b_1 is the coefficient of the first sine term in the Fourier series, which is proportional to the trap concentration.

Table 3.2: Energy positions and capture cross sections of deep levels observed in ion-implanted n-type 4H-SiC (σ: the capture cross section, N_T: the concentration of traps in Al^+-implanted SiC annealed at 1000°C or 1700°C).

label	$E_C - E_T$ (eV)	σ (cm^2)	N_T (1000°C) (cm^{-3})	N_T (1700°C) (cm^{-3})	corresponding center
IN1	0.28	10^{-17}	1.9×10^{14}	not observed	ET1 [17]
IN3	0.67	10^{-14}	1.9×10^{15}	2.8×10^{15}	$Z_{1/2}$ [2]
IN4	0.69	10^{-16}	1.7×10^{15}	not observed	EH_3 [16], HR_2 [18], ET2 [17]
IN5	0.73	10^{-16}	5.3×10^{15}	not observed	RD_1 [2, 9], EH_4 [16]
IN6	0.98	10^{-15}	4.2×10^{15}	not observed	RD_2 [2, 9], RD_3 [2], EH_5 [16], ET3 [17]
IN8	1.2	10^{-15}	2.7×10^{15}	not observed	
IN9	1.5	10^{-14}	2.8×10^{15}	8.3×10^{14}	$EH_{6/7}$ [16]

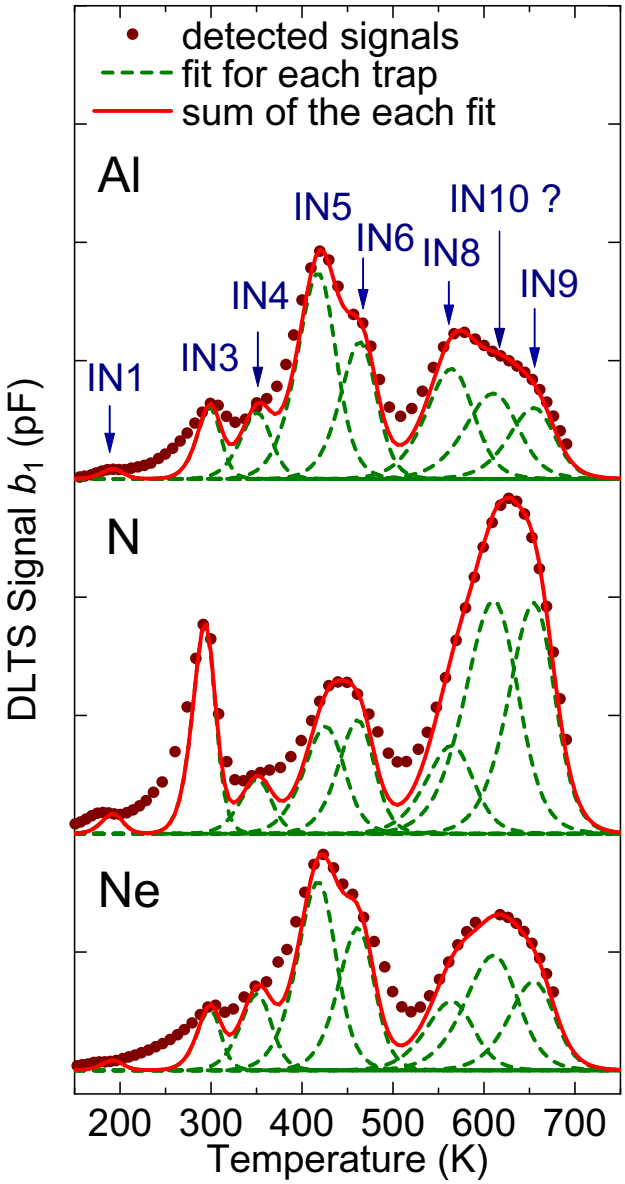

Figure 3.5: Fitting of each DLTS spectrum detected in n-type 4H-SiC implanted with Al^+, N^+, and Ne^+ annealed at 1000°C (filled circles: detected signals, dotted line: fit for each trap, solid line: sum of the each fit).

the height of each peak was changed to fit each DLTS spectrum. As shown in Fig. 3.5, the broad DLTS peaks at 440 K and 630 K seem to consist of major peaks: IN5 and IN6, IN8–IN10, respectively. In the fitting process, an additional DLTS peak (IN10) was introduced in between IN8 and IN9 to reproduce the observed DLTS spectra. However, the accurate energy level and capture cross section of this trap are not clear due to the severe overlapping of the peaks. In addition, other additional peaks may exist because the fitted spectra deviate in the "valleys" of DLTS spectra, which are also difficult to be separated due to the severe overlapping. After annealing at 1700°C, again the $Z_{1/2}$ and $EH_{6/7}$ peaks dominate, as in the case of Al^+-implantation. Similar results were also obtained for P^+-implanted (not shown) and Ne^+-implanted samples.

Thus, as well as in as-grown and electron-irradiated 4H-SiC epilayers, the $Z_{1/2}$ and $EH_{6/7}$ centers, which are regarded as intrinsic defects related to the carbon displacement [17, 19, 20], are dominant and thermally stable deep levels in any implanted epilayers as far as the implant dose is low. In addition, all the deep levels, IN1, IN3–IN6, IN8, IN9 (and IN10), may be also intrinsic defects because these traps were generated in the Al^+, N^+, P^+, and even Ne^+-implanted samples. From the energy levels and capture cross sections, the IN5 and IN6 centers may be assigned to the RD_1 and RD_2 centers [2, 9], respectively. These centers were detected in V^+-, Ti^+-, Al^+-, and B^+-implanted 4H-SiC by Dalibor et al. [2] and Troffer et al. [9], which are also suggested to be intrinsic defects (without any impurities) in the literatures. Deep levels containing particular implanted impurities may be generated when the implant dose is much higher.

Note that the trap concentrations in the implanted samples were very high; the $Z_{1/2}$ and $EH_{6/7}$ concentrations were 2×10^{15} cm^{-3} and 8×10^{14} cm^{-3}, respectively, in the Al^+-implanted sample after annealing at 1700°C, which is about two-orders-of-magnitude higher than those in the nonimplanted sample.

High-Dose Implantation

Fig. 3.6 shows the DLTS spectra obtained from high-dose (8.0×10^{13} cm^{-2}, $N_I \simeq 1 \times 10^{18}$ cm^{-3}) P^+-implanted n-type 4H-SiC after annealing at 1700°C in Ar ambient. In this sample, the IN2 ($E_C - 0.30$ eV), IN6 ($E_C - 1.0$ eV), and IN8 ($E_C - 1.2$ eV) centers were dominant, which are different from the defects dominating in low-dose implanted samples: the IN3 and IN9 centers. This means that the IN2, IN6, and IN8 centers could originate from complex (cluster) defects rather than single defects. The energy positions, capture cross sections, and concentrations of the deep levels are listed in Table 3.3. The IN2 center may be assigned to the ID_8 center detected in Ti^+-, V^+-, and Al^+-implanted n-type 4H-SiC after annealing at 1700°C for 30 min [2, 9]. Although the peak labeled IN8 is too broad to be a single level, other levels cannot be resolved due to severe overlapping. Note that the concentration of these deep levels is very high (e.g. IN8: $\sim 1 \times 10^{17}$ cm^{-3}), which can cause the degradation of the conductivity in the implanted region.

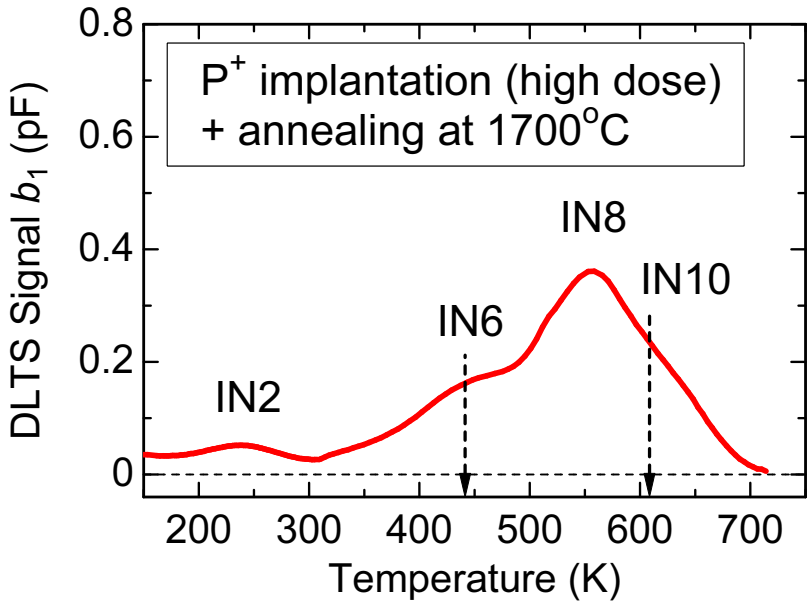

Figure 3.6: DLTS spectra of n-type 4H-SiC implanted with P^+ (implant dose: 8×10^{13} cm^{-2}) annealed at 1700°C.

Table 3.3: Energy positions, capture cross sections, and concentrations of deep levels observed in high-dose P^+-implanted n-type 4H-SiC.

label	$E_C - E_T$ (eV)	σ(cm^2)	N_T (cm^{-3})	corresponding center
IN2	0.30	10^{-18}	1×10^{16}	ID_8 [2, 9]
IN6	1.0	10^{-15}	5×10^{16}	RD_2 [2, 9], RD_3 [2], EH_5 [16], ET3 [17]
IN8	1.2	10^{-15}	1×10^{17}	

3.2.3 Hole Traps Detected in *p*-type Epilayers

In the DLTS spectra of nonimplanted *p*-type 4H-SiC (both as-grown and annealed at 1700°C), the D ($E_V + 0.63$ eV) [9, 21] and HK4 ($E_V + 1.4$ eV) [22] centers were dominant. The trap concentration was in the 10^{12} cm^{-3} range.

Fig. 3.7 shows the depth profiles of the net acceptor concentration for Al^+- and N^+-implanted (with low-dose condition) samples derived from *C*-*V* measurements. In the implanted samples after Ar annealing at 1000°C, a high-resistance region existed from the surface to a depth of about 1.3 μm (in a Al^+-implanted sample) or 1.0 μm (in a N^+-implanted sample), and disappeared after 1700°C annealing.

Low-Dose Implantation

Fig. 3.8 represents the DLTS spectra obtained from low-dose (5.6×10^{10} cm^{-2}, $N_I \simeq 7 \times 10^{14}$ cm^{-3}) Al^+-, N^+-, and Ne^+-implanted samples annealed at 1000°C and 1700°C. In the DLTS spectra for these samples, the IP1 ($E_V + 0.35$ eV) and IP3 ($E_V + 0.71$ eV) centers emerged after annealing at 1000°C. Table 3.4 summarizes the energy levels and capture cross section of deep levels observed in the implanted *p*-type 4H-SiC. By high-temperature annealing at 1700°C, the IP2 ($E_V + 0.39$ eV), IP4 ($E_V + 0.79$ eV), IP7 ($E_V + 1.3$ eV), and IP8 ($E_V + 1.4$ eV) centers were generated. In contrast, the IP1 and IP3 centers were almost annealed out by thermal treatment at 1700°C. All the traps observed in *p*-type 4H-SiC (IP1–IP4, IP6–IP8) may be attributed to intrinsic defects because these traps were detected even in the Ne^+-implanted sample. From the energy level and generation behaviors, the dominant levels after 1700°C annealing, IP2 and IP8, may be assigned to the HS1 [19, 23] (HH1 [16]) and HK4 [22] centers, respectively. The HS1 center is a thermally stable defect detected in electron-/proton-irradiated 4H-SiC. In a literature [23], the HS1 center is suggested to be correlated to the D_I defect [24–26] detected by photoluminescence (PL) measurements, which shows the peculiar peaks (no-phonon line L_1: 4272.6 Å [26]). The IP1 and IP4 centers may correspond to the UK1 [22] and HK0 [22], respectively. The UK1 and HK0 centers were detected in *p*-type 4H-SiC irradiated at energy over 160 keV and in samples treated with RIE, respectively.

Note that the concentration of the generated traps (the IP2, IP4, IP7, and IP8 centers) is 10^{13}–10^{14} cm^{-3}, which is about one order-of-magnitude higher than a trap concentration in the nonimplanted sample.

High-Dose Implantation

Fig. 3.9 shows the DLTS spectra obtained from high-dose (8.0×10^{13} cm^{-2}, $N_I \simeq 1 \times 10^{18}$ cm^{-3}) Al^+-implanted *p*-type 4H-SiC after annealing at 1700°C in Ar ambient. In this sample, the IP5 ($E_V + 0.98$ eV), IP6 ($E_V + 1.2$ eV), IP7 ($E_V + 1.3$ eV), and IP9 ($E_V + 1.5$ eV) centers were dominant, which are different from the defects dominating in low-dose implanted samples: the IP2 and IP8 centers. This implies that the IP5, IP6, IP7,

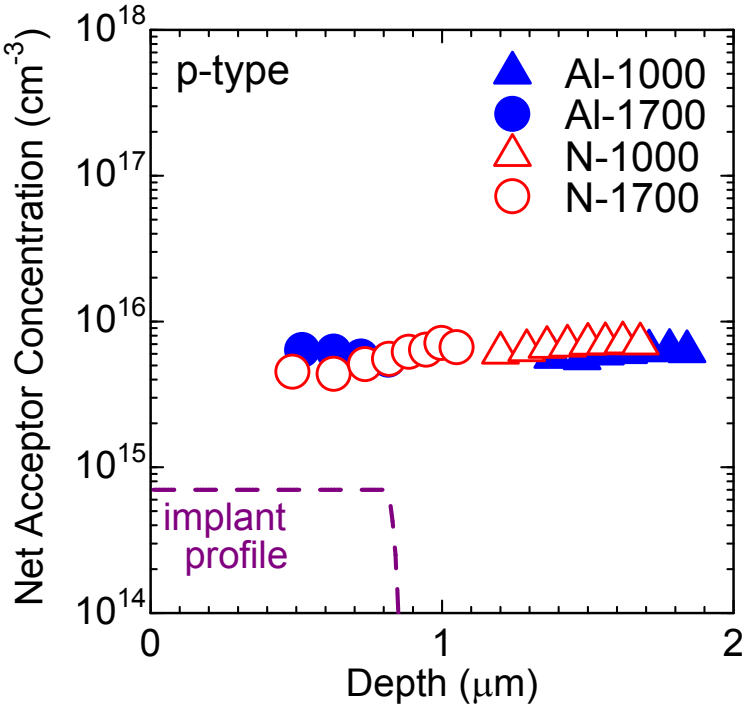

Figure 3.7: Depth profiles of net acceptor concentration (Al-1000: Al^+-implanted sample annealed at 1000°C, Al-1700: Al^+-implanted sample annealed at 1700°C, N-1000: N^+-implanted sample annealed at 1000°C, N-1700: N^+-implanted sample annealed at 1700°C). The high-resistance region does not exist in the sample annealed at 1700°C.

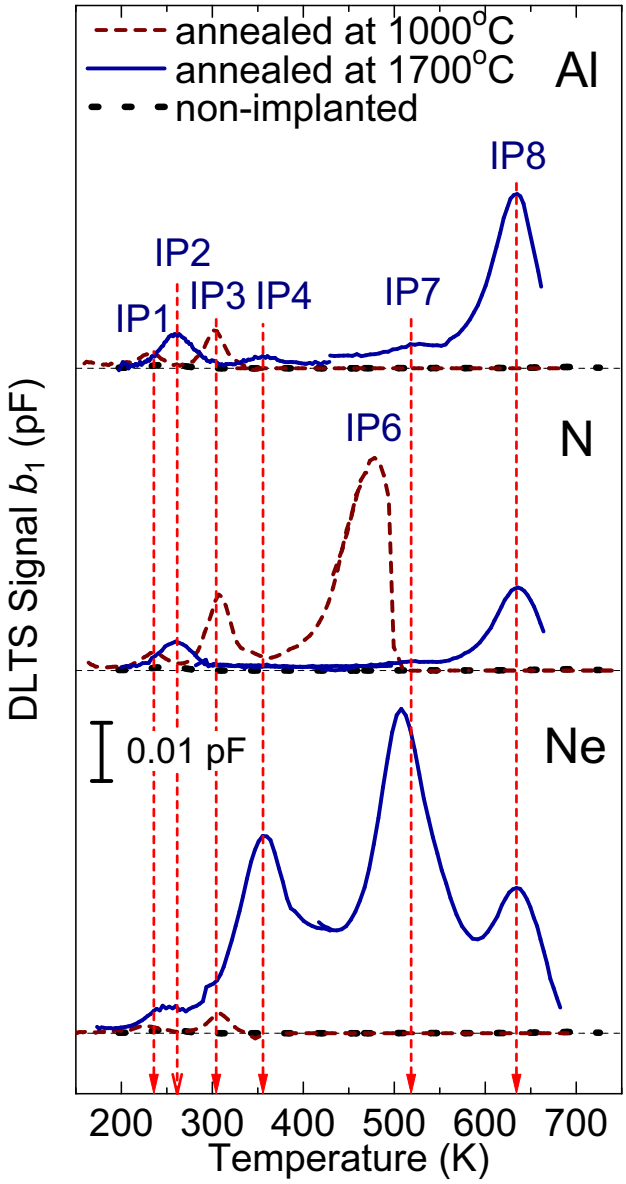

Figure 3.8: DLTS spectra of *p*-type 4H-SiC implanted with Al^+, N^+, and Ne^+ (implant dose: 5.6×10^{10} cm^{-2}) annealed at 1000°C (dashed line) and 1700°C (solid line). The spectrum of nonimplanted sample is indicated with a dotted line.

Table 3.4: Energy positions and capture cross sections of deep levels observed in ion-implanted p-type 4H-SiC (σ: the capture cross section, N_T: the concentration of traps in Al^+-implanted SiC annealed at 1000°C or 1700°C).

label	$E_T - E_V$ (eV)	σ (cm^2)	N_T (1000°C) (cm^{-3})	N_T (1700°C) (cm^{-3})	corresponding center
IP1	0.35	10^{-18}	8.2×10^{12}	not observed	UK1 [22]
IP2	0.39	10^{-18}	not observed	1.4×10^{13}	HS1 [23, 27], HH1 [16]
IP3	0.71	10^{-15}	2.6×10^{13}	not observed	UK2 [22]
IP4	0.79	10^{-16}	not observed	6.4×10^{12}	HK0 [22]
IP6	1.2	10^{-14}	9.7×10^{13} *	not observed	
IP7	1.3	10^{-14}	not observed	1.0×10^{13}	HK3 [22]
IP8	1.4	10^{-16}	not observed	1.9×10^{14}	HK4 [22]

*Data in the N^+-implanted sample.

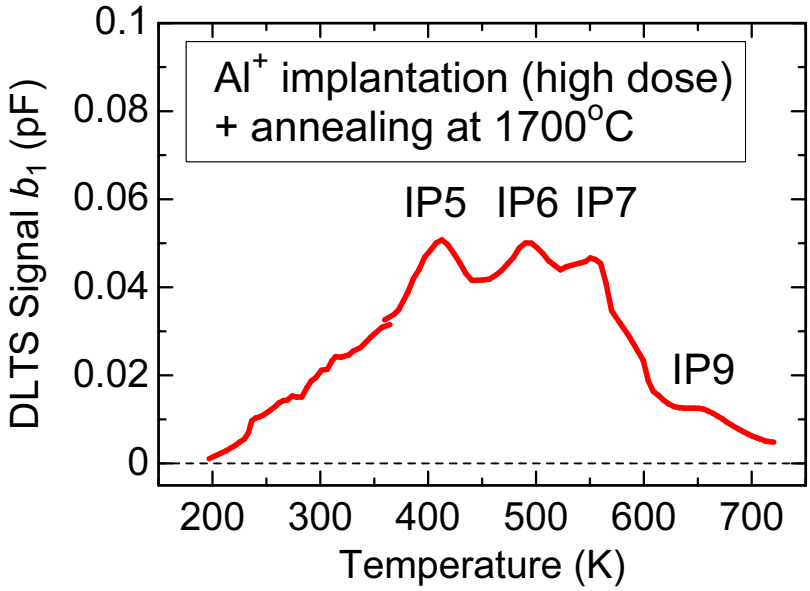

Figure 3.9: DLTS spectra of p-type 4H-SiC implanted with Al^+ (implant dose: 8×10^{13} cm^{-2}) annealed at 1700°C.

and IP9 centers originate from complex (cluster) defects rather than single defects. The parameters of these deep levels are listed in Table 3.5. Other levels, which cannot be resolved due to the overlapping of DLTS peaks, should also exist in this high-dose-implanted p-type sample. Note that the concentration of these deep levels is very high (e.g. IP5: 1×10^{16} cm^{-3}).

3.2.4 Discussion

An overview of deep levels detected in the 4H-SiC implanted with common dopant impurities are shown in Fig. 3.10, where the dominant and stable deep levels in the whole energy range of the bandgap are identified. Among these traps, the $Z_{1/2}$ (IN3) center showed a particular distribution after the ion implantation. Fig. 3.11 shows the depth profiles of $Z_{1/2}$ concentration for Al^+-, N^+-, and P^+-implanted (with low-dose condition) n-type 4H-SiC after 1700°C annealing for 30 min. The $Z_{1/2}$ concentration to a depth of 1.4 μm from the surface was measured by changing the bias voltage in DLTS measurements, whereas the concentration in a depth from about 1.0 μm to 2.3 μm was measured by the same way after removing the 0.7-μm-thick layer by RIE. The trap concentration in a nonimplanted sample is also plotted as the cross symbols. The $Z_{1/2}$ concentration gradually decreases with the depth, and it reaches a value of nonimplanted sample at a depth of 1.7–1.8 μm. From Fig. 3.11, three important insights are obtained. (i) The $Z_{1/2}$ center was generated in a much deeper region than the implant box profile simulated by a TRIM code (shown as a dashed line). Even though the implant profile cannot be confirmed by SIMS analyses due to the very low concentration ($< 7 \times 10^{14}$ cm^{-3}), the real implant profile should be deeper than the TRIM simulation profile because of channeling effects [28, 29], leading to the generation of the $Z_{1/2}$ center in the deep region. (ii) The $Z_{1/2}$ concentration near the surface after ion implantation ($> 1 \times 10^{15}$ cm^{-3}) is about 100 times higher than that before the implantation, which is several times higher than the implanted atom concentration (about 7×10^{14} cm^{-3}). This result also indicates that the $Z_{1/2}$ (and $EH_{6/7}$) centers do not contain any impurities. (iii) The N^+-implanted sample exhibited a slightly lower $Z_{1/2}$ concentration compared with P^+- and Al^+-implanted samples. This may be due to the smaller mass of N atoms and thereby smaller implantation damage.

Here, the effects of deep levels generated by ion implantation on SiC power devices are discussed. With high-dose condition, which is a standard condition for forming pn junctions, the total concentration of deep levels generated by ion implantation reached $\sim$ 15%/5% of the doping concentration in n-type/p-type SiC epilayers, leading to high compensation and thereby the degradation of the conductivity in the implanted reigon. In contrast, with low-dose condition, corresponding to the "implant-tail" region where minority carriers are injected under forward bias, the concentration of deep levels generated by ion implantation exceeded the implanted atom concentration. Such great amount of deep levels in the implant-tail region should lead to short carrier lifetimes.

Table 3.5: Energy positions, capture cross sections, and concentrations of deep levels observed in high-dose Al^+-implanted p-type 4H-SiC.

label	$E_T - E_V$ (eV)	$\sigma(cm^2)$	N_T (cm^{-3})	corresponding center
IP5	0.98	10^{-16}	1×10^{16}	HK2 [22]
IP6	1.2	10^{-14}	1×10^{16}	
IP7	1.3	10^{-14}	1×10^{16}	HK3 [22]
IP9	1.5	10^{-15}	6×10^{15}	

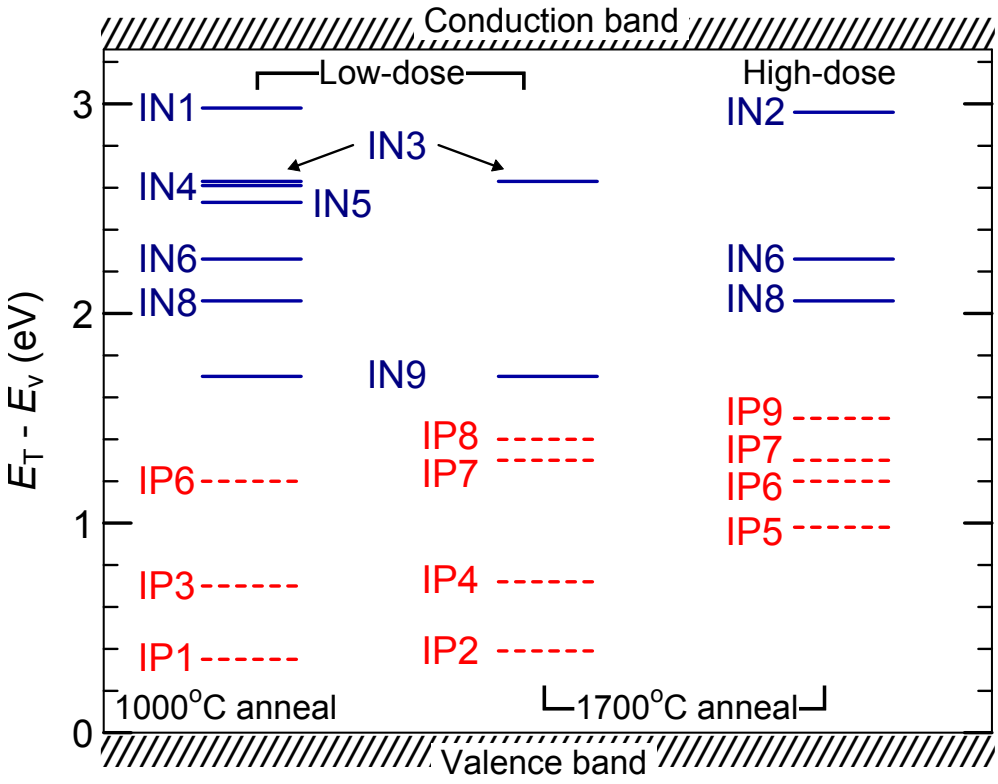

Figure 3.10: Overview of the deep levels detected in n-type (solid lines) and p-type (dashed lines) $Al^+/N^+/P^+/Ne^+$-implanted 4H-SiC.

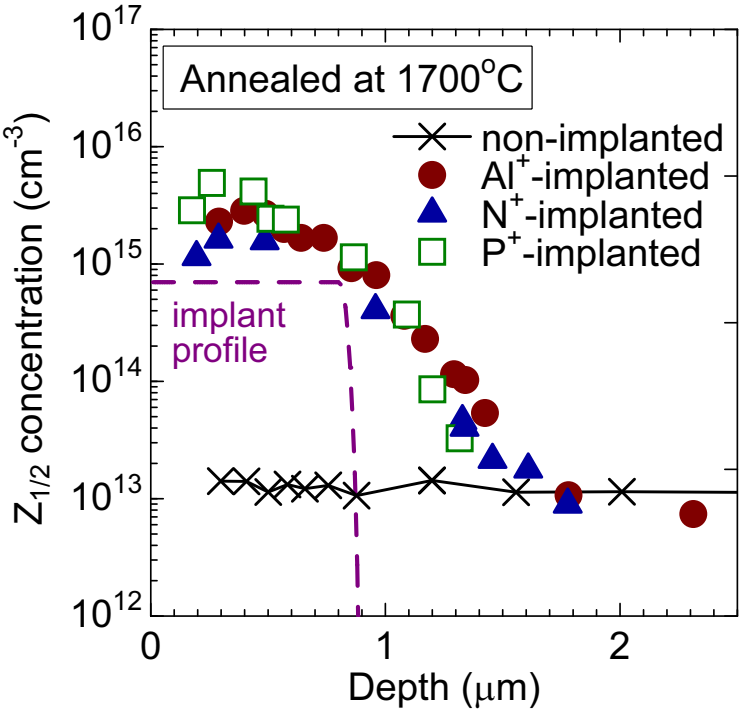

Figure 3.11: Depth profiles of $Z_{1/2}$ concentration for nonimplanted (cross marks) and Al^+(filled circles)-, N^+(filled triangles)-, P^+(open squares)-implanted *n*-type 4H-SiC after 1700°C annealing for 30 min. The dashed line shows the implant profile.

3.3 Deep Levels Generated by Reactive Ion Etching

Reactive Ion Etching (RIE) is an essential process for fabrication of SiC devices such as mesa diodes and trench MOSFETs, which require the etching of high aspect-ratio and selectivity. Some negative effects of RIE such as the reduction of barrier height and the degradation in forward characteristics in 4H-SiC Schottky barrier diodes have been reported [30], which may be due to lattice damage by ion bombardment during RIE. However, studies on deep levels generated by the etching process have not been reported. In this section, the author investigates deep levels in n-type and p-type 4H-SiC generated by RIE.

3.3.1 Experiments

The starting materials were N-doped n-type or Al-doped p-type 4H-SiC (0001) epilayers with a doping concentration of (7–8) $\times$ 10^{15} cm^{-3}. For the C-V and DLTS measurements, SBDs were fabricated in the same manner as described in Chapter 2. All DLTS spectra shown in this section were obtained with reverse bias of -1 V (for n-type) or 1 V (for p-type) and a pulse voltage of 0 V (the monitored depth was about 0.2 μm from the surface). The reverse and pulse voltages were accordingly changed in order to obtain depth profile of defect concentration. After the measurements taken on as-grown samples, RIE was performed for 7 min under a standard condition (CF_4: 5 sccm, O_2: 10 sccm, rf power: 150 W, pressure: 20 Pa), by which a layer of about 0.9 μm was etched off from the surface. After the etching, new Schottky contacts were prepared and C-V and DLTS measurements were repeated.

3.3.2 Electron Traps Detected in n-type Epilayers

Fig. 3.12 shows the DLTS spectra obtained from an as-grown epilayer (dashed line) and an RIE-etched epilayer before (solid line) and after (dotted line) Ar annealing at 1000°C for 30 min. In DLTS spectra for as-grown samples, no change was observed after Ar annealing at 1000°C (not shown). Deep levels named "INn" ($n = 1, 2, 3...$) are the same defect centers as those detected in ion (Al^+, N^+, P^+, or Ne^+)-implanted n-type 4H-SiC. The parameters of the deep levels detected in RIE-etched n-type 4H-SiC are summarized in Table 3.6. The corresponding centers were determined from the energy levels and the thermal stability.

After RIE, large DLTS peaks, IN4 ($E_C - 0.69$ eV) and IN6 ($E_C - 1.0$ eV), emerged, which exist only at depths shallower than $\sim$ 0.5 μm. After Ar annealing at 1000°C for 30 min, the IN4 and IN6 centers disappeared. These thermally unstable centers (IN4 and IN6) may be assigned to the ET2 [31] (EH_3 [16]) and ET3 [31] (RD_2 [2] or RD_3 [2]) centers, respectively, which are generated by electron irradiation at low energy (116 keV) and reduced by Ar annealing at 950°C for 30 min [31]. The IN4 and IN6 centers also correspond to the HR_2 [18] and EH_5 [16] centers, respectively. The HR_2 center was detected in H^+-implanted 4H-SiC and disappeared after annealing at 800°C for 20 min in N_2 [18], while the EH_5 center was observed in electron-irradiated (2.5 MeV [16], 15 MeV [18]) and H^+-implanted [18] 4H-

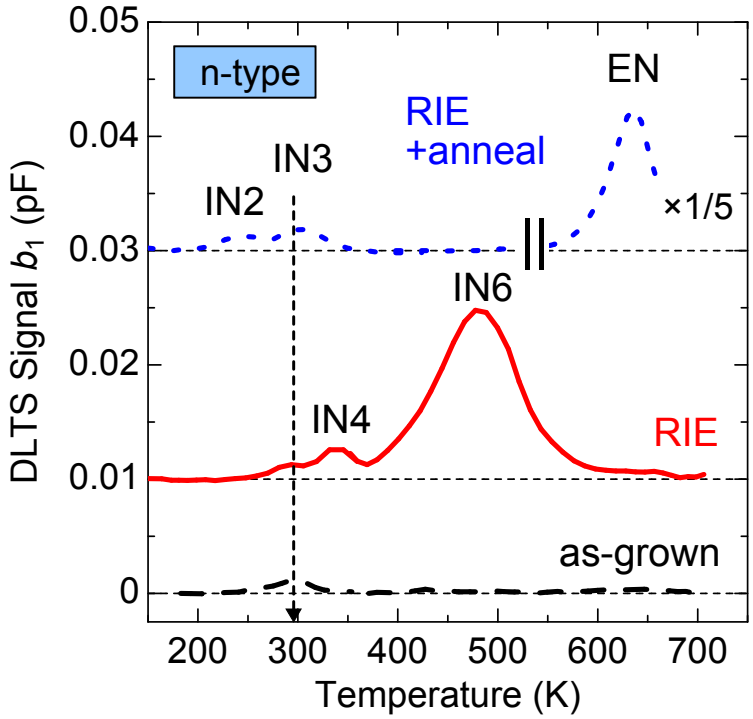

Figure 3.12: DLTS spectra obtained from as-grown (dashed line) and as-etched (solid line) *n*-type 4H-SiC. The spectrum for the sample after RIE followed by Ar annealed at 1000°C for 30 min (dotted line) is also shown.

Table 3.6: Energy positions and capture cross sections of deep levels observed in RIE-etched n-type 4H-SiC (σ: the capture cross section, N_T: the average of trap concentration from the depth of 0.3–1.0 μm in SiC after RIE, after RIE + annealing at 1000°C).

label	$E_C - E_T$ [eV]	σ (cm^2)	N_T (cm^{-3}) RIE	N_T (cm^{-3}) RIE + anneal	corresponding center
IN2	0.30	10^{-18}	not observed	1×10^{13}	ID_8 [2, 9]
IN3	0.67	10^{-14}	3×10^{13}	3×10^{13}	$Z_{1/2}$ [2]
IN4	0.69	10^{-16}	1×10^{13}	not observed	EH_3 [16], HR_2 [18], ET2 [17]
IN6	1.0	10^{-15}	3×10^{14}*	not observed	RD_2 [2, 9], RD_3 [2], EH_5 [16], ET3 [17]
EN	1.6	10^{-13}	not observed	2×10^{15}*	

* the value obtained at the depth of < 0.2 μm (The level exists only in the shallow region.)

SiC, which disappeared after annealing at 600°C for 20 min in N_2 [18]. In contrast, after the Ar annealing at 1000°C, the EN center ($E_C - 1.6$ eV) was observed as a dominant defect with a concentration over 1×10^{15} cm^{-3}. The IN2 ($E_C - 0.30$ eV) center also appeared after the annealing, which can be assigned to the ID_8 center [2, 9] detected in Ti^+-, V^+-, and Al^+-implanted n-type 4H-SiC after annealing at 1700°C for 30 min.

Fig. 3.13 shows the depth profile of the EN center, which was dominant in the RIE-etched n-type 4H-SiC after Ar annealing at 1000°C. The concentration of the EN center was very high near the surface ($\sim 1 \times 10^{15}$ cm^{-3} at 0.1 μm from the surface), whereas relatively low in deeper region ($\sim 4 \times 10^{13}$ cm^{-3} at depths of > 0.2 μm). The high density of the EN center near the surface may reflect the lattice damage by ion bombardment during RIE. Because the resolving of an $EH_{6/7}$ (IN9) peak from an EN peak is difficult due to the severe overlapping, the relatively low and flat trap distribution at depths deeper than 0.2 μm in Fig. 3.13 could possibly correspond to the $EH_{6/7}$ center.

3.3.3 Generation of Semi-Insulating Region in *p*-type Epilayers

Fig. 3.14 and Fig. 3.15 show the $1/C^2$-V plots obtained from n-type and p-type 4H-SiC, respectively, for an as-grown epilayer (filled circles) and RIE-etched epilayer before (triangles) and after (squares) annealing at 1000°C for 30 min in Ar ambient. The solid (as-grown), dashed (RIE), and dotted (RIE + annealing) lines show the corresponding fitting. The fitting procedure was conducted using the doping concentration (N_d or N_a) and the thickness of the compensated region d_C as parameters. In n-type samples, the doping concentration increased after RIE, indicating the generation of unknown shallow donors. In p-type samples after RIE, in contrast, the capacitance extremely decreased to ~ 5 pF (~ 120 pF at 0 V before RIE) and stayed almost independent of the bias. The small and constant capacitance of the RIE-etched p-type sample indicates the existence of a compensated or deactivated region. In view of 5 pF with a contact size of 1 mm, the thickness of the compensated (or deactivated) region is estimated to be about 14 μm, which is almost equal to the epilayer thickness. After Ar annealing at 1000°C for 30 min, the C-V characteristics were recovered to those of as-grown samples. The author also found that the capacitances could be recovered by the annealing for only 2 min.

It is unlikely that the 14-μm-thick depletion region is attributed to lattice damage introduced by ion bombardment during RIE process because the acceleration energy of impinging ions is only several hundred eV at the highest. Note that an implanted fluorine with 500 eV reaches below a depth of 4 nm, which is simulated by a SRIM [32] code. Therefore, the author speculates that the thick depletion region is caused by permeation of some atoms during RIE process, which was observed in Si [33]. In Si, shallow acceptors are passivated by hydrogen permeation, which recovers to an original state by annealing at 200°C [34]. Fig. 3.16 shows the depth profiles of impurities obtained by secondary ion mass spectrometry (SIMS) for RIE-etched p-type 4H-SiC. The filled circles, filled triangles, and squares correspond

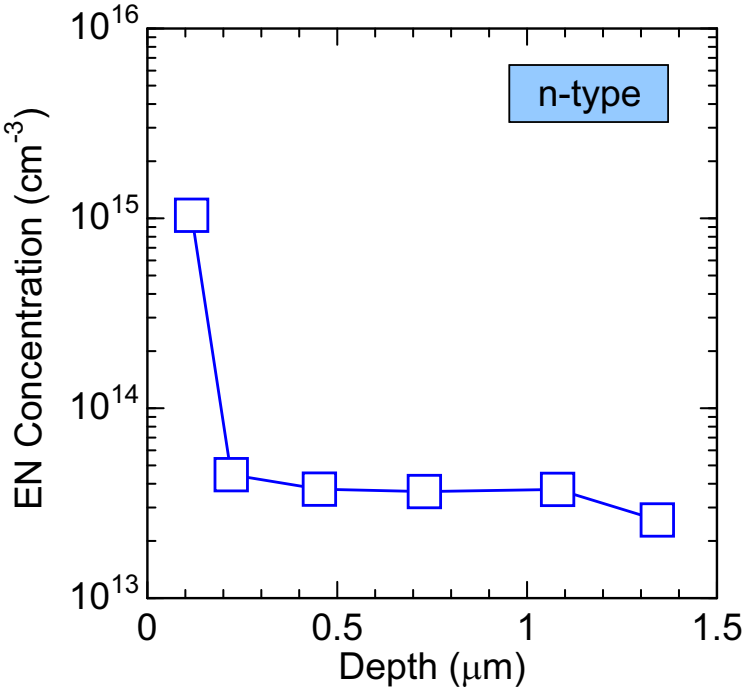

Figure 3.13: Depth profile of the EN defect in the RIE-etched n-type 4H-SiC after Ar annealing at 1000°C.

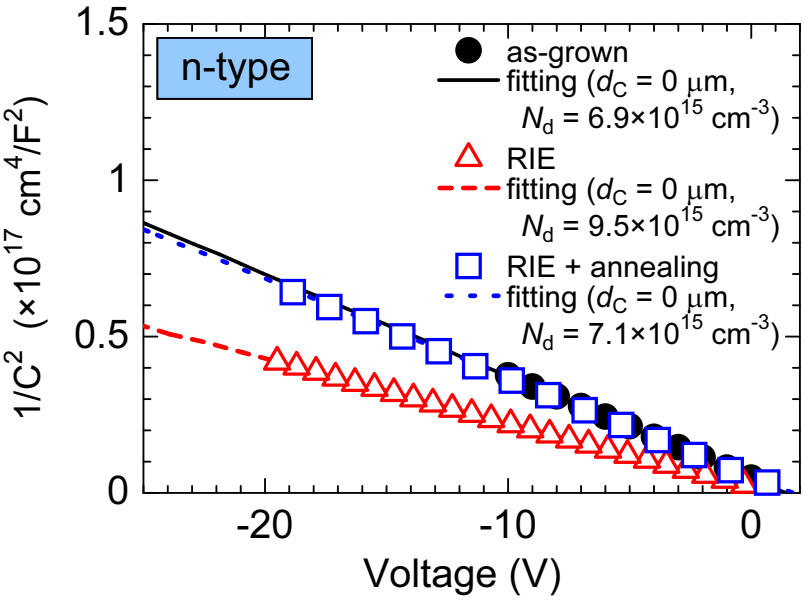

Figure 3.14: $1/C^2$-V plots obtained from n-type 4H-SiC for an as-grown epilayer (filled circles) and an RIE-etched epilayer before (triangles) and after (squares) Ar annealing at 1000°C. The solid, broken, and dotted lines are the fitting lines to the corresponding experimental data (N_d: donor concentration, d_C: thickness of the compensated region).

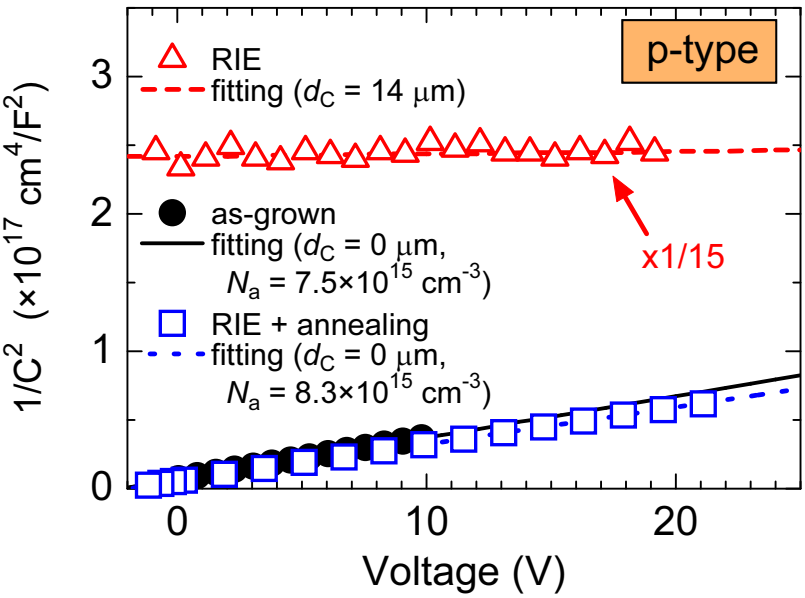

Figure 3.15: $1/C^2$-V plots obtained from p-type 4H-SiC for an as-grown epilayer (filled circles) and an RIE-etched epilayer before (triangles) and after (squares) Ar annealing at 1000°C.

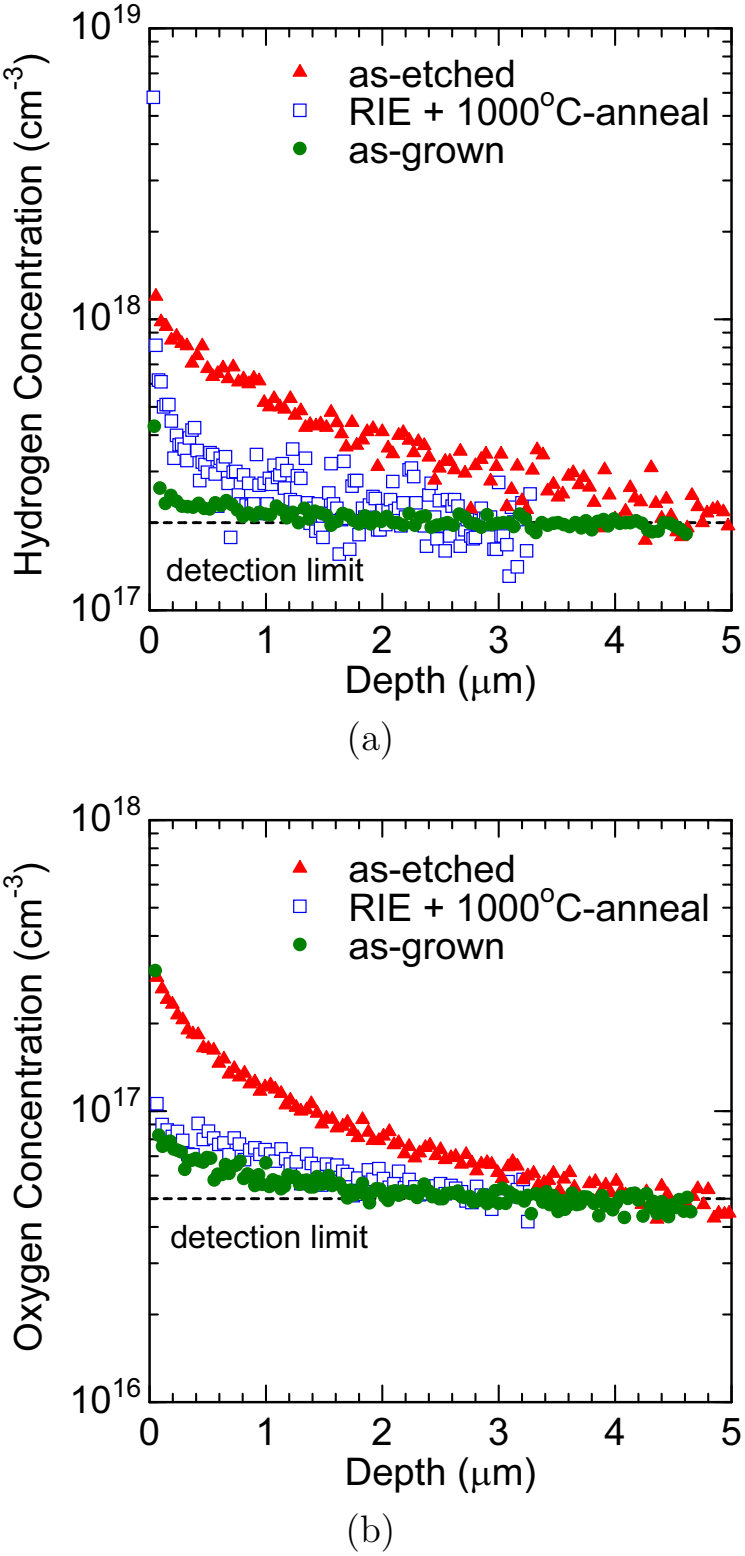

Figure 3.16: (a) Hydrogen and (b) oxygen depth profiles obtained by SIMS for an as-grown epilayer (filled circles), an epilayer after RIE (filled triangles), and after RIE followed by Ar annealing at 1000°C (squares).

to the impurity concentration in an as-grown p-type epilayer, an epilayer after RIE, and after RIE followed by Ar annealing at 1000°C, respectively. Hydrogen (Fig. 3.16(a)) and oxygen (Fig. 3.16(b)) atoms clearly permeated the samples after RIE, while fluorine atoms (not shown) did not. Hydrogen atoms may come from H_2O remaining in the RIE chamber, whereas oxygen atoms come from O_2 gas. The fluorine concentration in the RIE-etched sample (below 3×10^{15} cm^{-3}, which is nearly equal to the detection limit) was clearly below the doping concentration ($\sim 8 \times 10^{15}$ cm^{-3}), indicating that fluorine atoms were not related to the formation of the depletion region. Rather than hydrogen atoms, the origin of the thick depletion region is more likely to be oxygen atoms, because a high concentration of hydrogen atoms (over 2×10^{17} cm^{-3}) still remained near the surface after annealing at 1000°C, whereas the oxygen concentration decreased to the value in the as-grown sample.

3.3.4 Hole Traps Detected in p-type Epilayers

Fig. 3.17 shows the DLTS spectra obtained from as-grown (dashed line) and RIE-etched p-type 4H-SiC with annealing at 1000°C (solid line). The as-etched sample could not be measured due to the severe compensation (or deactivation) as discussed above. Compared to the DLTS spectrum of the as-grown sample, the etched sample showed very large DLTS peaks assigned to IP1 ($E_V + 0.35$ eV), IP2 (HS1 [23, 27]: $E_V + 0.39$ eV), IP4 ($E_V + 0.79$ eV), IP5 ($E_V + 0.98$ eV), IP7 ($E_V + 1.3$ eV), and EP ($E_V + 1.4$ eV). Deep levels named "IPm" ($m = 1, 2, 3...$) are the same defect centers as those detected in ion (Al^+, N^+, P^+, or Ne^+)-implanted p-type 4H-SiC. The parameters of the deep levels detected in RIE-etched p-type 4H-SiC are summarized in Table 3.7. The respective IP4, IP5, IP7, and EP (maybe IP8) centers correspond to the HK0, HK2, HK3, and HK4 centers, which have been detected in RIE-etched p-type 4H-SiC after annealing at 950°C for 30 min in Ar ambient [22]. From the energy level, the IP1 center may be the same as the UK1 center, which is one of dominant peaks in electron-irradiated p-type 4H-SiC after annealing at 950°C [22]. Among the observed peaks, the EP center exists with the highest concentration (over 1×10^{14} cm^{-3}).

Fig. 3.18 shows the depth profiles of the IP4 (circles) and EP (triangles) centers in the RIE-etched p-type 4H-SiC after annealing at 1000°C. The IP4 and EP centers are generated to a deep region over 1 μm by RIE (and 1000°C-annealing) with the high concentration. These trap distribution may reflect the permeation of hydrogen and/or oxygen atoms during RIE.

3.3.5 Discussion

As discussed in the last section, the dry etching process generates a variety of deep defects in n-type and p-type 4H-SiC. Fig. 3.19 shows the overview of deep levels detected in as-grown and RIE-etched 4H-SiC. The important effect of RIE on SiC is, in particular, that the capacitance of p-type samples is extremely low just after RIE, suggesting that the

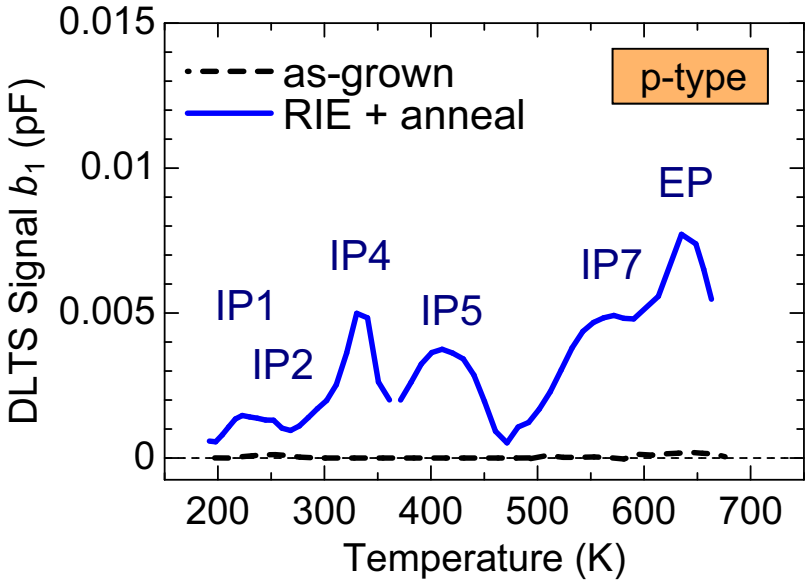

Figure 3.17: DLTS spectra obtained from as-grown (dashed line) and RIE-etched p-type 4H-SiC with annealing at 1000°C (solid line).

Table 3.7: Energy positions and capture cross sections of deep levels observed in p-type 4H-SiC after RIE followed by Ar aneealing at 1000°C (σ: the capture cross section, N_T: the average of trap concentration from the depth of 0.3–1.0 μm).

label	$E_T - E_V$ (eV)	σ (cm^2)	N_T (cm^{-3})	corresponding center
IP1	0.35	10^{-18}	2×10^{13}	UK1 [22]
IP2	0.39	10^{-18}	2×10^{13}	HS1 [23, 27], HH1 [16]
IP4	0.79	10^{-16}	9×10^{13}	HK0 [22]
IP5	0.98	10^{-16}	4×10^{13}	HK2 [22]
IP7	1.3	10^{-14}	7×10^{13}	HK3 [22]
EP	1.4	10^{-16}	2×10^{14}	IP8, HK4 [22]

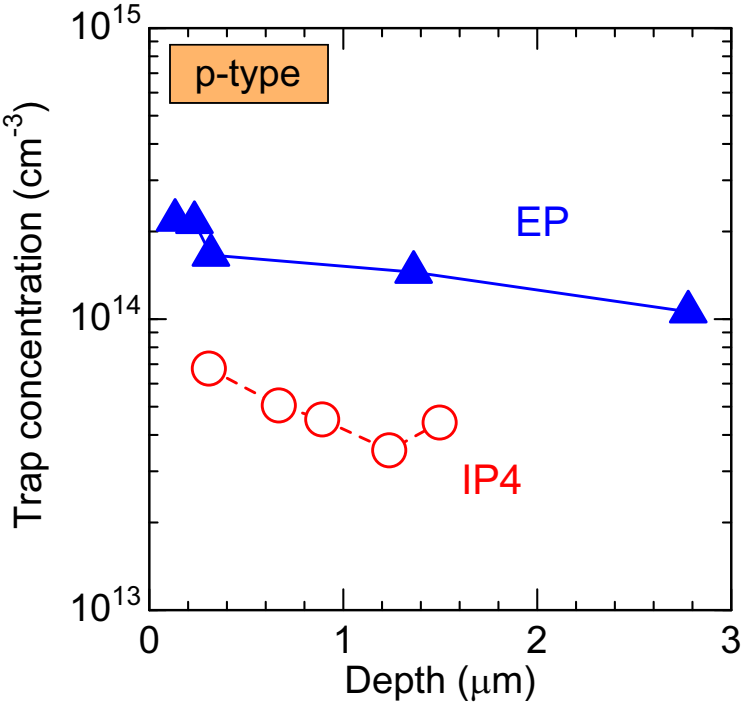

Figure 3.18: Depth profiles of the IP4 (circles) and EP (triangles) centers in RIE-etched *p*-type 4H-SiC after annealing at 1000°C.

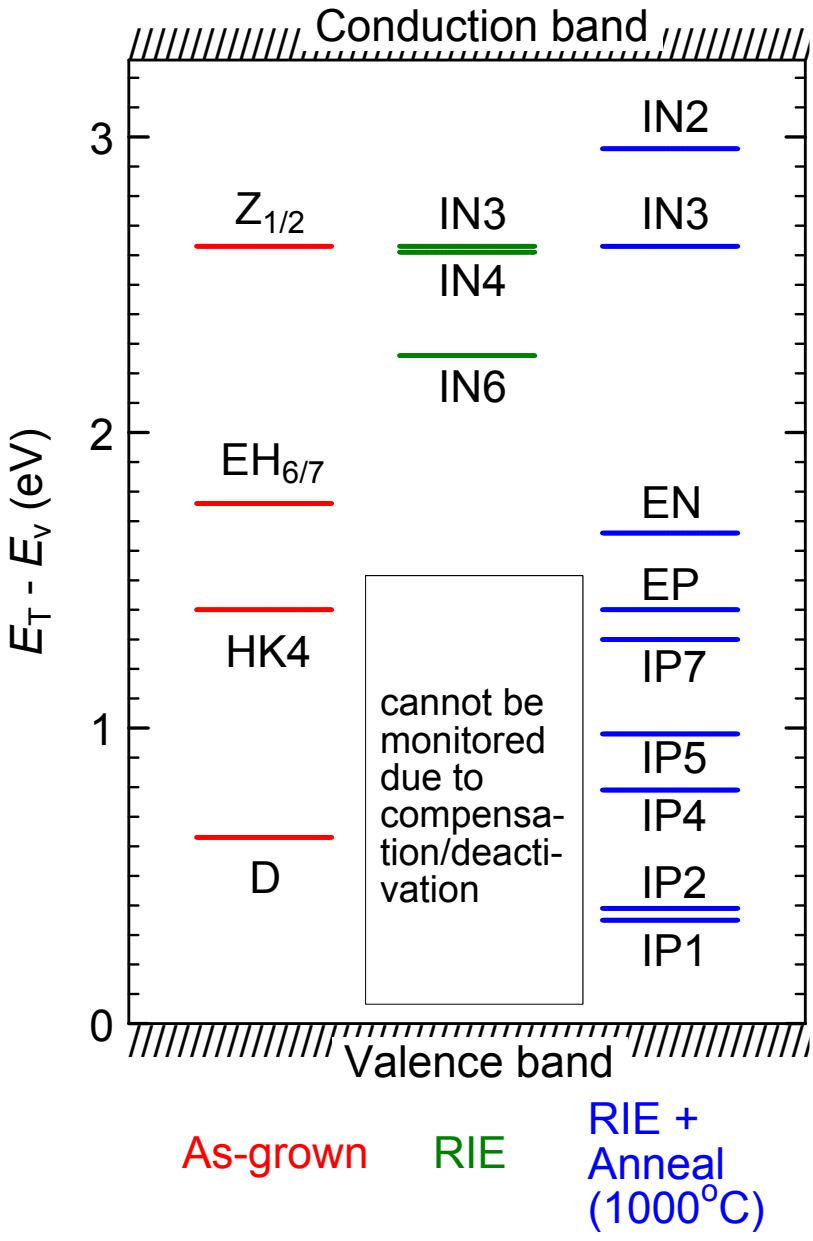

Figure 3.19: Overview of deep levels detected in as-grown and RIE-etched 4H-SiC.

acceptors are compensated by generated defects or are deactivated. The author also found that the extent of this compensation or deactivation (the thickness of the depletion region) depends on the RIE condition. When RIE is employed in SiC-device fabrication, subsequent annealing or optimization of RIE condition is required. Depth profiles obtained by SIMS for RIE-etched samples indicate that the compensation or deactivation might originate from oxygen permeation by RIE. Some oxygen-related defects have been reported to act as shallow donors in SiC [35], which agrees with the increase of the carrier concentration in the etched n-type epilayer (Fig. 3.14). Therefore, an oxygen-related defect may compensate or deactivate the acceptors, even though the annealing behavior of the defects obtained in this study differs from the behavior of the oxygen-related defects [35].

Although the low capacitance could be recovered by annealing at 1000°C, several deep defects remained. Based on DLTS investigations, the energy levels and the corresponding depth profiles of the major deep defects were determined. The INn (n = 2, 3, 4, 5, 6) and IPm (m = 1, 2, 4, 5, 7) centers are the same defects as those detected in ion (Al^+, N^+, P^+, or Ne^+)-implanted 4H-SiC, which may originate from intrinsic defects because all these levels were observed in ion-implanted samples irrespective of the implanted species. All of them (except for IN2) and EP (maybe IP8) centers are also observed in electron-irradiated samples (the corresponding centers are shown in Table 3.6 and Table 3.7), implying that these deep levels also originate from intrinsic defects. The EN ($E_C - 1.6$ eV) center exists only in the near-surface region and may be specific defects generated by RIE. In particular, the EN center showed an extremely high concentration over 1×10^{15} cm^{-3} at a depth of 0.1 μm from the surface. In p-type 4H-SiC, the EP ($E_V + 1.4$ eV) center exhibit the rather flat depth profile and the high concentration, which may originate from the permeation of hydrogen and/or oxygen atoms during RIE.

3.4 Summary

N^+, P^+, Al^+, or Ne^+ was implanted into n-type and p-type 4H-SiC epilayers. In n-type samples, seven peaks, IN1 (ET1, $E_C - 0.28$ eV), IN3 ($Z_{1/2}$, $E_C - 0.67$ eV), IN4 (EH_3, $E_C - 0.69$ eV), IN5 (EH_4, $E_C - 0.73$ eV), IN6 (EH_5, $E_C - 1.0$ eV), IN8 ($E_C - 1.2$ eV), and IN9 ($EH_{6/7}$, $E_C - 1.5$ eV), have emerged by low-dose (5.6×10^{10} cm^{-2}) implantation followed by Ar annealing at 1000°C, irrespective of the implanted species. The origins of these deep levels should be intrinsic defects because they are generated independently of the implanted species. After high-temperature annealing at 1700°C, most DLTS peaks disappeared, whereas the IN3 and IN9 centers survived with a high concentration (10^{15} cm^{-3}) over the implanted atom concentration. The depth profile of the $Z_{1/2}$ center extended to much deeper region than the implant profile. When the implantation dose was high (8.0×10^{13} cm^{-2}), three broad peaks, IN2 (ID_8, $E_C - 0.30$ eV), IN6 (EH_5, $E_C - 1.0$ eV), and IN8 ($E_C - 1.2$ eV), were observed with very high concentrations of about 10^{17} cm^{-3}.

In p-type samples, the IP1 (UK1, $E_V + 0.35$ eV) and IP3 (UK2, $E_V + 0.71$ eV) centers were detected after low-dose implantation followed by Ar annealing at 1000°C, whereas the IP2 (HS1, $E_V + 0.39$ eV), IP4 (HK0, $E_V + 0.79$ eV), IP7 (HK3, $E_V + 1.3$ eV), and IP8 (HK4, $E_V + 1.4$ eV) centers were dominant after the implantation followed by annealing at 1700°C, irrespective of the implanted species. These traps should also originate from intrinsic defects. When the implantation dose was high (8.0×10^{13} cm^{-2}), the IP5 (HK2, $E_V + 0.98$ eV), IP6 ($E_V + 1.2$ eV), IP7 (HK3, $E_V + 1.3$ eV), and IP9 ($E_V + 1.5$ eV) centers were observed at high concentrations of about 10^{16} cm^{-3}. From the high-dose implanted n-type/p-type samples, a standard condition for forming pn junctions, the author found that ion implantation could introduce high compensation and thereby the degradation of the conductivity in the implanted region. In contrast, the low-dose implantation results, corresponding to the "implant-tail" region, imply that carrier lifetimes degrade in ion-implanted samples due to generation of a high density of the $Z_{1/2}$ center.

The deep levels induced by RIE of n-type/p-type 4H-SiC were also investigated. In n-type samples, the IN4 (EH_3, $E_C - 0.69$ eV) and IN6 (EH_5, $E_C - 1.0$ eV) centers were generated by RIE, which disappeared after subsequent annealing at 1000°C in Ar ambient. After the annealing, however, new peaks, IN2 (ID_8, $E_C - 0.30$ eV) and EN ($E_C - 1.6$ eV), appeared, and the IN3 center kept a concentration of 3×10^{13} cm^{-3}. In particular, the EN center showed a high concentration over 1×10^{15} cm^{-3} near the surface, which may originate from lattice damage caused by ion bombardment. In p-type samples, the capacitance of a Schottky contact after RIE was abnormally small due to compensation or deactivation of acceptors extending to a depth of ~ 14 μm, which is nearly equal to the epilayer thickness. From the SIMS results, the compensation or deactivation may be attributed to permeation of oxygen atoms into SiC bulk during RIE. After Ar annealing at 1000°C, the capacitance recovered to that of a Schottky contact on as-grown samples. Even after the annealing, however, various kinds of defects, IP1 (UK1, $E_V + 0.35$ eV), IP2 (HS2, $E_V + 0.39$ eV), IP4 (HK0, $E_V + 0.79$ eV), IP5 (HK2, $E_V + 0.98$ eV), IP7 (HK3, $E_V + 1.3$ eV), and EP (HK4, $E_V + 1.4$ eV), remained with a high concentration (a typical concentration: 7×10^{13} cm^{-3}).

References

[1] Y. A. Vodakov and E. Mokhov, *Silicon Carbide 1973*, (University of South Carolina Press, Columbia, SC, 1974), p. 508.

[2] T. Dalibor, G. Pensl, H. Matsunami, T. Kimoto, W. J. Choyke, A. Schöner, and N. Nordell, *Physica Status Solidi (A)* **162**, 199 (1997).

[3] M. L. David, G. Alfieri, E. M. Monakhov, A. Hallén, C. Blanchard, B. G. Svensson, and J. F. Barbot, *Journal of Applied Physics* **95**, 4728 (2004).

[4] G. Alfieri, E. V. Monakhov, B. G. Svensson, and M. K. Linnarsson, *Journal of Applied Physics* **98**, 043518 (2005).

[5] G. Alfieri and T. Kimoto, *Journal of Applied Physics* **101**, 103716 (2007).

[6] S. Mitra, M. V. Rao, N. Papanicolaou, K. A. Jones, M. Derenge, O. W. Holland, R. D. Vispute, and S. R. Wilson, *Journal of Applied Physics* **95**, 69 (2004).

[7] M. Canino, A. Castaldini, A. Cavallini, F. Moscatelli, R. Nipoti, and A. Poggi, *Materials Science Forum* **527-529**, 811 (2006).

[8] J. Wong-Leung and B. G. Svensson, *Applied Physics Letters* **92**, 142105 (2008).

[9] T. Troffer, M. Schadt, T. Frank, H. Itoh, G. Pensl, J. Heindl, H. P. Strunk, and M. Maier, *Physica Status Solidi (A)* **162**, 277 (1997).

[10] D. Åberg, A. Hallén, and B. G. Svensson, *Physica B* **273-274**, 672 (1999).

[11] Y. Negoro, T. Kimoto, and H. Matsunami, *Journal of Applied Physics* **98**, 043709 (2005).

[12] M. Laube, F. Schmid, G. Pensl, G. Wagner, M. Linnarsson, and M. Maier, *Journal of Applied Physics* **92**, 549 (2002).

[13] D. Peters, R. Schörner, K. Holzlein, and P. Friedrichs, *Applied Physics Letters* **71**, 2996 (1997).

[14] J. F. Ziegler, *Nuclear Instruments and Methods in Physics Research Section B: Beam Interactions with Materials and Atoms* **136-138**, 141 (1998).

[15] Y. Negoro, K. Katsumoto, T. Kimoto, and H. Matsunami, *Journal of Applied Physics* **96**, 224 (2004).

[16] C. Hemmingsson, N. T. Son, O. Kordina, J. P. Bergman, E. Janzén, J. L. Lindström, S. Savage, and N. Nordell, *Journal of Applied Physics* **81**, 6155 (1997).

[17] K. Danno and T. Kimoto, *Journal of Applied Physics* **100**, 113728 (2006).

[18] G. Alfieri, E. V. Monakhov, B. G. Svensson, and A. Hallén, *Journal of Applied Physics* **98**, 113524 (2005).

[19] L. Storasta, A. Henry, J. Bergman, and E. Janzén, *Materials Science Forum* **457-460**, 469 (2004).

[20] L. Storasta, H. Tsuchida, T. Miyazawa, and T. Ohshima, *Journal of Applied Physics* **103**, 013705 (2008).

[21] S. G. Sridhara, L. L. Clemen, R. P. Devaty, W. J. Choyke, D. J. Larkin, H. S. Kong, T. Troffer, and G. Pensl, *Journal of Applied Physics* **83**, 7909 (1998).

[22] K. Danno and T. Kimoto, *Journal of Applied Physics* **101**, 103704 (2007).

[23] L. Storasta, F. H. C. Carlsson, S. G. Sridhara, J. P. Bergman, A. Henry, T. Egilsson, A. Hallén, and E. Janzén, *Applied Physics Letters* **78**, 46 (2001).

[24] W. Choyke and L. Patrick, *Physical Review B* **4**, 1843 (1971).

[25] L. Patrick and W. J. Choyke, *Physical Review B* **5**, 3253 (1972).

[26] T. Egilsson, J. Bergman, I. Ivanov, A. Henry, and E. Janzén, *Physical Review B - Condensed Matter and Materials Physics* **59**, 1956 (1999).

[27] L. Storasta, J. P. Bergman, E. Janzén, A. Henry, and J. Lu, *Journal of Applied Physics* **96**, 4909 (2004).

[28] S. Yaguchi, T. Kimoto, N. Ohyama, and H. Matsunami, *Japanese Journal of Applied Physics* **34**, 3036 (1995).

[29] M. Janson, A. Hallén, P. Godignon, A. Kuznetsov, M. Linnarsson, E. Morvan, and B. Svensson, *Materials Science Forum* **338**, II (2000).

[30] V. Khemka, T. Chow, and R. Gutmann, *Journal of Electronic Materials* **27**, 1128 (1998).

[31] K. Danno, D. Nakamura, and T. Kimoto, *Applied Physics Letters* **90**, 202109 (2007).

[32] J. F. Ziegler, M. D. Ziegler, and J. P. Biersack, *Nuclear Instruments and Methods in Physics Research Section B* **268**, 1818 (2010).

[33] G. S. Oehrlein, *Materials Science and Engineering B* **4**, 441 (1989).

[34] J. I. Pankove, R. O. Wance, and J. E. Berkeyheiser, *Applied Physics Letters* **45**, 1100 (1984).

[35] T. Dalibor, H. Trageser, G. Pensl, T. Kimoto, H. Matsunami, D. Nizhner, O. Shigiltchoff, and W. J. Choyke, *Materials Science and Engineering B* **61-62**, 454 (1999).

Chapter 4

Reduction of Deep Levels by Thermal Oxidation

4.1 Introduction

In the last chapter, deep levels and their depth profiles in ion-implanted or RIE-etched 4H-SiC were systematically investigated. Because the concentrations of these deep levels are very high, a way to reduce the defects must be established.

High temperature annealing in Ar ambient has commonly been employed to reduce deep levels in SiC epilayers [1–13]. Even after annealing at 1700–2000°C, however, a part of deep levels such as the $Z_{1/2}$ ($E_C - 0.67$ eV), $EH_{6/7}$ ($E_C - 1.5$ eV) , D ($E_V + 0.63$ eV), and HS1 ($E_V + 0.39$ eV) centers survives with concentrations of 10^{13}–10^{14} cm^{-3} [1, 3, 4, 6, 8, 9, 11, 13]. Thus, in addition to a high temperature annealing, new processes to reduce deep levels have been required.

C^+ implantation followed by Ar annealing [14, 15] and thermal oxidation [16] were recently found to be effective for the reduction of deep levels in as-grown 4H-SiC (the detail is shown in Chapter 5). In this study, the author attempts to reduce the deep levels generated by ion implantation and reactive ion etching (RIE) using thermal oxidation. The mechanisms of the trap reduction will be discussed in Chapter 5.

4.2 Deep Level Reduction in Ion-Implanted Epilayers

As shown in Chapter 3, the dominant defects in low-dose (total dose: 5.6×10^{10} cm^{-2}) implanted samples after Ar annealing at 1700°C were determined as the IN3 ($Z_{1/2}$: $E_C - 0.67$ eV), IN9 ($EH_{6/7}$: $E_C - 1.5$ eV), IP2 (HS1: $E_V + 0.39$ eV) and IP8 (HK4: $E_V + 1.4$ eV) centers, whereas in high-dose (total dose: 8.0×10^{13} cm^{-2}) implanted samples the IN8 ($E_C - 1.2$ eV), IP5 (HK2: $E_V + 0.98$ eV), IP6 ($E_V + 1.2$ eV), and IP7 (HK3: $E_V + 1.3$ eV) centers were dominant. Because the concentrations of these levels are very high (10^{14}–10^{15} cm^{-3} in low-dose samples, 10^{16}–10^{17} cm^{-3} in high-dose samples), a way to

reduce the defects must be established.

The ion-implanted 4H-SiC epilayers prepared in Chapter 3 (the Al^+-, N^+-, or P^+-implanted samples after Ar annealing at 1700°C for 30 min) were oxidized in O_2 ambient at 1150°C for 2 h, by which 25-nm-thick SiO_2 was formed. After removing the oxide, Schottky contacts were formed and DLTS measurements were performed. For the deep level transient spectroscopy (DLTS) measurements, a typical reverse bias is −1 V (for n-type) or 1 V (for p-type) and filling pulse voltage is 0 V.

4.2.1 Deep Levels in n-type Epilayers

Fig. 4.1 shows the DLTS spectra obtained from low-dose Al^+-implanted n-type 4H-SiC after Ar annealing at 1700°C for 30 min (filled triangles) and after the annealing followed by oxidation at 1150°C for 2 h (squares). A DLTS spectrum obtained from nonimplanted sample is also shown as filled circles, where the $Z_{1/2}$ [1] ($E_C - 0.67$ eV) and $EH_{6/7}$ [2] ($E_C - 1.5$ eV) centers are observed with concentrations of (1–2) $\times 10^{13}$ cm^{-3}. After the implantation, the concentration of the IN3 ($Z_{1/2}$) and IN9 ($EH_{6/7}$) centers increased and was higher than the implanted ion concentration even after Ar annealing at 1700°C. As shown by the square symbols, these thermally stable traps ($Z_{1/2}$ and $EH_{6/7}$) were reduced by the subsequent oxidation. Note that an only 15-nm-thick surface layer was consumed by the oxidation, meaning that the main body of the implanted region, (0.7–0.8) μm, almost remains. The parameters of the deep levels detected in low-dose ion-implanted n-type 4H-SiC are summarized in Table 4.1. The remarkable reduction of the $Z_{1/2}$ and $EH_{6/7}$ centers by thermal oxidation agrees with the recent results obtained for as-grown 4H-SiC [16].

Fig. 4.2 shows the depth profiles of the $Z_{1/2}$ defect observed in low-dose Al^+-implanted n-type 4H-SiC after 1700°C annealing (filled triangles) and after the annealing followed by oxidation (squares and inverse triangles). Here, "Ox.×2" means two successive oxidations at 1150°C for 2 h. The $Z_{1/2}$ center in nonimplanted sample (filled circles) is uniformly distributed with a concentration of (1-2) $\times 10^{13}$ cm^{-3} along the depth. The $Z_{1/2}$ profile extended to a depth of about 1.5 μm by the Al^+-implantation followed by annealing at 1700°C for 30 min, which significantly decreased after every oxidation. The $Z_{1/2}$ concentration was reduced from about 3×10^{15} cm^{-3} (filled triangles) to 1×10^{15} cm^{-3} (squares) by the first oxidation, and to 3×10^{14} cm^{-3} (inverse triangles) by the second oxidation at a depth of about 0.5 μm. The same phenomenon was observed for the $EH_{6/7}$ center (not shown), indicating that when the implant dose is relatively low all the major deep levels observed in ion-implanted n-type 4H-SiC can be remarkably reduced by oxidation. The corresponding deep levels in samples implanted with the other species (N^+, P^+) showed a similar behavior (not shown).

Fig. 4.3 shows the DLTS spectra obtained from high-dose P^+-implanted n-type 4H-SiC after annealing at 1700°C (filled triangles) and after the annealing followed by oxidation at 1150°C (squares and inverse triangles). In the implanted sample after annealing at 1700°C,

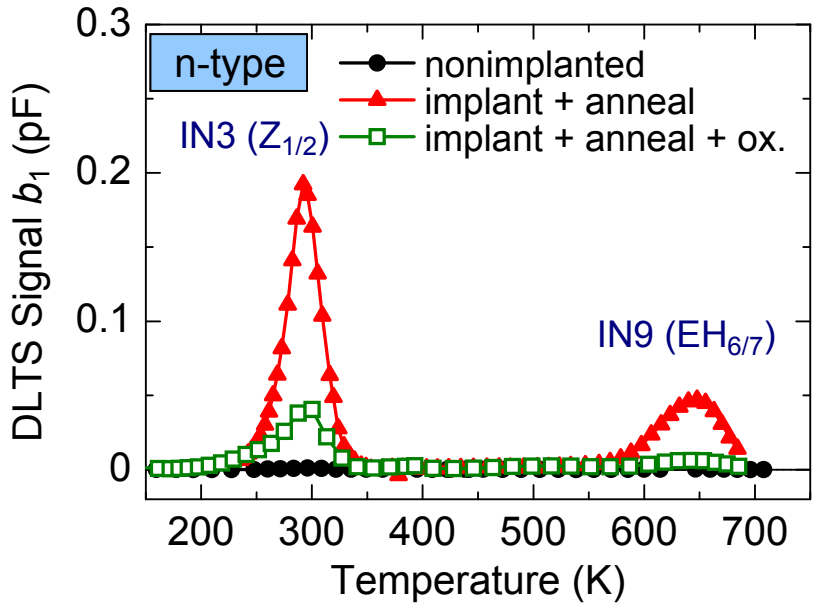

Figure 4.1: DLTS spectra of nonimplanted (filled circles) and low-dose Al^+-implanted n-type 4H-SiC after Ar annealing at 1700°C for 30 min (filled triangles) and after the annealing followed by oxidation at 1150°C for 2 h (squares).

Table 4.1: Energy positions and capture cross-sections of deep levels observed in low-dose ion-implanted n-type 4H-SiC (σ: the capture cross-section, N_T: the concentration of traps at about 0.5 μm from the surface in the Al^+-implanted SiC before and after oxidation at 1150°C for 2 h).

label	$E_C - E_T$ (eV)	σ (cm^2)	N_T (cm^{-3}) before Ox.	after Ox.	after Ox.×2	corresponding center
IN3	0.67	10^{-14}	3×10^{15}	1×10^{15}	2×10^{14}	$Z_{1/2}$ [1]
IN9	1.5	10^{-14}	8×10^{14}	5×10^{14}	2×10^{14}	$EH_{6/7}$ [2]

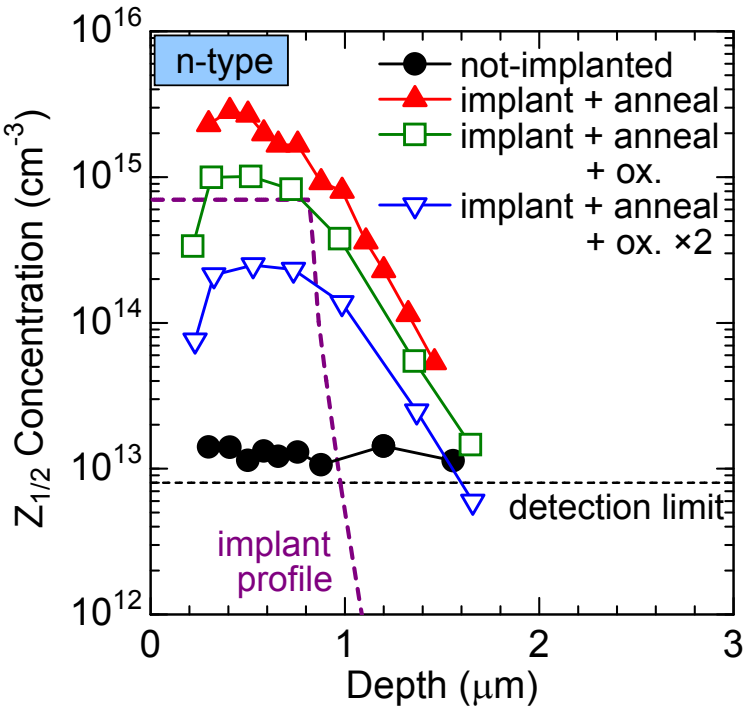

Figure 4.2: Depth profiles of the $Z_{1/2}$ center observed in nonimplanted (filled circles) and Al^+-implanted *n*-type 4H-SiC after Ar annealing at 1700°C for 30 min (filled triangles) and after the annealing followed by oxidation at 1150°C (squares and inverse triangles).

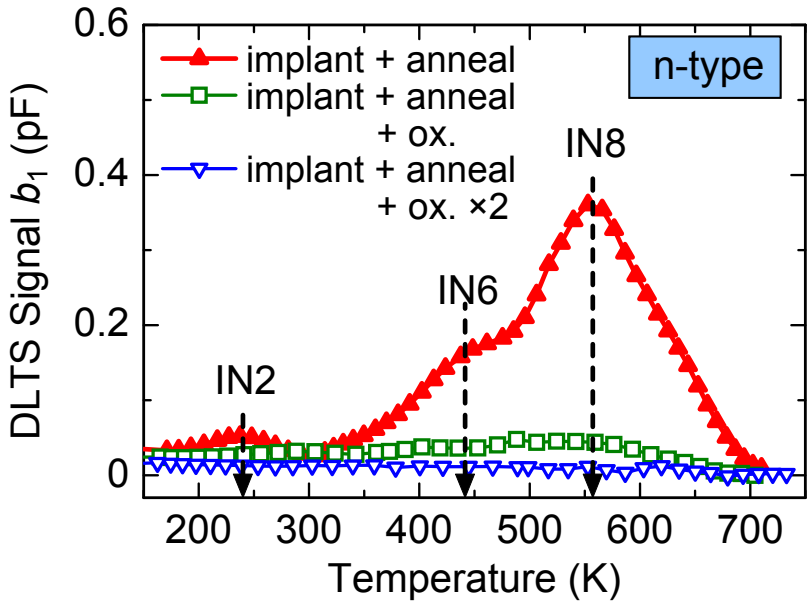

Figure 4.3: DLTS spectra of high-dose P^+-implanted *n*-type 4H-SiC after Ar annealing at 1700°C for 30 min (filled triangles) and after the annealing followed by oxidation at 1150°C (squares and inverse triangles).

the IN2 (ID_8 [1, 17], $E_C - 0.30$ eV), IN6 ($E_C - 1.0$ eV), and IN8 ($E_C - 1.2$ eV) centers were observed with high concentrations (IN8: $\sim 1\times10^{17}$ cm^{-3}). The parameters of the deep levels detected in high-dose ion-implanted n-type 4H-SiC are summarized in Table 4.2. Although the peak labeled IN8 is too broad to be a single level, other levels cannot be resolved due to severe overlapping. Note that all defects including the IN8 center remarkably decrease after every oxidation. The concentration of the IN8 center after the first or second oxidation (squares or inverse triangles in Fig. 4.3) is $\sim 2 \times 10^{16}$ cm^{-3} or lower than 7×10^{15} cm^{-3}.

4.2.2 Deep Levels in *p*-type Epilayers

Fig. 4.4 shows the DLTS spectra obtained from low-dose Al^+-implanted p-type 4H-SiC after Ar annealing at 1700°C for 30 min (filled triangles) and subsequent oxidation at 1150°C for 2 h (squares). A DLTS spectrum obtained from nonimplanted sample is also shown as filled circles, in which the D [17] ($E_V + 0.63$ eV) and IP8 (HK4 [13]: $E_V + 1.4$ eV) centers are detected with concentrations of about 3×10^{12} cm^{-3} and 3×10^{13} cm^{-3}, respectively. After the implantation, two traps, IP2 (HS1 [3, 7]: $E_V + 0.39$ eV) and IP8 (HK4), are dominant. In contrast to n-type samples, several levels, IP1 ($E_V + 0.35$ eV), IP4 ($E_V + 0.79$ eV), IP5 ($E_V + 0.98$ eV), and IP7 ($E_V + 1.3$ eV), are generated by the oxidation of the implanted p-type samples. The IP1, IP4, IP5, and IP7 centers may be the same defects as the UK1, HK0, HK2, and HK3 centers previously detected in p-type 4H-SiC [13]. The UK1 and HK0 centers were observed in irradiated samples after annealing at 950°C, whereas the HK2 and HK3 centers were first detected in as-grown samples [13]. The HK0 center is also generated by Reactive Ion Etching (RIE) followed by thermal oxidation [13]. Because these four levels were also observed in nonimplanted samples after thermal oxidation (the detail is discussed in Chapter 7), these levels will originate from intrinsic defects (e.g. C or Si interstitial(s), Si antisite), which do not contain the implanted species. The parameters of the deep levels detected in low-dose ion-implanted p-type 4H-SiC are summarized in Table 4.3.

Fig. 4.5 shows the depth profiles of the IP4 (HK0) and IP8 (HK4) centers observed in low-dose Al^+-implanted p-type 4H-SiC after annealing at 1700°C (HK4: filled triangles) and after the annealing followed by oxidation at 1150°C (HK4: squares, HK0: rhombuses). Before the oxidation, the HK4 center existed only near the surface reaching a depth of about 0.4 μm. After the oxidation, the HK0 center appeared and reached to a depth of about 0.8 μm while the HK4 center also showed similar distribution to the HK0 distribution. The corresponding deep levels in samples implanted with the other species (N^+, P^+) showed a similar behavior (not shown).

Fig. 4.6 shows the DLTS spectra obtained from high-dose Al^+-implanted p-type 4H-SiC after annealing at 1700°C (filled triangles) and after the annealing followed by oxidation (squares). Before the oxidation, the IP5 ($E_V + 0.98$ eV), IP6 ($E_V + 1.2$ eV), IP7 ($E_V + 1.3$ eV), and IP9 ($E_V + 1.5$ eV) centers were observed with high concentrations (IP5: 1×10^{16} cm^{-3}). In this high-dose-implanted p-type sample, other deep levels should also

Table 4.2: Energy positions and capture cross-sections of deep levels observed in high-dose ion-implanted n-type 4H-SiC (σ: the capture cross-section, N_T: the concentration of traps at about 0.02 μm from the surface in the P^+-implanted SiC before and after oxidation at 1150°C for 2 h).

label	$E_C - E_T$ (eV)	σ (cm^2)	N_T (cm^{-3}) before Ox.	after Ox.	after Ox.×2	corresponding center
IN2	0.30	10^{-18}	1×10^{16}	$< 6 \times 10^{15}$	$< 2 \times 10^{15}$	ID_8 [1, 17]
IN6	1.0	10^{-15}	5×10^{16}	$< 2 \times 10^{16}$	$< 7 \times 10^{15}$	
IN8	1.2	10^{-15}	1×10^{17}	$< 2 \times 10^{16}$	$< 4 \times 10^{15}$	

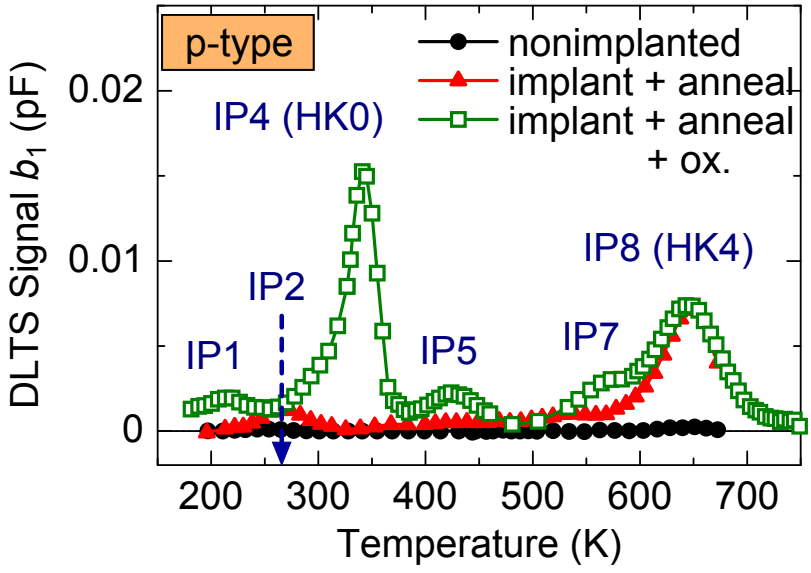

Figure 4.4: DLTS spectra of nonimplanted (filled circles) and low-dose Al^+-implanted p-type 4H-SiC after Ar annealing at 1700°C for 30 min (filled triangles) and after the annealing followed by oxidation at 1150°C for 2 h (squares).

Table 4.3: Energy positions and capture cross-sections of deep levels observed in low-dose ion-implanted p-type 4H-SiC (σ: the capture cross-section, N_T: the maximum concentration of traps at 0.1-0.6 μm from the surface in the Al^+-implanted SiC before and after oxidation at 1150°C for 2 h).

label	$E_T - E_V$ (eV)	σ (cm^2)	N_T (cm^{-3}) before Ox.	N_T (cm^{-3}) after Ox.	corresponding center
IP1	0.35	10^{-18}	Not observed	2×10^{13}	UK1 [13]
IP2	0.39	10^{-18}	2×10^{13}	$< 2 \times 10^{13}$	HS1 [3, 7], HH1 [2]
IP4	0.79	10^{-16}	6×10^{12}	3×10^{14}	HK0 [13]
IP5	0.98	10^{-16}	Not observed	3×10^{13}	HK2 [13]
IP7	1.3	10^{-14}	1×10^{13}	6×10^{13}	HK3 [13]
IP8	1.4	10^{-16}	2×10^{14}	2×10^{14}	HK4 [13]

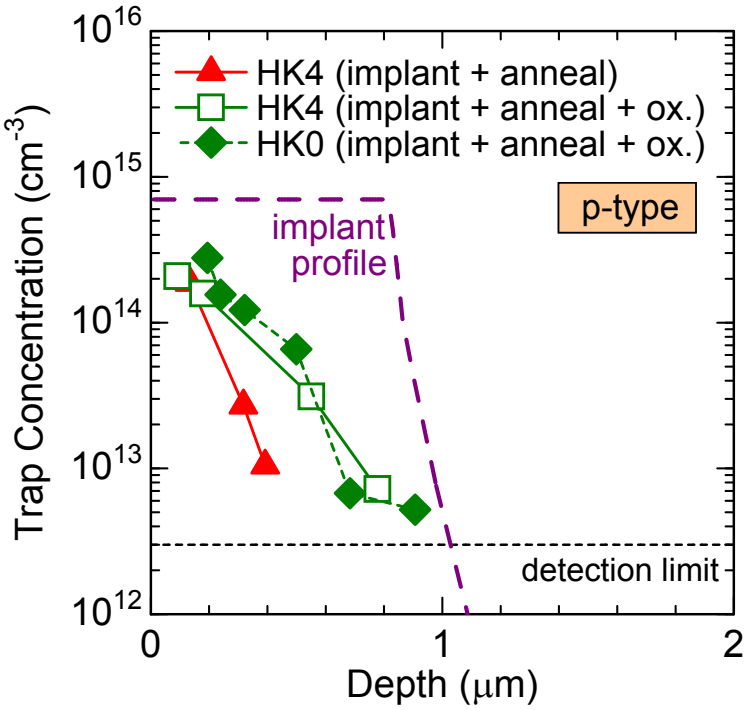

Figure 4.5: Depth profiles of the IP4 (HK0) and IP8 (HK4) centers observed in low-dose Al^+-implanted p-type 4H-SiC after Ar annealing at 1700°C for 30 min (HK4: filled triangles) and subsequent oxidation at 1150°C for 2 h (HK4: squares, HK0: rhombuses).

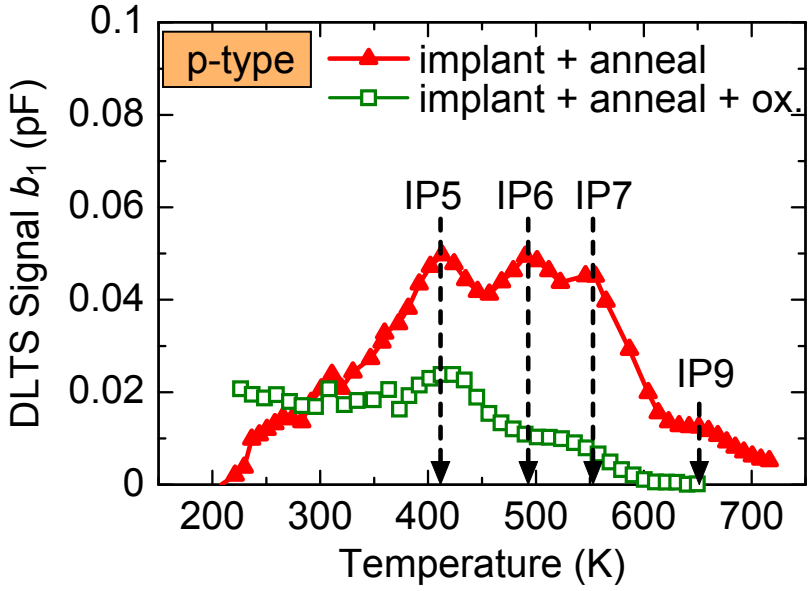

Figure 4.6: DLTS spectra of high-dose Al^+-implanted p-type 4H-SiC after Ar annealing at 1700°C for 30 min (filled triangles) and after the annealing followed by oxidation at 1150°C for 2 h (squares).

exist, which cannot be resolved due to the overlapping of DLTS peaks. After the oxidation, all these defects decreased (IP5: 6×10^{15} cm^{-3}). The parameters of the deep levels detected in high-dose Al^+-implanted p-type 4H-SiC are summarized in Table 4.4.

4.2.3 Discussion

All the deep levels detected in low-dose ion-implanted 4H-SiC may originate from intrinsic defects as discussed in Chapter 3. Also in high-dose implanted n-type samples, three major defects (IN2, IN6, IN8) were always observed irrespective of the implanted species (N and P), indicating that these are also intrinsic defects. It is, however, difficult to judge whether defects containing the implanted species do exist (or not) in the high-dose-implanted samples due to the severe overlapping of DLTS peaks.

Whereas almost all the deep levels generated by ion-implantation in the upper half of the bandgap were reduced by thermal oxidation, the IP4 (HK0) center ($E_V + 0.79$ eV) was generated by the oxidation. To fabricate high-performance SiC devices, thermal oxidation will be effective but an additional treatment for reducing the HK0 center should be conducted. In a previous report [13], the HK0 center was found to be annealed out by thermal treatment in Ar at 1550°C for 30 min. This high-temperature treatment, however, is not always compatible with the real device processing. For example, after gate oxidation for metal-oxide-semiconductor (MOS) devices, by which the HK0 center is generated, thermal treatment above 1400°C will cause severe degradation/decomposition of SiO_2.

To investigate the thermal stability of the HK0 center, the author annealed oxidized samples (nonimplanted) at 1300°C or 1400°C in N_2 ambient. The oxidation was performed in N_2O diluted with N_2 at 1300°C for 30 min resulting in an SiO_2 thickness of 4 nm. The observed defects are the same as the defects detected in the sample oxidized at 1150°C in O_2 ambient. Fig. 4.7 shows the depth profiles of the HK0 center observed in p-type 4H-SiC after oxidation (filled circles) and after the oxidation followed by N_2 annealing (triangles: at 1300°C for 30 min, filled squares: at 1300°C for 300 min, inverse triangles: at 1400°C for 30 min). The HK0 center was reduced in a depth > 0.4 μm and also in the near-surface region by annealing at 1300°C for 30 min, implying that a defect forming the HK0 center diffused towards a deeper region (towards the substrate) and also towards the surface during the annealing. When the annealing time was extended (filled squares in Fig. 4.7) or the annealing temperature was higher (inverse triangles in Fig. 4.7), the HK0 center almost disappeared also near the surface (~ 0.4 μm).

Table 4.4: Energy positions and capture cross-sections of deep levels observed in high-dose Al^+-implanted p-type 4H-SiC (σ: the capture cross-section, N_T: the concentration of traps at about 0.02 μm from the surface in the SiC before and after oxidation at 1150°C for 2 h).

label	$E_T - E_V$ (eV)	σ (cm^2)	N_T (cm^{-3}) before Ox.	N_T (cm^{-3}) after Ox.	corresponding center
IP5	0.98	10^{-16}	1×10^{16}	6×10^{15}	HK2 [13]
IP6	1.2	10^{-14}	1×10^{16}	$< 4 \times 10^{15}$	
IP7	1.3	10^{-14}	1×10^{16}	$< 3 \times 10^{15}$	HK3 [13]
IP9	1.5	10^{-15}	6×10^{15}	$< 7 \times 10^{13}$	

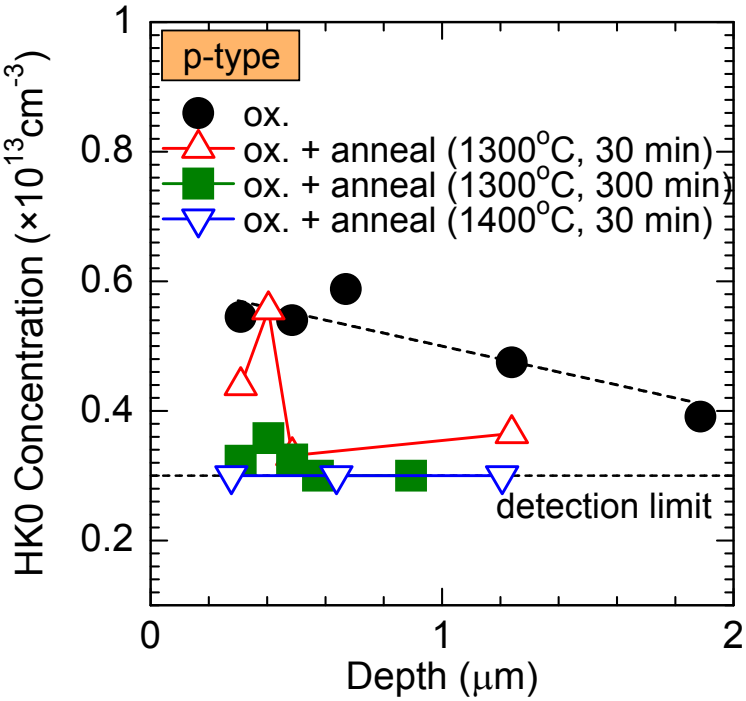

Figure 4.7: Depth profiles of the IP4 (HK0) center observed in p-type 4H-SiC after oxidation at 1300°C (filled circles) and after the oxidation followed by Ar annealing (triangles: at 1300°C for 30 min, filled squares: at 1300°C for 300 min, inverse triangles: at 1400°C for 30 min).

4.3 Deep Level Reduction in Epilayers after Reactive Ion Etching

In RIE-etched samples, even after Ar annealing at 1000°C for 30 min, the IN2 (ID_8, $E_C - 0.30$ eV), $Z_{1/2}$ ($E_C - 0.67$ eV), EN ($E_C - 1.6$ eV), IP1 (UK1, $E_V + 0.35$ eV), IP2 (HS2, $E_V + 0.39$ eV), HK0 ($E_V + 0.79$ eV), IP5 (HK2, $E_V + 0.98$ eV), IP7 (HK3, $E_V + 1.3$ eV), and EP (HK4, $E_V + 1.4$ eV) centers existed as shown in Chapter 3. The author sought to reduce these deep levels by dry oxidation.

The starting materials and etching condition were the same as those shown in Chapter 3. The RIE-etched samples were oxidized at 1100°C for 30 min in O_2 ambient, by which 5-nm-thick SiO_2 was formed. After removing the oxide, Schottky contacts were formed and DLTS measurements were performed. For the DLTS measurements, a typical reverse bias is -1 V (for n-type) or 1 V (for p-type) and filling pulse voltage is 0 V.

4.3.1 Deep Levels in *n*-type Epilayers

Fig. 4.8 shows the DLTS spectra obtained from RIE-etched n-type 4H-SiC after Ar annealing at 1000°C for 30 min (dashed line), after oxidation at 1100°C for 30 min (solid line), and after the oxidation followed by Ar annealing at 1400°C for 30 min (dotted line). After oxidation, the IN2 center disappeared, whereas the IN5 center ($E_C - 0.73$ eV) appeared near the surface (< 0.4 μm). The IN5 center may be assigned to the EH_4 center observed in electron-irradiated (2.5 MeV [2], 15 MeV [10]) and H^+-implanted [10] 4H-SiC. The $Z_{1/2}$, IN5, and EN centers still remained after Ar annealing at 1400°C for 30 min. As shown in Chapter 3, the IN5 center was eliminated by Ar annealing at 1700°C.

Fig. 4.9 shows the depth profiles of the EN defect in the same samples as those in Fig. 4.8. The EN center, dominant deep level in RIE-etched n-type samples, shows a high concentration near the surface ($\sim 1 \times 10^{15}$ cm^{-3} at 0.1 μm from the surface), whereas it shows a relatively low concentration ($\sim 4 \times 10^{13}$ cm^{-3}) in deeper region (> 0.2 μm). Near the surface, the EN center could not be eliminated even by thermal oxidation followed by Ar annealing.

4.3.2 Deep Levels in *p*-type Epilayers

Fig. 4.10 shows the DLTS spectra obtained from RIE-etched p-type 4H-SiC after Ar annealing at 1000°C for 30 min (dashed line), after oxidation at 1100°C for 30 min (solid line), and after the oxidation followed by Ar annealing at 1400°C for 30 min (dotted line). Although the EP center decreased in the oxidized sample, the HK0 center increased by oxidation. As an additional annealing step, the oxidized sample was annealed at 1400°C in Ar ambient, leading to the reduction of almost all the defects including the HK0 center. This result supports that the observed levels, IP1, IP5, IP7, and EP are respectively UK1, HK2, HK3,

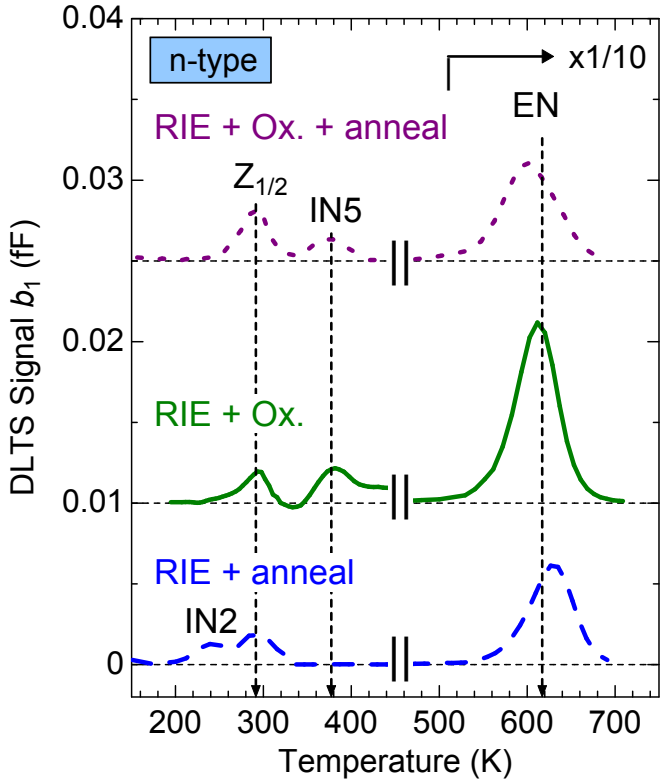

Figure 4.8: DLTS spectra obtained from RIE-etched n-type 4H-SiC after Ar annealing at 1000°C for 30 min (dashed line), after oxidation at 1100°C for 30 min (solid line), and after the oxidation followed by Ar annealing at 1400°C for 30 min (dotted line).

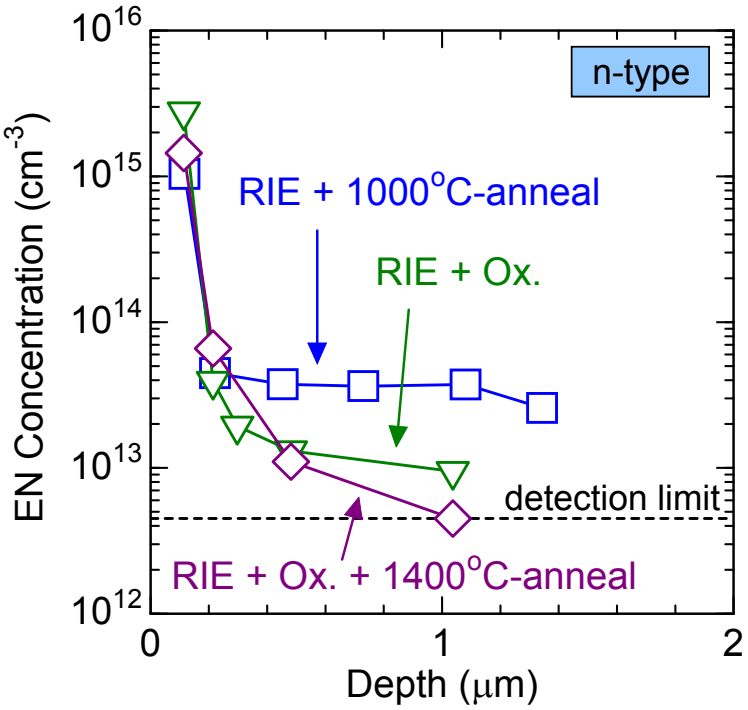

Figure 4.9: Depth profiles of the EN defect in the same samples as those in Fig 4.8.

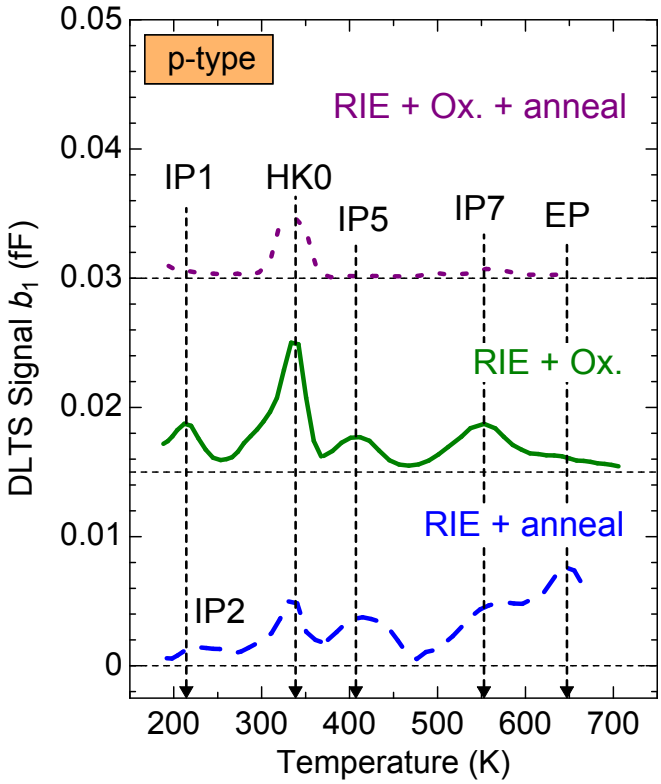

Figure 4.10: DLTS spectra obtained from RIE-etched *p*-type 4H-SiC after Ar annealing at 1000°C for 30 min (dashed line), after oxidation at 1100°C for 30 min (solid line), and after the oxidation followed by Ar annealing at 1400°C for 30 min (dotted line).

and HK4, which are reduced by annealing at temperatures above 1350°C [13].

Fig. 4.11 (a) shows the depth profile of the HK0 defect in the same samples as those in Fig. 4.10. The HK0 center was generated to a deep region over 1 μm by RIE (and annealing at 1000°C) and increased to over 1×10^{14} cm^{-3} after the oxidation. The subsequent annealing at 1400°C for 30 min, however, reduced the HK0 center by a factor of 2–3. The HK0 concentration can become lower by extending the annealing time. Fig. 4.11 (b) shows the depth profile of the EP defect in the same samples as those in Fig. 4.10. The EP concentration in the sample annealed at 1000°C was high (over 1×10^{14} cm^{-3}) from the near-surface region to a deep region over 1 μm, which was reduced by the oxidation unlike the HK0 center. The EP concentration decreased to the detection limit after the subsequent annealing at 1400°C.

4.3.3 Discussion

In the samples etched by RIE, only thermal oxidation was not very effective for elimination of deep levels; the HK0 center was generated by the oxidation. A subsequent annealing step at 1400°C clearly reduced the HK0 center and also other deep levels. As a consequence of this study, RIE-etched 4H-SiC should be annealed at 1400°C in Ar ambient after thermal oxidation, by which almost all deep levels in RIE-etched samples, IN2 (ID_8, $E_C - 0.30$ eV), IP1 (UK1, $E_V + 0.35$ eV), IP2 (HS1, $E_V + 0.39$ eV), HK0 ($E_V + 0.79$ eV), IP5 (HK2, $E_V + 0.98$ eV), IP7 (HK3, $E_V + 1.3$ eV), and EP (HK4, $E_V + 1.4$ eV) centers, decrease.

After the oxidation and annealing process, the EN center ($E_C - 1.6$ eV) remained with a very high concentration of about 1×10^{15} cm^{-3} near the surface region. The $Z_{1/2}$ center also remained in the RIE-etched samples after oxidation at 1100°C for 30 min, whereas it decreased in as-grown and ion-implanted samples after oxidation at 1150°C for 2 h, implying that the oxidation temperature/period is not sufficiently high/long to reduce the $Z_{1/2}$ center in the epilayers with a high density of deep levels induced by RIE. Dependences of deep level reduction on oxidation temperature/period and an initial concentration of deep levels are investigated in Chapter 5.

To achieve a deep-level-free epilayer after RIE, the following methods will be effective: (i) a high temperature or/and a long period oxidation (see Chapter 5), (ii) removal of the surface region by gas (e.g. H_2, HCl) etching, and (iii) optimization of RIE-etching conditions not to generate deep levels. The author attempted the method (iii) and found that RIE with a moderate condition generates deep levels with concentrations lower than a detection limit of DLTS measurements ($\sim 10^{11}$ cm^{-3} in the etched samples); the moderate condition is an rf power of 50 W and a pressure of 95 Pa, resulting in etching speed of 7 nm/min, whereas the standard condition used in this study is an rf power of 150 W and a pressure of 20 Pa, resulting in etching speed of 900 nm/min (used gas: 5 sccm of CF_4 and 10 sccm of O_2 in the both condition).

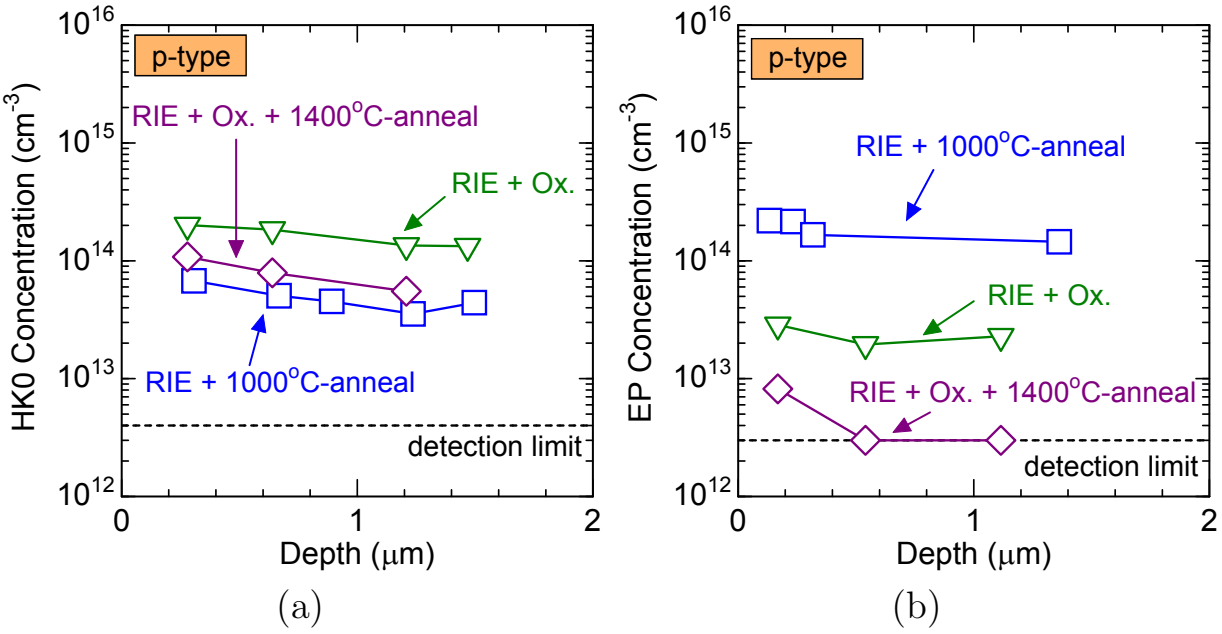

Figure 4.11: Depth profiles of the (a) HK0 and (b) EP defects in the same samples as those in Fig 4.10.

4.4 Summary

The effects of thermal oxidation on deep levels generated by ion implantation or RIE were investigated. As the same manner in as-grown samples, in ion-implanted samples the IN3 ($Z_{1/2}$, $E_C - 0.67$ eV) and IN9 ($EH_{6/7}$, $E_C - 1.5$ eV) centers could be reduced by thermal oxidation; the $Z_{1/2}$ concentration was reduced from 3×10^{15} cm^{-3} to 2×10^{14} cm^{-3} by oxidation at 1150°C for 4 h. The dominant defects in high-dose ion-implanted 4H-SiC, IN8 (in *n*-type samples), IP5, IP6, and IP7 (in *p*-type samples), were also reduced by thermal oxidation; the IN8 concentration was reduced from 1×10^{17} cm^{-3} to $< 4 \times 10^{15}$ cm^{-3} by oxidation at 1150°C for 4 h. In the lower of the bandgap (in *p*-type samples), however, several deep levels such as the IP4 (HK0) center (concentration: $\sim 3 \times 10^{14}$ cm^{-3}) was generated by oxidation, which was reduced by Ar annealing at 1400°C for 30 min. Consequently, to reduce all deep levels in ion-implanted 4H-SiC, oxidation followed by Ar annealing above 1400°C should be performed.

In RIE-etched samples, almost all deep levels, IN2 (ID_8, $E_C - 0.30$ eV), IP1 (UK1, $E_V + 0.35$ eV), IP2 (HS1, $E_V + 0.39$ eV), IP4 (HK0: $E_V + 0.79$ eV), IP5 (HK2, $E_V + 0.98$ eV), IP7 (HK3, $E_V + 1.3$ eV), and EP (HK4, $E_V + 1.4$ eV), were reduced by thermal oxidation at 1100°C for 30 min followed by Ar annealing at 1400°C for 30 min. The EN ($E_C - 1.6$ eV) centers, in contrast, remained with a high concentration over 1×10^{15} cm^{-3} after the oxidation and annealing, generation of which could be suppressed using a moderate RIE condition. A high temperature or/and a long period oxidation and removal of the surface region by gas etching will also be effective to achieve a deep-level-free epilayer after RIE.

References

[1] T. Dalibor, G. Pensl, H. Matsunami, T. Kimoto, W. J. Choyke, A. Schöner, and N. Nordell, *Physica Status Solidi (A)* **162**, 199 (1997).

[2] C. Hemmingsson, N. T. Son, O. Kordina, J. P. Bergman, E. Janzén, J. L. Lindström, S. Savage, and N. Nordell, *Journal of Applied Physics* **81**, 6155 (1997).

[3] L. Storasta, F. H. C. Carlsson, S. G. Sridhara, J. P. Bergman, A. Henry, T. Egilsson, A. Hallén, and E. Janzén, *Applied Physics Letters* **78**, 46 (2001).

[4] M. Weidner, T. Frank, G. Pensl, A. Kawasuso, H. Itoh, and R. Krause-Rehberg, *Physica B* **308-310**, 633 (2001).

[5] A. Kawasuso, F. Redmann, R. Krause-Rehberg, M. Weidner, T. Frank, G. Pensl, P. Sperr, W. Triftshauser, and H. Itoh, *Applied Physics Letters* **79**, 3950 (2001).

[6] A. Hallén, M. S. Janson, A. Y. Kuznetsov, D. Åberg, M. K. Linnarsson, B. G. Svensson, P. O. Persson, F. H. C. Carlsson, L. Storasta, J. P. Bergman, S. G. Sridhara, and Y. Zhang, *Nuclear Instruments and Methods in Physics Research Section B* **186**, 186 (2002).

[7] L. Storasta, J. P. Bergman, E. Janzén, A. Henry, and J. Lu, *Journal of Applied Physics* **96**, 4909 (2004).

[8] Y. Negoro, T. Kimoto, and H. Matsunami, *Applied Physics Letters* **85**, 1716 (2004).

[9] G. Alfieri, E. V. Monakhov, B. G. Svensson, and M. K. Linnarsson, *Journal of Applied Physics* **98**, 043518 (2005).

[10] G. Alfieri, E. V. Monakhov, B. G. Svensson, and A. Hallén, *Journal of Applied Physics* **98**, 113524 (2005).

[11] K. Danno and T. Kimoto, *Journal of Applied Physics* **100**, 113728 (2006).

[12] G. Alfieri and T. Kimoto, *Journal of Applied Physics* **101**, 103716 (2007).

[13] K. Danno and T. Kimoto, *Journal of Applied Physics* **101**, 103704 (2007).

[14] L. Storasta and H. Tsuchida, *Applied Physics Letters* **90**, 062116 (2007).

[15] L. Storasta, H. Tsuchida, T. Miyazawa, and T. Ohshima, *Journal of Applied Physics* **103**, 013705 (2008).

[16] T. Hiyoshi and T. Kimoto, *Applied Physics Express* **2**, 041101 (2009).

[17] T. Troffer, M. Schadt, T. Frank, H. Itoh, G. Pensl, J. Heindl, H. P. Strunk, and M. Maier, *Physica Status Solidi (A)* **162**, 277 (1997).

Chapter 5

Analytical Model for Trap Reduction by Thermal Oxidation

5.1 Introduction

Although reduction of the major deep levels in SiC was realized by thermal oxidation (and subsequent Ar annealing) as described in the last chapter, the trap reduction mechanism has not been fully understood. The purposes of this chapter are to reveal the trap reduction mechanism and to enable the prediction of the depth profiles of deep levels after oxidation in order to control deep levels by thermal oxidation. Considering that C^+ implantation followed by Ar annealing also reduce the $Z_{1/2}$ center, the author compares deep levels after thermal oxidation to those after C^+ implantation. The author also investigates the oxidation-temperature dependence, oxidation-time dependence, and initial-$Z_{1/2}$-concentration dependence of the defect reduction in both n-type and p-type 4H-SiC epilayers. Based on these data, an analytical model of defect reduction as well as the most effective way to reduce the $Z_{1/2}$ center are proposed.

5.2 Deep-Level Reduction Processes

There are two effective processes for the reduction of deep levels in as-grown SiC: thermal oxidation [1] and C^+ implantation followed by Ar annealing [2]. The both processes have attracted attention because they reduce the $Z_{1/2}$ center ($E_C - 0.67$ eV): a lifetime killer in n-type 4H-SiC. In this section, present knowledge for the trap reduction processes are introduced.

5.2.1 Carbon Implantation followed by Ar Annealing

It was reported that C^+ implantation with a dose of 2×10^{19} cm^{-3} followed by Ar annealing at 1800°C for 30 min eliminated the $Z_{1/2}$ center to a depth over 60 μm [3]. The trap

reduction mechanisms by the C^+ implantation are explained as follows [2, 3]. The implanted excess carbon atoms diffuse to the deeper region of an SiC epilayer during post-implantation annealing and fill carbon vacancies. Because the origin of the $Z_{1/2}$ center contains carbon vacancy (V_C) (the detail is discussed in Chapter 6), the $Z_{1/2}$ concentration decreases by the C^+ implantation.

5.2.2 Thermal Oxidation

By thermal oxidation at 1300°C for 5 h, interestingly, the $Z_{1/2}$ center was eliminated to a depth over 40 μm [1]. As shown in Fig. 5.1, the $Z_{1/2}$ reduction may be ascribed to the diffusion of interstitials generated at the SiO_2/SiC interface during oxidation. The interstitials might occupy V_C, contained in the origin of the $Z_{1/2}$ center, resulting in the reduction of the $Z_{1/2}$ center. There are several reports indicating the generation of interstitials at the SiO_2/SiC interface [4–7], which support this trap reduction model; (i) experimental oxidation rate of SiC can be well simulated by considering silicon and carbon emission from the oxidation interface [4], (ii) an increase of carbon-atom concentration at the SiO_2/SiC interface was observed by electron energy loss spectroscopy (EELS) [5, 6], (iii) *ab initio* calculation has predicted that carbon clusters are formed at the SiO_2/SiC interface during oxidation [7].

5.3 Experiments

The starting materials were n-type (N_d: 10^{14}–10^{15} cm^{-3}) and p-type (N_a: 10^{15}–10^{16} cm^{-3}) 4H-SiC (0001) epilayers. A series of samples was oxidized at different temperatures (1150–1400°C) for various times (1.3–16.5 h) in 100% oxygen ambient, while the other set of samples was implanted with 10-50 keV carbon ions with a total dose of 1×10^{13} cm^{-2} or 1×10^{14} cm^{-2} (corresponding implanted-atom concentration: 1×10^{18} cm^{-3} or 1×10^{19} cm^{-3}), forming a 140-nm box profile. The C^+-implanted samples were annealed in Ar ambient at various temperatures (1000–1800°C) for 20 min. The depth profiles of trap concentrations until 10-μm depth were measured by changing the reverse bias voltage up to 100 V in DLTS measurements. To monitor deeper regions (over 10 μm), the samples were mechanically polished from the surfaces, and DLTS measurements were repeated. Additional deep levels, though, did not appear by polishing.

5.4 Defect Distributions after Thermal Oxidation

At first, deep levels after the two trap-reduction processes are compared. Fig. 5.2/Fig. 5.3 shows the DLTS spectra of the n-type/p-type samples after dry oxidation at 1300°C for 1.3 h, as well as the samples after C^+ implantation (dose: 1×10^{14} cm^{-2}) followed by

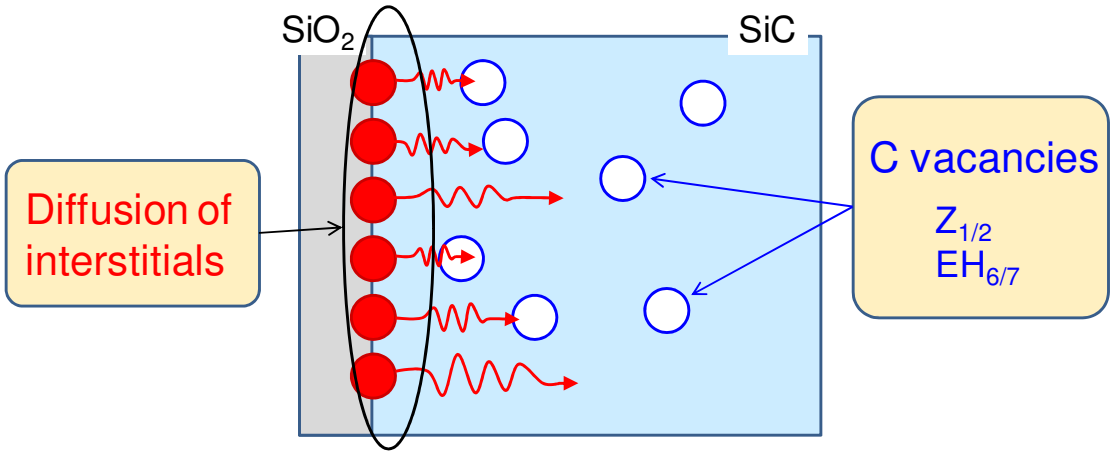

Figure 5.1: Schematic model for the reduction of the $Z_{1/2}$ and $EH_{6/7}$ centers during oxidation. Interstitials generated at the SiO_2/SiC interface diffuse into SiC bulk and occupy carbon vacancies related to the $Z_{1/2}$ and $EH_{6/7}$ centers.

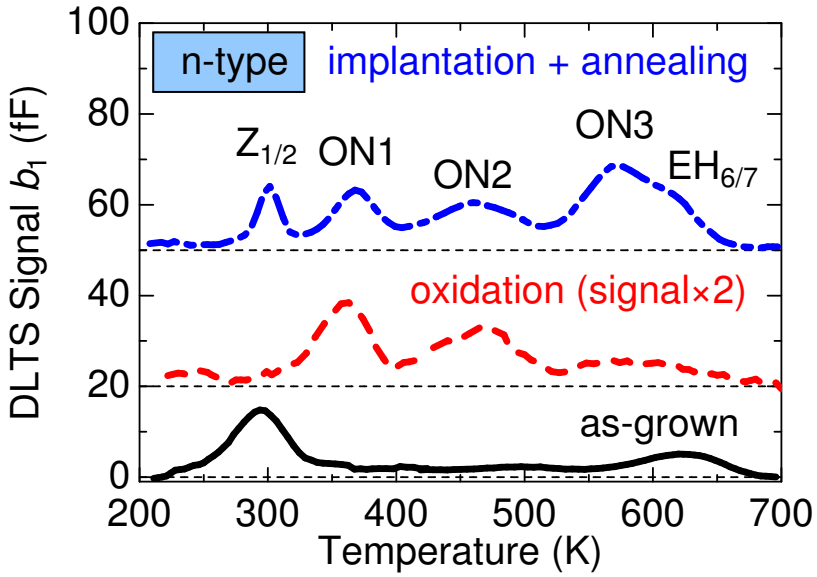

Figure 5.2: DLTS spectra of the n-type 4H-SiC after thermal oxidation at 1300°C for 1.3 h (dashed line) and C^+ implantation followed by Ar annealing at 1800°C for 20 min (dashed-dotted line).

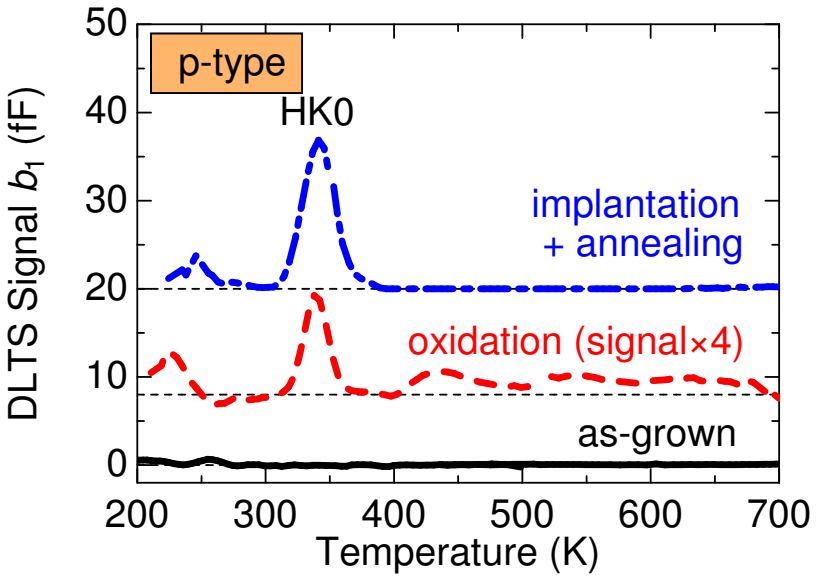

Figure 5.3: DLTS spectra of the *p*-type 4H-SiC after thermal oxidation at 1300°C for 1.3 h (dashed line) and C^+ implantation followed by Ar annealing at 1300°C for 20 min (dashed-dotted line).

Ar annealing at 1800°C/1300°C for 20 min. After C^+ implantation followed by annealing (dashed-dotted lines), the new peaks, ON1 ($E_C - 0.84$ eV), ON2 ($E_C - 1.1$ eV), and ON3 ($E_C - 1.6$ eV) in n-type SiC (Fig. 5.2), and HK0 [8, 9] ($E_V + 0.79$ eV) in p-type SiC (Fig. 5.3), appeared, while the same four peaks were also observed after thermal oxidation (dashed lines). The ON1 and ON2 centers should correspond to the deep levels reported as "new traps" in 4H-SiC after C^+ implantation [3]. In contrast, two major deep levels, $Z_{1/2}$ ($E_C - 0.67$ eV) and $EH_{6/7}$ ($E_C - 1.5$ eV), were reduced in n-type SiC after thermal oxidation as shown by the dashed line in Fig. 5.2. The $Z_{1/2}$ and $EH_{6/7}$ centers were also reduced to below the detection limit by C^+ implantation followed by Ar annealing at 1500°C (not shown), whereas these were regenerated by high-temperature (over 1700°C) annealing as shown by the dashed-dotted line in Fig. 5.2. The reduced deep levels as well as generated levels by the trap-reduction processes are summarized in Table 5.1. The defect behaviors (generation and reduction) for thermal oxidation well agree with those for the C^+ implantation, indicating that similar phenomena (such as interstitial diffusion) may occur in the two processes.

It is important to investigate the depth profiles of generated and reduced defects in order to understand what kinds of phenomena occur during the trap-reduction processes. Fig. 5.4 shows the depth profiles of the ON1 center (generated defect) after oxidation at various temperatures for 1.3 h. With increasing oxidation temperature, the ON1 concentration increased and was distributed to a deeper region, suggesting that the ON1 center is related to the atoms, most likely interstitials, diffusing from the SiO_2/SiC interface. The ON2 and HK0 centers (other generated defects) showed similar behaviors to the ON1 center (not shown). Fig. 5.5 shows the depth profiles of the $Z_{1/2}$ center (reduced defect) after oxidation at various temperatures for 1.3 h. In this particular case, the initial $Z_{1/2}$ concentration was increased to 1.7×10^{14} cm^{-3} by electron irradiation (energy: 150 keV, fluence: 1×10^{17} cm^{-2}) in order to investigate trap reduction in the sample with high initial $Z_{1/2}$ concentration. With increasing oxidation temperature, the $Z_{1/2}$ concentration decreased and was eliminated to a deeper region, suggesting that the $Z_{1/2}$ center is related to the (carbon) vacancies occupied by the diffusing interstitials. In addition, the depth of the $Z_{1/2}$-elimination region is proportional to the square root of the oxidation time ($t_{ox}^{1/2}$) [1]. These results suggest that the diffusion phenomena is taking place in the SiC bulk region during thermal oxidation.

5.5 Calculation of Defect Distributions after Thermal Oxidation

As discussed above, the reduction of the $Z_{1/2}$ center by oxidation can be explained by diffusion of interstitials and recombination with vacancies. Denoting the concentration of interstitials (carbon interstitial (C_I) or silicon interstitial (Si_I))/vacancies (carbon vacancy (V_C) or silicon vacancy (V_{Si})) by n_I/n_V, the diffusion coefficient of the interstitials by D, and

Table 5.1: Reduced and generated defects in SiC by C^+ implantation followed by Ar annealing and by thermal oxidation. The conduction types of the samples where each defect is observed are shown in parentheses.

C^+ implantation + Ar annealing		Thermal oxidation	
Reduced defects	Generated defects	Reduced defects	Generated defects
$Z_{1/2}$ (n-type)	ON1 (n-type)	$Z_{1/2}$ (n-type)	ON1 (n-type)
$EH_{6/7}$ (n-type)	ON2 (n-type)	$EH_{6/7}$ (n-type)	ON2 (n-type)
	ON3 (n-type)		ON3 (n-type)
	HK0 (p-type)		HK0 (p-type)

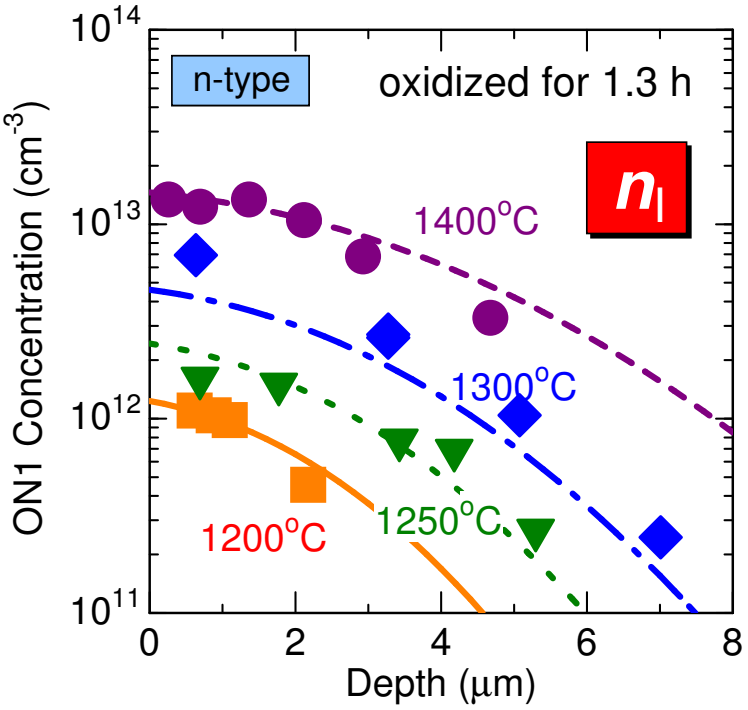

Figure 5.4: Depth profiles of the ON1 center after oxidation at various temperatures for 1.3 h. Each symbol indicates the experimental data and each line indicates the calculated n_I distribution obtained from Eqs. (5.1)–(5.8).

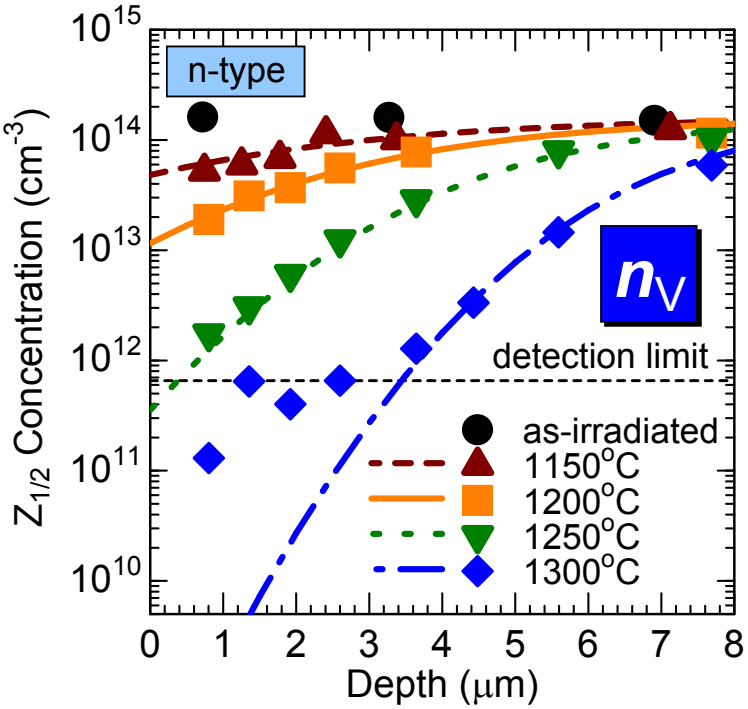

Figure 5.5: Depth profiles of the $Z_{1/2}$ center after oxidation at various temperatures for 1.3 h. The initial $Z_{1/2}$ concentration is 1.7×10^{14} cm^{-3}. Each symbol indicates the experimental data and each line indicates the calculated n_V distribution obtained from Eqs. (5.1)–(5.8).

the recombination coefficient between the interstitial and the vacancy by γ, the distribution of interstitials after oxidation is found by solving the diffusion equations:

$$\frac{\partial n_{\mathrm{I}}}{\partial t} = D \cdot \frac{\partial^2 n_{\mathrm{I}}}{\partial x^2} - \gamma \cdot n_{\mathrm{I}} \cdot n_{\mathrm{V}}, \tag{5.1}$$

$$\frac{\partial n_{\mathrm{V}}}{\partial t} = -\gamma \cdot n_{\mathrm{I}} \cdot n_{\mathrm{V}}, \tag{5.2}$$

where the boundary and initial conditions are fixed as

$$-D \cdot \frac{\partial n_{\mathrm{I}}}{\partial x} \mid_{x=0} = F_0 \cdot t^{-\alpha} \ (t \neq 0), \tag{5.3}$$

$$n_{\mathrm{I}} \mid_{t=0} = 0, \tag{5.4}$$

$$n_{\mathrm{V}} \mid_{t=0} = n_{\mathrm{V0}}. \tag{5.5}$$

When the calculated results are compared with experiments, fitting parameters, D_∞, E_{aD} $F_{0\infty}$, E_{aF}, γ_∞, and $E_{\mathrm{a}\gamma}$, are obtained from

$$D = D_\infty \cdot \exp(-\frac{E_{\mathrm{aD}}}{kT}), \tag{5.6}$$

$$F_0 = F_{0\infty} \cdot \exp(-\frac{E_{\mathrm{aF}}}{kT}), \tag{5.7}$$

$$\gamma = \gamma_\infty \cdot \exp(-\frac{E_{\mathrm{a}\gamma}}{kT}). \tag{5.8}$$

In this model, vacancies (corresponding to the $Z_{1/2}$ center) are assumed to be immobile and decrease through the recombination with diffusing interstitials as described in Eq. (5.2). Equation (5.3) indicates the boundary condition of interstitial emission at the oxidation interface, which is described with F_0: flux of interstitials emitted from the SiO_2/SiC interface when $t_{\mathrm{ox}} = 1$ s (t_{ox}: oxidation time). Because the oxidation rate slows down with time, the gradual decrease in flux of the emitted interstitials as oxidation (time) proceeds was taken into account by introducing a slow-down coefficient α. The flux of the interstitials should be in proportion to the oxidation rate. The slowdown of the oxidation reaction at the interface can be estimated from Fig. 5.6, showing the dependence of the oxide growth rate on oxidation time at different oxidation temperatures. A result on oxidation at 1100°C reported by Hijikata et al. [4] is also plotted in the same figure. When the slope of the plot is described as $-\alpha$, the oxidation rate is proportional to $t_{\mathrm{ox}}^{-\alpha}$. Therefore, interstitial emission can be assumed to decrease in proportion to $t_{\mathrm{ox}}^{-\alpha}$ as shown in Eq. (5.3). For simplicity, the time-dependent oxidation rate is expressed in the two stages; high-oxidation-rate stage ($t_{\mathrm{ox}} < 0.8$ h), where α is unity for oxidation at 1150–1300°C and 0.48 for 1400°C; and low-oxidation-rate stage (0.8 h $< t_{\mathrm{ox}}$), where α is 0.23 for oxidation at 1150–1300°C and 0.48 for 1400°C. In Eq. (5.4), n_{I} before oxidation is assumed to be negligible compared with that after oxidation. A parameter n_{V0} in Eq. (5.5) denotes the initial vacancy distribution before oxidation. As shown in Eqs. (5.6)–(5.8), each parameter is described as a function of temperature. The parameters, E_{aD}, E_{aF}, and $E_{\mathrm{a}\gamma}$, signify the respective activation energies corresponding to the energy barriers for the migration of interstitials, the generation of interstitials, and the recombination of interstitials with vacancies.

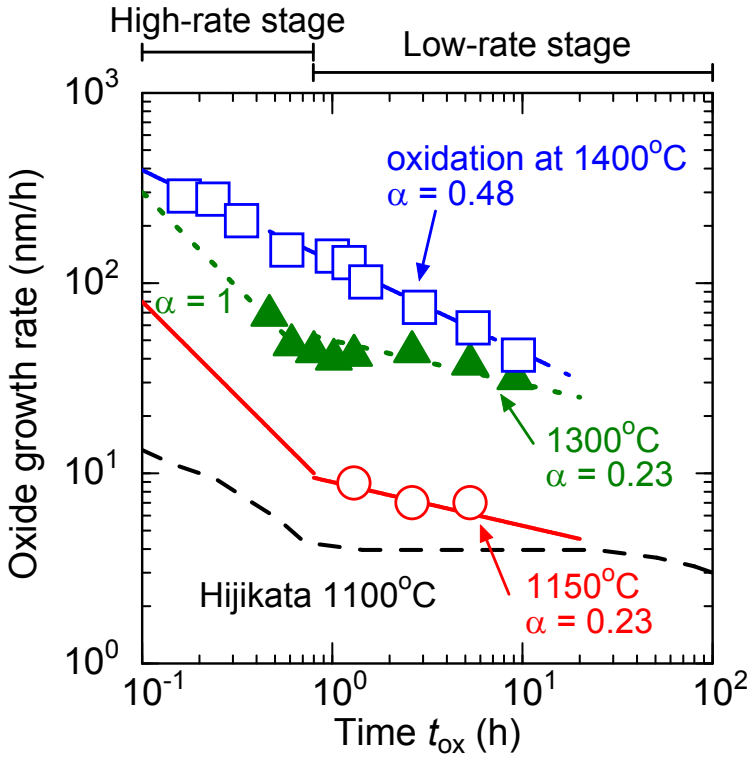

Figure 5.6: Dependence of the oxide growth rate on oxidation time at different oxidation temperatures. A result (1100°C) reported by Hijikata et al. [4] is also shown as a solid line.

5.6 Comparison between Experimental $Z_{1/2}$ Profiles and Calculated Vacancy Profiles after Thermal Oxidation

Based on Eqs. (5.1)–(5.8), the depth profiles of n_I and n_V can be calculated, which are dependent on six fitting parameters: E_{aD}, D_∞, E_{aF}, $F_{0\infty}$, $E_{a\gamma}$, and γ_∞. As shown as symbols in Fig. 5.5 and Fig. 5.7, the author experimentally obtained the depth profiles of $Z_{1/2}$ concentration after oxidation at different temperatures for several samples with different initial $Z_{1/2}$ concentrations (1.7×10^{14} cm^{-3} and 2.0×10^{13} cm^{-3}). These experimental depth profiles were fitted with the n_V profiles calculated from Eqs. (5.1)–(5.8). In the calculation, arbitrary n_V profile can be obtained by changing D, F_0, and γ. Fig. 5.8 shows the effects of changing these three parameters on the calculated n_V profile. When D becomes higher, n_V becomes relatively higher in the shallow region and lower in the deep region as shown by the dashed line, while opposite phenomena occur in the case of higher γ as shown by the dashed-dotted line. Higher F_0 leads lower n_V in the whole depth region as shown by the dotted line. The fitting parameters are uniquely determined through fitting of a series of $Z_{1/2}$ profiles in the samples with different initial $Z_{1/2}$ concentration after oxidation at different temperatures. The calculated n_V profiles after the fitting are shown as curved lines in Fig. 5.5 and Fig. 5.7. The obtained values of fitting parameters are summarized in Table 5.2, which are used in all cases in this study. The activation energy for diffusion coefficient (E_{aD}) of interstitials reducing the $Z_{1/2}$ center was determined as 0.6 eV in this study. Note that the migration barrier for carbon/silicon interstitials in n-type SiC has been reported to be (0.5–0.7) eV/(1.4–1.5) eV by Bockstedte et al. based on theoretical calculation using density functional theory (DFT) in the local density approximation (LDA) [10], and by Gao et al. using molecular dynamics (MD) simulations [11]. The activation energy for the diffusion coefficient of interstitials obtained in this study (0.6 eV) agrees with the reported migration energy for carbon interstitials (0.5–0.7 eV), which is consistent with the model that carbon interstitials diffuse from the oxidation interface and fill carbon vacancies. Much higher diffusivity of C_I than that of Si_I ($D_C \gg D_{Si}$) in SiC has also been obtained as experimental results [12–15]. From these results, the diffusing atoms responsible for the reduction of the $Z_{1/2}$ center during oxidation should be carbon atoms.

Using the same parameter values shown in Table 5.2, the oxidation-time dependence of $Z_{1/2}$ profiles was predicted assuming that the n_V profile corresponds to the $Z_{1/2}$ profile. In Fig. 5.9 (initial $Z_{1/2}$ concentration: 1.3×10^{13} cm^{-3}) and Fig. 5.10 (initial $Z_{1/2}$ concentration: 2×10^{12} cm^{-3}), the predicted $Z_{1/2}$ profiles after oxidation at 1300°C are shown as curved lines, whereas corresponding experimental data are shown as symbols. In various oxidation conditions, the experimental $Z_{1/2}$ profiles well agreed with the calculated (predicted) results. Note that these are not fitted results but the n_V profiles were calculated before experiments. This agreement indicates the potential to enable prediction of the $Z_{1/2}$ distributions after

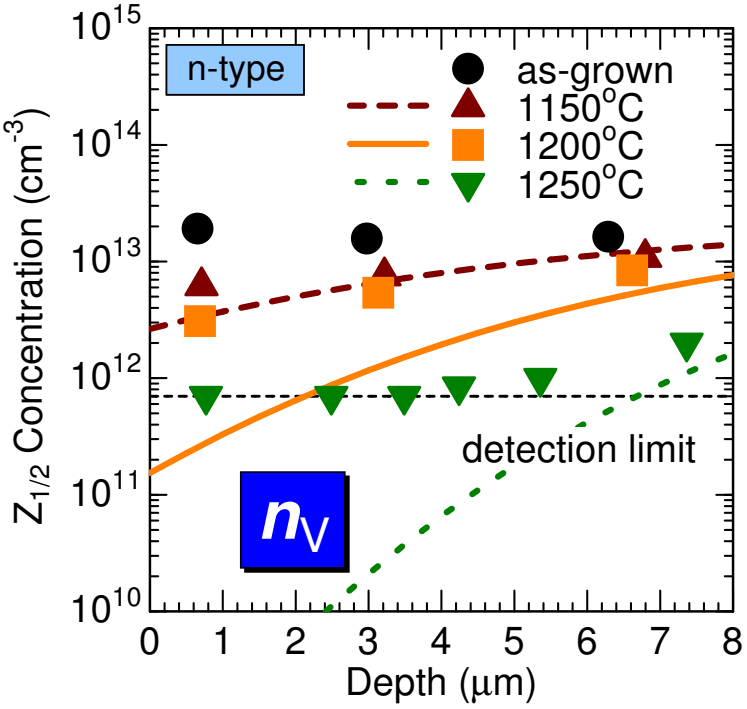

Figure 5.7: Depth profiles of $Z_{1/2}$ center after oxidation at various temperatures for 1.3 h. The initial $Z_{1/2}$ concentration is 2×10^{13} cm^{-3}. Each symbol indicates the experimental data and each line indicates the calculated n_V distribution obtained from Eqs. (5.1)–(5.8).

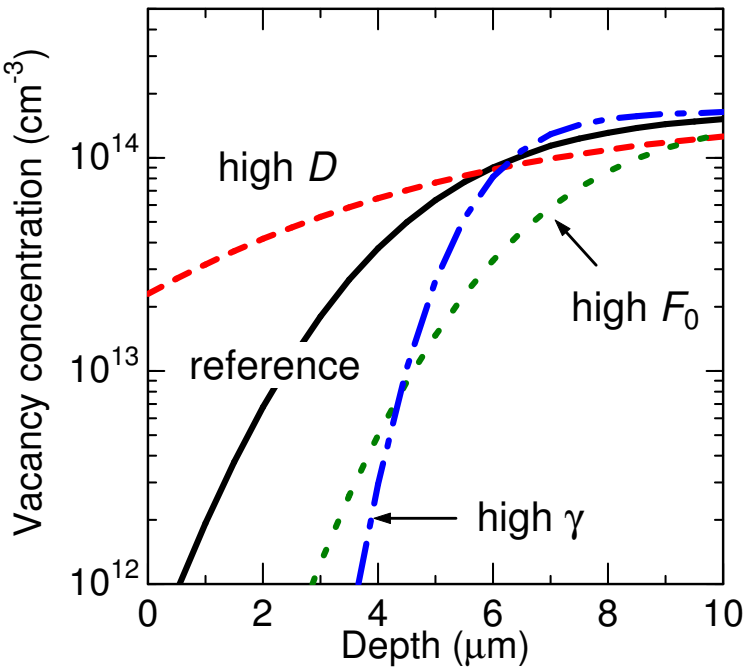

Figure 5.8: Effects of changing parameters, D, F_0, and γ, on a calculated n_V profile. Higher $D/F_0/\gamma$ is used in the calculation for dashed/dotted/dashed-dotted line compared to the calculation for reference (solid line).

Table 5.2: Parameter values obtained by the fitting results of calculated n_V profiles based on Eqs. (5.1)–(5.8) and experimental $Z_{1/2}$ profiles shown in Fig 5.5. The top row indicates the "X" in the first column.

	D	F_0	γ
Activation energy E_{aX}	0.6 eV	1.4 eV	2.1 eV
Coefficient X_∞	9.7×10^{-9} cm^{2}s^{-1}	4.4×10^{14} cm^{-2}s$^{\alpha-1}$	1.4×10^{-10} cm^{3}s^{-1}

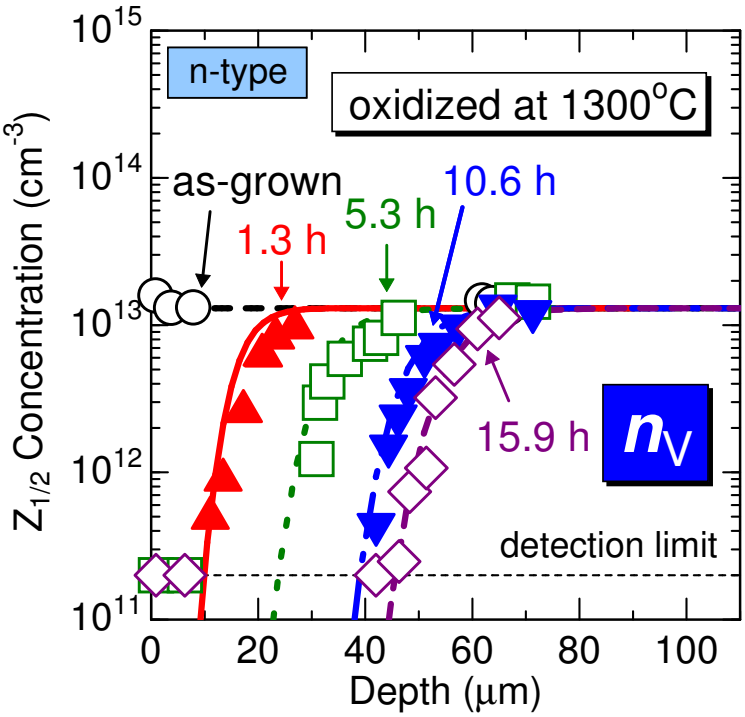

Figure 5.9: Depth profiles of the $Z_{1/2}$ center (initial $Z_{1/2}$ concentration: 1.3×10^{13} cm^{-3}) after oxidation at 1300°C for 1.3–15.9 h. Each symbol indicates the experimental data and each line indicates the calculated n_V distribution.

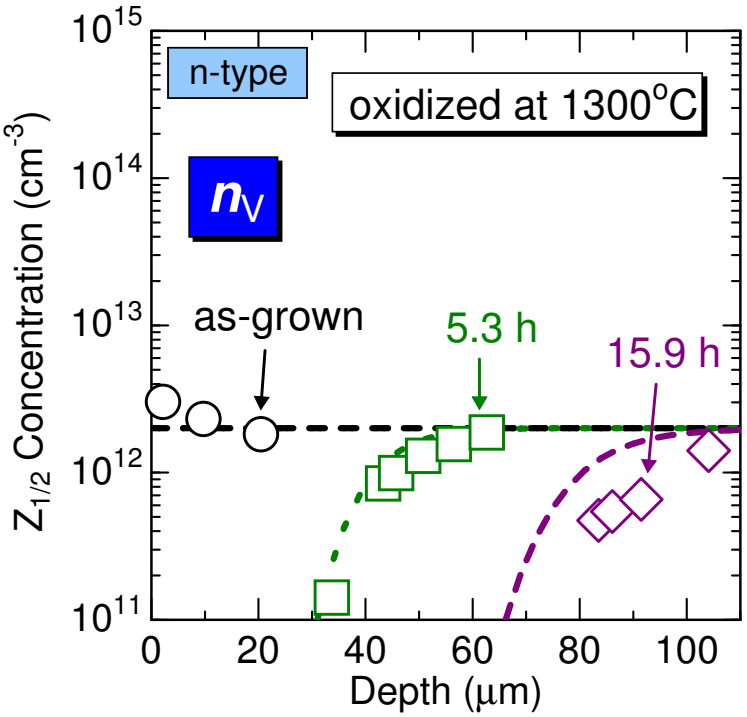

Figure 5.10: Depth profiles of the $Z_{1/2}$ center (initial $Z_{1/2}$ concentration: 2×10^{12} cm^{-3}) after oxidation at 1300°C for 5.3–15.9 h. Each symbol indicates the experimental data and each line indicates the calculated n_V distribution.

oxidation at any temperature, for any oxidation time, and any initial $Z_{1/2}$ concentration.

5.7 $Z_{1/2}$ Elimination in Whole Region of Thick Epilayers

The author sought to eliminate the $Z_{1/2}$ center to a depth of 100 μm, which is required for 10-kV-class bipolar devices. Fig. 5.11 shows the calculated results of the $Z_{1/2}$ (n_V) profiles for various oxidation times and different initial $Z_{1/2}$ concentrations (2×10^{12} cm^{-3} and 1.3×10^{13} cm^{-3}) using the parameters (in Table 5.2) obtained in Section 5.6. When the initial $Z_{1/2}$ concentration is low, 2×10^{12} cm^{-3}, oxidation at 1300°C for 30 h is enough for the elimination of the $Z_{1/2}$ center in the 100-μm-thick epilayer. For high initial $Z_{1/2}$ concentration ($> 10^{13}$ cm^{-3}), however, oxidation over 50 h is required to eliminate the $Z_{1/2}$ center. To minimize the oxidation time, the author proposes three approaches: (i) removing the oxide layer during oxidation, (ii) high-temperature annealing after oxidation, and (iii) higher-temperature oxidation.

(i) Removing the oxide layer during oxidation: In the initial oxidation stage, the interstitial emission rate from the SiO_2/SiC interface is high as shown in Fig. 5.6. Therefore, removing the oxide layer during oxidation should promote the interstitial emission and thereby $Z_{1/2}$ reduction. Fig. 5.12 shows the depth profiles of the $Z_{1/2}$ center after oxidation at 1300°C for 15.9 h. Each line indicates an n_V profile calculated with the parameters in Table 5.2, whereas each symbol indicates experimental data. The rhombuses denote the result for continuous 15.9-h oxidation, whereas reverse triangles for 15.9-h oxidation with removing the oxide layer after every 5.3-h oxidation, which reduces the $Z_{1/2}$ center to a deeper region. Removing the oxide layer was effective for enhancing the reduction of the $Z_{1/2}$ center. In the calculation, the effect of removing oxide layer is included by resetting the flux of emitted interstitials, which decreases as the oxidation proceeds, to the initial value after every (in this case 5.3 h) oxidation. The good agreement between the experimental data and the calculated results again supports the analytical model for the trap reduction proposed in this study.

(ii) High-temperature annealing after oxidation: Diffusing interstitials should remain in an epilayer after oxidation. Therefore, subsequent high-temperature annealing will enhance the diffusion of the residual interstitials to a deeper region and promote $Z_{1/2}$ reduction. Fig. 5.13 shows the $Z_{1/2}$ profiles after oxidation as well as after oxidation followed by high-temperature (1500°C) annealing. The solid line indicates the calculated n_V profile just after oxidation at 1300°C for 15.9 h, and the dashed line denotes that after oxidation and followed by annealing at 1500°C for 2 h in Ar ambient. To calculate the effects of Ar annealing at 1500°C, the parameters in Table 5.2 were used except that $F_0 = 0$ (no additional emission of interstitials during the Ar annealing). As shown in Fig. 5.13, the $Z_{1/2}$ center is eliminated to the deeper region by the subsequent annealing. The experimental data shown as symbols

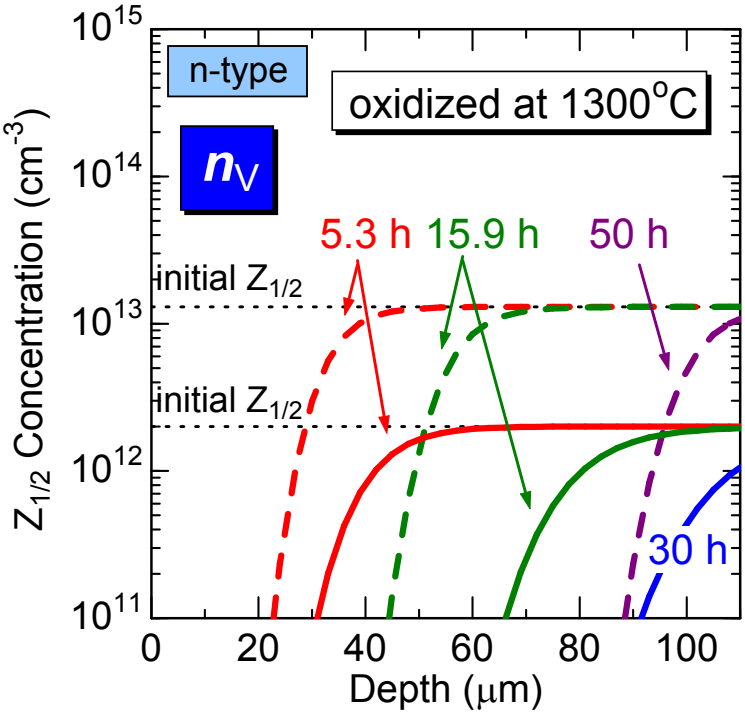

Figure 5.11: Calculated $Z_{1/2}$ profiles for various oxidation times and different initial $Z_{1/2}$ concentrations (solid lines: for 2×10^{12} cm^{-3}, dashed lines: for 1.3×10^{13} cm^{-3}) using the parameters in Table 5.2. Here, n_V is assumed to correspond to the $Z_{1/2}$ concentration.

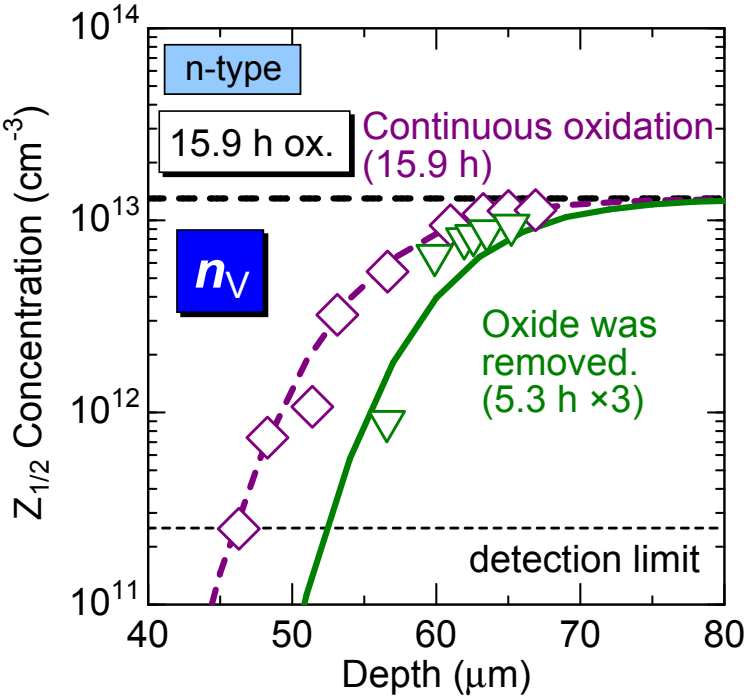

Figure 5.12: Depth profiles of the $Z_{1/2}$ center after oxidation at 1300°C for 15.9 h. The rhombuses denote the experimental result for continuous 15.9-h oxidation (dashed line: calculated n_V result with the parameters in Table 5.2), and reverse triangles for 15.9-h oxidation with removing the oxide layer after every 5.3-h oxidation (solid line: calculated n_V result with the parameters in Table 5.2).

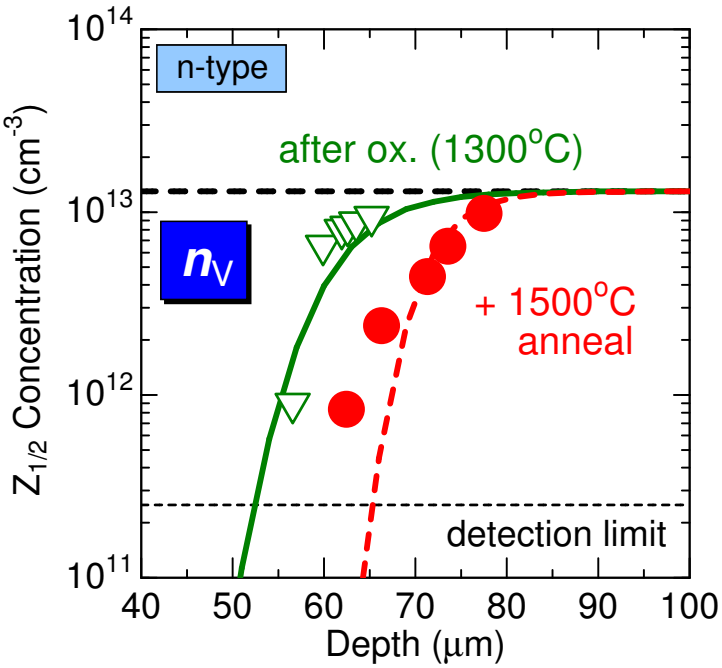

Figure 5.13: $Z_{1/2}$ profiles after oxidation and after oxidation followed by 1500°C annealing. The reverse triangles denote the experimental result for after oxidation at 1300°C for 15.9 h (solid line: calculated n_V profile with the parameters in Table 5.2), and the filled circles for the oxidation followed by annealing at 1500°C for 2 h in Ar ambient (dashed line: calculated n_V profile with the parameters in Table 5.2).

(reverse triangles: after oxidation; filled circles: after oxidation followed by Ar annealing at 1500°C) well agree with the predicted lines, indicating that the present analytical model is useful for predicting trap distributions not only after oxidation but also after subsequent Ar annealing. In addition, this annealing reduced the HK0 center generated in p-type SiC by thermal oxidation, which also means that residual interstitials further diffuse to the deeper region and promote the $Z_{1/2}$ reduction by the subsequent annealing.

(iii) Higher-temperature oxidation: Because all parameters, D, F_0, and γ, should increase at higher temperature, oxidation at higher temperature must be effective in reduction of the $Z_{1/2}$ center. Fig. 5.14 shows the depth profiles of the $Z_{1/2}$ center after oxidation at 1400°C for 5.5 h and 16.5 h. Each line indicates the n_V profile calculated with the parameters in Table 5.2, and each symbol indicates experimental data. Note that surface morphology of a SiC epilayer oxidized at 1400°C for 16.5 h was almost the same as that of an as-grown epilayer. By atomic force microscopy (AFM) measurements, root-mean-square (RMS) roughness of the oxidized epilayer surface (after removing the oxide) was found to be ~ 0.55 nm with a scanned area of 10 μm square, whereas that before oxidation was ~ 0.44 nm[1]. The $Z_{1/2}$ center was eliminated to a depth of about 60 μm after oxidation for 5.5 h, which also agrees with the calculated result. After oxidation for 16.5 h, the $Z_{1/2}$ center could further be reduced but appear to remain at a depth of about 95 μm, whereas it was completely eliminated in the calculated result. (Calculated n_V-distribution after 16.5-h oxidation is not shown because the n_V is lower than 1×10^{10} cm^{-3} in the epilayer.) Note that in this sample the interface between the epilayer and the substrate is located at a depth of about 96 μm from the surface, implying that the data points near the interface contain the substrate information (a high concentration of the $Z_{1/2}$ center exists in the substrate). Nevertheless, it was clarified that thermal oxidation at 1400°C is very effective in accelerating $Z_{1/2}$ reduction.

In addition to the above three approaches, higher-rate-oxidation processes such as wet oxidation and plasma oxidation at a high temperature may be effective in reducing required oxidation time.

5.8 Summary

To clarify the mechanism of the trap reduction by thermal oxidation, the author investigated deep levels after two trap-reduction processes: thermal oxidation and C^+ implantation followed by Ar annealing. Based on the two results shown below, the author concluded that the same phenomena, diffusion of interstitials, occur during these processes. (i) Deep

[1]By optical microscope, however, pits (diameter: ~ 2 μm) with a concentration of $\sim 1 \times 10^3$ cm^{-2} were observed, which may be attributed to enhancement of an oxidation rate at the surface where threading screw dislocations (TSD) are located. To remove the pits, mechanical polishing (or gas etching) should be effective. Improving quality of SiC epilayers (reducing a TSD density) will also reduce a density of the pits.

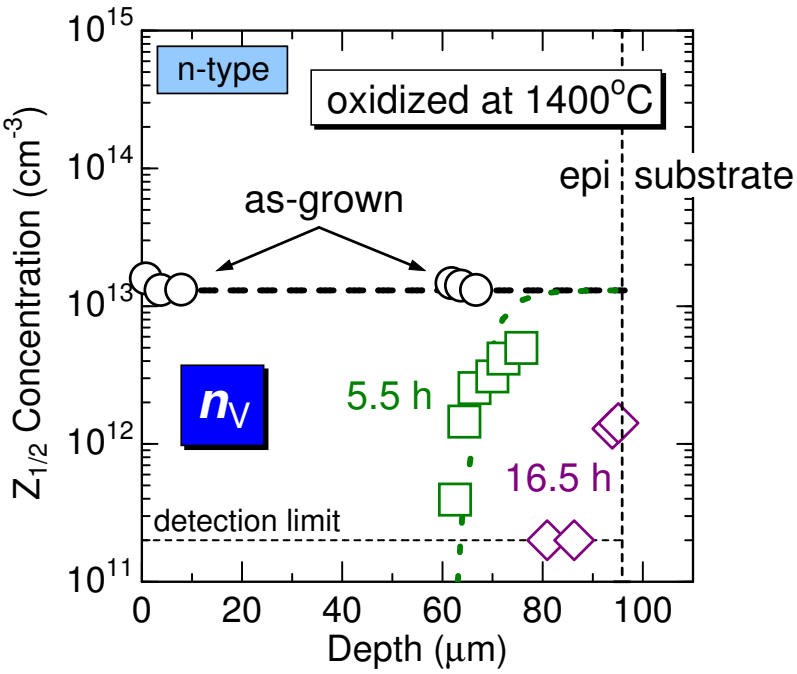

Figure 5.14: Depth profiles of the $Z_{1/2}$ center after oxidation at 1400°C for 5.5 h and 16.5 h. The dotted line indicates the n_V profile after 5.5-h oxidation calculated with the parameters in Table 5.2 and each symbol indicates the experimental data. The calculated line for 16.5-h oxidation is not shown because the n_V is lower than 1×10^{10} cm^{-3} in the 96-μm-thick epilayer.

levels generated by thermal oxidation were the same as those generated by C^+ implantation followed by Ar annealing. (ii) The depth profiles of generated/reduced defects represented the distribution of interstitials/vacancies after interstitial diffusion from the surface to the SiC bulk.

Using diffusion equations, moreover, the author proposed an analytical model enabling the prediction of $Z_{1/2}$ distribution after thermal oxidation. In SiC epilayers with different initial $Z_{1/2}$ concentrations, this model could reproduce the depth profiles of the $Z_{1/2}$ center after oxidation at any temperatures and for any oxidation periods. Using the calculation, the author found that long-time oxidation is required for the elimination of the $Z_{1/2}$ center when the initial $Z_{1/2}$ concentration is high. For achieving long carrier lifetimes, thus, it is important to keep the initial $Z_{1/2}$ concentration low ($< 10^{13}$ cm^{-3}) and to enhance the $Z_{1/2}$ reduction. The initial $Z_{1/2}$ concentration depends on the conditions of epitaxial growth and performed device processes. To enhance the $Z_{1/2}$ reduction and reduce the process time, three methods, removing the oxide layer during oxidation, Ar annealing at 1500°C after oxidation, and higher-temperature oxidation, were proposed and experimentally proved to be effective. In particular, increasing oxidation temperature was the most effective for enhancement of the $Z_{1/2}$ reduction. The $Z_{1/2}$ center with an initial concentration of 1.3×10^{13} cm^{-3} could be eliminated to a depth of > 90 μm after oxidation at 1400°C for 16.5 h. Therefore, to achieve a thick $Z_{1/2}$-free region in an SiC epilayer with a high initial $Z_{1/2}$ concentration ($> 10^{13}$ cm^{-3}), thermal oxidation at a high temperature (1400°C) is recommended.

References

[1] T. Hiyoshi and T. Kimoto, *Applied Physics Express* **2**, 041101 (2009).

[2] L. Storasta and H. Tsuchida, *Applied Physics Letters* **90**, 062116 (2007).

[3] L. Storasta, H. Tsuchida, T. Miyazawa, and T. Ohshima, *Journal of Applied Physics* **103**, 013705 (2008).

[4] Y. Hijikata, H. Yaguchi, and S. Yoshida, *Applied Physics Express* **2**, 021203 (2009).

[5] K. C. Chang, N. T. Nuhfer, L. M. Porter, and Q. Wahab, *Applied Physics Letters* **77**, 2186 (2000).

[6] T. Zheleva, A. Lelis, G. Duscher, F. Liu, I. Levin, and M. Das, *Applied Physics Letters* **93**, 022108 (2008).

[7] J. M. Knaup, P. Deák, T. Frauenheim, A. Gali, Z. Hajnal, and W. J. Choyke, *Physical Review B* **71**, 235321 (2005).

[8] K. Danno and T. Kimoto, *Journal of Applied Physics* **101**, 103704 (2007).

[9] T. Hiyoshi and T. Kimoto, *Applied Physics Express* **2**, 091101 (2009).

[10] M. Bockstedte, A. Mattausch, and O. Pankratov, *Physical Review B* **69**, 235202 (2004).

[11] F. Gao, W. J. Weber, M. Posselt, and V. Belko, *Physical Review B* **69**, 245205 (2004).

[12] M. Hon and R. Davis, *Journal of Materials Science* **14**, 2411 (1979).

[13] M. Hon, R. Davis, and D. Newbury, *Journal of Materials Science* **15**, 2073 (1980).

[14] J. D. Hong and R. F. Davis, *Journal of the American Ceramic Society* **63**, 546 (1980).

[15] J. D. Hong, R. F. Davis, and D. E. Newbury, *Journal of Materials Science* **16**, 2485 (1981).

Chapter 6

Origin of $Z_{1/2}$ Center

6.1 Introduction

The $Z_{1/2}$ center is one of the most important deep levels in 4H-SiC, known as a carrier lifetime killer [1, 2]. To reveal the origin of the lifetime killer is very important scientifically and also for complete control of carrier lifetimes in SiC epilayers. The origin of the $Z_{1/2}$ center, however, has not been identified as that of other deep levels in SiC has not. In this study, the author seeks to reveal the origin of the $Z_{1/2}$ center comparing $Z_{1/2}$ concentration determined by deep level transient spectroscopy (DLTS) with point-defect concentration by electron paramagnetic resonance (EPR) in each sample. Here, EPR spectroscopy is a powerful method to determine the configuration of point defects in semiconductors [3].

The direct comparison of DLTS and EPR results is, however, not easy and has not so far been possible due to the following reasons.

(i) EPR measurements are suitable for relatively high defect concentrations (over $\sim 10^{12}$ spins, which correspond to concentrations over $\sim 10^{15}$ cm^{-3}). For DLTS measurements, however, a low trap concentration N_T is required compared with a donor concentration N_d; $N_T < 0.2N_d$ is required (typical N_d in as-grown SiC epilayers is 10^{14}–10^{18} cm^{-3}).

(ii) By DLTS, only regions near the surface are monitored (a trap volume density near the surface is obtained), whereas EPR has no spatial resolution (EPR signal results from all spins in the whole sample and thereby an area density of a defect is obtained). To compare a trap volume density measured by DLTS with an area density of a defect by EPR, a depth profile of the trap volume density has to be known.

(iii) The detectable defects by EPR depend on the charge state of the defects; for carbon vacancy (V_C), V_C^- is detectable whereas V_C^{2-} and V_C^0 are not. (Note that the author speculates that the $Z_{1/2}$ center originates from a single V_C defect, which is discussed

in Section 6.3.) Because the V_C defect has a negative-U nature[1], most V_C defects are undetectable V_C^{2-} or V_C^0 under equilibrium condition.

Due to the restriction (i), in previous studies, electron irradiation fluences for samples measured by DLTS were much lower than those for samples by EPR [4], which prevented the deep-level and point-defect concentrations from being quantitatively compared.

In this study, the author overcame the restrictions (i)–(iii) by the following solutions (i)–(iii), respectively.

(i) n-type 4H-SiC epilayers with relatively high doping concentrations (10^{16}–10^{18} cm^{-3}) were irradiated by low-energy (250 keV) electrons with various electron fluences, leading to various concentrations of the $Z_{1/2}$ center; in a part of these samples, DLTS results and EPR results could be compared.

(ii) Because the $Z_{1/2}$ center did not uniformly distributed along the depth in the irradiated samples (described in Section 6.5), the author measured the $Z_{1/2}$ concentration at each depth by DLTS measurements after each of several-times mechanical polishing, and integrated the volume concentrations over the depth (resulting in the trap area density, which can be compared with an area density of a defect measured by EPR).

(iii) By light excitation, the author made V_C^- from V_C^{2-} and measured it by EPR. The ratio of V_C concentration in each charge state was consistently taken into account for comparison between $Z_{1/2}$ concentration and V_C defect concentration.

6.2 Electron Paramagnetic Resonance Spectroscopy

In EPR measurements, the interaction between electromagnetic radiation and magnetic moments (mainly from unpaired electrons) is observed [3]. The electron-spin magnetic moment along the direction of the magnetic field $\boldsymbol{B}$ applied along the direction $\boldsymbol{z}$ is

$$\mu_z = -g_e \mu_B M_S, \tag{6.1}$$

where g_e denotes the free-electron g factor, μ_B Bohr magneton, and M_S the quantum number for electrons. Thus, the energy of a magnetic dipole U is expressed as

$$U = g_e \mu_B M_S \boldsymbol{B}. \tag{6.2}$$

For a single unpaired electron, the possible values of M_S are $+\frac{1}{2}$ and $-\frac{1}{2}$, leading to the separation of the energy levels:

$$\Delta U = g_e \mu_B \boldsymbol{B}. \tag{6.3}$$

[1]For a negative-U center, the energy gain by capturing the second electron is higher than by capturing the first electron due to a local rearrangement of the lattice, whereas for a positive-U center by the second capturing is lower due to Coulombic repulsion of the two electrons.

When the incident radiant energy $h\nu$ is equal to the separation energy ΔU, resonance occurs and the incident microwave is absorbed. The absorption lineshape after differentiation is used as an EPR signal.

For unpaired electrons belonging to defects in semiconductors, spin-orbit coupling slightly shifts the g factor from g_e: 2.0023193. Furthermore, an electron spin also interacts with neighbor nuclear spins (hyperfine (hf) interaction), which splits each electron energy level. Because the g factor (g tensor) and the hyperfine interaction (hf tensor) depend on the defect configuration, EPR measurements can give important informations about the microscopic structure of a point defect.

6.3 Present Knowledge about Origin of $Z_{1/2}$ Center

From the following three experimental results, the origin of the $Z_{1/2}$ center has been speculated to be a V_C-related defect.

(i) The $Z_{1/2}$ center is generated by low-energy (100–200 keV) electron irradiation, which displaces only C atoms, without subsequent annealing [5, 6].

(ii) The $Z_{1/2}$ concentration is lower in the samples grown under C-rich condition (higher C/Si ratio) [7].

(iii) The $Z_{1/2}$ center is a thermally stable defect [5, 8] showing no change of the concentration up to 1600°C, at which temperature interstitials can easily diffuse.

These three experimental results, however, do not give the configuration of the origin (e.g. single V_C), nor directly prove that the origin is a V_C-related defect. In this study, the author speculates that the $Z_{1/2}$ center originates from the single V_C defect and attempts to quantitatively prove this.

6.4 Experiments

The starting materials are 100-μm-thick n-type 4H-SiC epilayers. The doping concentration N_d is varied by wafers: (A) 1.8×10^{16} cm^{-3}, (B) 3.8×10^{16} cm^{-3}, (C) 1.1×10^{17} cm^{-3}, (D) 1.6×10^{17} cm^{-3}, and (E) 1.2×10^{18} cm^{-3}. The epilayers were irradiated with 250 keV electrons with different fluences of 1×10^{15}–1×10^{19} cm^{-2}. For C-V, I-V, and DLTS measurements, Schottky barrier diodes (SBDs) were fabricated in the same manner as described in Chapter 2, while for EPR the substrate of the other set of samples was removed by mechanical polishing. In DLTS measurements, the reverse bias voltage was varied in the range from 0 V to -100 V, which corresponds to monitored depths of about 0.1–1.4 μm in samples of the wafer B (named B samples). EPR measurements were performed by an X-band ($\sim$9.4 GHz) Bruker E500 spectrometer equipped with a continuous He-flow cryostat, allowing the sample temperature regulation in the range of 4–295 K. In photoexcitation

EPR (photo-EPR) experiments, a 200 W halogen lamp and appropriate optical filters were used for excitation.

6.5 Defect Distribution after Electron Irradiation

6.5.1 Deep levels in electron-irradiated samples

Fig. 6.1 shows DLTS spectra observed in D samples (N_d: 1.6×10^{17} cm^{-3}) irradiated with an electron fluence of (a) 7.5×10^{18} cm^{-2} and (b) 3.1×10^{18} cm^{-2}. The lower temperature region of the spectrum in Fig. 6.1(a) was obtained by current DLTS (I-DLTS) because the very low capacitance (caused by severe compensation) disturbed capacitance DLTS (C-DLTS) measurements. At higher temperatures (> 400 K), the capacitance recovered to the value before electron irradiation, which enabled C-DLTS measurements of the sample. In contrast, the sample irradiated with relatively low electron fluence could be measured by C-DLTS in whole temperature range of 150–700 K (Fig. 6.1(b)). As shown in Fig. 6.1, ET1 ($E_C - 0.30$ eV) [5], EH1 ($E_C - 0.34$ eV) [9], $Z_{1/2}$ ($E_C - 0.67$ eV) [8], EH3 ($E_C - 0.72$ eV) [9], EH5 ($E_C - 1.3$ eV) [9], ET4 ($E_C - 1.3$ eV), and $EH_{6/7}$ ($E_C - 1.5$ eV) [9] centers were observed in the irradiated samples. The activation energy was derived by assuming temperature-independent capture cross section. Taking into account that the barrier for capturing the second electron to the $Z_{1/2}$ level is 0.074 eV [10, 11], the energy level of the $Z_{1/2}$ center is recalculated as $E_C - 0.59$ eV. All these deep levels are often observed in irradiated 4H-SiC except for the ET4 center, which is not easy to be separated from the $EH_{6/7}$ center because of severe overlapping. Among these centers, the $Z_{1/2}$ center showed the highest concentration in the irradiated samples.

6.5.2 Formation of Compensated Region

Fig. 6.2 shows the C-V characteristics at room temperature (RT) obtained from the D samples irradiated with different fluences. The capacitance of the D samples was very small and almost constant independent of the bias voltage, indicating that these samples had a completely compensated region (CR) caused by electron capture of deep levels. (These samples had a very thick depletion region even under 0 V bias). Fig. 6.3 shows the dependence of the CR thickness (d_{CR}) on the electron fluence, which was derived from the equation: $d_{CR} = \epsilon S/C$ (ϵ: dielectric constant, S: contact area, C: capacitance obtained from C-V measurements). Electron irradiation with higher fluence or for lower doped samples led to a thicker d_{CR}, indicating that the compensating source was not uniformly distributed along the depth (this will be discussed in Section 6.5.3).

Fig. 6.4 shows the carrier concentration and the Fermi level in the CR of the D samples. The carrier concentration n in the CR was roughly estimated from the resistivity ρ in the CR of each sample using the equation: $n = 1/e\rho\mu$. The ρ value was calculated from the

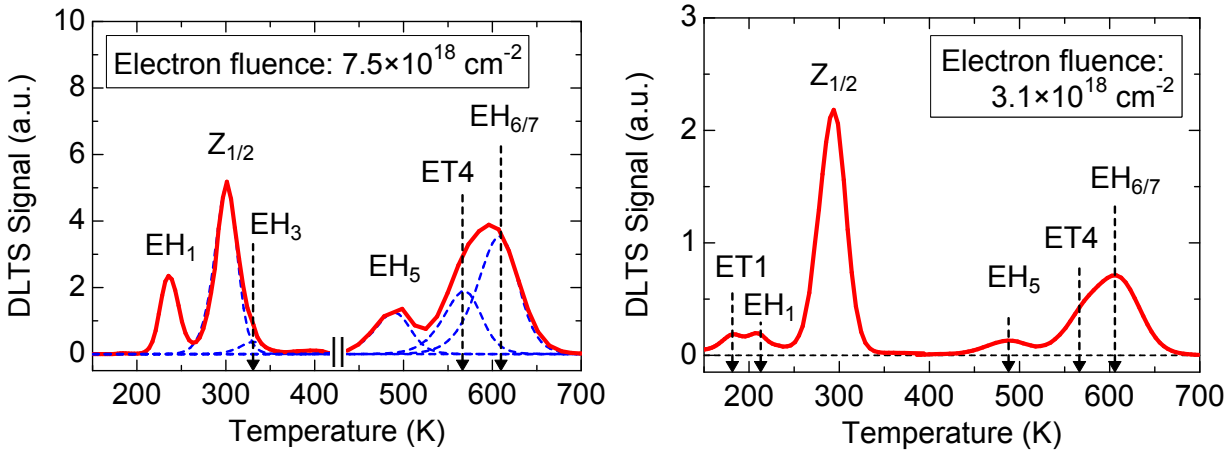

(a) (b)

Figure 6.1: DLTS spectra observed in the D samples (N_d: 1.6×10^{17} cm^{-3}) irradiated with an electron fluence of (a) 7.5×10^{18} cm^{-2} and (b) 3.1×10^{18} cm^{-2}. The lower temperature region of the spectrum in sample (a) was obtained by current DLTS (I-DLTS).

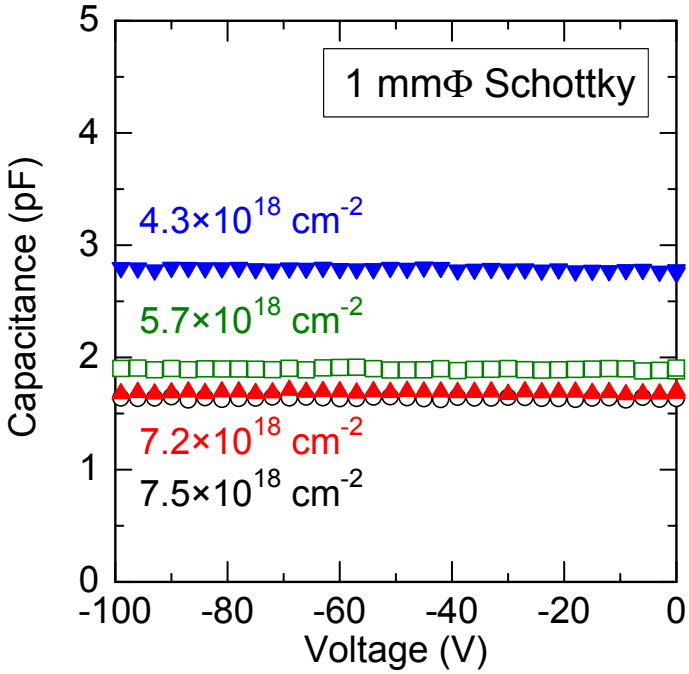

Figure 6.2: *C-V* characteristics at room temperature (RT) of the D samples irradiated by low-energy (250 keV) electrons with various fluences (circles: 7.5×10^{18} cm^{-2}, triangles: 7.2×10^{18} cm^{-2}, squares: 5.7×10^{18} cm^{-2}, reverse triangles: 4.3×10^{18} cm^{-2}).

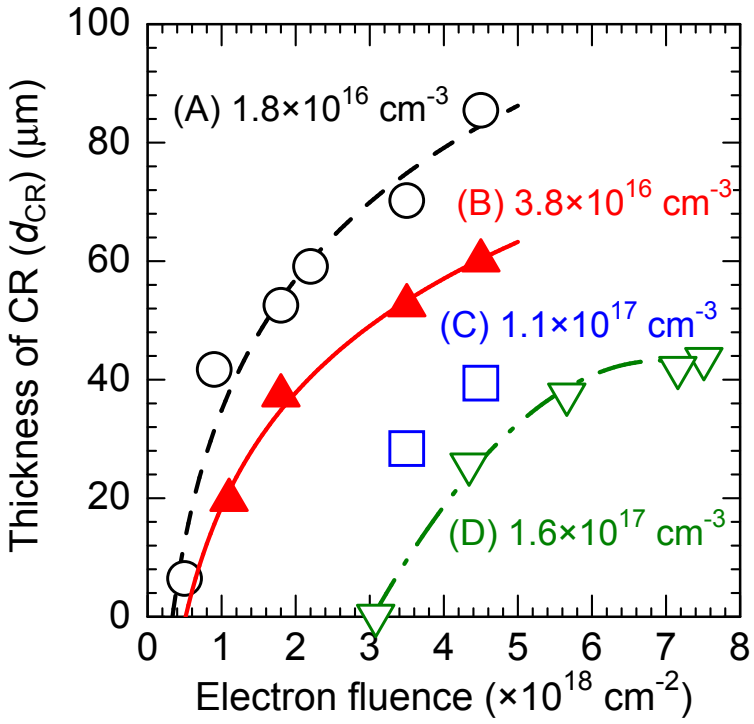

Figure 6.3: Dependence of the compensated-region (CR) thickness (d_{CR}) in the A–D samples (circles: A samples, triangles: B samples, squares: C samples, reverse triangles: D samples) derived from C-V results on an irradiated electron fluence.

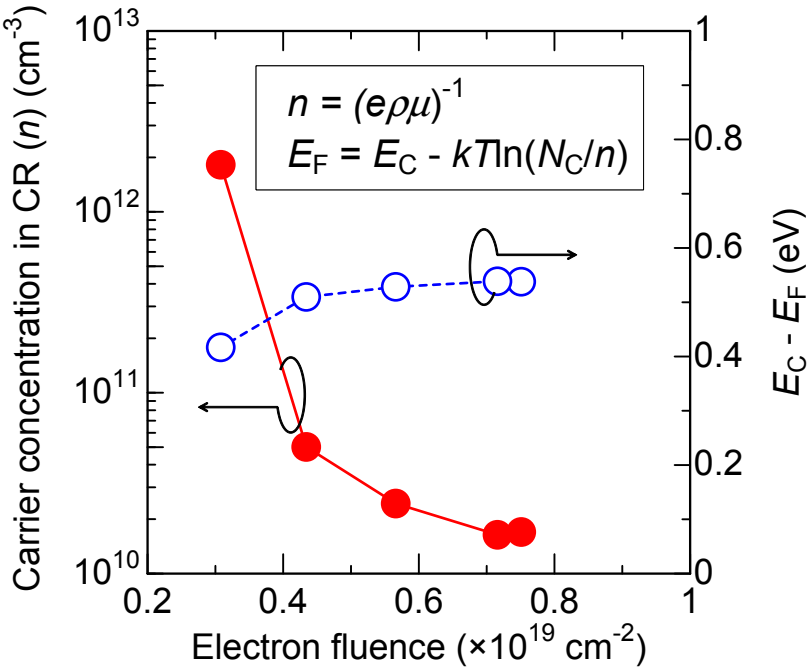

Figure 6.4: Dependence of the carrier concentration n and the Fermi level at 300 K in the CR of the D samples on an irradiated electron fluence. Here, n was estimated from the resistivity ρ in the CR of each sample.

series resistance of the SBDs (R) obtained from I-V measurements, using the equation: $\rho = RS/d_{\mathrm{CR}}$. The electron mobility μ in the CR was assumed to be 370 $\mathrm{cm^2/Vs}$ using empirical equations given in a paper [12]. For this estimation of μ, an impurity (that causes an electron scattering) concentration of 3.2×10^{17} $\mathrm{cm^{-3}}$ was used because there should be 1.6×10^{17} $\mathrm{cm^{-3}}$ of ionized donor (positive charge) and 1.6×10^{17} $\mathrm{cm^{-3}}$ of traps filled with electrons (negative charge). The Fermi level E_{F} in the CR was estimated from the carrier concentration n using the equation: $E_{\mathrm{F}} = E_{\mathrm{C}} - kT\ln(N_{\mathrm{C}}/n)$ (N_{C}: the effective density of states in the conduction band). In the samples irradiated with high electron fluences over 4.0×10^{18} $\mathrm{cm^{-2}}$, E_{F} was located at an energy level of $\sim E_{\mathrm{C}} - 0.53$ eV, which is close to the energy level of the $Z_{1/2}$ center ($E_{\mathrm{C}} - 0.59$ eV). With this Fermi level ($E_{\mathrm{C}} - 0.53$ eV), the $Z_{1/2}$ center ($E_{\mathrm{C}} - 0.59$ eV) is occupied with electrons (the occupancy $\sim 91\%$ at 300 K). Note that E_{F} is not sensitive to μ; when μ become twice or a half of the original value (370 $\mathrm{cm^2/Vs}$), E_{F} shifts ~ 0.02 eV toward the valence band or the conduction band, respectively. Taking into account that the $Z_{1/2}$ center has the highest concentration (over 1×10^{17} $\mathrm{cm^{-3}}$) among the deep levels observed in these samples, this defect should be the dominant compensating center, creating the CR.

6.5.3 Depth Profiles of $Z_{1/2}$ Center Obtained by Deep Level Transient Spectroscopy and C-V Measurements

By DLTS and C-V measurements, the $Z_{1/2}$ concentration in the irradiated samples was investigated. Note that after electron irradiation the $Z_{1/2}$ center does not uniformly distribute along the depth of the epilayers. Fig. 6.5 shows depth profiles of the $Z_{1/2}$ center in low-doped epilayers (donor concentration N_{d}: 1.6×10^{15} $\mathrm{cm^{-3}}$, initial $Z_{1/2}$ concentration: 1.7×10^{13} $\mathrm{cm^{-3}}$) after irradiation with 250-keV electrons with low fluences (3×10^{15} $\mathrm{cm^{-2}}$–2×10^{16} $\mathrm{cm^{-2}}$). The distribution of the $Z_{1/2}$ center could be roughly fitted by the following equation:

$$N_{\mathrm{T}}(x) = N_0 + N_{\mathrm{surf}}\exp(-3.8\times10^4 x^2), \tag{6.4}$$

where x signifies the distance from the surface (cm), N_{surf} the $Z_{1/2}$ concentration at the surface, and N_0 the initial $Z_{1/2}$ concentration before electron irradiation. The N_{surf} values in the irradiated samples were measured by DLTS. Fig. 6.6 shows the dependence of N_{surf} on irradiated electron fluence (electron energy: 200 keV or 250 keV), which is in proportion to the electron fluence. The proportional coefficients between the $Z_{1/2}$ concentration and electron fluence are 4.5×10^{-2} $\mathrm{cm^{-1}}$ for 200-keV electrons and 3.5×10^{-2} $\mathrm{cm^{-1}}$ for 250-keV electrons, which does not conflict with a previous report [13] (the slight difference may be due to a difference of the monitored depth).

The depth profiles of the $Z_{1/2}$ center can also be estimated by the thickness of a CR (d_{CR}). The CR is formed where the $Z_{1/2}$ concentration exceeds N_{d} due to the capture of almost all electrons by a high density of the $Z_{1/2}$ center. When $N_{\mathrm{T}}(d_{\mathrm{CR}}) = N_{\mathrm{d}}$ is applied to the Eq. (6.4), the N_{surf} value in each sample can be obtained from each d_{CR} (derived

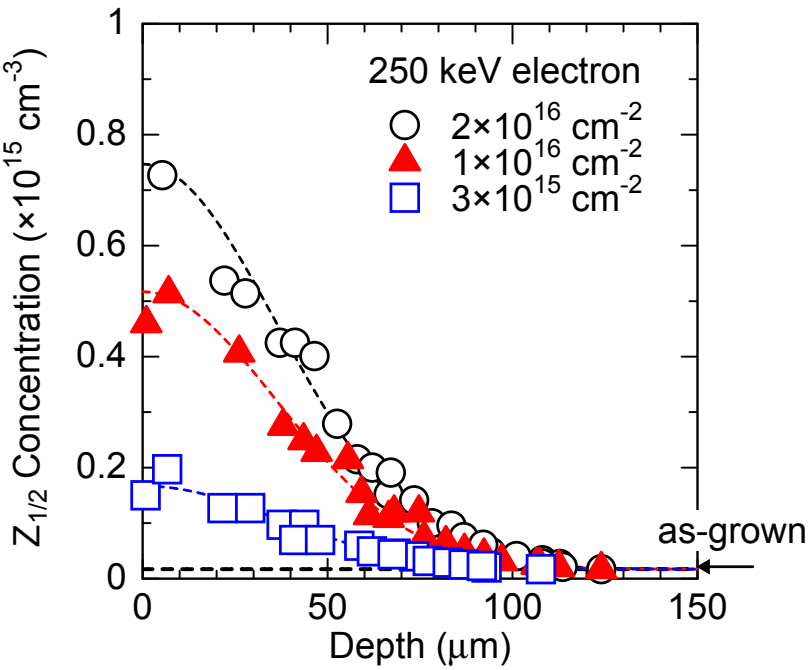

Figure 6.5: Depth profiles of the $Z_{1/2}$ center in low-doped 4H-SiC epilayers (N_d: 1.6×10^{15} cm^{-3}, initial $Z_{1/2}$ concentration: 1.7×10^{13} cm^{-3}) after irradiation with 250-keV electrons with low fluences (circles: 2×10^{16} cm^{-2}, triangles: 1×10^{16} cm^{-2}, squares: 3×10^{15} cm^{-2}). Each line indicates a fitting line following the Eq. (6.4).

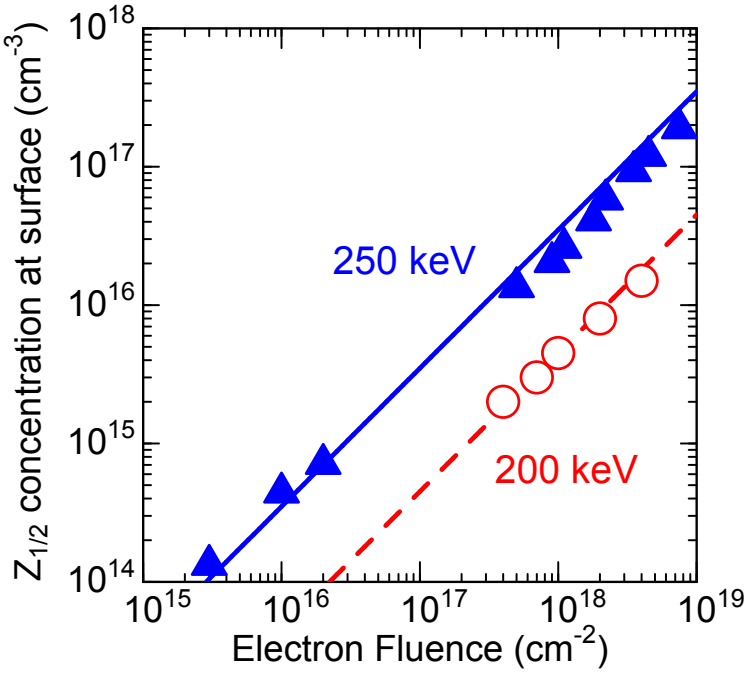

Figure 6.6: Dependence of the $Z_{1/2}$ concentration near the surface measured by DLTS on the irradiated electron fluence (electron energy: 200 keV or 250 keV).

from C-V results). Fig. 6.7 shows the $N_{\rm surf}$ values of A–C samples obtained from DLTS measurements and from C-V measurements. The plots from C-V measurements are roughly on a line independent of the donor concentration, suggesting that the depth profiles of the $Z_{1/2}$ center estimated from C-V results are valid. The slight difference between the DLTS results and the C-V results may be attributed to the overestimation of $N_{\rm surf}$ values in Eq. (6.4). In this study, the $Z_{1/2}$ depth profiles derived from C-V results (profiles obtained from $d_{\rm CR}$ determined by the points where $N_{\rm T} = N_{\rm d}$) are employed for the comparison between $Z_{1/2}$ concentration and $V_{\rm C}$ concentration.

6.6 Charge States of Carbon Vacancy in Darkness and under Illumination

In the bandgap of 4H-SiC, $V_{\rm C}$ can be in several charge states such as $V_{\rm C}^{2-}$, $V_{\rm C}^{-}$, $V_{\rm C}^{0}$, $V_{\rm C}^{+}$, or $V_{\rm C}^{2+}$ [14–17], among which $V_{\rm C}^{2-}$, $V_{\rm C}^{-}$, and $V_{\rm C}^{0}$ should be dominant in n-type materials. Because $V_{\rm C}^{2-}$ and $V_{\rm C}^{0}$ cannot be detected by EPR, $V_{\rm C}^{-}$ concentration in the irradiated samples was investigated. Fig. 6.8 shows EPR spectra for the C sample irradiated with a fluence of 4.5×10^{18} cm^{-2} measured at 100 K in darkness or under illumination filtered with a 780 nm ($\sim$1.6 eV) low-pass filter. In all samples having a CR, two signals, showing g values ($\boldsymbol{B} \parallel \boldsymbol{c}$) of 2.00475 and 2.00398, were dominant. From the obtained g tensor and the Si hf tensors, the spectra were identified to be related to $V_{\rm C}^{-}$ in cubic site ($V_{\rm C}^{-}$(k)) and in hexagonal site ($V_{\rm C}^{-}$(h)) [18]. Under illumination, a $V_{\rm C}^{-}$(h) signal clearly increased compared with in darkness and a $V_{\rm C}^{-}$(k) signal appeared, which can be explained [18] by negative-U nature of $V_{\rm C}$ [17, 18]; most of $V_{\rm C}$ were $V_{\rm C}^{0}$ or $V_{\rm C}^{2-}$ in darkness because of the negative-U nature, whereas some electrons were emitted from $V_{\rm C}^{2-}$ and thereby $V_{\rm C}^{-}$ increased under illumination.

Fig. 6.9 shows the schematic diagram for the electron transitions between the $V_{\rm C}$ levels ($V_{\rm C}^{2-/0}$ level[2] and $V_{\rm C}^{-/0}$ level) and the conduction band. The ratio of $V_{\rm C}$ concentration in each charge state ($[V_{\rm C}^{2-}] : [V_{\rm C}^{-}] : [V_{\rm C}^{0}]$) should be determined by the electron capture (c) and emission (e) rate:

$$c = \sigma v_{\rm th} n, \tag{6.5}$$

$$e = \sigma v_{\rm th} N_{\rm C} \exp\left(-\frac{E_{\rm C} - E_{\rm T}}{kT}\right) + \alpha A(\Delta E_{\rm light}), \tag{6.6}$$

where σ denotes the electron capture cross section, $v_{\rm th}$ the thermal velocity of electrons, n the carrier concentration (electrons in the conduction band), α the probability of electron excitation by photons. In Eq. (6.6), the first term corresponds to thermal emission of electrons from a trap located at $E_{\rm T}$ to the conduction band edge, whereas the second

[2]When the Fermi is located above/below this level, $V_{\rm C}^{2-}/V_{\rm C}^{0}$ is energetically favorable. However, note that this level corresponds to the $V_{\rm C}$ transitions between $V_{\rm C}^{2-}$ and $V_{\rm C}^{-}$.

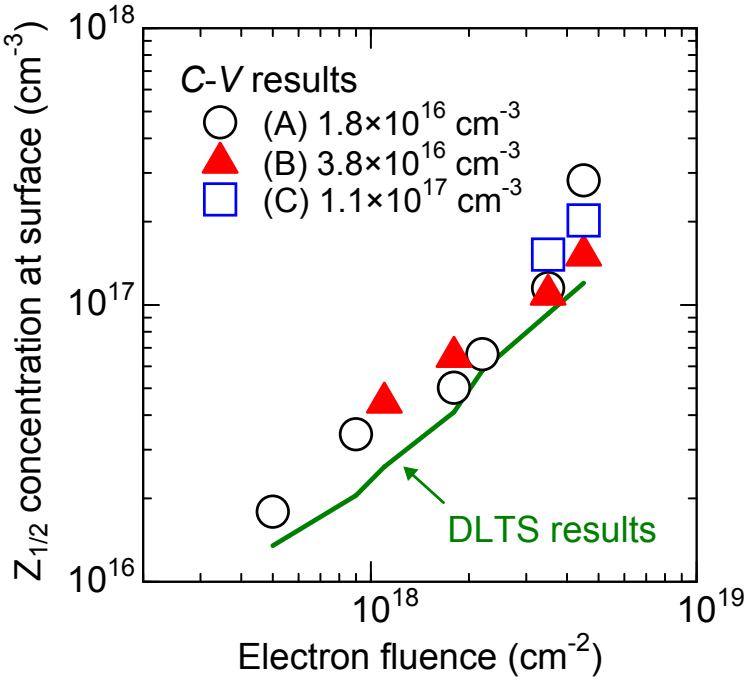

Figure 6.7: $Z_{1/2}$ concentration near the surface (N_{surf}) of the A–C samples obtained from DLTS measurements and C-V results with Eq. (6.4).

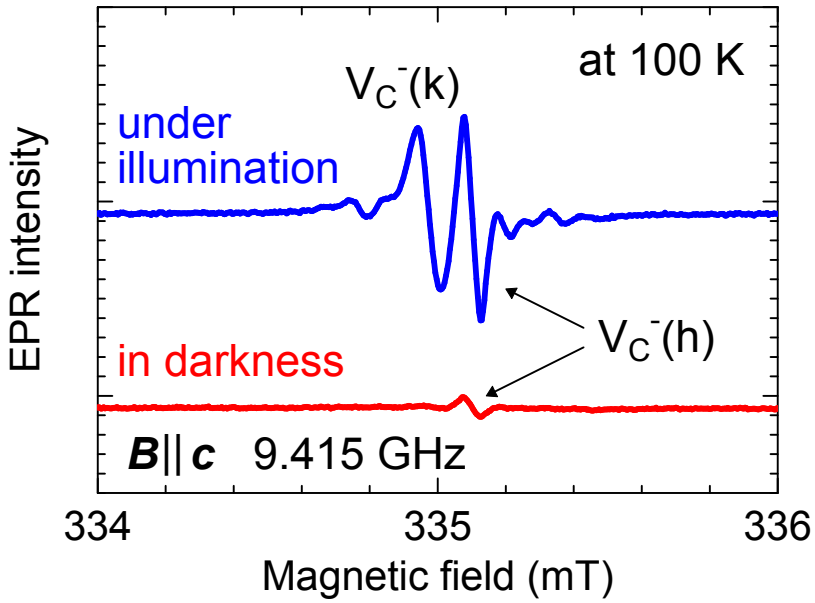

Figure 6.8: EPR spectra for the C sample irradiated with a fluence of 4.5×10^{18} cm^{-2} measured at 100 K in darkness or under illumination filtered with a 780-nm (∼1.6 eV) low-pass filter.

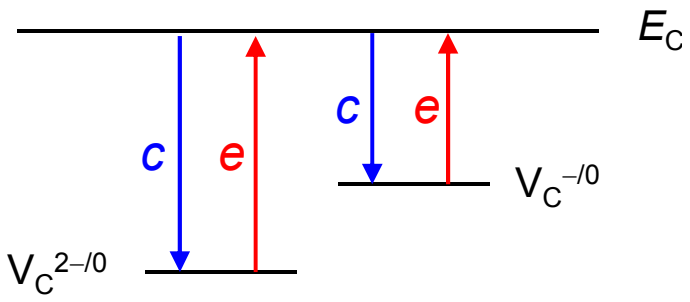

Figure 6.9: Schematic diagram for the electron transitions between the V_C levels ($V_C^{2-/0}$ and $V_C^{-/0}$) and the conduction band.

term corresponds to electron emission by photoexcitation. A is a function of $\Delta E_{\rm light} = E_{\rm light} - (E_{\rm C} - E_{\rm T} + E_{\rm FC})$ ($A = 0$ when $\Delta E_{\rm light} \leq 0$), where $E_{\rm FC}$ signifies the Franck-Condon shift and $E_{\rm light}$ the excitation light energy. When the occupancy ratio of a trap is given as f, the relation of f, c, and e is described as

$$\frac{f}{1-f} = \frac{c}{e}. \tag{6.7}$$

When the Eqs. (6.5)–(6.7) are applied for all traps located in the bandgap of the samples (e.g. $V_C^{2-/0}$(h), $V_C^{2-/0}$(k), $V_C^{-/0}$(h), $V_C^{-/0}$(k)), accurate occupancy ratio of the traps can be achieved. Even without solving all the equations, most behaviors of V_C^- signals during EPR measurements can qualitatively be explained as follows. Any V_C^- signals could not be observed in the samples with a high doping concentration (E samples: $N_{\rm d} = 1.2\times10^{18}$ cm^{-3}). In the region where the doping concentration exceeds the trap concentration, the carrier concentration n is much higher than in CR. Therefore, in the E samples, which have no CR, the electron capture rate c was very high (from Eq. (6.5)), resulting in that almost all V_C was V_C^{2-}. In other words, when there exists a high density of electrons in the conduction band, all the V_C immediately capture electrons and become V_C^{2-} even under illumination.

6.7 Comparison between $Z_{1/2}$ Concentration and Carbon Vacancy Concentration

In this section, the V_C^- area density $[V_C^-]_{\rm A}$ measured by EPR in the A–C samples irradiated with various electron fluences is compared with the "maximum V_C^- area density $[V_C^-]_{\rm MAX}$" derived from DLTS and C-V results. As mentioned in the section 6.5.3, the depth profiles of the $Z_{1/2}$ center can be estimated from the DLTS and C-V results. Using the depth profile of the $Z_{1/2}$ center, $[V_C^-]_{\rm MAX}$ can be estimated as the area shown as "$[V_C^-]_{\rm MAX}$" in Fig. 6.10. Fig. 6.10 shows the schematic diagram of the depth profiles of the $Z_{1/2}$ center and V_C in the sample irradiated with a high electron fluence. The thickness of a CR ($d_{\rm CR}$) can be defined by the depth at the cross point of the donor concentration $N_{\rm d}$ and the $Z_{1/2}$ volume density $[Z_{1/2}]_{\rm V}$. (Here, the author defines the $Z_{1/2}$ volume density as the electron concentration that the $Z_{1/2}$ center can capture.) Almost all V_C located out of CR should be V_C^{2-} because in the region many electrons exist in conduction band, leading to the high electron-capture rate of V_C (from Eq. (6.5)). Within the CR, in contrast, the $[V_C^-]_{\rm V}$ is limited by $[V_C]_{\rm V}$ and $N_{\rm d}$ because an electron is needed for V_C to become V_C^-.

Fig. 6.11 shows $[V_C^-]_{\rm A}$ as a function of the electron fluence in the A–C samples measured by EPR under illumination with a 780-nm low-pass filter (symbols), and $0.6\times[V_C^-]_{\rm MAX}$ estimated from DLTS and C-V results (lines). 60% of $[V_C^-]_{\rm MAX}$ well agreed with $[V_C^-]_{\rm A}$ measured by EPR irrespective of the doping concentration and the electron fluence, suggesting that the V_C^- concentration and the $Z_{1/2}$ concentration have an one-to-one correspondence, and the V_C^- concentration was not the maximum value even under illumination maybe due to a

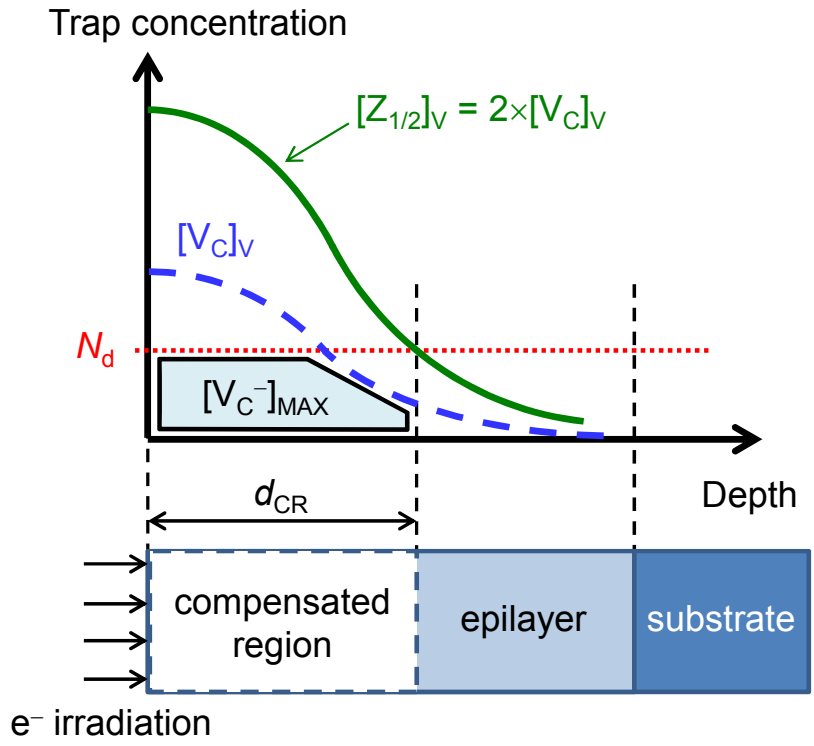

Figure 6.10: Schematic diagram of the depth profiles of $Z_{1/2}$ volume density $[Z_{1/2}]_V$ and V_C volume density $[V_C]_V$ in the sample irradiated with a high electron fluence. The area shown as "$[V_C^-]_{MAX}$" denotes the maximum V_C^- area density.

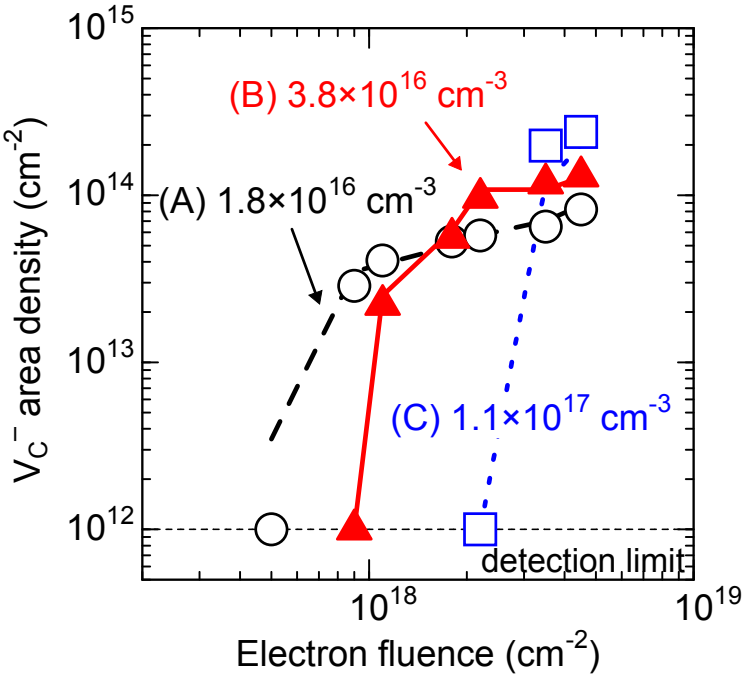

Figure 6.11: V_C^- area density as a function of the electron fluence in the A–C samples measured by EPR under illumination with a 780 nm low-pass filter (symbols), and 0.6 × $[V_C^-]_{MAX}$ estimated from DLTS and C-V results (lines).

high electron-capture rate of V_C^-. The charge states of the V_C defects are further discussed in Section 6.8.1. Fig. 6.12 shows $[V_C^-]_A$ measured by EPR as a function of $[V_C^-]_{MAX}$ determined from the depth profiles of $[Z_{1/2}]_V$. All the plotted data shows $[V_C^-]_A \simeq [V_C^-]_{MAX}$, indicating that the V_C concentration corresponds to the $Z_{1/2}$ concentration. From this quantitative investigation, it is concluded that the origin of $Z_{1/2}$ center is a single V_C defect.

6.8 Discussion

6.8.1 Charge States of Carbon Vacancy

The ratio of $[V_C]_V$ in each charge state ($[V_C^{2-}]_V : [V_C^-]_V : [V_C^0]_V$) should further be discussed because it is a key point of the comparison between the $Z_{1/2}$ concentration and the V_C concentration. To discuss this ratio, the energy state of a V_C defect in each charge state must be considered. Fig. 6.13 shows the configuration-coordinate diagram for the V_C (in h-site) levels with taking into account that the $Z_{1/2}$ center originates from the V_C defect. Note that (i) the negative-U nature of the $Z_{1/2}$ center (V_C level) is described as the higher activation energy of $Z_{1/2}^{2-/0}$ than $Z_{1/2}^{-/0}$, leading to the dominance of V_C^0 or V_C^{2-}, (ii) the photoionization energy (0.78 eV [18] and 0.74 eV [18]) is different from the activation energy (0.59 eV (in this study) and 0.52 eV [10]), which is called Franck-Condon shift, (iii) a barrier exist for the transition "V_C^- to V_C^{2-}" (0.065 eV [10]), corresponding to the temperature dependence of the cross section of the second electron capture to the $Z_{1/2}$ center [10, 11]. Taking account of this configuration-coordinate diagram, the author focused on the three particular behaviors of the V_C^- signals for the A–C samples.

(i) The carrier concentration (the electron concentration in the conduction band) in CR is very low even under illumination. During the EPR measurements of the samples possessing a CR, both in darkness and light, the quality factor (Q) kept a high value, which means that the microwave was little absorbed by free carriers. In addition, at temperatures lower than 200 K, the V_C^- signal intensity was almost unchanged after turning off the light, indicating that there were few electrons in the conduction band even under illumination due to large capture cross section of $V_C^{-/0}$ and that few V_C^- became V_C^{2-} after turning off the light due to activation energy for the transition "V_C^- to V_C^{2-}" [18]. In fact, $Z_{1/2}^{-/0}$ has a large capture cross section over 1×10^{-14} cm^{-2}, whereas $Z_{1/2}^{2-/0}$ has that of 10^{-20}–10^{-19} cm^{-2} at 100 K with an activation energy for the transition "$Z_{1/2}^-$ to $Z_{1/2}^{2-}$" of 0.065-0.08 eV [10, 11].

(ii) The electron excitation probability by photons α (Eq. (6.6)) was nearly unity under the illumination condition (there exist sufficient photons to interact with electrons). The intensity of V_C^- signal was almost constant when the power of excitation light was changed in the range over an order of magnitude, indicating that the excitation probability was saturated.

(iii) The electron emission rate by light excitation is much higher than that by thermal excitation (the first term of the Eq. (6.6) is negligible) under the illumination at 100–

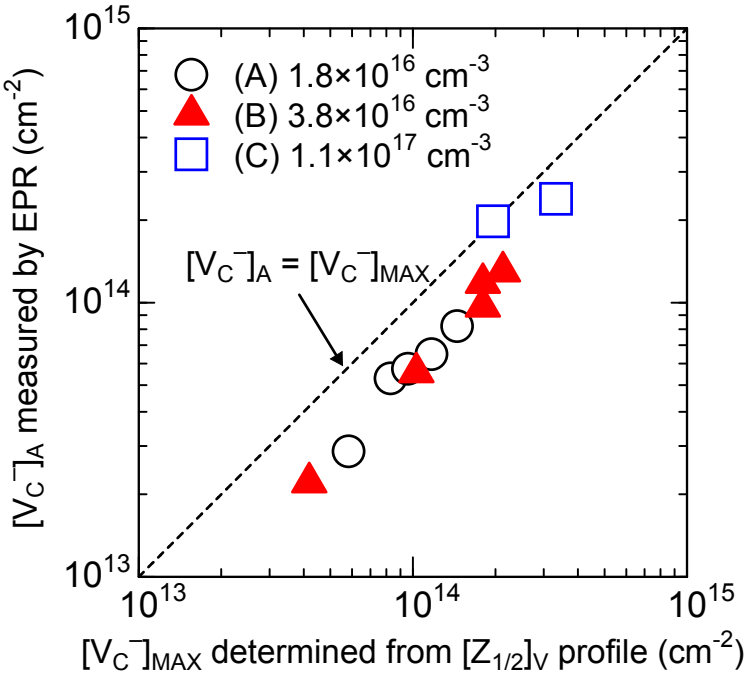

Figure 6.12: V_C^- area density $[V_C^-]_A$ as a function of $[V_C^-]_{MAX}$ determined from the depth profiles of the $Z_{1/2}$ volume density $[Z_{1/2}]_V$, which was obtained from the A–C samples.

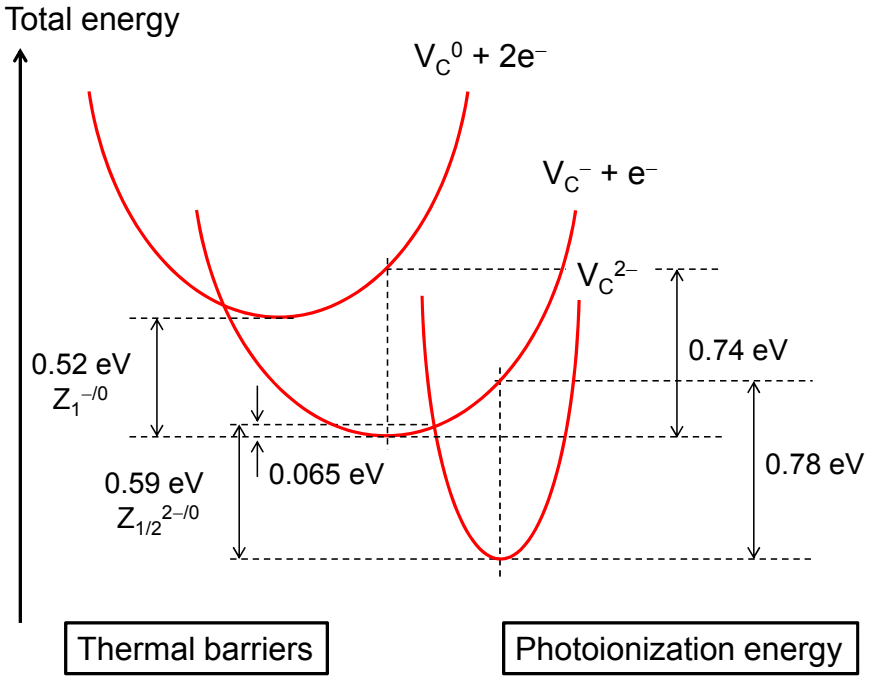

Figure 6.13: Configuration-coordinate diagram for the V_C (h-site) levels with taking into account that the $Z_{1/2}$ center originates from the V_C defect. e^- signifies an electron at the conduction band edge. The photoinoization energy was obtained from literature [18], and the activation energy for the transitions "V_C^- to V_C^0" and "V_C^- to V_C^{2-}" was from reference [10].

200 K. Fig. 6.14 shows the temperature dependence of $[V_C]_A$ in the A sample irradiated with a fluence of 4.5×10^{18} cm^{-2} in darkness and under illumination. By light excitation, $[V_C^-]_A$ increased by about two orders of magnitude and did not depend on the measurement temperature, suggesting that thermal excitation of electrons is negligible under illumination. $[V_C^-]_V$ in darkness can be estimated using the equations:

$$f_{(-/0)} = \frac{[V_C^-]_V}{[V_C^0]_V + [V_C^-]_V} = \frac{1}{1 + \exp\left(\frac{E_{T(-/0)} - E_F}{kT}\right)}, \tag{6.8}$$

$$f_{(2-/0)} = \frac{[V_C^{2-}]_V}{[V_C^-]_V + [V_C^{2-}]_V} = \frac{1}{1 + \exp\left(\frac{E_{T(2-/0)} - E_F}{kT}\right)}, \tag{6.9}$$

under the binding condition, $[V_C]_V = [V_C^{2-}]_V + [V_C^-]_V + [V_C^0]_V$ and $N_d = n + 2[V_C^{2-}]_V + [V_C^-]_V$, where $E_{T(-/0)}$ and $E_{T(2-/0)}$ signify the energy levels of $V_C^{-/0}$ and $V_C^{2-/0}$, respectively. Eqs. (6.8) and (6.9) suggest that the occupancy ratio of traps in darkness can be described by the Fermi-Dirac distribution function. As parameters, $E_C - E_{T(-/0)}$ and $E_C - E_{T(2-/0)}$ of 0.52 and 0.59 eV for h-site, 0.45 and 0.76 eV for k-site [10], N_d of 1.8×10^{16} cm^{-3}, and $[V_C]_V$ of 3×10^{16} cm^{-3} were assumed, where $[V_C]_V$ does not influence on the calculated results very much if the value sufficiently exceeds the half of N_d. The calculation results $[V_C^-]_A$ ($= [V_C^-]_V \cdot d_{CR}$) are shown in Fig. 6.14 as a dashed line ($[V_C^-(h)]_A$) and a solid line ($[V_C^-(k)]_A$). The calculated $[V_C^-]_A$ depends on the sites (h or k) and increases with the temperature due to the temperature dependence of the Fermi-Dirac distribution function. Although $[V_C^-(h)]_A$ and $[V_C^-(k)]_A$ were individually calculated for simplicity (all levels have to be solved together for an accurate calculation), the experimental results (circles) do not conflict with the calculation results (dashed line and solid line); the experimental $[V_C^-]_A$ are located between the calculated $[V_C^-(h)]_A$ and $[V_C^-(k)]_A$. In addition, the calculated $[V_C^-]_A$ (under dark condition) is much lower than the experimental results under illumination, which is consistent with the suggestion that thermal excitation is negligible compared with light excitation.

It is easy to compare the $Z_{1/2}$ concentration with the V_C concentration if all V_C are V_C^- where $N_T < N_d$, and all electrons are captured by V_C and there exist no V_C^{2-} where $N_T > N_d$. In this study, however, many V_C capture two electrons and become V_C^{2-} even under illumination. To increase the ratio of $[V_C^-]_V$, enhancement of the electron emission from V_C^{2-} and/or reduction of the electron capture to V_C^- will be effective. Here, note that increase of V_C^0 is negligible compared with that of V_C^- because of the large capture cross section of the $V_C^{-/0}$ level. Although the excitation probability α was already saturated ($\alpha \sim 1$), the emission rate can be enhanced by increase of the light energy E_{light} (Eq. (6.6)). Increasing the E_{light} beyond 1.6 eV, however, will cause the electron emission from V_C^0, and also the electron excitation from the valence band to V_C levels, which make it difficult to estimate V_C concentration. To decrease the electron capture rate, the thermal velocity of electrons or the carrier concentration should be reduced (Eq. (6.5)). Therefore, measurements of samples with a lower doping concentration and irradiated with higher electron fluence could be

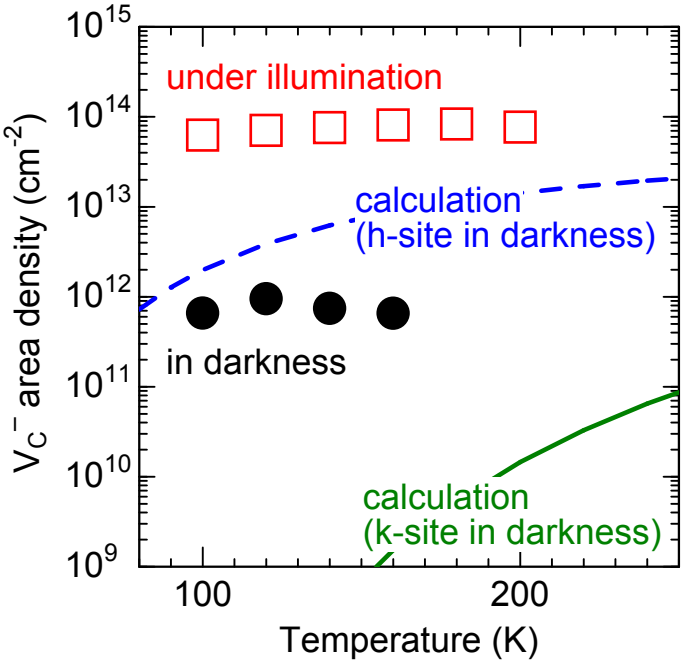

Figure 6.14: Temperature dependence of V_C^- area density $[V_C^-]_A$ in the A sample irradiated with the fluence of 4.5×10^{18} cm^{-2} in darkness (circles) and under illumination (squares). The lines indicate $[V_C^-]_A$ for h- or k-site in darkness (under equilibrium condition) estimated using Eqs. (6.8) and (6.9).

effective to obtain a higher $[V_C^-]_V/[V_C^{2-}]_V$ ratio.

6.8.2 Origin of the $Z_{1/2}$ Center

From DLTS, *C-V*, and EPR measurements, the author found that (i) the dominant deep level in the all irradiated samples was the $Z_{1/2}$ center and the dominant point defect was V_C and (ii) Fermi level in CR was located near the $Z_{1/2}$ level (which should also be near a V_C level), indicating that the compensation in the irradiated samples was caused by electron capture by the $Z_{1/2}$ center and in parallel by an acceptor level of V_C. In addition, the V_C^- area density $[V_C^-]_A$ measured by EPR was almost the same as the maximum V_C^- area density ($[V_C^-]_{MAX}$) determined from the depth profiles of the $Z_{1/2}$ concentration, suggesting that the V_C concentration corresponds to the $Z_{1/2}$ concentration. Therefore, the $Z_{1/2}$ center should unambiguously originate from the V_C defect.

Fig. 6.15 shows the activation energy (E_{act}) of deep levels obtained by DLTS and the optical transitions related to V_C levels (E_{exc}) determined by photo-EPR [18] with respect to the conduction band ($E_C = 0$). To compare E_{exc} with E_{act}, a possible Franck-Condon shift involved in the optical transitions has to be taken into account ($E_{act} = E_{exc} - E_{FC}$). The activation energies of V_C have also been obtained by *ab initio* calculations (density functional theory) [14–17], among which the latest results reported by Hornos et al. are shown in Fig. 6.15. The $Z_{1/2}$ level by DLTS, the $V_C^{2-/0}$ level by photo-EPR, and the calculated $V_C^{2-/0}$ level well agree. Note that the EH_7 center ($E_C - 1.6$ eV) originates from the same defect as for the $Z_{1/2}$ center [5, 19] and can be related to the (0/+) charge state of V_C [18].

From these results, the $Z_{1/2}$ center, which can also be described as $Z_{1/2}^{2-/0}$ taking account of the negative-U nature, should be the acceptor level of V_C ($V_C^{2-/0}$).

6.9 Summary

Using *n*-type (with different N doping levels) 4H-SiC epitaxial layers irradiated with low-energy (250 keV) electrons, which can mainly create defects in the C sub-lattice (V_C, carbon interstitial (C_I), and their associated defects) with different fluences, the author was able to use different techniques (*C-V*, DLTS and EPR) to quantitatively compare the $Z_{1/2}$ center with the V_C defect in the same samples. The $Z_{1/2}$ center and V_C defect were found to be the dominant defects responsible for the carrier compensation observed in the irradiated samples. After the electron irradiation, the $Z_{1/2}$ center did not uniformly distribute along the depth, which could be reproduced by an equation with a parameter: the $Z_{1/2}$ concentration near the surface N_{surf} or the compensated region thickness d_{CR}. The $Z_{1/2}$ profiles estimated from the N_{surf} measured by DLTS agreed with those from the d_{CR} measured by *C-V* irrespective of the doping concentration and the electron fluence, which means that the estimation of the $Z_{1/2}$ profiles by the proposed equation is reasonable. With the depth profiles of the $Z_{1/2}$ center, maximum V_C^- area densities $[V_C^-]_{MAX}$ were estimated and compared

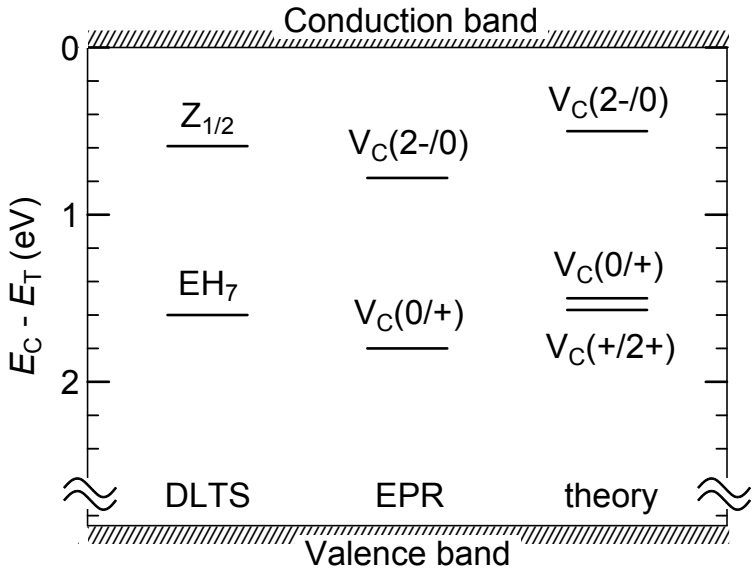

Figure 6.15: Overview of the activation energy of deep levels obtained by DLTS and the energy of the (2-/0) and (0/+) levels of V_C determined by photo-EPR [18] with respect to the conduction band minimum. The optical transitions determined by EPR involve a possible Franck-Condon shift, which has to be taken into account to be compared with the activation energy determined by DLTS. The energy levels for V_C in different charge states obtained by *ab initio* calculation [17] are also shown for comparison.

with the V_C^- area densities measured by EPR. 60% of $[V_C^-]_{MAX}$ well agreed with the V_C^- area density measured by EPR irrespective of the doping concentration and the electron fluence (in more than ten samples). Moreover, the energy level of $V_C^{2-/0}$ obtained by EPR and *ab initio* calculation well agrees with that of the $Z_{1/2}$ center, all of which show negative-U nature. Therefore, the $Z_{1/2}$ center must correspond to the $(2-/0)$ level of V_C.

References

[1] P. B. Klein, B. V. Shanabrook, S. W. Huh, A. Y. Polyakov, M. Skowronski, J. J. Sumakeris, and M. J. O'Loughlin, *Applied Physics Letters* **88**, 052110 (2006).

[2] K. Danno, D. Nakamura, and T. Kimoto, *Applied Physics Letters* **90**, 202109 (2007).

[3] J. A. Weil and J. R. Bolton, *Electron Paramagnetic Resonance*, John Wiley & Sons, Inc., 2007.

[4] P. Carlsson, N. Son, F. Beyer, H. Pedersen, J. Isoya, N. Morishita, T. Ohshima, and E. Janzén, *Physica Status Solidi - Rapid Research Letters* **3**, 121 (2009).

[5] K. Danno and T. Kimoto, *Journal of Applied Physics* **100**, 113728 (2006).

[6] L. Storasta, J. P. Bergman, E. Janzén, A. Henry, and J. Lu, *Journal of Applied Physics* **96**, 4909 (2004).

[7] T. Kimoto, S. Nakazawa, K. Hashimoto, and H. Matsunami, *Applied Physics Letters* **79**, 2761 (2001).

[8] T. Dalibor, G. Pensl, H. Matsunami, T. Kimoto, W. J. Choyke, A. Schöner, and N. Nordell, *Physica Status Solidi (A)* **162**, 199 (1997).

[9] C. Hemmingsson, N. T. Son, O. Kordina, J. P. Bergman, E. Janzén, J. L. Lindström, S. Savage, and N. Nordell, *Journal of Applied Physics* **81**, 6155 (1997).

[10] C. G. Hemmingsson, N. T. Son, A. Ellison, J. Zhang, and E. Janzén, *Physical Review B* **58**, R10119 (1998).

[11] T. Kimoto, T. Yamamoto, Z. Y. Chen, H. Yano, and H. Matsunami, *Journal of Applied Physics* **89**, 6105 (2001).

[12] S. Kagamihara, H. Matsuura, T. Hatakeyama, T. Watanabe, M. Kushibe, T. Shinohe, and K. Arai, *Journal of Applied Physics* **96**, 5601 (2004).

[13] H. Kaneko and T. Kimoto, *Applied Physics Letters* **98**, 262106 (2011).

[14] A. Zywietz, J. Furthmller, and F. Bechstedt, *Physical Review B* **59**, 15166 (1999).

[15] L. Torpo and M. Marlo, *Journal of Physics: Condensed Matter* **13**, 6203 (2001).

[16] M. Bockstedte, A. Mattausch, and O. Pankratov, *Physical Review B* **69**, 235202 (2004).

[17] T. Hornos, A. Gali, and B. G. Svensson, *Materials Science Forum* **679-680**, 261 (2011).

[18] N. T. Son, X. T. Trinh, L. S. Løvlie, B. G. Svensson, K. Kawahara, J. Suda, T. Kimoto, T. Umeda, J. Isoya, T. Makino, T. Ohshima, and E. Janzén, *Physical Review Letters* **109**, 187603 (2012).

[19] S. Sasaki, K. Kawahara, G. Feng, G. Alfieri, and T. Kimoto, *Journal of Applied Physics* **109**, 013705 (2011).

Chapter 7

Origin of Deep Levels Generated by Thermal Oxidation

7.1 Introduction

As discussed in Chapters 4 and 5, there are two effective methods to reduce the $Z_{1/2}$ center, (i) C^+ implantation followed by Ar annealing [1] and (ii) thermal oxidation [2]. In both, excess carbon atoms induced by C^+ implantation/oxidation diffuse into the deeper region of an SiC epilayer during post-implantation annealing/oxidation and fill carbon vacancies (carbon vacancy (V_C)) [1, 2] (described in Chapter 5), which are the origin of the $Z_{1/2}$ center (described in Chapter 6).

In contrast, new deep levels, ON1 ($E_C - 0.84$ eV) and ON2 ($E_C - 1.1$ eV) centers in n-type 4H-SiC, HK0 ($E_V + 0.79$ eV) and HK2 ($E_V + 0.98$ eV) centers in p-type samples, are observed after thermal oxidation or C^+ implantation, which are probably related to the interstitials diffusing from the SiO_2/SiC interface (oxidation) or from the implanted region (C^+ implantation) [2] (described in Chapter 5). Although the effect of the ON1, ON2, and HK0 centers on carrier lifetimes is negligibly small compared with that of the $Z_{1/2}$ center, these centers could affect the lifetime when the $Z_{1/2}$ center is eliminated. In this study, the author investigates the deep levels generated by thermal oxidation, comparing with those by C^+ or Si^+ implantation, electron irradiation, and N_2O (or NO) oxidation, and discusses the origin of these traps.

7.2 Deep Levels in n-type Epilayers

7.2.1 Experiments

The starting materials were n-type (N_d: 10^{15}–10^{16} cm^{-3}) 4H-SiC (0001) epilayers (thickness: 10-100 μm). The first set of samples was oxidized at 1150–1400°C for 1.3–16.5 h, whereas the second set of samples was implanted with 10–50 keV carbon (or 25–110 keV silicon)

ions with a total dose of 1.4×10^{13} cm^{-2} or 1.4×10^{14} cm^{-2} (corresponding implanted atom concentration $N_{\rm I}$: 1×10^{18} cm^{-3} or 1×10^{19} cm^{-3}), forming a 140-nm-box profile. The C^+-implanted (or Si^+-implanted) samples were annealed in Ar ambient at 1000–1800°C for 20 min. After the annealing, about (0.3–1.0)-μm-thick layers from the surface were etched off by mechanical polishing or reactive ion etching (RIE) under a moderate condition (CF_4: 5 sccm, O_2: 10 sccm, rf power: 50 W, pressure: 95 Pa, etching speed: 7 nm/min). The author confirmed that additional deep levels were not generated during the RIE nor polishing. The third set of the samples was oxidized in N_2O or NO ambient (10% diluted in N_2) at 1200–1300°C for 28 min–1.3 h. The depth profiles of trap concentrations up to 10 μm were measured by changing the reverse bias voltage up to 100 V in the DLTS measurements. To monitor deeper regions (over 10 μm), the samples were mechanically polished from the surfaces, and the DLTS measurements were repeated.

7.2.2 Deep Levels Generated by O_2 Oxidation

Fig. 7.1 shows the DLTS spectra of an as-grown sample and after thermal oxidation at 1300°C for 1.3 h. The dominant deep levels in as-grown samples, $Z_{1/2}$ ($E_{\rm C} - 0.67$ eV) [3] and $EH_{6/7}$ ($E_{\rm C} - 1.5$ eV) [4] centers, disappeared after oxidation, while ON1 ($E_{\rm C} - 0.84$ eV) and ON2 ($E_{\rm C} - 1.1$ eV) centers were generated. As discussed in Chapter 6, the reduction of the $Z_{1/2}$ and $EH_{6/7}$ centers should be caused by occupation of $V_{\rm C}$ by interstitials diffusing from the SiO_2/SiC interface during oxidation, whereas the generated ON1 and ON2 centers will contain the diffusing interstitials. Note that the ON2 center showed very similar behaviors with the ON1 center in all samples (but lower concentration).

Fig. 7.2 (a) shows the depth profiles of the ON1 center after oxidation at various temperatures for 1.3 h. When oxidation temperature was elevated, the ON1 concentration became higher and the ON1 center distributed to the deeper region, which is consistent with a distribution of the interstitials diffusing from the SiO_2/SiC interface. The distribution of interstitials after oxidation was calculated by solving the Eqs. (5.1)–(5.7). For the calculation of the ON1 distributions, the author used a simple model that defects (interstitials) diffuse from the SiO_2/SiC interface into the SiC bulk during oxidation without any recombination phenomena ($\gamma = 0$). Fitting parameters obtained from the temperature dependence of the ON1 distribution (Fig. 7.2 (a)) are summarized in Table 7.1. Although these parameters can be referred only as a guide due to the simplification of the calculation model, the relatively low $E_{\rm aD}$ (0.5 eV) is comparable to the carbon interstitial ($C_{\rm I}$) (theoretical value: 0.5–0.74 eV for $C_{\rm I}$, 1.4–1.5 eV for silicon interstitial ($Si_{\rm I}$) [5, 6]). By using these parameters shown in Table 7.1, the dependence of the ON1 distribution on oxidation time can be predicted. Fig. 7.2 (b) shows the depth profiles of the ON1 center after oxidation at 1300°C for 28 min–15.9 h. Longer oxidation resulted in deeper ON1 distribution. Because the experimental data (symbols) well agreed with the calculation (lines), the origin of the ON1 center should contain (carbon) interstitials diffusing from the SiO_2/SiC interface

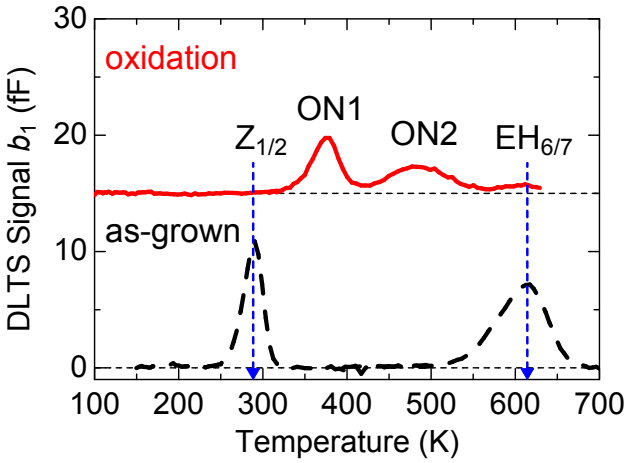

Figure 7.1: DLTS spectra for as-grown n-type 4H-SiC before (dashed line) and after (solid line) thermal oxidation at 1300°C for 1.3 h. The base line for DLTS spectrum of the oxidized sample is shifted for clarity.

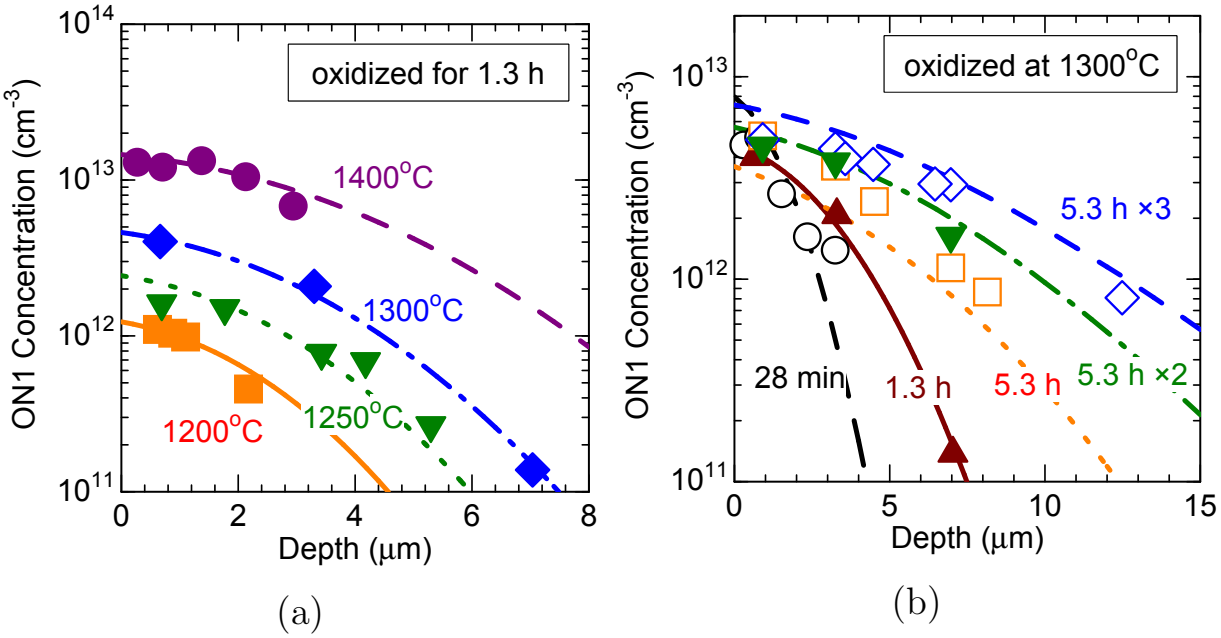

Figure 7.2: Depth profiles of the ON1 center after oxidation (a) at various temperatures for 1.3 h, and (b) at 1300°C for various periods. Each symbol indicates experimental data and each line denotes the calculated n_{I} distribution obtained from Eqs. (5.1)–(5.7).

Table 7.1: Parameter values obtained by fitting of the interstitial profiles calculated based on the diffusion equations (Eqs. (5.1)–(5.7)) to experimental ON1 profiles shown in Fig. 7.2. The top row indicates the "X" in the first column. γ was assumed to be zero.

	D	F_0
Activation energy E_{aX}	0.50 eV	3.1 eV
Coefficient X_∞	2.8×10^{-10} cm^{2}s^{-1}	1.7×10^{18} cm^{-2}s$^{\alpha-1}$

during oxidation.

Fig. 7.3 shows depth profiles of the ON1 and ON2 centers in samples after oxidation at 1300°C for 15.9 h and after the oxidation followed by Ar annealing at 1500°C for 2 h. The ON1 and ON2 centers increased after the subsequent annealing in the whole range of the depth, which could result from defect conversion from a C_I-related defect generated by the oxidation to the ON1 and ON2 centers rather than further diffusion of the ON1 and ON2 centers by the subsequent annealing. If further interstitial diffusion occurs without the supply of additional interstitials from the surface, the interstitial concentration should decrease near the interface while it increases in the deeper region. It is surprising that the ON1 and ON2 centers survive after Ar annealing at a very high temperature (1500–1700°C), considering that these are interstitial-related defects. Therefore, the origin of the ON1 and ON2 centers is a complex defect rather than a single interstitial such as C_I.

7.2.3 Deep Levels Generated by C^+ or Si^+ Implantation

The ON1 and ON2 centers were generated also by C^+ or Si^+ implantation followed by Ar annealing at temperatures over $\sim$ 1400°C. Fig. 7.4 shows DLTS spectra of n-type 4H-SiC before and after Si^+ implantation (dose: 1.4×10^{13} cm^{-2}) followed by Ar annealing at 1700°C for 20 min (a similar spectrum was obtained also after C^+ implantation)[1]. These DLTS spectra were very similar to those for oxidized samples (Fig. 7.1); the $Z_{1/2}$ and $EH_{6/7}$ centers disappeared after C^+ or Si^+ implantation, while the ON1 and ON2 centers appeared. Note that the ON1 and ON2 centers are thermally stable defects, keeping a similar concentration even after Ar annealing at 1700°C.

Fig. 7.5 shows the depth profiles of implanted atoms and C_I generated by the collision of implanted ions, just after implantation, which were simulated using a SRIM code [7]; SRIM is an acronym for stopping and range of ions in matter. The C_I concentration in the Si^+-implanted samples is higher than that in the C^+-implanted samples due to the higher energy of Si^+ implantation (10–50 keV for C^+ implantation and 25–110 keV for Si^+ implantation) and larger mass of Si^+. The distribution of V_C/silicon vacancy (V_{Si}) is almost the same as that of C_I/Si_I in the simulation (the difference is within 1 nm, not shown), which means that carbon atoms/silicon atoms are not knocked far away from their original positions by collisions with implanted atoms. In contrast, the distribution of Si_I and V_{Si} shows a little lower concentration ($\sim$ 70%) than that of C_I (and V_C) because of the higher displacement energy of 35 eV for a silicon atom compared with 21 eV for a carbon atom [8]. Note that a large amount of the interstitials and vacancies generated by ion bombardment should recombine during the subsequent Ar annealing because these are located closely to each

[1]Note that comparing the deep levels observed in this C^+- or Si^+-implanted sample (N_I: 1×10^{18} cm^{-3}, Fig. 7.4) with those in the N^+- or P^+-implanted sample with an implant dose of 8×10^{13} cm^{-2} (N_I: 1×10^{18} cm^{-3}, Fig. 3.6 in Chapter 3) is difficult because the implanted region in the C^+- or Si^+-implanted sample was removed after Ar annealing whereas that in the N^+- or P^+-implanted sample was not.

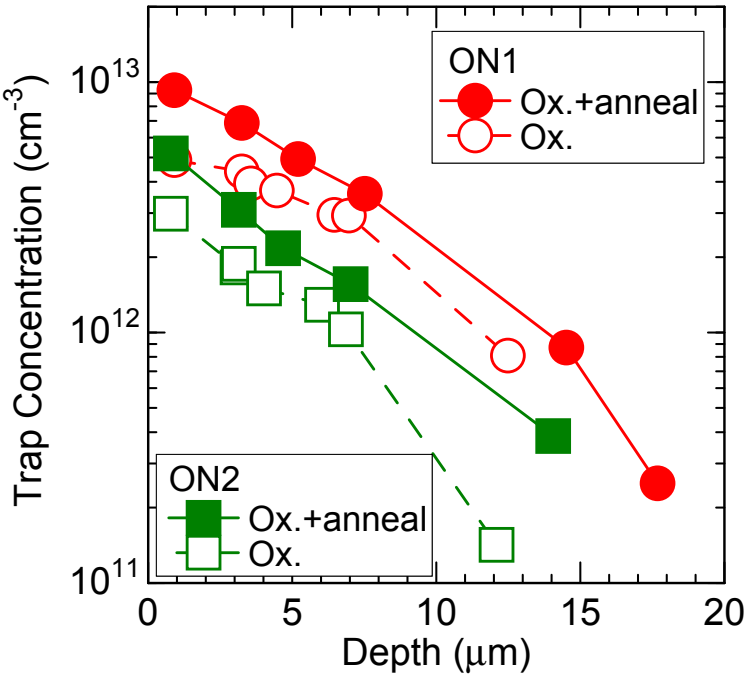

Figure 7.3: Depth profiles of the ON1 (circles) and ON2 (squares) centers in 4H-SiC after oxidation at 1300°C for 15.9 h (open symbols) and after the oxidation followed by Ar annealing at 1500°C for 2 h (filled symbols).

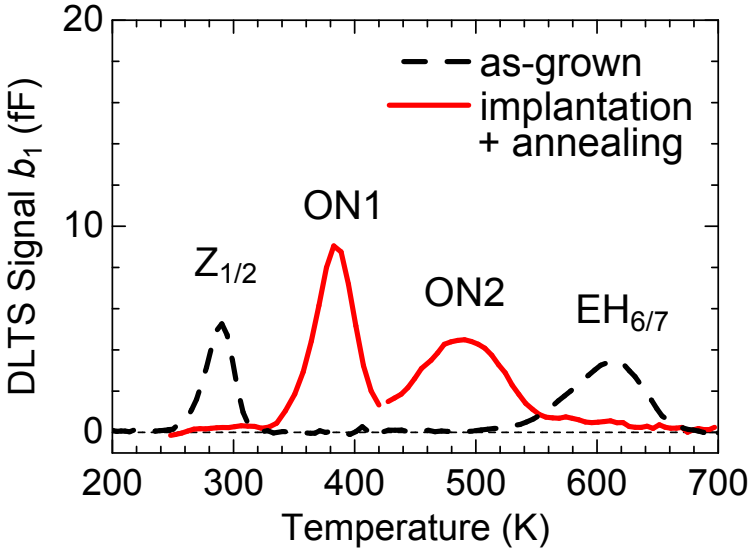

Figure 7.4: DLTS spectra of n-type 4H-SiC before (dashed line) and after (solid line) Si^+ implantation (dose: 1.4×10^{13} cm^{-2}) followed by Ar annealing at 1700°C for 20 min.

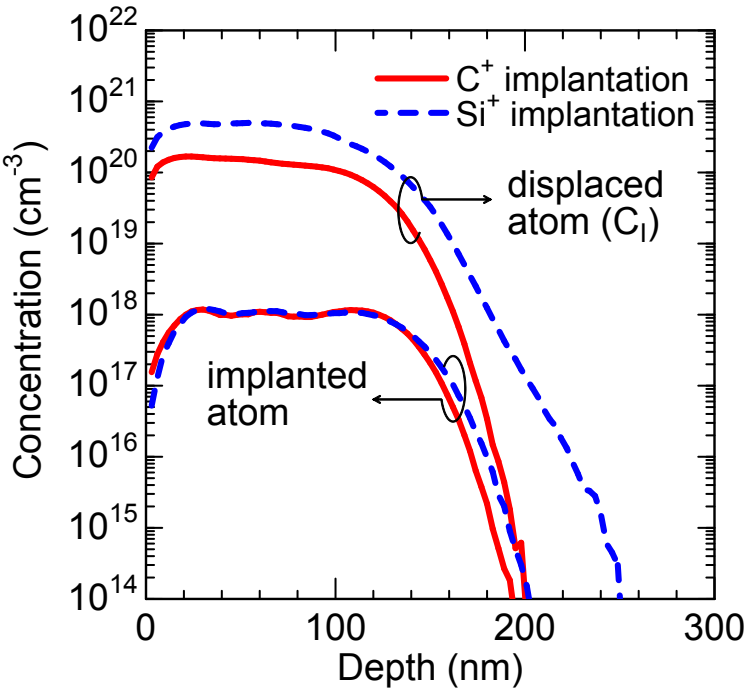

Figure 7.5: Depth profiles of implanted atoms and carbon interstitials after C^+ and Si^+ implantation (total dose: 1.4×10^{13} cm^{-2}) simulated by SRIM code.

other after implantation.

Fig. 7.6 shows the depth profiles of the ON1 center after C^+ and Si^+ implantation (dose: 1.4×10^{13} cm^{-2} and 1.4×10^{14} cm^{-2}) followed by Ar annealing (1700°C, 20 min). Si^+ implantation or higher dose implantation (which leads a higher density of defects near the surface as shown in Fig. 7.5) led to a higher concentration of the ON1 center, suggesting that defects generated by ion bombardment near the surface diffused to the SiC bulk and formed the ON1 center during Ar annealing.

7.2.4 Enhancement of Deep Level Generation by N_2O Oxidation

The author found that oxidation in N_2O ambient enhances the generation of the ON1 and ON2 centers compared with O_2 oxidation. Fig. 7.7 shows the depth profiles of the ON1 center in samples after oxidation at 1300°C for 28 min in O_2, in NO (diluted to 10% by N_2), and in N_2O (diluted to 10% by N_2) ambient. Although the oxidation rate in N_2O ambient (∼5.5 nm/28 min) was much lower than that in O_2 (∼41 nm/28 min), the ON1 concentration after N_2O oxidation was more than twice as high as after O_2 oxidation. Oxidation in NO (oxidation rate: ∼2.0 nm/28 min) ambient also enhanced generation of the ON1 and ON2 centers. The ON1 concentration in the samples oxidized in NO ambient was slightly lower than that in N_2O, whereas the reduction of the $Z_{1/2}$ center (originating from V_C) in NO was slightly smaller than that in N_2O.

Fig. 7.8 shows the depth profiles of the ON1 center in samples after oxidation at 1200°C and 1300°C for 1 h in N_2O ambient, and after N_2O oxidation at 1300°C followed by Ar annealing at 1400 and 1600°C for 30 min. The ON1 concentration was higher after oxidation at higher temperatures and increased after subsequent Ar annealing over 1400°C, which is similar to the results obtained in the samples oxidized in O_2 ambient (Fig. 7.3). Note that the ON1 profile after N_2O oxidation followed by Ar annealing at 1600°C agreed with that at 1400°C, indicating that all C_I-related defects generated by the oxidation could be converted to the ON1 and ON2 centers at 1400°C.

The author speculates that NO molecules or N atoms give impacts on the ON1 and ON2 generation because of the two experimental results: (i) the reduction of the $Z_{1/2}$ center, a deep level originating from V_C, by the N_2O oxidation is smaller than that by the O_2 oxidation (about a half, not shown), indicating that single C interstitials diffusing during N_2O oxidation were less than that during O_2 oxidation, (ii) the depth profiles of the ON1 and ON2 centers after oxidation in 10% O_2 ambient are almost the same as those in 100% O_2 ambient (not shown), indicating that the partial pressure of O_2 is not a major factor in the generation of the ON1 and ON2 centers.

In fact, it has been predicted by *ab initio* calculation that a carbon-split-interstitial $(C\text{-}C)_C$ approaching a nitrogen donor N_C can form $(N\text{-}C)_C$ with an activation energy of 2.0 eV and a final energy gain of 1.4 eV [9]. During N_2O oxidation, a high concentration of $(N\text{-}C)_C$ can be formed due to a high concentration of C [10, 11] and N [12] atoms near the SiO_2/SiC

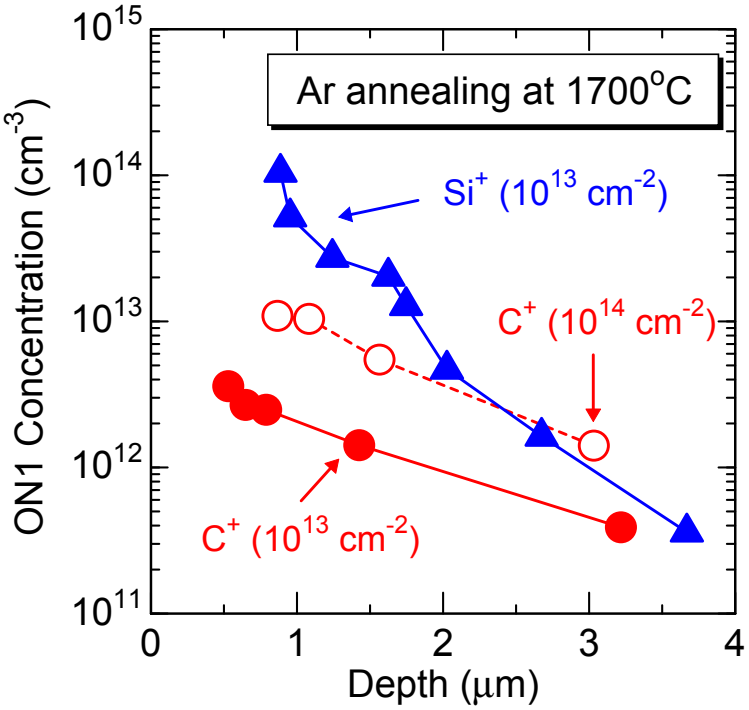

Figure 7.6: Depth profiles of the ON1 center after C^+ and Si^+ implantation (dose: 1.4×10^{13} cm^{-2} and 1.4×10^{14} cm^{-2}) followed by Ar annealing at 1700°C for 20 min.

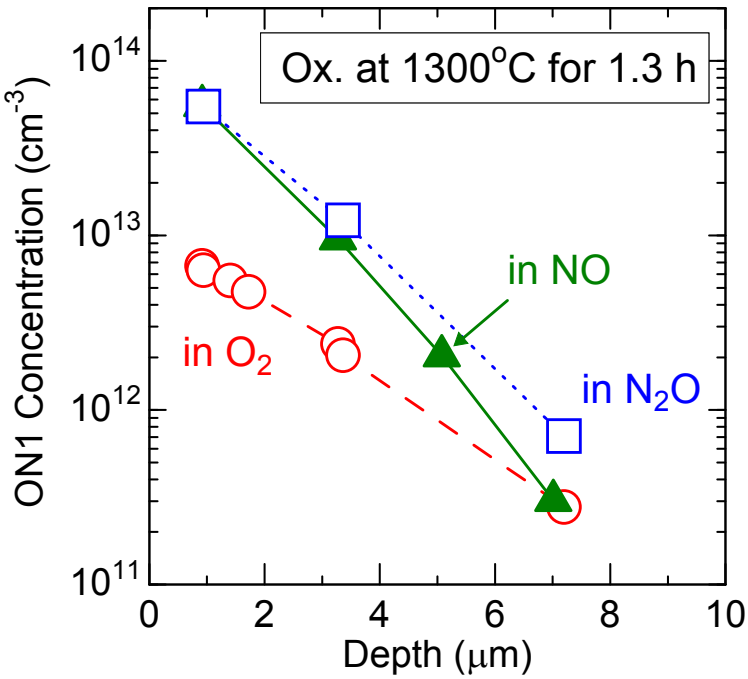

Figure 7.7: Depth profiles of the ON1 center in samples after oxidation at 1300°C for 1 h in O_2 ambient (circles), in NO (triangles), and in N_2O ambient (squares).

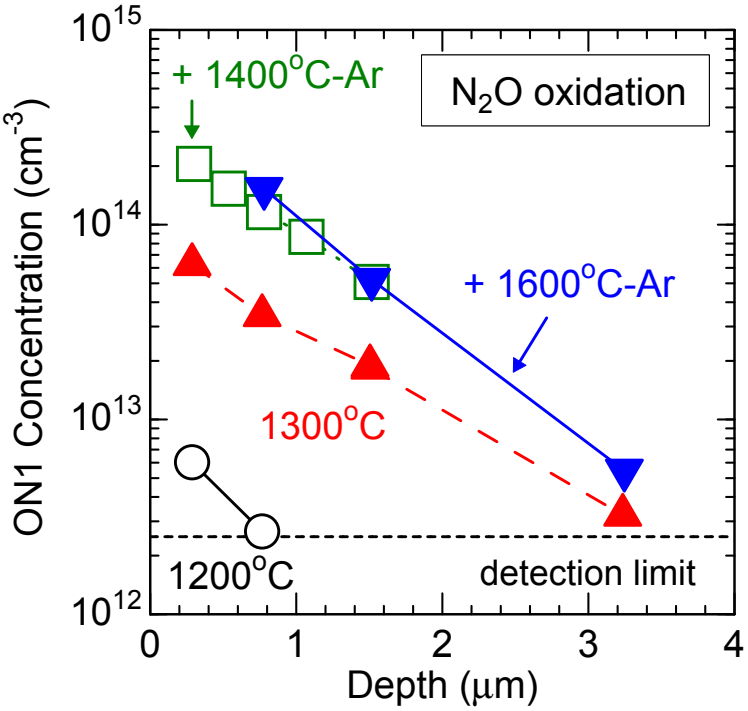

Figure 7.8: Depth profiles of the ON1 center in samples after oxidation at 1200°C and 1300°C for 1 h in N_2O ambient, and after N_2O oxidation at 1300°C followed by Ar annealing at 1400 and 1600°C for 30 min.

interface, whereas during O_2 oxidation $(N\text{-}C)_C$ is formed only when $(C\text{-}C)_C$ approaches N_C. Because the $(N\text{-}C)_C$ is a mobile defect (activation energy for moving to the next carbon cite is 2.5 eV) [9], $(N\text{-}C)_C$ could diffuse to a deeper region and form more thermally stable defects: the ON1 and ON2 centers.

7.2.5 Discussion

As shown in Fig. 7.3, the depth profiles of the ON1 and ON2 centers are always similar. Fig. 7.9 shows the relation between the ON1 concentration and ON2 concentration in all samples investigated in this study, which presents an one-to-one correspondence. Thus, the ON1 and ON2 centers could originate from the same defect in different charge states. Here, the author speculates that the ON1 and ON2 peaks (Fig. 7.1) contains two peaks in each, because (i) the ON2 peak is too broad as a single peak and (ii) the ON2 concentration is always about a half of the ON1 concentration; the two peaks in the ON1 peak completely overlap whereas those in the ON2 peak are slightly separated (the two peaks might correspond to the two kinds of site in 4H-SiC: cubic and hexagonal sites).

7.3 Deep Levels in *p*-type Epilayers

7.3.1 Experiments

The starting materials were Al-doped p-type 4H-SiC (0001) epilayers (12-μm thickness with acceptor concentration (N_a) of 7×10^{15} cm^{-3}, or 120-μm thickness with N_a of 7×10^{14} cm^{-3}). (i) The first set of samples was oxidized at different temperatures (1150, 1200, 1300, and 1400°C) for various periods (1.3–16.5 h) in 100% oxygen ambient, whereas (ii) the second set of samples was irradiated with 150 keV electrons (fluence: 1.0×10^{17} cm^{-2}). (iii) The third set of samples was implanted with 10–50 keV carbon (or 25–110 keV silicon) ions with a total dose of 1.4×10^{13} cm^{-2} or 1.4×10^{14} cm^{-2} (implanted atom concentration: 1×10^{18} cm^{-3} or 1×10^{19} cm^{-3}), forming a 140-nm box profile. The C^+-implanted (or Si^+-implanted) samples were annealed in Ar ambient at various temperatures (1000, 1300, 1440, 1500, 1700, and 1800°C) for 20 min.

7.3.2 Deep Levels Generated by O_2 Oxidation

Fig. 7.10 shows the DLTS spectra obtained from a depth of $\sim$ 4 μm for p-type 4H-SiC before and after thermal oxidation at 1300°C for 15.9 h. In the as-grown sample, GP1 ($E_V + 0.46$ eV) and D ($E_V + 0.63$ eV) centers were observed. The GP1 center is located at a deeper level than the boron acceptor (shallow boron level, $E_V + (0.26\text{–}0.39)$ eV [13, 14]). In contrast, the D center is a well-known deep level in p-type 4H-SiC ($E_V + (0.54\text{–}0.73)$ eV) [13–16], which has been attributed to a boron atom in a silicon site with an adjacent carbon vacancy (B_{Si}-V_C) [14, 17, 18]. After oxidation, the D center disappeared whereas the HK0

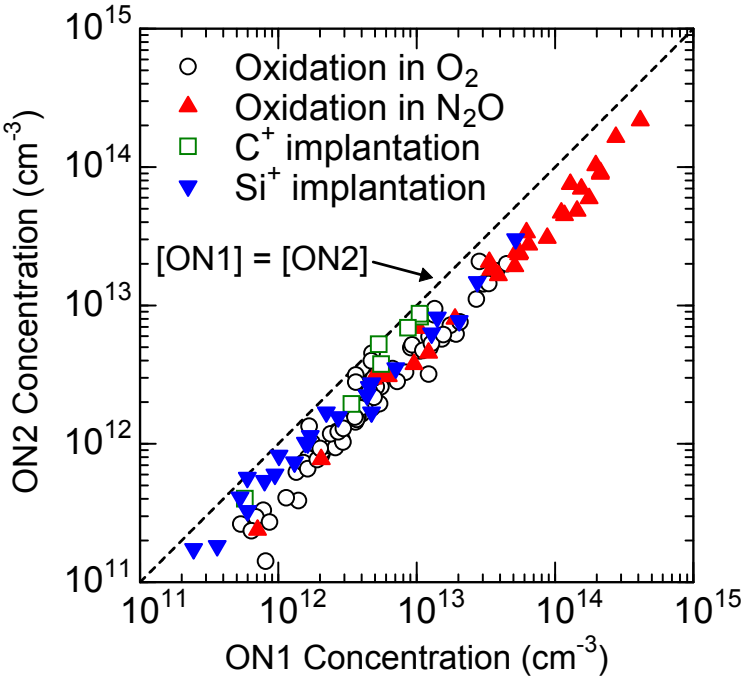

Figure 7.9: Relation between the ON1 concentration and ON2 concentration in O_2-oxidized (circles), N_2O-oxidized (triangles), C^+-implanted (squares), and Si^+-implanted (reverse triangles) 4H-SiC epilayers.

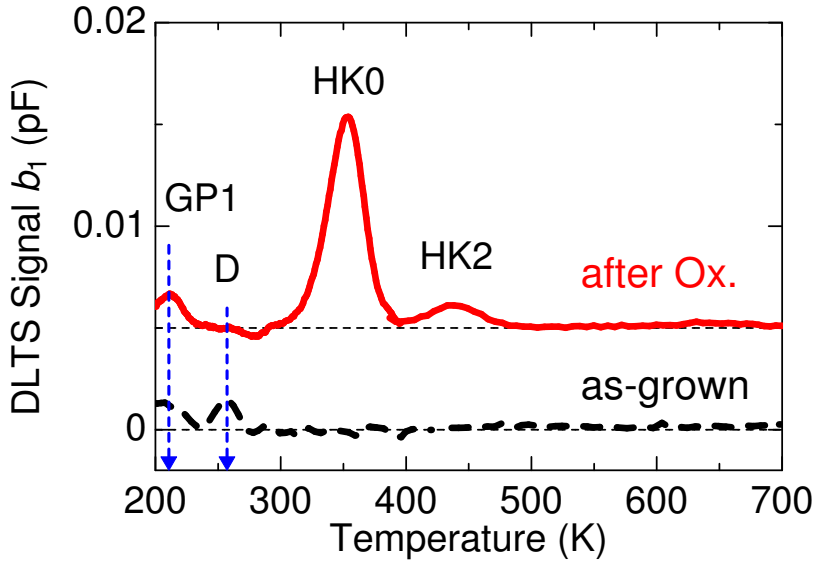

Figure 7.10: DLTS spectra for the *p*-type 4H-SiC (dashed line) before and after thermal oxidation at 1300°C for 15.9 h (solid line).

($E_V + 0.79$ eV) and HK2 ($E_V + 0.98$ eV) centers appeared. The HK0 and HK2 centers are both observed in RIE-etched samples [16] and electron-irradiated samples [16] after Ar annealing (950–1000°C), whereas the HK2 center is detected occasionally in as-grown samples [16]. Because these two centers are observed after thermal oxidation, the two deep levels may be related to the C (or Si) interstitials diffusing from the SiO_2/SiC interface during the oxidation.

7.3.2.1 Comparison between Experimental Defect Profiles and Calculated Interstitial Profiles after Thermal Oxidation

Fig. 7.11 shows depth profiles of the HK0 center after oxidation at various temperatures for 1.3 h. When oxidation is conducted at higher temperatures, the defect concentration is higher and the HK0 center is distributed to a deeper region, which is consistent with an expected distribution of interstitials after diffusion from the SiO_2/SiC interface. The distribution of interstitials after oxidation was calculated in the same manner mentioned in Section 7.2.2. Fitting parameters used for the HK0 distributions are shown in Table 7.2.

With these parameters, the dependence of the HK0 distribution on oxidation time can also be fitted. Fig. 7.12 shows the depth profiles of the HK0 center after oxidation at 1300°C for 1.3–15.9 h. Longer oxidation leads to a deeper HK0 distribution. Here, 5.3 h × 3 in Fig. 7.12 (squares and dotted line) indicates that the oxides were removed by hydrofluoric acid treatment after every 5.3 h of oxidation, which enhances the oxidation speed compared with continuous oxidation because, as mentioned above, the oxidation rate slows down with time. Using the same parameters listed in Table 7.2, the calculated results can reproduce the enhancement in HK0 generation by repeated oxidation and oxide removal. Because the calculation (lines) almost fit the experimental data (symbols), the origin of the HK0 center must contain interstitials diffusing from the SiO_2/SiC interface during oxidation.

Here, the activation energy of the diffusion coefficient (E_{aD}) listed in Table 7.2 is discussed. The diffusivity of mobile interstitials (Si_I and C_I are considered) depends on the charge state. Fig. 7.13 represents temperature dependence of the Fermi level in the p-type samples used in this study. Because in this study the oxidation temperature is in the range of 1150–1400°C, the Fermi level is located at 1.2–1.4 eV from the valence band edge during the oxidation. Fig. 7.14 shows energy levels of Si_I and C_I obtained by *ab initio* calculation [19, 20]. When the Fermi level is at $E_V + (1.2–1.4)$ eV, the charge state of Si_I can be neutral (Si_I^0), whereas that of C_I can be neutral (C_I^0) or double positive (C_I^{2+}, only in the case of the C_I level reported by Gali et al. [20]). The activation energy for Si_I^0 diffusion (E_{aD} of Si_I^0) has been theoretically estimated to be 1.4–1.53 eV [5, 6], whereas E_{aD} of C_I^0 is 0.5–0.74 eV [5, 6] and C_I^{2+} is 1.4 eV [5]. These values are much lower than 3.6 eV obtained in this study as E_{aD} (Table 7.2), which could be attributed to the simplification of the diffusion model ($\gamma = 0$, no aggregation of interstitials during oxidation).

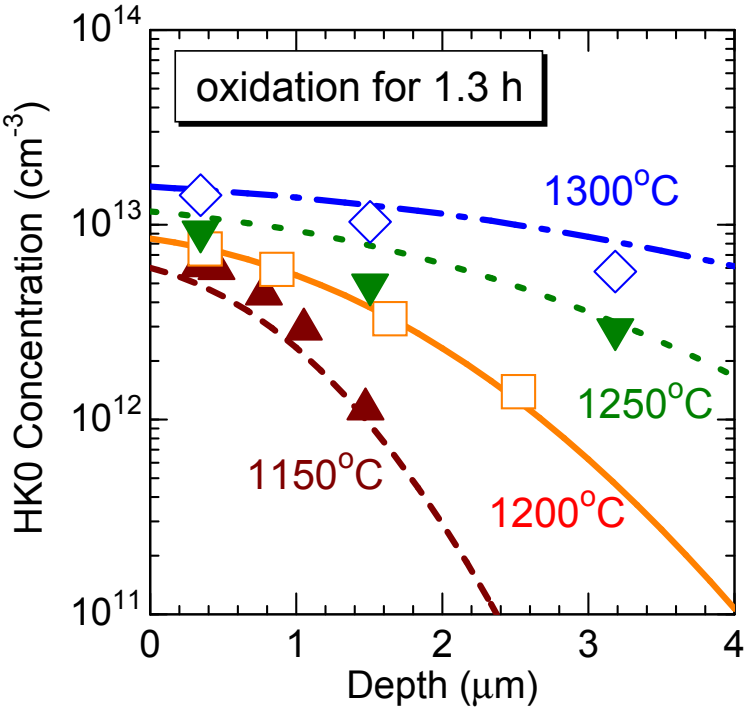

Figure 7.11: Depth profiles of HK0 center after oxidation at various temperatures for 1.3 h. Each symbol indicates experimental data and each line indicates the calculated n_{I} distribution obtained from Eqs. (5.1)–(5.7).

Table 7.2: Parameter values obtained by fitting of the interstitial profiles calculated based on the diffusion equations (Eqs. (5.1)–(5.7)) to experimental HK0 profiles shown in Fig. 7.11. The top row indicates the "X" in the first column. γ was assumed to be zero.

	D	F_0
Activation energy E_{aX}	3.6 eV	2.9 eV
Coefficient X_∞	1.4 $\mathrm{cm^2 s^{-1}}$	1.4×10^{18} $\mathrm{cm^{-2} s^{\alpha-1}}$

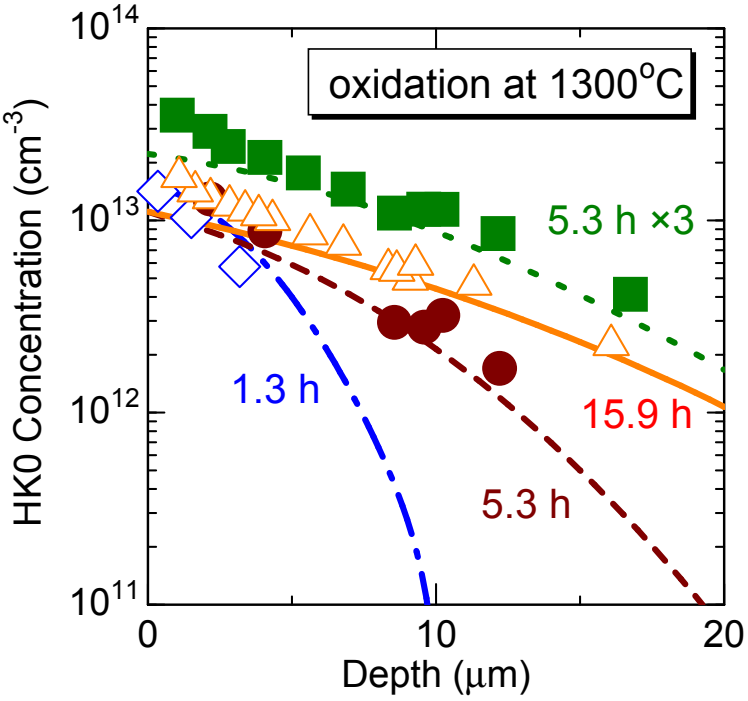

Figure 7.12: Depth profiles of the HK0 center after oxidation at 1300°C for 1.3–15.9 h. Each symbol indicates experimental data and each line indicates the calculated n_{I} distribution obtained from Eqs. (5.1)–(5.7).

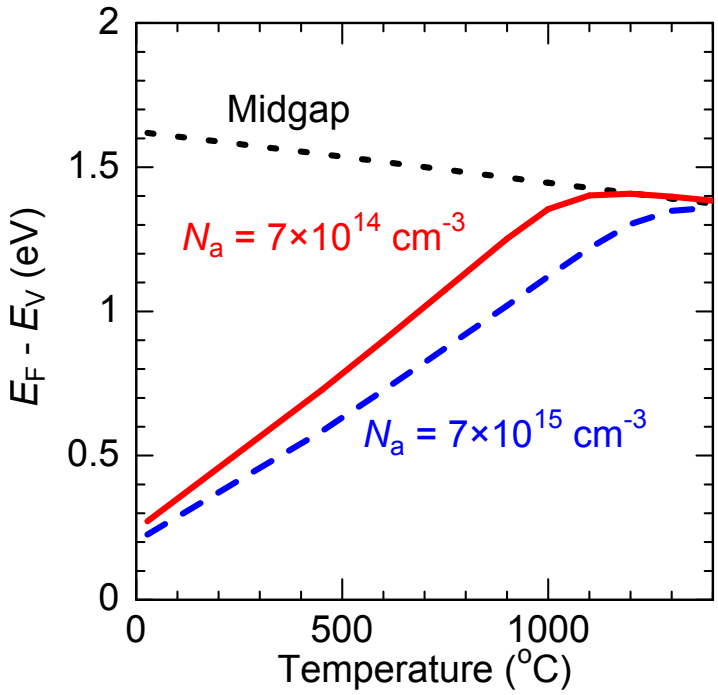

Figure 7.13: Temperature dependence of the Fermi level in p-type 4H-SiC with different acceptor concentration.

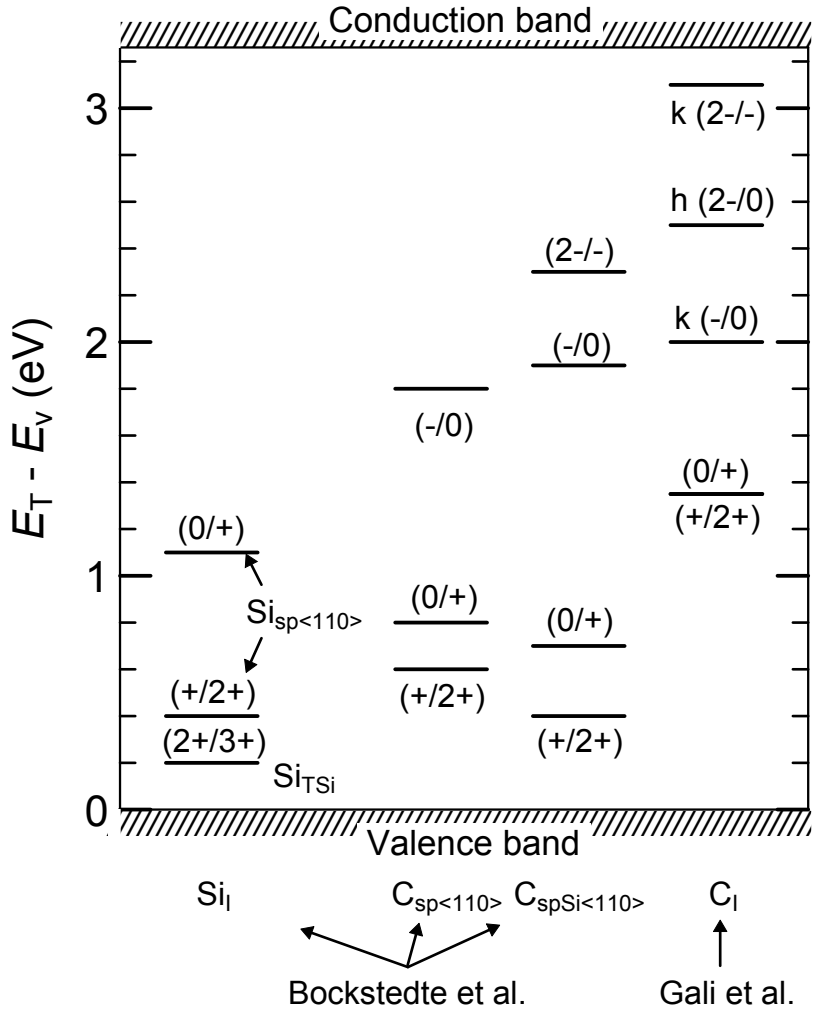

Figure 7.14: Energy levels of silicon interstitial (Si_I) and carbon interstitial (C_I) obtained by *ab initio* calculation [19, 20].

7.3.2.2 Specific Behaviors of The HK0 Center during Oxidation and Subsequent Ar Annealing

The author found that neither generation nor diffusion of the HK0 center itself occurs by Ar annealing at temperatures lower than 1300°C. Fig. 7.15 shows depth profiles of the HK0 center after oxidation at 1150°C for 1.3 h, and after oxidation followed by Ar annealing at 1150°C for 4.3 h. The HK0 distribution did not change by the subsequent annealing at 1150°C in Ar ambient, which indicates that the HK0 center does not diffuse by Ar annealing at 1150°C. That HK0 diffuses during oxidation and not during Ar annealing can be explained as follows: during oxidation, interstitials generated at the SiO_2/SiC interface diffuse to the SiC bulk and form more stable defects that is the origin of the HK0 center, resulting in termination of the diffusion. Therefore, rather than a single interstitial, the origin of the HK0 center could be a complex such as an interstitial cluster or an interstitial-impurity complex. From *ab initio* calculations, the formation of a carbon di-interstitial ($(C_I)_2$) seems to be energetically favorable for a pair of carbon interstitials [5, 20–22], and that the $(C_I)_2$ defect forms energy levels at 0.1–1.2 eV above the valence band edge in the lower half of the bandgap of 4H-SiC [5, 20, 23], which does not conflict with the energy level of the HK0 ($E_V + 0.79$ eV) center detected by DLTS. The energy levels of the carbon di-interstitial ($(C_I)_2$) obtained by *ab initio* calculation [5, 20, 23] are shown in Fig. 7.16, which indicates that the $(C_I)_2$ is a candidate as the origin of the HK0 center.

The HK0 center is not stable at temperatures higher than 1400°C. Fig. 7.17 shows the DLTS spectra of the sample after thermal oxidation at 1300°C for 15.9 h, and after the oxidation followed by Ar annealing at 1500°C for 2 h. All deep levels including the HK0 center disappeared after the subsequent Ar annealing at 1500°C (the HK0 center disappears at temperatures over 1400°C as described in Chapter 4). The dotted line in Fig. 7.17 shows the DLTS spectrum of the sample after thermal oxidation at 1400°C for 16.5 h. In contrast with the oxidation at 1300°C, the HK0 and HK2 centers were not generated by the high-temperature oxidation at 1400°C. If the origin of the HK0 center is assumed to be an interstitial complex, as previously mentioned, these results (in Fig. 7.17) indicate that at temperatures over 1400°C excess interstitial atoms exist as (i) single interstitials (the origin of HK0 center is dissociated and diffuses at the high temperature), or (ii) more thermally stable defects possessing higher binding energy than the origin of the HK0 center.

In the last decade, interstitial complexes in SiC have extensively been investigated by photoluminescence (PL) [24–29], and these results have been compared with *ab initio* calculations [21, 25, 28, 30]. Several kinds of C-related defects have been suggested to exist in electron-irradiated 4H-SiC and 6H-SiC [24–30]. The identified PL signals are: T1 (a center), T2/T3 (b center), and T4 (c center) centers as $(C_2)_{Si}$ [26–29]; U center (471.8 nm zero phonon line (ZPL) in 4H-SiC) as $(C_3)_{Si}$ [25, 26, 29]; G center (493.5 nm ZPL in 4H-SiC) as $((C_2)_{Si})_2$ [26, 29]; Z center (maybe 599.3 nm ZPL in 4H-SiC) as $(C_I)_2$ [25, 26]. The dissociation energy was calculated to be about 5.5 eV for $(C_I)_2$ [5, 20, 21], 3.6 eV for $(C_2)_{Si}$ [21],

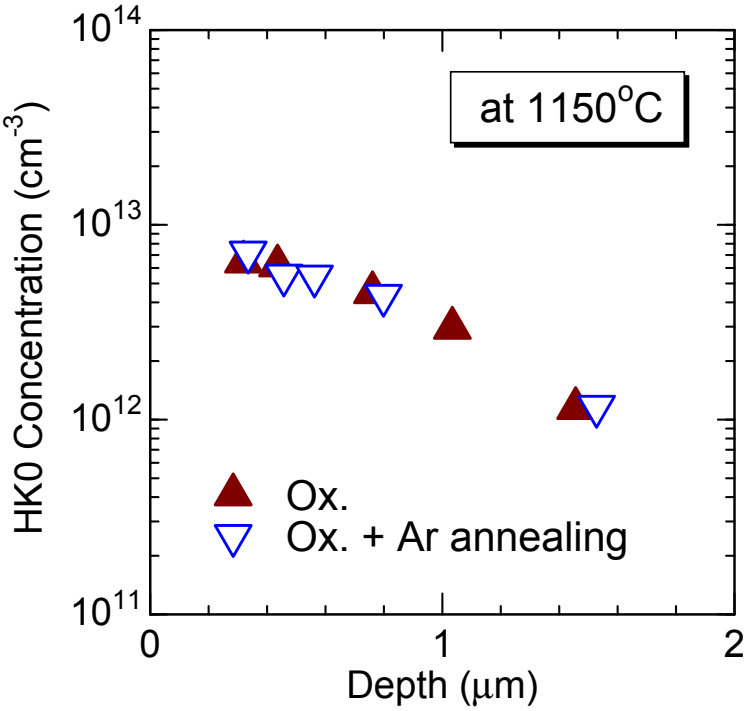

Figure 7.15: Depth profiles of the HK0 center after oxidation at 1150°C for 1.3 h (filled triangles), and after the oxidation followed by Ar annealing at 1150°C for 4.3 h (reverse triangles).

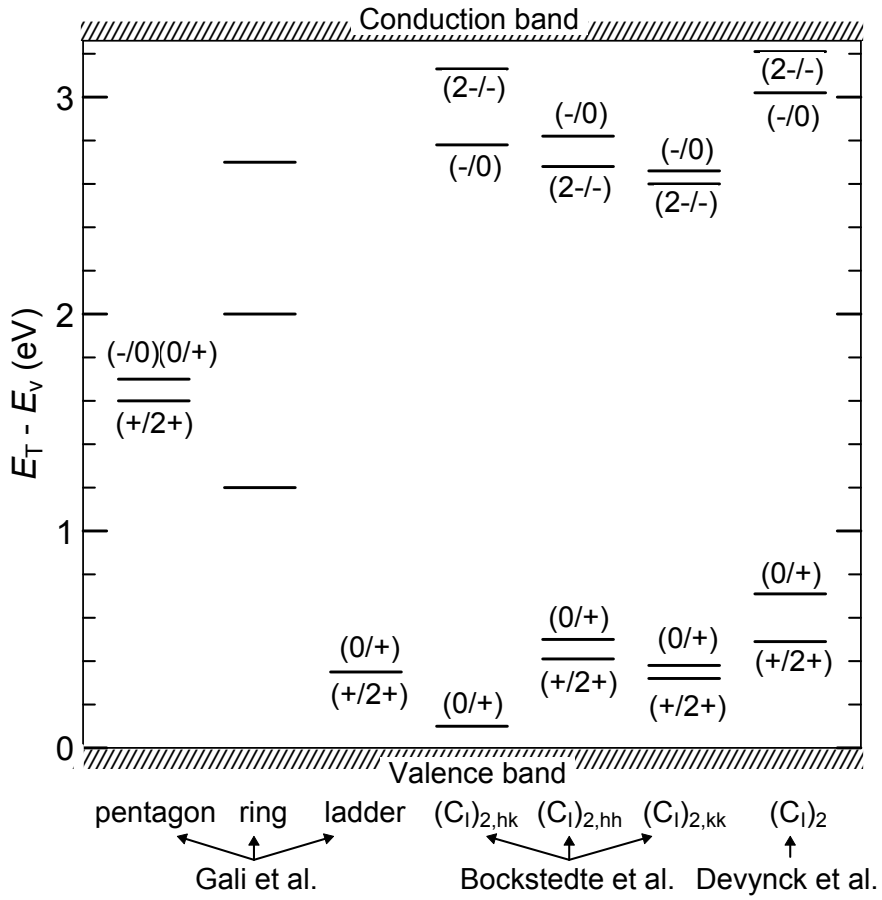

Figure 7.16: Energy levels of carbon di-interstitial $(C_I)_2$ obtained by *ab initio* calculation [5, 20, 23].

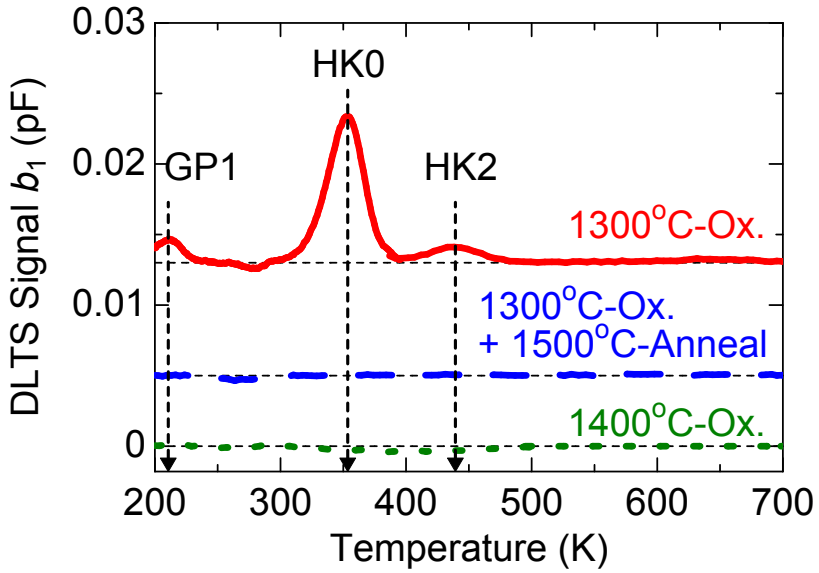

Figure 7.17: DLTS spectra of the *p*-type 4H-SiC after thermal oxidation at 1300°C for 15.9 h (solid line), and after the oxidation followed by Ar annealing at 1500°C for 2 h (dashed line). DLTS spectrum of the sample after thermal oxidation at 1400°C for 16.5 h is also shown as a dotted line.

5.8 eV for $(C_3)_{Si}$ [21], and 6.7 eV for $((C_2)_{Si})_2$ [21], which is consistent with relatively high thermal stability of the defect centers observed in PL [26]. Note that post-irradiation annealing behaviors of the U center (ZPL at 471.8 nm in 4H-SiC) and the G center (ZPL at 493.5 nm in 4H-SiC) are similar with that of the HK0 center detected by DLTS in this study. The U/G centers appear after annealing at 1100°C/950°C, remain at 1300°C/1200°C and disappear at 1400°C/1300°C (all annealing is 30-min long) [26], whereas the HK0 center appears after annealing at 950°C, remains at 1300°C, and disappears at 1400°C.

Therefore, the origin of the HK0 center could be $(C_I)_2$, $(C_3)_{Si}$, or $((C_2)_{Si})_2$, which is formed from single carbon interstitials generated and diffusing during oxidation at lower than 1300°C. $(C_3)_{Si}$ and $((C_2)_{Si})_2$ can be formed when the diffusing carbon atoms occupy silicon vacancies or displace silicon atoms.

7.3.3 Deep Levels Generated by Electron Irradiation

As described in the last section, the origin of the HK0 center could be carbon-related complexes. To obtain more insights of the origin, the author investigated p-type samples irradiated with 150 keV electrons (fluence: 1.0×10^{17} cm^{-2}), where displacement of only the carbon atoms occurs [31, 32]. Fig. 7.18 shows DLTS spectra of the samples after electron irradiation and after subsequent oxidation at 1150°C for 1.3 h. UK1 ($E_V + 0.35$ eV) [16], HS2 ($E_V + 0.63$ eV) [16, 31], UK2 ($E_V + 0.71$ eV) [16], and HK4 ($E_V + 1.4$ eV) [16] centers were detected after electron irradiation. The HS2 center has been reported to appear after electron irradiation with the energy of 116 keV–9 MeV [16, 31], whereas the UK1 and UK2 centers appear with 160 keV–400 keV electrons [16]. The HK4 center has also been observed in as-grown samples [16]. As evident in Fig. 7.18, after subsequent oxidation at 1150°C for 1.3 h, the HS2 and HK4 centers disappear, and the HK0 and HK2 centers emerge. The HK0 and HK2 centers cannot originate from a single interstitial because the HK0 and HK2 centers were not detected in as-irradiated samples but in samples after subsequent oxidation (or Ar annealing [16]).

Fig. 7.19 shows depth profiles of (a) UK1, HS2, and HK4 centers in the p-type 4H-SiC after electron irradiation, and (b) HK0 and HK2 centers after the irradiation followed by thermal oxidation at 1150°C for 1.3 h. The HK0 center after electron irradiation followed by thermal oxidation shows higher concentration and is distributed to a deeper region compared with the HK0 center after only thermal oxidation (Fig. 7.11), which means that irradiation-induced damage is the main cause of the HK0 generation in these samples. Fig. 7.20 shows depth profiles of the HK0 center in the samples after electron irradiation followed by thermal oxidation at different temperatures for 1.3 h. The HK0 distribution in the samples after electron irradiation followed by thermal oxidation is almost independent of oxidation temperature, which also means that the HK0 center generated by thermal oxidation is negligible compared with the HK0 generation caused by irradiation damage.

The other four deep levels, UK1, HS2, HK2, and HK4, show similar distribution to the

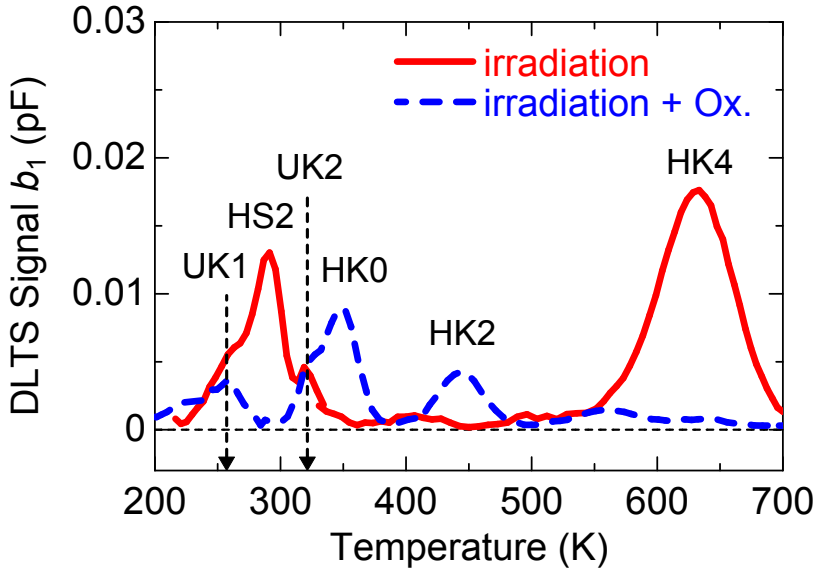

Figure 7.18: DLTS spectra of the p-type 4H-SiC irradiated with 150 keV electrons (solid line), and after electron irradiation followed by oxidation at 1150°C for 1.3 h (dashed line).

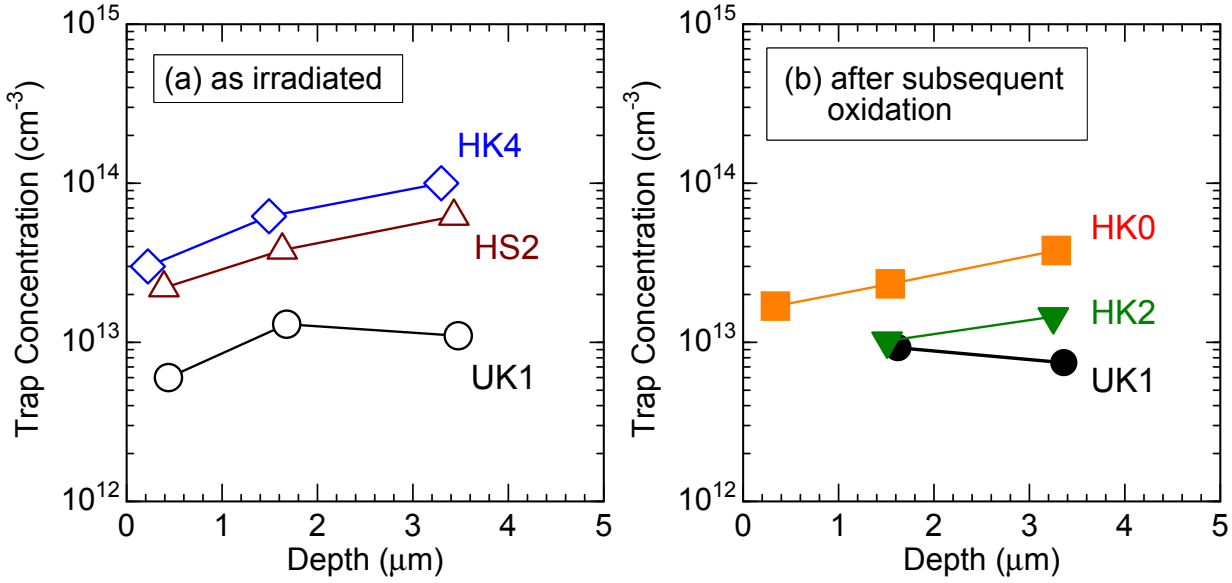

Figure 7.19: Depth profiles of (a) UK1 (circles), HS2 (triangles), and HK4 (rhombuses) centers in the p-type 4H-SiC after electron irradiation (150 keV, 1.0×10^{17} cm^{-2}), and (b) HK0 (squares) and HK2 (reverse triangles) centers after irradiation followed by thermal oxidation at 1150°C for 1.3 h.

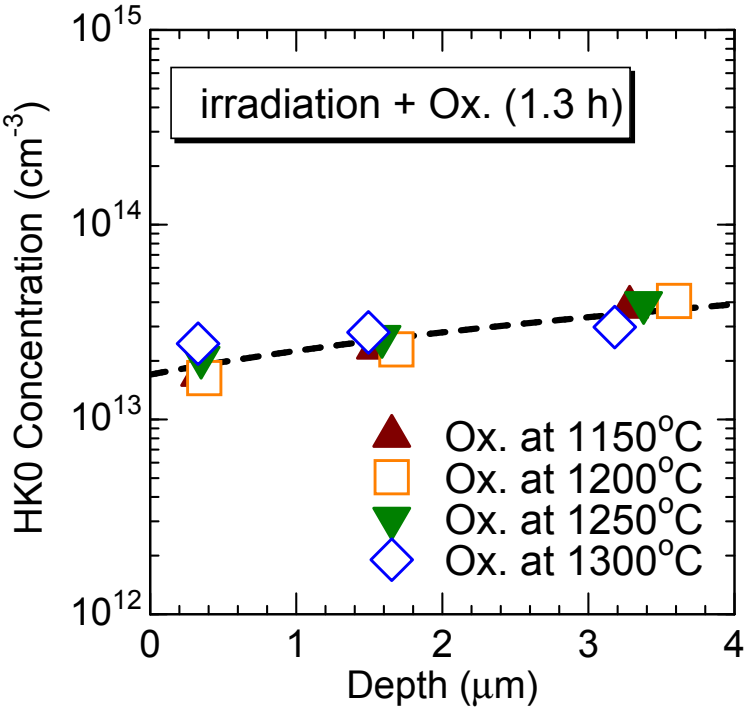

Figure 7.20: Depth profiles of the HK0 center in the *p*-type 4H-SiC after electron irradiation (150 keV, 1.0×10^{17} cm^{-2}) followed by thermal oxidation at different temperatures for 1.3 h.

HK0 distribution (Fig. 7.19), which may indicate that these also originate from irradiation-induced damage (related to C_I or/and V_C). The HK0 and HK2 centers were detected only after post-irradiation annealing, whereas the UK1, HS2, and HK4 centers were detected just after electron irradiation. Therefore, the origin of the HK0 center (and the HK2 center) should be a carbon-related complex defect (and not single interstitial), which is consistent with the results obtained in the last section.

7.3.4 Deep Levels Generated by C^+ or Si^+ Implantation

Investigation on the deep levels in C^+- or Si^+-implanted samples must be helpful for clarifying the origin of the deep levels. Thus, C^+ or Si^+ implantation was performed on the *p*-type SiC epilayers with an implant dose of 1.4×10^{13} cm^{-2} or 1.4×10^{14} cm^{-2}, followed by Ar annealing at various temperatures (1000–1800°C) for 30 min. Fig. 7.21 shows DLTS spectra of the *p*-type 4H-SiC after C^+ implantation followed by Ar annealing at 1300°C and 1500°C. In the C^+-implanted samples, the same deep levels, UK1, UK2, HK0, and HK2 centers, are observed as those observed in the electron-irradiated samples (Fig. 7.18) that must be related to the carbon displacement as discussed above. When the temperature of the subsequent annealing was 1500°C, no DLTS peaks could be observed as indicated in Fig. 7.21 by the dotted line. This is consistent with the results obtained in the oxidized samples where all DLTS peaks disappeared after annealing over 1400°C (Fig. 7.17). For Si^+ implantation, a similar behavior for the deep levels was observed (not shown).

Fig. 7.22 shows the depth profiles of deep levels in the (a) C^+- and (b) Si^+-implanted samples followed by Ar annealing at 1300°C for 20 min, respectively. Depth profiles of carbon interstitials just after C^+ and Si^+ implantation simulated by the SRIM code are also shown as a solid line in the same figures. The deep levels can be categorized into two groups; the UK1 and UK2 centers as Group A, and the HK0 and HK2 centers as Group B. Group A has low diffusivity, distribution of which is not much different from that of C_I (or the other intrinsic defects just after ion implantation) simulated by the SRIM code (the real tail region of the C_I distribution should spread to a deeper region because the SRIM code assumes a completely amorphous material as a target). Therefore, the UK1 and UK2 centers could originate from immobile defect(s) induced by collision of implanted atoms (e.g. vacancy, complex). The similarity in the depth profiles of the UK1 and UK2 centers probably reflects that (i) these originate from the same defect and correspond to different charge states (thermal stability of the UK1 and UK2 centers is similar [16]), or (ii) the origin of these is different but simply show a similar distribution (simulation results show similar distributions for V_C, C_I, V_{Si}, and Si_I just after the implantation, as mentioned above). In contrast, Group B (HK0 and HK2) is distributed to a much deeper region after Ar annealing at 1300°C than the depth profile of implanted atoms, indicating that the origin of these defects contains a mobile defect such as C_I and Si_I. The concentration of the HK0 center is about three times higher than that of the HK2 center in the whole monitored area. In

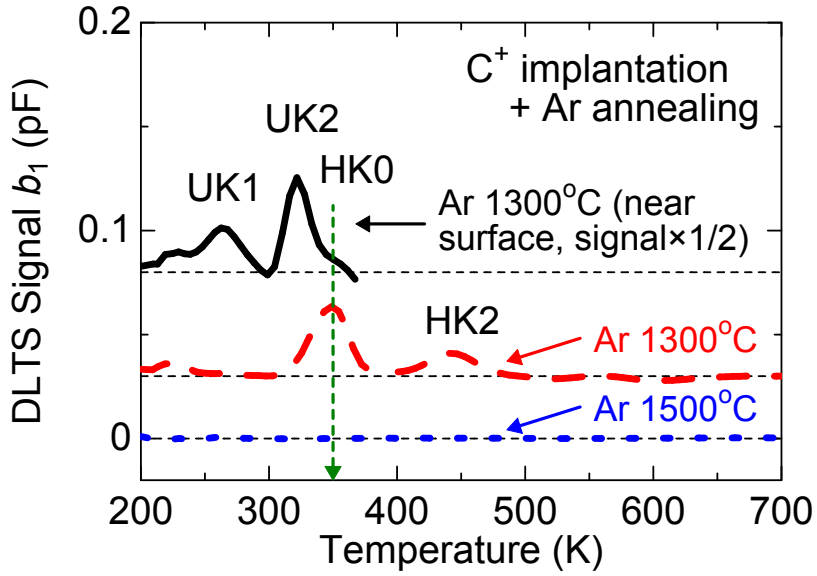

Figure 7.21: DLTS spectra of the p-type 4H-SiC after C^+ implantation followed by Ar annealing at 1300°C (solid line is the signal obtained near the surface (< 1 μm), and dashed line in the deeper region) and 1500°C (dotted line).

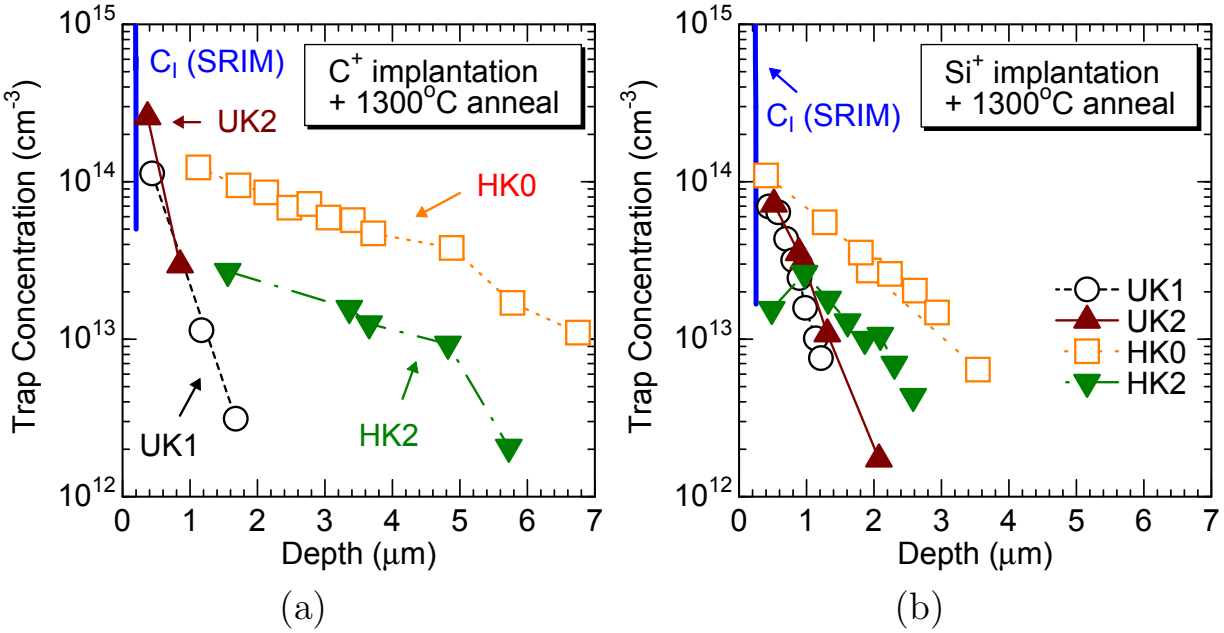

Figure 7.22: Depth profiles of deep levels in the p-type 4H-SiC after (a) C^+ and (b) Si^+ implantation (dose: 1.4×10^{13} cm^{-2}) followed by Ar annealing at 1300°C for 20 min. A depth profile of carbon interstitials just after C^+ implantation simulated by SRIM code is also shown as a solid line.

other words, the concentration of the HK0 center is different from that of the HK2 center, but the diffusion coefficient of HK0 is the same as that of the HK2, indicating that these centers could contain the same defect but form different configurations, such as C_I, $(C_I)_2$, $(C_2)_{Si}$, $(C_3)_{Si}$, and $((C_2)_{Si})_2$.

Fig. 7.23 shows the depth profiles for the HK0 center in the samples after implantation with C^+ and Si^+ followed by Ar annealing at 1300°C for 20 min. The HK0 concentration after implantation is clearly higher than that after thermal oxidation at 1300°C for 20 min (filled squares, dotted line). This should come as a result of the high amounts of interstitials near the surface region induced by ion implantation, either C^+ or Si^+. The HK0 center in C^+-implanted samples is distributed to a deeper region with higher concentration compared with that in Si^+-implanted samples, indicating that the origin of the HK0 center is C_I-related defects. If the HK0 center originates from other defects (e.g. Si_I) generated by implantation bombardment (some of the defects might not recombine and thus diffuse during Ar annealing), the HK0 concentration in the Si^+-implanted samples must be higher than that in the C^+-implanted samples because the amount of displaced atoms in the Si^+-implanted samples is higher than that in the C^+-implanted samples under this implantation condition, as calculated by the SRIM code (Fig. 7.5). Therefore, the HK0 in the C^+-implanted samples can be determined mainly by the diffusion of implanted carbon atoms (excess carbon atoms), whereas the distribution in the Si^+-implanted samples mainly by diffusion of C_I generated by implantation bombardment. The author also investigated the dependence of the HK0 distribution on implantation dose. In Fig. 7.23, filled/open symbols indicate the HK0 distribution for doses 1.4×10^{13} cm^{-2}/1.4×10^{14} cm^{-2}. The HK0 concentration in the samples implanted at the higher dose is almost the same or slightly higher than that at the lower dose, suggesting that the amount of C_I diffusion is not much different in the two samples (1.4×10^{13} cm^{-2}/1.4×10^{14} cm^{-2} dose). Because too high a concentration of C_I defects (e.g. 1×10^{18} cm^{-3}) is thermodynamically unfavorable, this concentration should be reduced to a certain level during Ar annealing by either conversion to other defects or diffusion to the sample surface.

7.3.5 Discussion

In *p*-type 4H-SiC, eight deep levels, GP1 ($E_V + 0.46$ eV), D ($E_V + 0.63$ eV) [13–16], HS2 ($E_V + 0.63$ eV) [16, 31], HK4 ($E_V + 1.4$ eV) [16], UK1 ($E_V + 0.35$ eV) [16], UK2 ($E_V + 0.71$ eV) [16], HK0 ($E_V + 0.79$ eV) [16], and HK2 ($E_V + 0.98$ eV) [16] centers, were detected; a summary is given in Table 7.3.

- The GP1 center was occasionally detected in as-grown samples (Fig. 7.10) and disappeared after oxidation at 1400°C (Fig. 7.17) or Ar annealing at 1440°C (not shown). This type of deep level was not found in previous reports.
- The D center, which has been attributed to B_{Si}-V_C [14, 17, 18], was detected in all

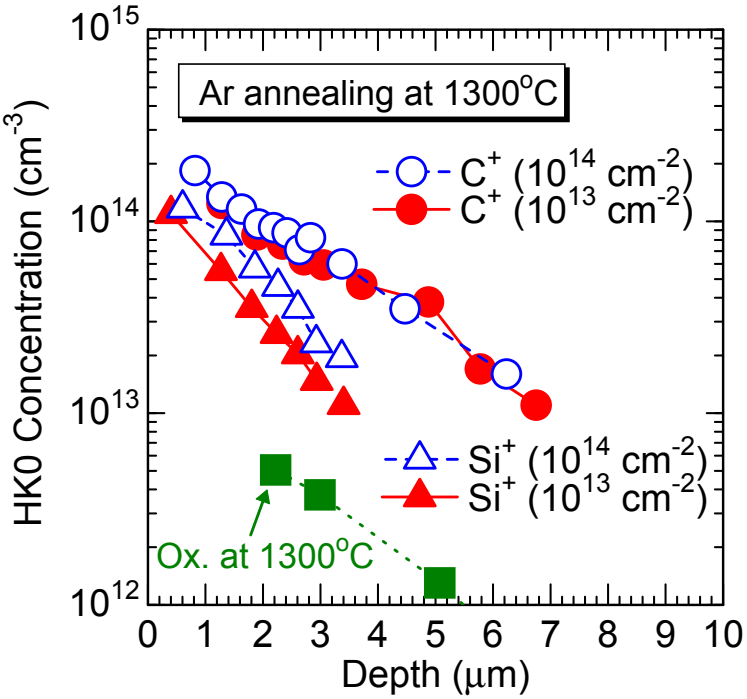

Figure 7.23: Depth profiles of HK0 center in the *p*-type 4H-SiC after C^+ (circles) and Si^+ (triangles) implantation followed by Ar annealing at 1300°C for 20 min. A depth profile of HK0 center in the sample oxidized at 1300°C for 20 min is also shown as square symbols.

Table 7.3: Deep levels observed in *p*-type 4H-SiC and the condition for generation and elimination. The speculated origins are also shown.

Label	$E_T - E_V$ (eV)	Generated by	Eliminated by	Origin (speculation)
GP1	0.46	as-grown	1440°C Ar annealing	unknown
D	0.63		1150°C oxidation	B_{Si}-V_C [14, 17, 18]
HS2	0.63	electron irradiation	1150°C oxidation or 1350°C Ar annealing [16]	C-related
HK4	1.4		1150°C oxidation or 1550°C Ar annealing [16]	
UK1	0.35	electron irradiation or C^+/Si^+ implantation	1440°C Ar annealing	C-related and immobile
UK2	0.71			
HK0	0.79	oxidation or electron irradiation or C^+/Si^+ implantation	1400°C Ar annealing	$(C_I)_2$ or $(C_3)_{Si}$ or $((C_2)_{Si})_2$
HK2	0.98			

as-grown samples and disappeared after thermal oxidation (Fig. 7.10). V_C in the D center will be filled with diffusing C_I emitted from the oxidizing interface.

- The HS2 and HK4 centers were generated by electron irradiation and disappeared after thermal oxidation at 1150°C (Fig. 7.18). The HS2 and HK4 centers should be related to C_I or/and V_C, because depth profiles for these centers after irradiation with 150 keV electrons, causing displacement of only carbon atoms, seem to reflect the irradiation damage (Fig. 7.19).
- The UK1 and UK2 centers were generated by electron irradiation (Fig. 7.18) or C^+/Si^+ implantation (Fig. 7.21), which remained after Ar annealing at 1300°C (Fig. 7.22) but eliminated at 1440°C (not shown). The depth profiles of the UK1 and UK2 centers followed irradiation damage (Fig. 7.19) or C^+/Si^+ implantation damage (Fig. 7.22), and did not change after Ar annealing at 1300°C (Fig. 7.22), indicating that these originate from carbon-related and immobile defects.
- The HK0 and HK2 centers must be related to interstitials (not vacancy) because (i) the HK0 distribution after oxidation can be fitted by the interstitial distribution calculated from the diffusion equations (5.1)–(5.7) (Fig. 7.11 and Fig. 7.12), and (ii) these centers are distributed to much deeper regions compared with the other deep levels (UK1 and UK2) after C^+ or Si^+ implantation followed by Ar annealing (Fig. 7.22). In addition, the HK0 and HK2 centers must be carbon-related defects (not silicon-related defect) because (i) these are generated by irradiation with 150 keV electrons, and (ii) higher concentrations of the HK0 and HK2 centers are observed in C^+-implanted samples than in Si^+-implanted samples (Fig. 7.23); nevertheless the amount of displaced atoms by Si^+ implantation is higher than that by C^+ implantation. Furthermore, the HK0 and HK2 centers are inferred to be complex defects (not single C_I) from the results that (i) the HK0 center is generated (through diffusion of carbon interstitials) during thermal oxidation, but does not diffuse by subsequent Ar annealing at the same temperature (Fig. 7.15), and (ii) the HK0 and HK2 centers are not detected just after irradiation, but detected after the subsequent annealing (Fig. 7.18). From these results, the origin of the HK0 center should be a complex that includes carbon interstitial(s) like $(C_I)_2$, $(C_3)_{Si}$, or $((C_2)_{Si})_2$. This defect should decompose or be converted to other defects at temperatures over 1400°C (Fig. 7.17 and Fig. 7.21). PL signals corresponding to these C_I-related complexes have been reported in electron-irradiated SiC [21, 24–30], thermal stability of which is similar to that of the HK0 center.

The author speculates that point defects during thermal oxidation should behave as follows. Carbon interstitials (and also silicon interstitials) are generated at the SiO_2/SiC interface and diffuse into SiC bulk during thermal oxidation. The concentration of silicon interstitials in SiC bulk after oxidation is much lower than that of carbon interstitials because of the low diffusivity [33, 34]. Many diffusing carbon interstitials recombine with carbon vacancies, leading to a reduction in $Z_{1/2}$ centers. Other carbon interstitials combine

with one another (or combine and occupy silicon vacancies) and form C_I-related complexes (the origin of HK0 center) during oxidation when the oxidation temperature is below 1300°C. Subsequent Ar annealing at over 1400°C decomposes the source of the HK0 center and/or form more thermally stable defects. In oxidation at over 1400°C, C_I defects do not combine with others (or form very thermally stable defects) during oxidation, resulting in no DLTS peaks in the lower half of the bandgap in 4H-SiC.

Those thermally stable defects formed during high temperature (> 1400°C) oxidation/annealing might be the ON1 and ON2 centers, even though it is largely conjectural. After thermal oxidation, Ar annealing at temperatures over 1400°C increases the ON1 and ON2 concentration (Fig. 7.3, Fig. 7.8), while it eliminates the HK0 center (Fig. 7.17, Fig. 7.21). In Fig. 7.24, the depth profiles of the HK0 center in oxidized (1300°C, 15.9 h) samples before and after subsequent Ar annealing (1500°C, 2 h) are compared with those of the ON1 center. Because (i) the distribution of the HK0 is similar to that of the ON1 center, (ii) HK0 concentration is much higher than the ON1 concentration, and (iii) both HK0 and ON1 centers may originate from C_I-related defect, a part of the HK0 center might be converted to the ON1 and ON2 centers when the HK0 center disappears at high temperature annealing over 1400°C.

7.4 Summary

The author sought to reveal the origins of the deep levels observed in n-type/p-type 4H-SiC after thermal oxidation by comparing deep levels observed in electron-irradiated, C^+- or Si^+-implanted, and N_2O-annealed samples. The ON1 ($E_C - 0.84$ eV) and ON2 ($E_C - 1.1$ eV) centers showed very similar behaviours in the oxidized, C^+- or Si^+-implanted, and N_2O-annealed samples, where the ON1 concentration and ON2 concentration have an one-to-one correspondence. Thus, the ON1 and ON2 centers could originate from the same defects in different charge states. Because the depth profiles of the ON1 and ON2 centers after oxidation at various temperatures for different periods can well be fitted by the interstitial distribution calculated from diffusion equations (Eqs. (5.1)–(5.7)) with a set of fitting parameters (Table 7.1), the origin of the ON1 and ON2 centers should be related to the interstitials diffusing from the SiO_2/SiC interface during oxidation. The migration barrier for the interstitial in the fitting parameters (0.5 eV) is comparable to that of C_I (0.5–0.74 eV), indicating that the ON1 and ON2 centers are more likely to be related to C_I than Si_I. In addition, the ON1 and ON2 centers may also be related to N atoms because oxidation in N_2O (or NO) ambient enhances the generation of the ON1 and ON2 centers compared with oxidation in O_2.

The HK0 ($E_V + 0.79$ eV) and HK2 ($E_V + 0.98$ eV) centers were generated by thermal oxidation, electron irradiation, or C^+/Si^+ implantation, and eliminated by Ar annealing at temperatures over 1400°C. These defects were generated by the irradiation with 150 keV

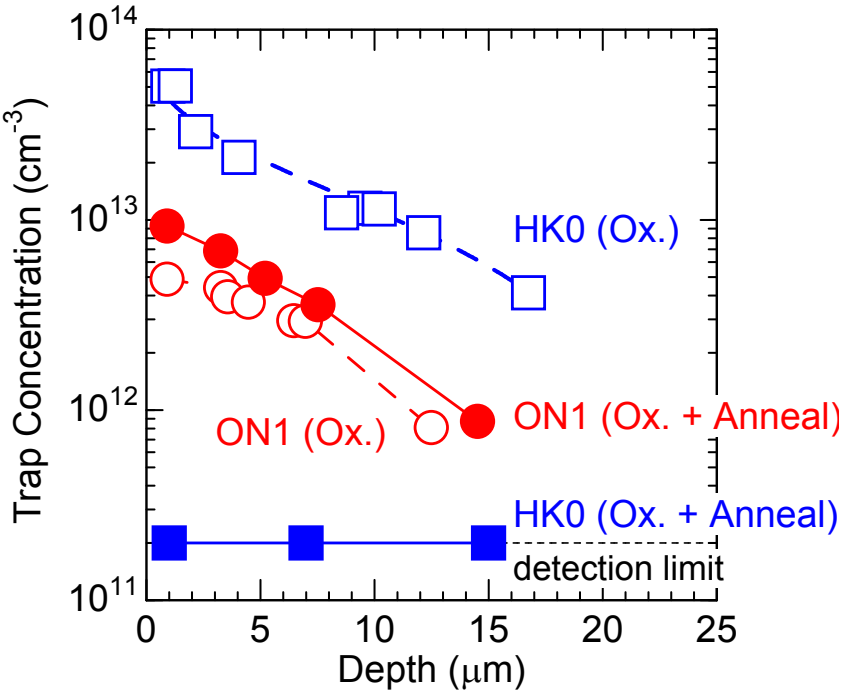

Figure 7.24: Depth profiles of the HK0 center in p-type 4H-SiC after oxidation at 1300°C for 15.9 h (open squares) and after the oxidation followed by Ar annealing at 1500°C for 2 h (filled squares). Depth profiles of the ON1 center in n-type 4H-SiC after the oxidation (open circles) and after the oxidation and Ar annealing (filled circles) are also shown.

electrons, where only carbon displacement occurs. In addition, the HK0 distribution after oxidation could be well fitted by the interstitial distribution calculated from diffusion equations. Furthermore, the HK0 center was generated during thermal oxidation at 1150°C, but did not diffuse by subsequent Ar annealing at the same temperature. From the generation and elimination behaviours above, the HK0 and HK2 centers may originate from a complex including carbon interstitial(s) such as $(C_I)_2$, $(C_3)_{Si}$, or $((C_2)_{Si})_2$. PL signals corresponding to these C_I-related complexes have been reported in electron-irradiated SiC, thermal stability of which is similar to that of the HK0 center. Following the all results, the author could describe the behavior of the point defects (and deep levels) in SiC during oxidation and during subsequent Ar annealing.

References

[1] L. Storasta, H. Tsuchida, T. Miyazawa, and T. Ohshima, *Journal of Applied Physics* **103**, 013705 (2008).

[2] T. Hiyoshi and T. Kimoto, *Applied Physics Express* **2**, 041101 (2009).

[3] T. Dalibor, G. Pensl, H. Matsunami, T. Kimoto, W. J. Choyke, A. Schöner, and N. Nordell, *Physica Status Solidi (A)* **162**, 199 (1997).

[4] C. Hemmingsson, N. T. Son, O. Kordina, J. P. Bergman, E. Janzén, J. L. Lindström, S. Savage, and N. Nordell, *Journal of Applied Physics* **81**, 6155 (1997).

[5] M. Bockstedte, A. Mattausch, and O. Pankratov, *Physical Review B* **69**, 235202 (2004).

[6] F. Gao, W. J. Weber, M. Posselt, and V. Belko, *Physical Review B* **69**, 245205 (2004).

[7] J. F. Ziegler, M. D. Ziegler, and J. P. Biersack, *Nuclear Instruments and Methods in Physics Research Section B* **268**, 1818 (2010).

[8] R. Devanathan and W. Weber, *Journal of Nuclear Materials* **278**, 258 (2000).

[9] U. Gerstmann, E. Rauls, T. Frauenheim, and H. Overhof, *Physical Review B* **67**, 205202 (2003).

[10] K. C. Chang, N. T. Nuhfer, L. M. Porter, and Q. Wahab, *Applied Physics Letters* **77**, 2186 (2000).

[11] T. Zheleva, A. Lelis, G. Duscher, F. Liu, I. Levin, and M. Das, *Applied Physics Letters* **93**, 022108 (2008).

[12] T. Kimoto, Y. Kanzaki, M. Noborio, H. Kawano, and H. Matsunami, *Japanese Journal of Applied Physics* **44**, 1213 (2005).

[13] T. Troffer, M. Schadt, T. Frank, H. Itoh, G. Pensl, J. Heindl, H. P. Strunk, and M. Maier, *Physica Status Solidi (A)* **162**, 277 (1997).

[14] S. G. Sridhara, L. L. Clemen, R. P. Devaty, W. J. Choyke, D. J. Larkin, H. S. Kong, T. Troffer, and G. Pensl, *Journal of Applied Physics* **83**, 7909 (1998).

[15] M. Ikeda, H. Matsunami, and T. Tanaka, *Physical Review B* **22**, 2842 (1980).

[16] K. Danno and T. Kimoto, *Journal of Applied Physics* **101**, 103704 (2007).

[17] A. Duijn-Arnold, T. Ikoma, O. G. Poluektov, P. G. Baranov, E. N. Mokhov, and J. Schmidt, *Physical Review B* **57**, 1607 (1998).

[18] P. Baranov, I. Il'in, and E. Mokhov, *Physics of the Solid State* **40**, 31 (1998).

[19] M. Bockstedte, A. Mattausch, and O. Pankratov, *Physical Review B* **68**, 205201 (2003).

[20] A. Gali, N. T. Son, and E. Janzén, *Physical Review B* **73**, 033204 (2006).

[21] A. Mattausch, M. Bockstedte, and O. Pankratov, *Physical Review B* **70**, 235211 (2004).

[22] X. Shen, M. P. Oxley, Y. Puzyrev, B. R. Tuttle, G. Duscher, and S. T. Pantelides, *Journal of Applied Physics* **108**, 123705 (2010).

[23] F. Devynck, A. Alkauskas, P. Broqvist, and A. Pasquarello, *AIP Conference Proceedings* **1199**, 108 (2010).

[24] G. Evans, J. Steeds, L. Ley, M. Hundhausen, N. Schulze, and G. Pensl, *Physical Review B* **66**, 352041 (2002).

[25] A. Mattausch, M. Bockstedte, O. Pankratov, J. W. Steeds, S. Furkert, J. M. Hayes, W. Sullivan, and N. G. Wright, *Physical Review B* **73**, 161201 (2006).

[26] J. W. Steeds and W. Sullivan, *Physical Review B* **77**, 195204 (2008).

[27] J. W. Steeds, W. Sullivan, S. A. Furkert, G. A. Evans, and P. J. Wellmann, *Physical Review B* **77**, 195203 (2008).

[28] F. Yan, R. P. Devaty, W. J. Choyke, A. Gali, T. Kimoto, T. Ohshima, and G. Pensl, *Applied Physics Letters* **100**, 132107 (2012).

[29] I. G. Ivanov, A. Gällström, R. Coble, R. Devaty, W. Choyke, and E. Janzén, *Materials Science Forum* **717-720**, 259 (2012).

[30] A. Gali, P. Deák, P. Ordejón, N. T. Son, E. Janzén, and W. J. Choyke, *Physical Review B* **68**, 125201 (2003).

[31] L. Storasta, J. P. Bergman, E. Janzén, A. Henry, and J. Lu, *Journal of Applied Physics* **96**, 4909 (2004).

[32] K. Danno and T. Kimoto, *Journal of Applied Physics* **100**, 113728 (2006).

[33] J. D. Hong and R. F. Davis, *Journal of the American Ceramic Society* **63**, 546 (1980).

[34] J. D. Hong, R. F. Davis, and D. E. Newbury, *Journal of Materials Science* **16**, 2485 (1981).

Chapter 8

Control of Carrier Lifetimes in SiC

8.1 Introduction

As discussed in Chapter 1, a carrier lifetime is an important parameter determining the energy dissipation of bipolar power devices. Long carrier lifetimes lead to sufficient conductivity modulation, resulting in low ON-state resistance. Too long carrier lifetime, in contrast, will cause large reverse recovery time, leading to limited switching frequency and excessive switching loss. Thus, the control of carrier lifetimes is required for achieving low-loss SiC power devices. In this chapter, the author sought to control carrier lifetimes by controlling the concentration and depth profiles of the $Z_{1/2}$ center.

The $Z_{1/2}$ center acts as a lifetime killer in n-type 4H-SiC [1–3]. Fig. 8.1 shows carrier lifetimes measured by microwave photoconductance decay (μ-PCD) in 50-μm-thick n-type 4H-SiC epilayers possessing different $Z_{1/2}$ concentrations [2]. When the $Z_{1/2}$ concentration is higher than 1–2×10^{13} cm^{-3}, the inverse of carrier lifetime is proportional to the $Z_{1/2}$ concentration, suggesting that the carrier recombination via the $Z_{1/2}$ center dominates carrier lifetimes in the samples. This "bulk" carrier lifetime τ_{SRH} most affects on the conductivity modulation in bipolar power devices, which is described by the Shockley-Read-Hall (SRH) model. When the $Z_{1/2}$ concentration is lower, in contrast, other processes such as recombination at the surface and the substrates govern carrier lifetimes. This carrier lifetime τ_{other} improves in thicker epilayers [2–5], enabling proper measurements of τ_{SRH}. A "measured" carrier lifetime τ is described as:

$$\frac{1}{\tau} = \frac{1}{\tau_{\mathrm{SRH}}} + \frac{1}{\tau_{\mathrm{other}}}. \tag{8.1}$$

For introduction of a high density of the $Z_{1/2}$ center (leading to the reduction of carrier lifetimes) electron irradiation was used, whereas for reduction of the $Z_{1/2}$ center (leading to the enhancement of carrier lifetimes) thermal oxidation was performed.

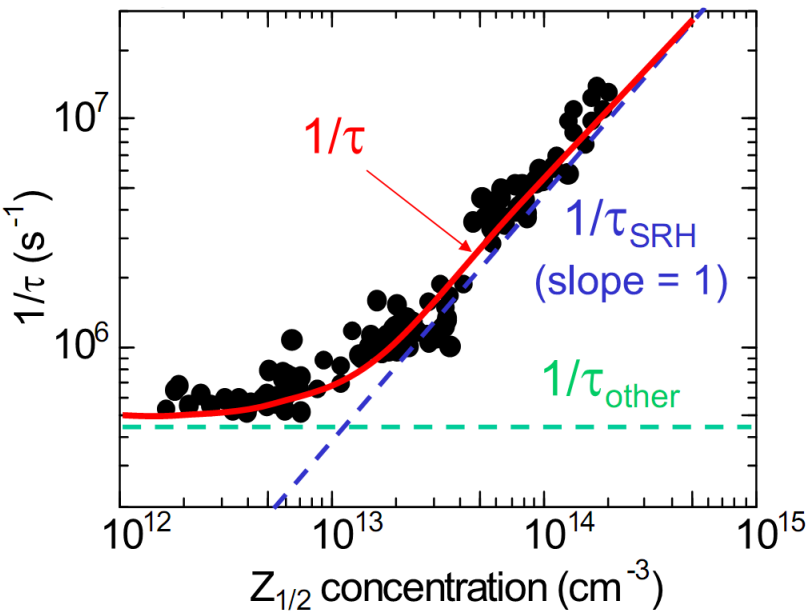

Figure 8.1: Carrier lifetimes in n-type 4H-SiC epilayers with different $Z_{1/2}$ concentrations [2].

8.2 Microwave Photoconductance Decay Measurements

μ-PCD has commonly been used for carrier lifetime measurements in semiconductors [6], by which carrier lifetimes of whole wafer can be measured in a short time without contacts. During μ-PCD measurements, (i) excess carriers are created by laser pulses and (ii) a part of these carriers are recombined via deep levels while others diffuse to the surface and the epilayer/substrate interface and then are recombined. In μ-PCD measurements, the decay of photoconductance is monitored by the microwave reflection, which is in proportion to the conductance [7].

In this study, carrier lifetimes were measured at room temperature by μ-PCD equipped with an yttrium lithium fluoride (YLF)-third harmonic generation (3HG) laser ($\lambda = 349$ nm) as an excitation source. The optical absorption coefficient of 4H-SiC at the excitation laser wavelength (349 nm) was obtained as 330 cm^{-1} (penetration depth: $\sim$ 30 μm) from a literature [8]. To increase the signal-to-noise ratio, the difference in microwave (frequency: 26 GHz) reflectivity between areas with and without laser illumination was used as output.

8.3 Reduction of Carrier Lifetimes by Electron Irradiation

In our group, intentional reduction of carrier lifetimes in SiC epilayers has been achieved by electron irradiation with various fluences [2]. In a literature [2], a carrier lifetime was shorter in the area irradiated with higher fluence and very uniformly distributed in each area.

Bulk carrier lifetimes in the epilayer (τ_{SRH}) are described by the SRH model [9] (under high injection condition):

$$\tau_{\mathrm{SRH}} = \left(\frac{1}{\sigma_{\mathrm{p}} v_{\mathrm{th,p}}} + \frac{1}{\sigma_n v_{\mathrm{th,n}}} \right) \frac{1}{N_{\mathrm{T}}} = \alpha \frac{1}{N_{\mathrm{T}}}, \tag{8.2}$$

where σ_{n} and σ_{p} are the capture cross section of the recombination center for electrons and holes, $v_{\mathrm{th,n}}$ and $v_{\mathrm{th,p}}$ the thermal velocities of electrons and holes, and N_{T} the concentration of the recombination center. From Fig. 8.1, the proportionality constant α for the $Z_{1/2}$ center is obtained as $\sim 2 \times 10^{13}$ $\mu\mathrm{s/cm}^3$.

The $Z_{1/2}$ concentrations at the surfaces after irradiation with relatively low-energy electrons (200, 250 keV) with various fluences were obtained in Chapter 6, whereas those with 100–250 keV electrons have also been reported in literatures [2, 10–12]. In addition, the dependence of the $Z_{1/2}$ concentration at the surface on irradiated electron energy can also be obtained from Fig. 8.2 [12]. Using Eq. (8.2) and the dependence of the $Z_{1/2}$ center on irradiation condition, bulk carrier lifetimes can arbitrarily be reduced.

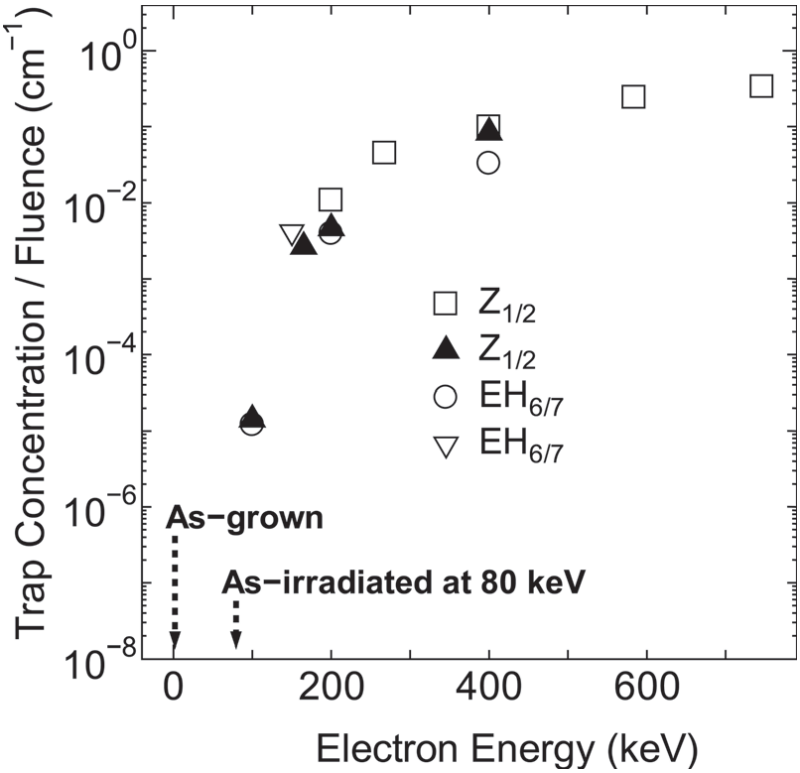

Figure 8.2: $Z_{1/2}$ and $EH_{6/7}$ concentrations in electron-irradiated 4H-SiC normalized by the electron fluence vs the electron energy [12].

8.4 Enhancement of Carrier Lifetimes by Thermal Oxidation

As shown in Chapter 5, the $Z_{1/2}$ center is reduced by thermal oxidation, and the depth profiles depend on the oxidation condition such as the oxidation temperature and the time. In this section, the author sought to enhance bulk carrier lifetimes in the epilayer by thermal oxidation and reveal the relation between the depth profiles of the $Z_{1/2}$ center and measured carrier lifetimes.

8.4.1 Correlation between Measured Carrier Lifetimes and $Z_{1/2}$ Distribution

Fig. 8.3 shows μ-PCD decay curves for the 96-μm-thick n-type SiC epilayers (N_d: 2×10^{15} cm^{-3}) on the n-type SiC substrates (thickness: $\sim$ 350 μm) after different oxidation processes. The oxidation temperature was 1300°C in Fig. 8.3 except for the signal labeled "1400°C". The irradiated photon density was 1.1×10^{14} cm^{-2}, leading to a high carrier injection level of $\sim 10^{16}$ cm^{-3}. The carrier lifetimes were derived from the slopes of the decay curves at the points where the μ-PCD signals decreased to e^{-3} of the initial intensity because the initial fast decay severely suffered from carrier recombination at the surface and in the substrate [4, 5, 13]. The carrier lifetime increased from 0.6 μs (as-grown) to 6.5 μs by oxidation at 1400°C for 16.5 h. Fig. 8.4 indicates the depth profiles of $Z_{1/2}$ concentration (measured by deep level transient spectroscopy (DLTS)) in the same samples as in Fig. 8.3. A longer lifetime was measured in a sample with a deeper $Z_{1/2}$-eliminated region, suggesting that a bulk lifetime was enhanced by the elimination of the $Z_{1/2}$ center and thereby a measured lifetime was improved.

8.4.2 Estimation of Measured Carrier Lifetimes

Here, the author attempted to quantitatively estimate the relation between measured carrier lifetimes and the $Z_{1/2}$ profiles by a numerical simulation. Note again that the "measured" carrier lifetime does not represent the "bulk" carrier lifetime in the epilayer itself because there are other recombination paths of excess carriers; (i) excess carriers generated by the excitation laser recombine at the surface as well as in the epilayer, (ii) the carriers excited in the epilayer also diffuse toward the surface and the substrate due to a gradient of the carrier density, promoting carrier recombination at the surface and in the substrate. Therefore, the measured carrier lifetime contains the effects of carrier diffusion and recombination at the surface, in the epilayer, and in the substrate [4, 5, 13].

The measured carrier lifetimes were estimated from the diffusion equation [5]:

$$\frac{\partial p}{\partial t} = D\frac{\partial^2 p}{\partial x^2} - \frac{p}{\tau_{SRH}}, \tag{8.3}$$

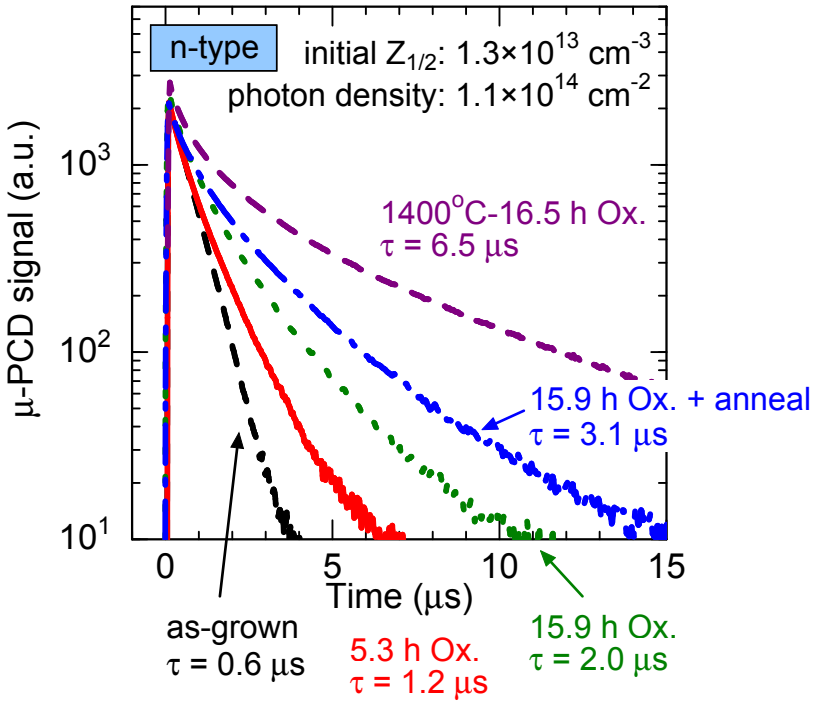

Figure 8.3: μ-PCD decay curves for the 96-μm-thick n-type 4H-SiC epilayers after different oxidation processes. The oxidation temperature is 1300°C except for the signal labeled "1400°C".

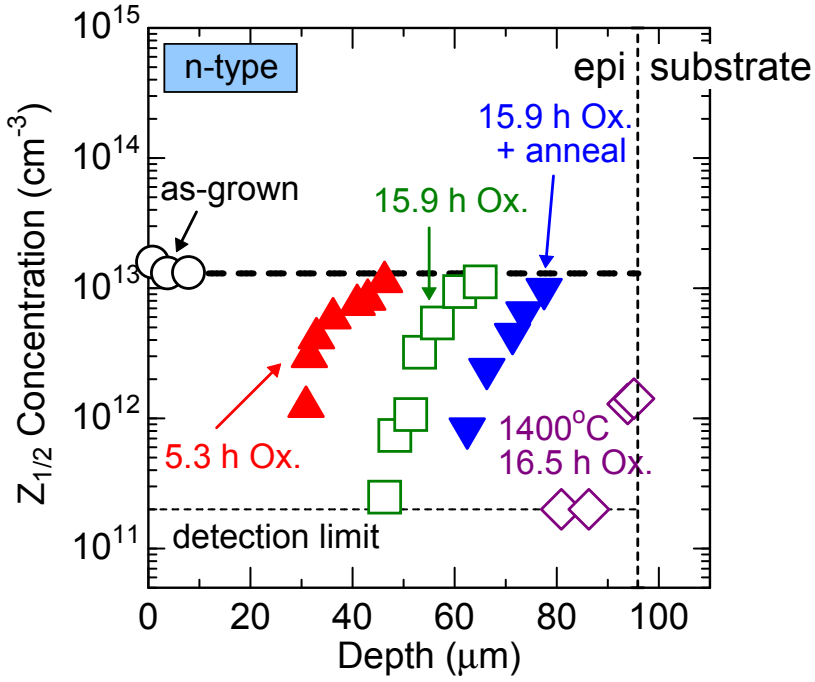

Figure 8.4: Depth profiles of $Z_{1/2}$ concentration in the same samples as in Fig. 8.3.

where p denotes the excess-carrier concentration, and D signifies an ambipolar diffusion constant of 4.2 cm^2/s (D_{epi}) [14] for the epilayer or a standard hole diffusion constant of 0.3 cm^2/s for the substrate. Fig. 8.5 shows a schematic illustration of an SiC epilayer grown on an SiC substrate after thermal oxidation. The boundary conditions are fixed as

$$D\frac{\partial p}{\partial x}\,|_{x=0} = S_{r1}p, \tag{8.4}$$

$$D\frac{\partial p}{\partial x}\,|_{x=446\ \mu m} = -S_{r2}p, \tag{8.5}$$

where S_{r1} and S_{r2} denote the surface and backside recombination velocity, respectively. In this calculation, the epilayer was divided into two regions, the $Z_{1/2}$-eliminated region ($Z_{1/2}$ concentration $< 2 \times 10^{11}$ cm^{-3}) and the $Z_{1/2}$-remaining region ($Z_{1/2}$ concentration $= 1.3 \times 10^{13}$ cm^{-3} (initial value)). Taking account of results in literatures [5, 15], surface recombination velocity (S_{r1}) was assumed to be 1000 cm/s (smooth surfaces were assumed). Because the backside recombination velocity (S_{r2}) has a very little effect on the measured lifetime due to the thick substrate (over 300 μm) and low carrier lifetime in the substrate ($\tau_{sub} = 0.04$ μs), it was assumed as infinity. From Fig. 8.4, the boundaries between the $Z_{1/2}$-eliminated region and the $Z_{1/2}$-remaining region were defined to be 35 μm for a sample oxidized at 1300°C for 5.3 h, 55 μm for oxidized at 1300°C for 15.9 h, 70 μm for oxidized at 1300°C for 15.9 h followed by Ar annealing, and 96 μm for oxidized at 1400°C for 16.5 h from the surface. From the carrier lifetime measured in the as-grown sample, 0.6 μs, the bulk carrier lifetime in the $Z_{1/2}$-remaining region of the epilayer (τ_Z) could be estimated as 0.7 μs. Note again that the "measured" carrier lifetime, 0.6 μs, is shorter than the "bulk" carrier lifetime, 0.7 μs, due to the recombination at the surface and in the substrate[1].

Using these simulation model and parameters, carrier lifetimes obtained from μ-PCD decay curves were estimated. Fig. 8.6 shows decay curves of an excess-carrier area density (corresponding to μ-PCD decay curves) calculated with a bulk carrier lifetime in the $Z_{1/2}$-eliminated region (τ_{noZ}) of 50 μs for a part of the samples in Fig. 8.3. Carrier lifetimes were obtained from slopes of the calculated decay curves, which are almost linear. Here, note that initial fast decay of an excess carrier concentration, which is observed in experimental μ-PCD decay curves (Fig. 8.3), is not obtained in the calculation results (Fig. 8.6). The initial fast decay might be attributed to high S_{r1} at the beginning of μ-PCD measurements. At surfaces of SiC epilayers, a potential barrier for electrons exists due to electrons captured by surface states, leading to lower S_{r1}. By an exitation laser, however, electrons trapped by the surface states are emitted, resulting in reduction of the potential barrier and thereby higher S_{r1}. Table 8.1 shows the comparison between the carrier lifetimes measured by μ-PCD and the calculated lifetimes. The carrier lifetimes calculated with τ_{noZ} of 50 μs well agreed with

[1]How to determine the τ_Z: In the case of as-grown samples, the bulk carrier lifetime in the whole region of the epilayer is τ_Z (there is no $Z_{1/2}$-eliminated region). When the bulk carrier lifetime (τ_Z) is assumed to be 0.7 μs, 0.6 μs is obtained as calculated τ. Because this 0.6 μs is equal to the measured carrier lifetime in as-grown sample, τ_Z is determined to be 0.7 μs.

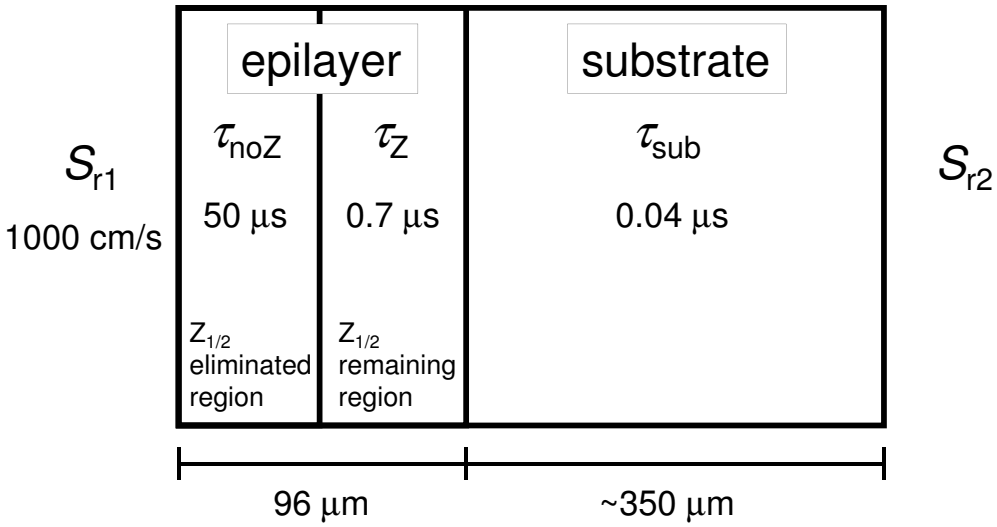

Figure 8.5: Schematic illustration of an SiC epilayer grown on an SiC substrate after thermal oxidation. From a comparison between experimental and calculated carrier lifetimes, bulk carrier lifetimes in the $Z_{1/2}$-eliminated region and the $Z_{1/2}$-remaining region were estimated to be 50 μs and 0.7 μs, respectively.

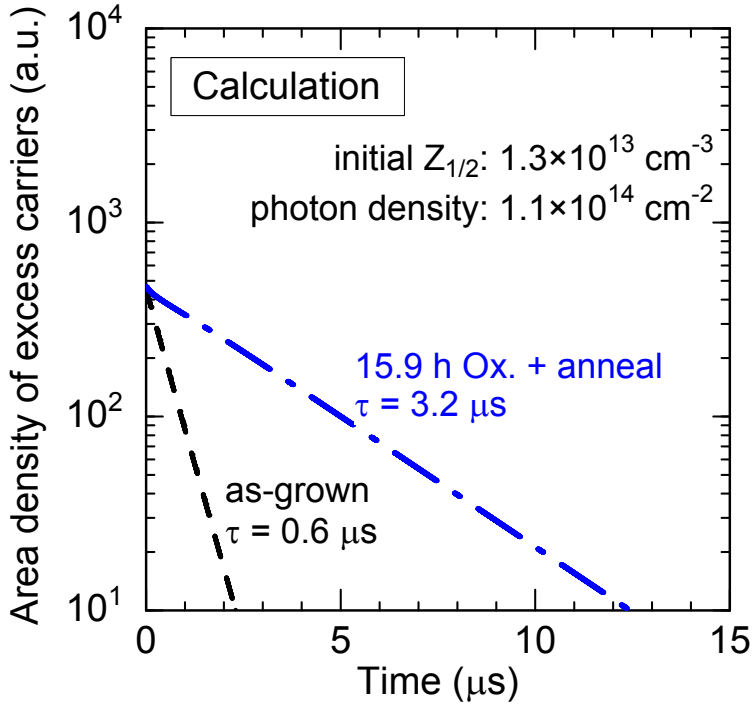

Figure 8.6: Decay curves of an excess-carrier area density (corresponding to μ-PCD decay curves) cauclated from the simulation model shown in Fig 8.5 for a part of the samples in Fig 8.3.

Table 8.1: Comparison between carrier lifetimes measured by μ-PCD and those predicted by calculation based on a diffusion equation. Initial $Z_{1/2}$ concentration is 1.3×10^{13} cm^{-3}.

	as-grown	1300°C-5.3-h Ox.	1300°C-15.9-h Ox.	1300°C-15.9-h Ox. + anneal	1400°C-16.5-h Ox.
μ-PCD	0.6 μs	1.2 μs	2.0 μs	3.1 μs	6.5 μs
calculation	0.6 μs	1.5 μs	2.4 μs	3.2 μs	3.9 μs

the measured carrier lifetimes, even though for oxidation at 1400°C the measured carrier lifetime (6.5 μs) was longer than the calculated lifetime (3.9 μs), which may result from that the $Z_{1/2}$ center in the substrate near the epilayer/substrate interface was also reduced by the intensive oxidation. This result indicates that the long-bulk-carrier-lifetime (50 μs) region expands from the surface to the deeper region by thermal oxidation at higher temperature for longer period.

8.4.3 Enhancement of Carrier Lifetimes

Taking account of the insights obtained in this chapter, the authors sought to realize a long measured carrier lifetime. To suppress the carrier recombination at the surface and substrate, thick (220 μm) epilayers were used as the starting materials. The concentration of the $Z_{1/2}$ center was $\sim 1 \times 10^{13}$ cm^{-3} for the as-grown samples. After oxidation at 1400°C for 48 h, by which the $Z_{1/2}$ center should be eliminated in the whole epilayer (from Eqs. (5.1)–(5.8)), the surface was passivated with a 20-nm-thick deposited oxide annealed in nitric oxide (NO) at 1250°C for 30 min. Fig. 8.7 shows the results of μ-PCD measurements for the samples [16], where a carrier lifetime improved from 1.1 μs (as-grown) to 26.1 μs after the oxidation and further increased to 33.2 μs after the oxidation followed by the passivation. Following the model suggested in this chapter, measured carrier lifetimes were improved and achieved the longest lifetime ever reported in SiC.

8.5 Discussion

To fabricate high-performance SiC bipolar power devices, an optimum carrier lifetime, which depends on an application of a device, and a uniform distribution of a carrier lifetime in a epilayer are required. To realize such lifetime control, the author proposes the following processes. (i) An SiC epilayer is oxidized at high temperature (e.g. I400°C) for a long period, leading to a sufficiently long carrier lifetime in the whole epilayer. (ii) Using electron irradiation, a carrier lifetime in the oxidized epilayer is uniformly reduced to the optimum carrier lifetime.

When the calculation model for the prediction of a $Z_{1/2}$ profile (shown in Chapter 5) is used, bulk carrier lifetimes can be enhanced only in a certain depth. The reverse recovery time of PiN diodes strongly depends on the carrier lifetime in the middle of the intrinsic layer because excess carriers in this region require time to sweep out especially for a thick epilayer [9]. Thus, the elimination of the $Z_{1/2}$ center only to a depth near the middle of the intrinsic layer (the $Z_{1/2}$ center at the middle remains) by controlling oxidation time (or temperature) should be reasonable for the low ON-resistance and short recovery time of SiC PiN diodes.

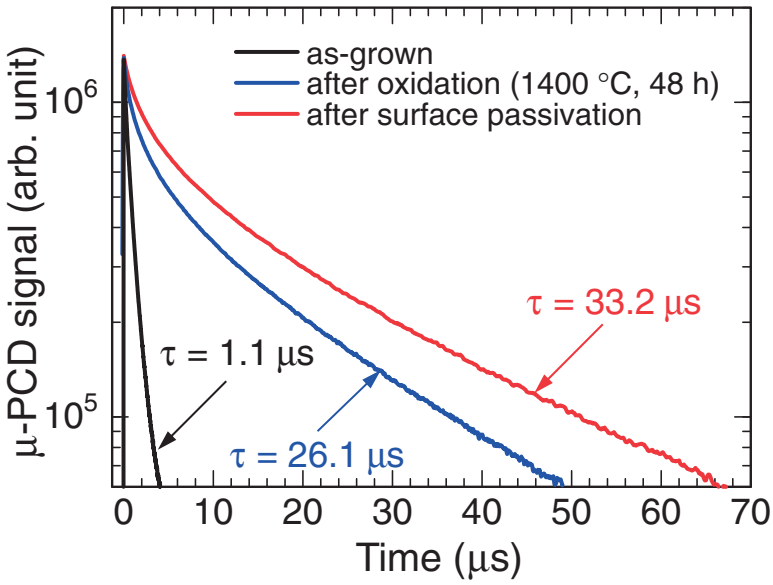

Figure 8.7: μ-PCD decay carves at room temperature obtained from a 220-μm-thick n-type 4H-SiC epilayer [16]. The decay curves for an as-grown epilayer and after $Z_{1/2}$ elimination via thermal oxidation at 1400°C for 48 h are demonstrated. The decay curve for the sample passivated with a deposited oxide annealed in NO is also shown.

8.6 Summary

The author attempted to control bulk carrier lifetimes in SiC by controlling the $Z_{1/2}$ concentration. By electron irradiation, bulk carrier lifetimes can arbitrarily be reduced, using SRH model and experimental data about the effects of the irradiation condition (the electron energy and fluence) on the $Z_{1/2}$ center.

In contrast, creating a thick $Z_{1/2}$-free region by thermal oxidation improved measured carrier lifetimes (from 0.6 μs to 6.5 μs in a 96-μm thick epilayer by oxidation at 1400°C for 16.5 h). Using the calculation based on the diffusion equation that considers excited-carrier diffusion and recombination in the epilayer, in the substrate, and at the surface, this enhancement of measured carrier lifetimes was found to be attributed to the expansion of long-bulk-carrier-lifetime (50 μs) region from the surface by the elimination of the $Z_{1/2}$ center.

By oxidation at a high temperature and for a long period, a bulk carrier lifetime in the whole epilayer can be enhanced to about 50 μs. After this oxidation, using electron irradiation, the carrier lifetime in the oxidized epilayer can be uniformly reduced to a carrier lifetime required for each SiC device. In this manner, bulk carrier lifetimes in SiC epilayers can be controlled by electron irradiation and thermal oxidation.

References

[1] P. B. Klein, B. V. Shanabrook, S. W. Huh, A. Y. Polyakov, M. Skowronski, J. J. Sumakeris, and M. J. O'Loughlin, *Applied Physics Letters* **88**, 052110 (2006).

[2] K. Danno, D. Nakamura, and T. Kimoto, *Applied Physics Letters* **90**, 202109 (2007).

[3] P. B. Klein, *Journal of Applied Physics* **103**, 033702 (2008).

[4] P. B. Klein, R. Myers-Ward, K. Lew, B. L. VanMil, C. R. Eddy, D. K. Gaskill, A. Shrivastava, and T. S. Sudarshan, *Journal of Applied Physics* **108**, 033713 (2010).

[5] T. Kimoto, T. Hiyoshi, T. Hayashi, and J. Suda, *Journal of Applied Physics* **108**, 083721 (2010).

[6] J. M. Borrego, R. J. Gutmann, N. Jensen, and O. Paz, *Solid-State Electronics* **30**, 195 (1987).

[7] M. Kunst and G. Beck, *Journal of Applied Physics* **60**, 3558 (1986).

[8] S. G. Sridhara, R. P. Devaty, and W. J. Choyke, *Journal of Applied Physics* **84**, 2963 (1998).

[9] B. J. Baliga, *Fundamentals of Power Semiconductor Devices*, Springer Science+Business Media, LLC, NY, USA, 2008.

[10] L. Storasta, J. P. Bergman, E. Janzén, A. Henry, and J. Lu, *Journal of Applied Physics* **96**, 4909 (2004).

[11] S. Sasaki, K. Kawahara, G. Feng, G. Alfieri, and T. Kimoto, *Journal of Applied Physics* **109**, 013705 (2011).

[12] H. Kaneko and T. Kimoto, *Applied Physics Letters* **98**, 262106 (2011).

[13] P. Ščajev, V. Gudelis, K. Jarašiūnas, and P. B. Klein, *Journal of Applied Physics* **108**, 023705 (2010).

[14] P. Grivickas, J. Linnros, and V. Grivickas, *Journal of Materials Research* **16**, 524 (2001).

[15] M. Kato, A. Yoshida, and M. Ichimura, *Japanese Journal of Applied Physics* **51**, 02BP12 (2012).

[16] S. Ichikawa, K. Kawahara, J. Suda, and T. Kimoto, *Applied Physics Express* **5**, 101301 (2012).

Chapter 9

Conclusions

9.1 Conclusions

To achieve high-performance SiC bipolar power devices, deep levels in SiC epilayers have been investigated. Deep levels generated by device fabrication processes, ion implantation and reactive ion etching (RIE), in the whole bandgap of 4H-SiC were investigated by deep level transient spectroscopy (DLTS) on both n-type and p-type epilayers. The generated deep levels were sought to be reduced by thermal oxidation, which was recently found to reduce the $Z_{1/2}$ center, a lifetime killer in n-type 4H-SiC epilayers, in as-grown materials. The mechanism of the trap reduction by thermal oxidation was discussed comparing two trap reduction methods: thermal oxidation and C^+ implantation followed by Ar annealing. In addition, carrier lifetimes in SiC epilayers were attempted to be controlled by controlling the $Z_{1/2}$ concentration using two techniques, electron irradiation (for generation of the $Z_{1/2}$ center) and thermal oxidation (for reduction of the $Z_{1/2}$ center). Furthermore, the origin of the $Z_{1/2}$ center was investigated using DLTS and electron paramagnetic resonance (EPR). The major conclusions obtained in this study are summarized as follows.

In Chapter 2, the principle of DLTS, and the sample preparation process for evaluation of deep levels in SiC by DLTS were explained. The typical deep levels detected in as-grown n-type 4H-SiC are the ET1 ($E_C - 0.39$ eV), EH_1 ($E_C - 0.50$ eV), $Z_{1/2}$ ($E_C - 0.67$ eV), GN3 ($E_C - 1.1$ eV), UT_1 ($E_C - 1.4$ eV), and $EH_{6/7}$ ($E_C - 1.5$ eV) centers, among which the $Z_{1/2}$ and $EH_{6/7}$ centers are often dominant. In as-grown p-type 4H-SiC, in contrast, the GP1 ($E_V + 0.46$ eV), D ($E_V + 0.63$ eV), and HK4 ($E_V + 1.4$ eV) centers are major deep levels. When the growth condition is optimized, the concentration of deep levels in as-grown n-type and p-type 4H-SiC epilayers can be suppressed to about 1×10^{12} cm^{-3}.

In Chapter 3, deep levels generated by ion (N^+, P^+, Al^+, or Ne^+) implantation or RIE in the whole energy range of the bandgap of 4H-SiC were investigated. When the implanted dose was relatively low (5.6×10^{10} cm^{-2}), the dominant deep levels were the $Z_{1/2}$ and $EH_{6/7}$ centers in the upper half of bandgap, and the HS1 ($E_V + 0.39$ eV) and HK4 centers in the lower half of bandgap. The origins of these deep levels should be intrinsic defects because

they were generated independently of the implanted species. Even after Ar annealing at 1700°C, the concentrations of the $Z_{1/2}$ and $EH_{6/7}$ centers in ion-implanted samples were about 100 times higher than those in nonimplanted samples. When the implanted dose was high (8.0×10^{13} cm^{-2}), the ID_8 ($E_C - 0.30$ eV), EH_5 ($E_C - 1.0$ eV), and IN8 centers were observed in n-type samples with very high concentrations of about 10^{17} cm^{-3}, while the HK2 ($E_V + 0.98$ eV), IP6 ($E_V + 1.2$ eV), HK3 ($E_V + 1.3$ eV), and IP9 ($E_V + 1.5$ eV) centers were observed in p-type samples with concentrations of about 10^{16} cm^{-3}.

In as-etched p-type samples, a thick (> 10 μm) semi-insulating (SI) region was formed, which disappeared after Ar annealing at 1000°C. Depth profiles obtained by secondary ion mass spectrometry (SIMS) indicated that the thick depletion region might originate from oxygen permeation during RIE. Even after the annealing, various deep levels, ID_8, EN ($E_C - 1.6$ eV), UK1 ($E_V + 0.35$ eV), HS2 ($E_V + 0.39$ eV), HK0 ($E_V + 0.79$ eV), HK2, HK3, and HK4, were observed in n-type and p-type samples. After RIE followed by Ar annealing at 1000°C, a typical concentration of the deep levels near the surface was 2×10^{13} cm^{-3} in the upper half of the bandgap and 7×10^{13} cm^{-3} in the lower half.

In Chapter 4, the effects of thermal oxidation on deep levels generated by ion implantation or by RIE were investigated. In ion-implanted n-type 4H-SiC epilayers, by thermal oxidation at 1150°C for 4 h, all deep levels could be reduced to a concentration of about one order of magnitude lower than that before oxidation. In p-type samples, however, additional defects such as the HK0 center appeared after oxidation, whereas the dominant deep levels in high-dose-implanted samples, HK2, IP6, and HK3, were remarkably reduced. To reduce all the deep levels generated by ion implantation, thermal oxidation followed by Ar annealing at temperatures over 1400°C is recommended.

Almost all deep levels in RIE-etched samples, ID_8, UK1, HS1, HK0, HK2, HK3, and HK4, were reduced by thermal oxidation followed by Ar annealing at 1400°C. Only the EN center, showing a very high concentration of about 1×10^{15} cm^{-3} near the surface region, remained after the oxidation followed by Ar annealing, the generation of which could be suppressed using a moderate RIE condition.

In Chapter 5, to clarify the mechanism of trap reduction by thermal oxidation, the author compared deep levels after two trap-reduction processes: thermal oxidation and C^+ implantation followed by Ar annealing. As the results, the same phenomena, diffusion of interstitials, were revealed to occur during these two processes. Using diffusion equations, the author proposed a calculation model enabling the prediction of $Z_{1/2}$ distribution after thermal oxidation. In SiC epilayers with different initial $Z_{1/2}$ concentrations, this model could reproduce the depth profiles of the $Z_{1/2}$ center after oxidation at any temperatures and for any oxidation periods. To enhance the $Z_{1/2}$ reduction and reduce the process time, three methods, removing the oxide layer during oxidation, Ar annealing at 1500°C after oxidation, and higher temperature oxidation, were proposed and experimentally proved to be effective. The $Z_{1/2}$ center with an initial concentration of 1.3×10^{13} cm^{-3} could be eliminated to a depth of > 90 μm after oxidation at 1400°C for 16.5 h. Therefore, to

achieve a thick $Z_{1/2}$-free region in an SiC epilayer with a high initial $Z_{1/2}$ concentration ($> 10^{13}$ cm^{-3}), thermal oxidation at a high temperature (1400°C) is recommended.

In Chapter 6, using n-type (with different N doping levels) 4H-SiC epitaxial layers irradiated by low-energy (250 keV) electrons with different fluences, which mainly causes carbon displacement, the author was able to use different techniques (C-V, DLTS and EPR) to quantitatively compare the $Z_{1/2}$ center with the carbon vacancy (V_C) in the same samples. The $Z_{1/2}$ center and V_C defect were found to be the dominant defects responsible for the carrier compensation observed in the irradiated samples. In addition, the $Z_{1/2}$ concentration corresponds to the V_C concentration irrespective of the doping concentration and the electron fluence. Moreover, the energy level of $V_C^{2-/0}$ obtained by photo-EPR and *ab initio* calculation well agrees with that of the $Z_{1/2}$ center, all of which show negative-U nature. Thus, the $Z_{1/2}$ center must correspond to the $(2-/0)$ level of V_C.

In Chapter 7, the origin of deep levels generated by thermal oxidation was discussed. The ON1 ($E_C - 0.84$ eV) and ON2 ($E_C - 1.1$ eV) centers showed very similar behaviours in oxidized, C^+- or Si^+-implanted, and N_2O-oxidized samples, where the ON1 concentration and ON2 concentration have an one-to-one correspondence. Thus, the ON1 and ON2 centers could originate from the same defects in different charge states. In addition, these centers may be related to both of carbon interstitial (C_I) and N atoms because (i) the depth profiles after oxidation followed the C_I distribution calculated from diffusion equations and (ii) a higher concentration of these centers was generated after N_2O (or NO) oxidation compared with O_2 oxidation.

The HK0 ($E_V + 0.79$ eV) and HK2 ($E_V + 0.98$ eV) centers were generated by thermal oxidation, electron irradiation, and C^+/Si^+ implantation, and eliminated by Ar annealing at temperatures over 1400°C. From the generation and elimination behaviours of the HK0 and HK2 centers, they may originate from a complex including carbon interstitial(s) such as $(C_I)_2$, $(C_3)_{Si}$, or $((C_2)_{Si})_2$. PL signals corresponding to these C_I-related complexes have been reported in electron-irradiated SiC, thermal stability of which is similar to that of the HK0 center. Following all the results, the author could describe the behavior of the point defects (and deep levels) in SiC during oxidation and during subsequent Ar annealing.

In Chapter 8, the author attempted to control bulk carrier lifetimes in SiC epilayers by controlling the $Z_{1/2}$ concentration. By electron irradiation, bulk carrier lifetimes could arbitrarily be reduced, using SRH model and experimental data about the effects of the irradiation condition (the electron energy and fluence) on the $Z_{1/2}$ center. In contrast, creating a thick $Z_{1/2}$-free region by thermal oxidation improved measured carrier lifetimes. Using the calculation based on a diffusion equation, this enhancement of measured carrier lifetimes was found to be attributed to the expansion of long-bulk-carrier-lifetime (50 μs) region from the surface by the elimination of the $Z_{1/2}$ center. By oxidation at a high temperature and for a long period, a bulk carrier lifetime in the whole epilayer can be enhanced to about 50 μs. After this oxidation, using electron irradiation, the carrier lifetime in the oxidized epilayer can be uniformly reduced to a carrier lifetime required for each SiC

device. In this manner, bulk carrier lifetimes in SiC epilayers can be controlled by electron irradiation and thermal oxidation.

9.2 Future Outlook

Through this study, several issues in deep levels in SiC and the impacts on carrier lifetimes have been clarified. However, there remain several issues to be solved, and there have emerged several goals to be accomplished in the future.

- **Impacts of deep levels on SiC device performance:**

  Although the relation between the $Z_{1/2}$ center and a carrier lifetime was revealed, the impacts of other deep levels on SiC device performance are not clear. The type (donor-like or acceptor-like) of the deep levels should be clarified because acceptor-like levels compensate donors, whereas donor-like levels compensate acceptors. In addition, studies on a deep level that limits a carrier lifetime in $Z_{1/2}$-free epilayers are important.

- **A lifetime killer in *p*-type SiC epilayers:**

  In *p*-type SiC epilayers, measured carrier lifetimes are ~ 3 μs even in about 150 μm-thick epilayers after thermal oxidation [1]. Although several post-oxidation treatments such as surface passivation has been attempted [2, 3], the carrier lifetime is much lower than that of *n*-type epilayers, suggesting that a bulk carrier lifetime in *p*-type materials is suppressed by another recombination path. Revealing this path should lead to control of carrier lifetimes in *p*-type epilayers and thereby realization of high-performance SiC switching devices such as thyristors and *p*-channel insulated gate bipolar transistors (IGBTs).

- **Effects of structural defects on carrier lifetime:**

  When the $Z_{1/2}$ center was eliminated by thermal oxidation, carrier lifetimes in some area of the oxidized samples were limited to relatively low values (e.g. 2 μs, not shown). In general, various kinds of structural defects such as threading dislocations, basal plane dislocations, and stacking faults exist in SiC epilayers, which could reduce carrier lifetimes. Some of the structural defects are known to appear and expand by annealing [4, 5], which should be considered when a carrier lifetime is controlled using thermal oxidation and Ar annealing. For complete control of carrier lifetimes in SiC epilayers, structural defects that influence carrier lifetimes and generation condition of these defects should be ascertained.

- **Temperature dependence of carrier lifetimes:**

Although temperature dependence of carrier lifetimes in a semiconductor is very important for high-reliability power devices, that in SiC has not sufficiently been understood. To fabricate high-reliability SiC power devices, carrier lifetimes at high temperatures (room temperature–500°C) should be investigated in n-type and p-type SiC epilayers. Note that lifetimes at very high temperatures (> 200°C) are also important for SiC power devices because these are attracting attention as high-temperature-operating devices. This investigation can also leads to understanding recombination processes of excess carriers in SiC epilayers and thereby complete control of carrier lifetimes.

- **Origin of deep levels:**

  In this study, the origin of the $Z_{1/2}$ center was clarified using DLTS and EPR. The combination of these measurements should be powerful to identify the origin of other deep levels. Using this method, deep levels related to a single C_I, silicon vacancy (V_{Si}), and silicon interstitial (Si_I) should be investigated.

- **Acceleration of the $Z_{1/2}$ reduction:**

  The reduction of the $Z_{1/2}$ center was enhanced by several ways, leading to ~ 100 μm-thick-$Z_{1/2}$-free epilayers. To obtain thicker $Z_{1/2}$-free epilayers in samples with a higher initial $Z_{1/2}$ concentration, however, a more efficient method is required. Oxidation at higher temperatures (> 1400°C) is one of the candidate.

References

[1] T. Hayashi, K. Asano, J. Suda, and T. Kimoto, *Journal of Applied Physics* **109**, 014505 (2011).

[2] T. Hayashi, K. Asano, J. Suda, and T. Kimoto, *Journal of Applied Physics* **109**, 114502 (2011).

[3] T. Hayashi, K. Asano, J. Suda, and T. Kimoto, *Journal of Applied Physics* **112**, 064503 (2012).

[4] P. O. Å. Persson, L. Hultman, M. Janson, A. Hallén, and R. Yakimova, *Journal of Applied Physics* **93**, 9395 (2003).

[5] M. Nagano, H. Tsuchida, T. Suzuki, T. Hatakeyama, J. Senzaki, and K. Fukuda, *Journal of Applied Physics* **108**, 013511 (2010).

List of Publications

A. Full Length Papers and Letters

1. K. Kawahara, G. Alfieri, and T. Kimoto,
"Detection and Depth Analyses of Deep Levels Generated by Ion Implantation in n- and p-type 4H-SiC,"
Journal of Applied Physics **106**, 013719 (2009).

2. K. Kawahara, M. Krieger, J. Suda, and T. Kimoto,
"Deep Levels Induced by Reactive Ion Etching in n- and p-type 4H-SiC,"
Journal of Applied Physics **108**, 023706 (2010).

3. K. Kawahara, J. Suda, G. Pensl, and T. Kimoto,
"Reduction of Deep Levels Generated by Ion Implantation into n- and p-type 4H-SiC,"
Journal of Applied Physics **108**, 033706 (2010).

4. S. Sasaki, K. Kawahara, G. Feng, G. Alfieri, and T. Kimoto,
"Major Deep Levels with the Same Microstructures Observed in n-type 4H-SiC and 6H-SiC,"
Journal of Applied Physics **109**, 013705 (2011).

5. K. Kawahara, J. Suda, and T. Kimoto,
"Analytical Model for Reduction of Deep Levels in SiC by Thermal Oxidation,"
Journal of Applied Physics **111**, 053710 (2012).

6. S. Ichikawa, K. Kawahara, J. Suda, and T. Kimoto,
"Carrier Recombination in n-Type 4H-SiC Epilayers with Long Carrier Lifetimes,"
Applied Physics Express **5**, 101301 (2012).

7. N. T. Son, X. T. Trinh, L. S. Løvlie, B. G. Svensson, K. Kawahara, J. Suda, T. Kimoto, T. Umeda, J. Isoya, T. Makino, T. Ohshima, and E. Janzén,
"Negative-U System of Carbon Vacancy in 4H-SiC,"
Physical Review Letters **109**, 187603 (2012).

8. K. Kawahara, J. Suda, and T. Kimoto,
"Deep Levels Generated by Thermal Oxidation in p-type 4H-SiC,"
Journal of Applied Physics **113**, 033705 (2013).

9. K. Kawahara, X. T. Trinh, N. T. Son, E. Janzén, J. Suda, and T. Kimoto,
"Investigation on Origin of $Z_{1/2}$ Center in SiC by Deep Level Transient Spectroscopy and Electron Paramagnetic Resonance,"
to be submitted to *Applied Physics Letters*.

10. K. Kawahara, J. Suda, and T. Kimoto,
"Deep Levels Generated by Thermal Oxidation in n-type 4H-SiC,"
in preparation.

11. K. Kawahara, X. T. Trinh, N. T. Son, E. Janzén, J. Suda, and T. Kimoto,
"Quantitative Comparison between $Z_{1/2}$ Center and Carbon Vacancy in 4H-SiC,"
in preparation.

B. International Conferences

1. K. Kawahara, G. Alfieri, and T. Kimoto,
"Deep Levels Generated by Ion-implantation in n- and p-type 4H-SiC,"
Materials Science Forum **615-617**, 365 (2009).
(*Proc. of the 7th European Conf. on Silicon Carbide and Related Materials, Barcelona, Spain, 2008.*)

2. K. Kawahara, G. Alfieri, M. Krieger, and T. Kimoto,
"Reactive-Ion-Etching Induced Deep Levels Observed in n-type and p-type 4H-SiC,"
Materials Science Forum **645-648**, 759 (2010).
(*Proc. of the 13th Int. Conf. on Silicon Carbide and Related Materials, Nürnberg, Germany, 2009.*)

3. K. Kawahara, G. Alfieri, T. Hiyoshi, G. Pensl, and T. Kimoto,
"Effects of Thermal Oxidation on Deep Levels Generated by Ion Implantation into n-type and p-type 4H-SiC,"
Materials Science Forum **645-648**, 651 (2010).
(*Proc. of the 13th Int. Conf. on Silicon Carbide and Related Materials, Nürnberg, Germany, 2009.*)

4. K. Kawahara, J. Suda, and T. Kimoto,
"Deep Levels in n- and p-type 4H-SiC Generated by Reactive Ion Etching and Their Reduction,"
2010 Spring Meeting of Mater. Res. Soc. Symp., San Francisco, 2010, B5-2.

5. T. Kimoto, T. Hayashi, K. Kawahara, Y. Nishi, and J. Suda,
"Improvement of Carrier Lifetimes in n-type 4H-SiC Epilayers",
2010 Spring Meeting of Mater. Res. Soc. Symp., San Francisco, 2010, B5-1.

6. T. Kimoto, M. Noborio, T. Hiyoshi, K. Kawahara, and J. Suda,
"Ion Implantation Technology for Advanced SiC Power Devices" (Invited),
The 18th Int. Conf. on Ion Implantation Technology, Kyoto, 2010, Tu-2.

7. K. Kawahara, J. Suda, and T. Kimoto,
"Diffusion Model for Reduction of Deep Levels in 4H-SiC by Thermal Oxidation,"
The 8th European Conf. on Silicon Carbide and Related Materials, Oslo, Norway, 2010, WeP-40.

8. T. Kimoto, G. Feng, T. Hiyoshi, K. Kawahara, M. Noborio, and J. Suda,
"Defect Control in Growth and Processing of 4H-SiC for Power Device Applications" (Plenary),
Materials Science Forum **645-648**, 645 (2010).
(*Proc. of the 8th European Conf. on Silicon Carbide and Related Materials, Oslo, Norway, 2010.*)

9. S. Sasaki, K. Kawahara, G. Feng, G. Alfieri, and T. Kimoto,
"Major Deep Levels with the Same Microstructures Observed in n-type 4H- and 6H-SiC,"
The 8th European Conf. on Silicon Carbide and Related Materials, Oslo, Norway, 2010, WeP-34.

10. K. Kawahara, J. Suda, and T. Kimoto,
"Elimination of Deep Levels in Thick SiC Epilayers by Thermal Oxidation and Proposal of the Analytical Model" (invited),
Materials Science Forum **717-720**, 241 (2012).
(*Proc. of the 14th Int. Conf. on Silicon Carbide and Related Materials, Cleveland, USA, 2011.*)

11. K. Kawahara, X. T. Trinh, N. T. Son, E. Janzén, J. Suda, and T. Kimoto,
"Investigation on Origin of $Z_{1/2}$ Center in SiC by DLTS and EPR,"
The 9th European Conf. on Silicon Carbide and Related Materials, St.Petersburg, Russia, 2012, Tu5-3.

12. T. Kimoto, J. Suda, K. Kawahara, H. Niwa, T. Okuda, N. Kaji, and S. Ichikawa,
"Defect Electronics toward Ultrahigh-Voltage SiC Bipolar Devices" (Invited),
The 9th European Conf. on Silicon Carbide and Related Materials, St.Petersburg, Russia, 2012, We6-1.

13. N. T. Son, X. T. Trinh, K. Kawahara, J. Suda, T. Kimoto, L. S. Løvlie, B. G. Svensson, T. Umeda, J. Isoya, T. Makino, T. Ohshima, and E. Janzén,
"$Z_{1/2}$ center in SiC: a negative-U system of carbon vacancy,"
The 9th European Conf. on Silicon Carbide and Related Materials, St.Petersburg, Russia, 2012, TuP-92 LN.

14. T. Kimoto, J. Suda, G. Feng, H. Miyake, K. Kawahara, H. Niwa, T. Okuda, S. Ichikawa, and Y. Nishi,
"Defect Electronics in SiC and Fabrication of Ultrahigh-Voltage Bipolar Devices" (Plenary),
ECS Transactions **50**, 25 (2012).
(*Proc. of Electrochem. Soc. Fall Meeting 2012, Honolulu, 2012.*)